UNIVERSIDAD DE CHILE

FACULTAD DE CIENCIAS FÍSICAS Y MATEMÁTICAS

DEPARTAMENTO DE GEOLOGÍA

DETERMINATION OF CRUSTAL ANATEXIS CONDITIONS FROM THERMODYNAMIC MODELLING AND ZIRCON DATA: THE CASE OF THE LATE TRIASSIC A- AND S-TYPE GRANITES IN THE HIGH ANDES OF CENTRAL CHILE (~30ºS)

TESIS PARA OPTAR AL GRADO DE DOCTOR EN CIENCIAS, MENCIÓN GEOLOGÍA

PABLO GUILLERMO MOLINA CANCINO

PROFESOR GUÍA:
MIGUEL ÁNGEL PARADA REYES

MIEMBROS DE LA COMISIÓN:
KATJA DECKART
FRANCISCO HERVÉ ALLAMAND
ALCIDES NÓBREGA SIAL

SANTIAGO DE CHILE

2022

RESUMEN DE LA TESIS PARA OPTAR AL GRADO DE: Doctor en Ciencias, Mención Geología.
POR: Pablo Guillermo Molina Cancino.
FECHA: 2022
PROFESOR GUÍA: Miguel Ángel Parada Reyes.

DETERMINACIÓN DE CONDICIONES DE ANATEXIA CORTICAL SEGÚN MODELACIÒN TERMODINÁMICA Y CONDICIONES DE CRISTALIZACIÓN DE CIRCÓN: EL CASO DE LOS GRANITOS A Y S DEL TRIÁSICO TARDÍO, ALTOS ANDES, CHILE CENTRAL (~30ºS)

Esta tesis se focaliza en las condiciones termodinámicas que favorecen la generación de fundidos anatécticos en distintos escenarios y en el origen de plutones corticales del Triásico Tardío en los Altos Andes de Chile Central, como estudio de caso. El ambiente magmático en el que los circones cristalizan y se preservan, heredados desde sus fuentes, sitúan el contexto petrogenético de estos últimos.

En ambientes de subducción, el escenario termal que explicaría la fusión de la corteza podría corresponder a efectos combinados de un incremento en la producción de calor radiactivo y advección de calor por surgencia e intrusión de magmas mantélicos, entre otros. Para fundir parcialmente la corteza, dentro de la ventana de eficiencia de extracción de líquidos residuales (cristalinidades de 50 a 70 vol.%), se requeriría una adición energética de 0.2 kJ/g. Los magmas generados en la corteza inferior alcanzarían la cristalinidad antedicha en un rango de temperatura amplio, en contraste con aquellos generados en la corteza media y superior donde una cristalinidad de >50 vol.% se obtiene a no más de *ca.* 50º de sus respectivos *solidus*. Líquidos de composición peraluminosa, se reproducen en todo el intervalo de temperaturas modelado, para la corteza inferior, mientras que para la corteza media y superior solo se reproducen líquidos de composiciones peralcalinas a temperaturas >700ºC.

El caso de estudio corresponde a rocas de la actividad ígnea del Triásico Superior de Chile Central, que constituye una fase de magmatismo de arco caracterizada por poseer algunos plutones con una singular signatura geoquímica de granitoides post-orogénicos de tipo A y S. Los cuerpos ígneos formados en este período penetran la raíz del arco del Paleozoico Superior, y alcanzan un nivel de emplazamiento epizonal. Los granitoides de tipo A poseen asociaciones minerales agpaíticas e hypersolvus, en contraste, los de tipo S presentan abundantes nódulos cordieríticos; ambos evidencian texturas de enfriamiento rápido de fases peritécticas metaestables. Este trabajo revela edades de U-Pb en circón en los intervalos 214±2 a 241±2(1σ) Ma y 209±3 a 236±2 (1σ) Ma, para dos muestras correspondientes al granito cordierítico peraluminoso del plutón Los Tilos, y el leucogranito anorogénico de hedenbergita y Fe-edenita del plutón Monte Grande, respectivamente. El amplio rango de edades de cada una de las muestras sugiere la presencia de una importante fracción de circones foráneos o heredados. En efecto, los modelos termodinámicos y cinéticos desarrollados para la preservación de circones, transportados en fundidos anatécticos, muestran que podrían corresponder a cristales heredados en condiciones de extracción, ascenso, y cristalización, excepcionalmente rápidas (llegando al *solidus* en menos de 12 kyr). Se infiere que estos circones fueron cristalizados en sus fuentes por enriquecimiento sustantivo de zirconio en los fundidos anatécticos primarios, no por variaciones en la temperatura; esto refleja consistencia con el cálculo de modelos de estrés cristalino de circones y con los bajos valores de Ti (ppm) reportados. En este caso, el ascenso adiabático de fundidos subsaturados en H_2O habría ocurrido aprovechando discontinuidades estructurales heredadas de ciclos tectónicos previos, remanentes de la etapa de amalgamación final de Gondwana. Estos fundidos habrían ascendido rápidamente hacia niveles de emplazamiento epizonal lo que habría evitado su cristalización súbita y mantenido la herencia cristalina desde sus fuentes corticales.

RESUMEN DE LA TESIS PARA OPTAR AL GRADO DE: Doctor en Ciencias, Mención Geología
POR: Pablo Guillermo Molina Cancino.
FECHA: 2022.
PROFESOR GUÍA: Miguel Ángel Parada Reyes.

DETERMINATION OF CRUSTAL ANATEXIS CONDITIONS FROM THERMODYNAMIC MODELLING AND ZIRCON DATA: THE CASE OF THE LATE TRIASSIC A- AND S-TYPE GRANITES IN THE HIGH ANDES OF CENTRAL CHILE (~30ºS)

This thesis is focalized in the thermodynamic conditions that favor the generation of anatectic melts in different scenarios, and also as a study case, about the origin of crust-related plutons of the Late Triassic, in the High Andes of Central Chile. The magmatic environment in which zircon is crystallized and preserved, inherited from source, is also disentangled in light of the anatectic conditions achieved.

In a subduction setting, the thermal scenario that explains crust *anatexis* could correspond to combined effects due to an increased production of radioactive heat, and/or heat advection by upwelling of mantle magmas, among many others. To partially melt the crust, within the *melt extraction efficiency window* (crystallinities between 50 to 70 vol.%), an addition of 0.2 kJ/g would be required. Magmas generated in the Lower Crust reach these crystallinities in a wide temperature interval, in contrast with those generated in the Middle and Upper Crust, in which crystallinities <50 vol.% are set to be held at temperatures no higher than 50° from their respective *solidii*. Peraluminous melts are reproduced in the whole modeled range, for the Lower Crust, whereas anatectic melts of peralkaline composition are mostly common in the Middle and Upper crust, at temperatures above 700°C.

This study case corresponds to rocks generated in the igneous activity of the Late Triassic, in Central Chile. This activity is characterized by a phase of arc magmatism, in which some singular plutons share geochemical signatures related to post-orogenic A- and S-type granites. The igneous bodies formed in this period pierce the root of the Upper Paleozoic arc, reaching an epizonal level of emplacement. The A-type granites show agpaitic and hypersolvus mineral associations, whereas S-type granites highlight abundant cordieritic nodules. Both of them show clear evidence of rapid cooling of metastable peritectic minerals (cordierite, β-quartz paramorphs, and hedenbergite). This work reveals U-Pb in zircon ages within the 214±2 to 241±2(1σ) Ma and 209±3 to 236±2 (1σ) Ma, for samples corresponding to the peraluminous cordierite-bearing granite of the Los Tilos pluton, and for the peralkaline hedenbergite and Fe-edenite-bearing leucogranite of the Monte Grande pluton, respectively. The ample age range, in each of the selected samples, suggests the presence of an important fraction of foraneous zircons as xenocrysts and/or crystals inherited from the source. The thermodynamic and kinetic models developed in this study, reveal that zircons dragged in anatectic melts could correspond to inherited crystals formed at depth, and carried in rapidly ascending melts (reaching the granite *solidus* in less than 12 kyr after extraction). It is inferred that zircon grains were crystallized in the feeding magma's source, by zirconium enrichment of the primary anatectic melts, not by temperature variations; this is consistent with lattice stress models calculations, and with the remarkably low Ti-in-zircon concentration reported here. In this case, the adiabatic ascent of water-undersaturated melts might have been facilitated by structural discontinuities inherited from previous tectonic cycles, remnants of the final amalgamation of Gondwana. These melts reached an epizonal level of emplacement, rapidly enough to prevent melt stagnation *en route* to the surface, by which efficient crystal inheritance from their crustal source was achieved.

A Emilia, mi hija

A mis padres

A mis hermanos

AGRADECIMIENTOS

Agradezco al Proyecto CONICYT-FONDAP 15090013, del Centro de Excelencia en Geotermia de los Andes (CEGA), que financió asistencia a congresos, terrenos y análisis efectuados en el desarrollo de esta tesis, como también a la beca de doctorado CONICYT (Folio 21150905) por su apoyo en manutención económica y arancelaria.

Un afectuoso reconocimiento a Miguel Ángel Parada y Francisco Gutiérrez, quienes acogieron gustosos todas mis inquietudes e interrogantes petrológicas, desde mis estudios de pregrado, y a lo largo de mi estadía en posgrado en el Departamento de Geología de la Universidad de Chile. Agradezco también a quienes indujeron ideas e interrogantes fundacionales en el desarrollo de mi pensamiento científico crítico: Francisco Hervé y Mario Vergara. Especial mención a Scott Paterson y Calvin Barnes, por su disposición a entablar discusiones que derivaron en inferencias fructíferas en la capitalización de mis escritos finales.

A mis compañeros de ruta petrológica, Ítalo Payacán y Javier Reyes.

Un infaltable agradecimiento a mis amigos y eximios miembros del connotado grupo RAP: Javier Álvarez, Sebastián Bascuñán, Iván Gómez, Sebastián Herrera y Matías Peña.

A Constanza Ernst y Daniela Becerra, del Centro Psicológico 1006, por el apoyo emocional en esta difícil recta final.

Al personal administrativo y colegas del Laboratorio de Microscopía Electrónica y Análisis de Rayos X (LAMARX), de la Universidad Nacional de Córdoba, por su calidad humana y apoyo analítico en mi breve estadía en su Departamento.

Agradezco a todo el personal del Departamento de Geología de la Universidad de Chile, del Laboratorio de Preparación de Muestras del mismo, y del Centro de Excelencia en Geotermia de los Andes (CEGA), por su disponibilidad, profesionalismo, y apoyo absoluto en todo momento.

Table of Content

FIGURES AND TABLES INDEX

CHAPTER 1. MOTIVATION

The motivation of this study comes from the observation that high-temperature zircons are inherited in many peralkaline intrusive bodies related to attenuated lithosphere settings (e.g. Williams, 1992) (see the discussion on the geochemistry of zircon forming magmas in **Chapter 2**). The contrast in zircon saturation temperatures in different tectonomagmatic settings (bearing somewhat similar G values) reveals that zirconium enrichment explains the early crystallization of zircons in magmas formed in rift and anorogenic settings, compared to the lower zircon saturation temperatures displayed by calc-alkaline magmas (**Fig. 1.1**), in which zircon is commonly a late-stage accessory phase. In the former tectonomagmatic contexts, preservation and inheritance of metastable zircons (e.g. Kemp et a., 2005) could be explained by rapid magma ascent through the lithosphere (e.g. Bea et al., 2007) and armoring by high-temperature silicates (Watson, 1996; Paterson et al., 2016). This study explores the different petrogenetic variables that may influence the magma's zircon inheritance and how they relate to a thinned lithosphere geotectonic context. Additionally, insights into the meaning of zircon age spectra in other geological settings will be provided.

The chosen study cases correspond to Late Triassic A- and S-type granite bodies registered in the High Andes of Central Chile (Parada, 1988), that culminates a long period of post-collisional arc magmatism (Spalletti and Limarino, 2017), followed by orogenic collapse, crustal thinning, and subsequent migration of arc *loci* to the west (*ca*. 100 km). This event is characterized by a bimodal expression of crustal and mantle magmas (e.g. Morata et al., 2000). Particularly, high-silica rhyolites (González et al., 2017), mafic dike swarms (Creixell et al., 2007), and the post-orogenic intrusions of the Coastal Range and High Andes of Central Chile (Gana, 1991; Vásquez et al., 2008; Casquet et al., 2014; Oliveros et al., 2018), emplaced at around 217.4±0.5 Ma ($^{40}Ar/^{39}Ar$ in biotite; Murillo et al., 2017), have been recognized. The geochemical and source diversity of such coeval magmatism, and apparent zircon inheritance (**Fig. 1.2**), depict a unique case to address the weight of the different petrogenetic factors that could influence the magma potential to crystallize and preserve zircons at magmatic temperatures.

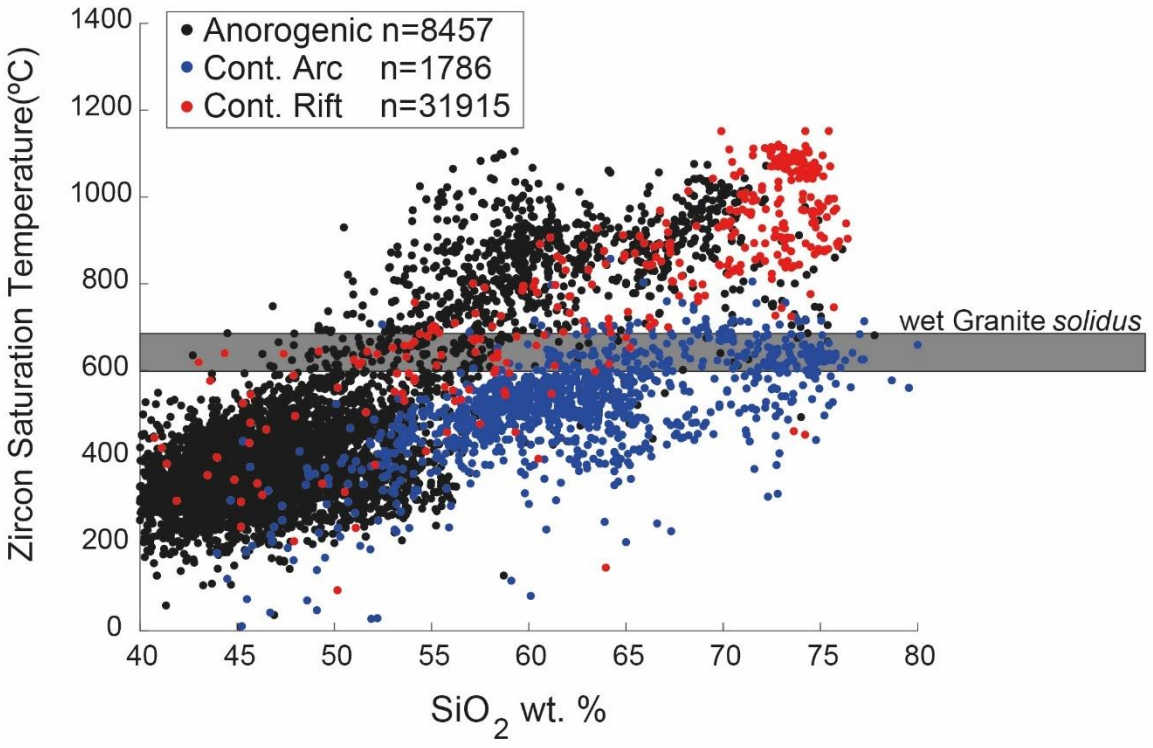

Figure 1.1: Zircon saturation temperatures (°C) were calculated after the formulation of Gervasoni et al. (2016) for the whole geochemistry of anorogenic magmas (Cenozoic circum-Mediterranean anorogenic igneous province; Lustrino and Wilson, 2007), continental arc magmas (Meso-Cenozoic magmatic rocks of the Central Andes; Mamani et al., 2010), and continental rift magmas (East African Rift System; GEOROC database, Max Planck Institute for Chemistry, georoc.mpch-mainz.gwdg.de/georoc). Displayed values on the ordinate axis differ, showing greater values for thinned lithosphere contexts (anorogenic and continental rift settings), compared with those of 'normal' lithosphere (continental arc magmas). This is a consequence of different zirconium contents of sources. See text for discussion. Wet granite *solidus* temperature range (>1 kbar pressure) after Holtz and Johannes (1994).

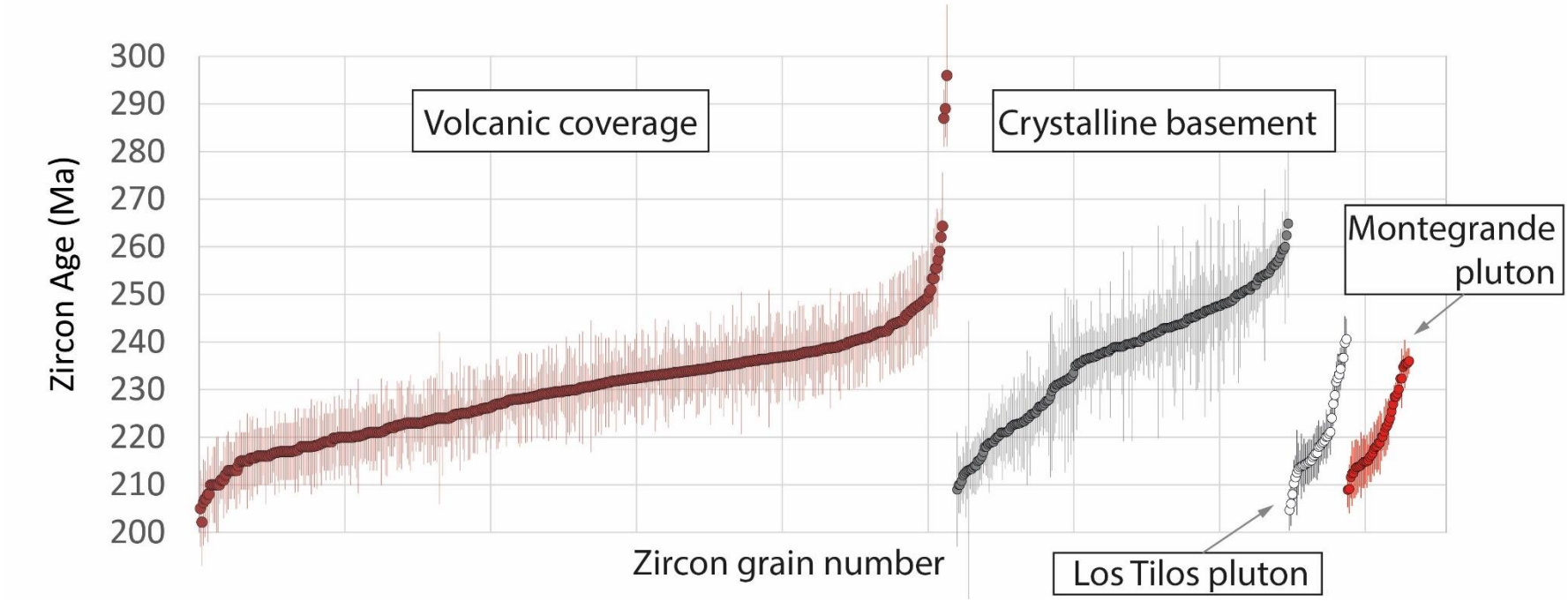

Figure 1.2: Zircon ages distribution (U-Pb dating by SHRIMP and LA-ICP-MS methods) of the igneous units referred to in this thesis, depicting the geochronological onlap recognized in the upper Paleozoic to early Mesozoic magmatism, and could be ascribed to zircon inheritance to some extent. Dated grains ages are reported within a 2σ confidence interval. Volcanic coverage rocks (Salazar et al., 2013; Hervé et al., 2014; Ortiz and Merino, 2015; Murillo et al., 2017); Crystalline basement rocks (Salazar et al., 2013; Hervé et al., 2014; Ortiz and Merino, 2015; Murillo et al., 2017); Monte Grande pluton (MGp) (Hervé et al., 2014 and this work); Los Tilos pluton (LTp) (Hervé et al., 2014 and this work). The emplacement date of the post-orogenic plutons (MGp and LTp) is around 217.4±0.5 Ma ($^{40}Ar/^{39}Ar$ in host-rock biotite; Murillo et al., 2017).

CHAPTER 2. INTRODUCTION

Zircon geochronology has been a widely used tool to estimate the duration of granite formation and emplacement processes (e.g. Paterson et al., 2016; Ratschbacher et al., 2018; Ardill et al., 2018), and also to constrain the timing of regional deformation (e.g. Paterson and Tobisch, 1988). This mineral has become a clue petrogenetic phase of upmost importance in geochronology and petrogenesis (Siégel et al., 2017). Its resilient nature is reflected by its capability to survive dissolution by magmatic reworking (Watson, 1996; Miller et al., 2003; Bea et al., 2007; Gómez-Tuena et al., 2018). This fact, along with sluggish cation diffusion rates (Cherniak et al., 1997) and vastly studied U-Pb isotope systematics (Cherniak and Watson, 2001), have been used to unravel the complex petrogenetic history of collisional, post-collisional anatectic terranes, and subduction-related plutons (Noble and Searle, 1995; Bacon et al., 2005; Miller et al., 2007; Claiborne et al., 2010; Broderick et al., 2015; Marsh et al., 2015; Rocha et al., 2016).

To address the meaning of pluton zircon ages, several works have tackled this issue through thermal modeling (e.g. Glazner et al., 2004). These studies have shown that there is a direct correlation between the volume of emplaced magma, the time span of reservoir survival over *solidus* temperatures, and rates of magma supply (de Saint Blanquat et al., 2011; Ratschbacher et al., 2018) (**Fig. 2.1**). This is a consequence of the development of crystalline mush rejuvenation processes, driven by incremental growth of igneous bodies (Annen, 2009; Menand et al., 2015), wholesale magma chamber convection (e.g. Gutiérrez and Parada, 2010), advection of felsic segregates (Aravena et al., 2017), and late-stage latent heat buffering (Huber et al., 2009; Namur et al., 2014). Discrepancies between the displayed time span of dated zircons and calculated time-dependent thermal models may be ascribed to overlooked reheating mechanisms (e.g. Glazner et al., 2004; Molina et al., 2015; Schmidt et al., 2016). Furthermore, it is widely accepted that, in some cases, a fraction of the zircon grain budget might be inherited from the source or due to previous stagnation events (Hansmann and Oberli, 1991; Miller et al., 2007; Scott et al., 2011). These facts difficult the interpretation of thermal models and entail a need for a better understanding of the systematics of zircon inheritance and crystallization in disparate magmatic systems.

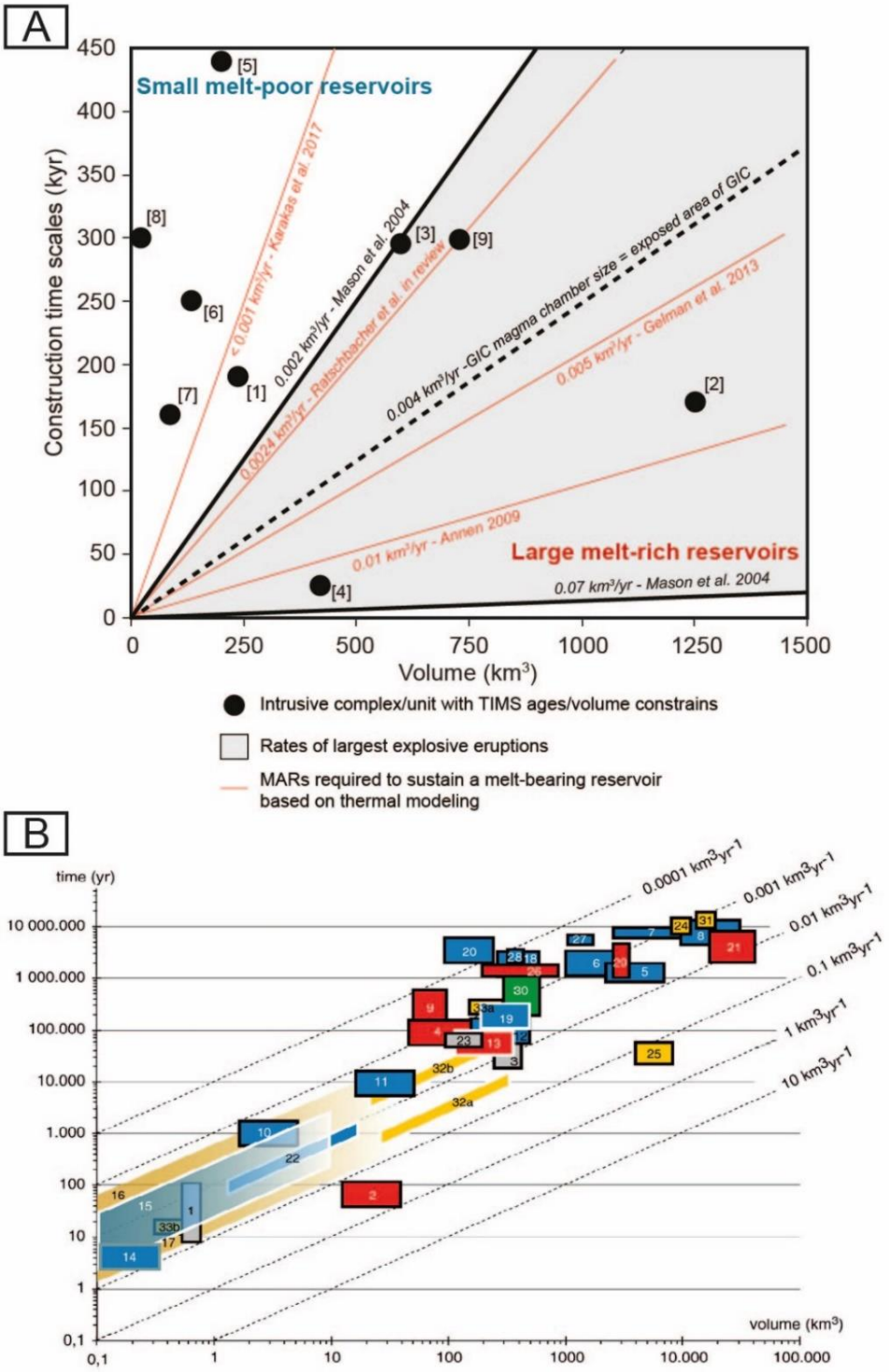

Figure 2.1: Plots showing the relationship between obtained timespan over *solidus* temperatures (from U-Pb zircon geochronology), the estimated volume of reservoirs, and calculated Magma Addition Rates (MAR) (km^3/yr). **A.** Observed melt-poor reservoirs plot at the low MAR field, whereas melt-rich reservoirs plot at the high MAR field. Refer to its source for a detailed explanation and symbology (Ratschbacher et al., 2018). **B.** A comparison between pluton construction rates, volume, and timespan, for magmas emplaced in different tectonic settings (showing no correlation with the latter qualitative variable). See De Saint Blanquat et al. (2011) for a detailed explanation.

2.1. The duration of magma pulses in light of the water budget of reservoirs

Since several decades, a wide diversity of experimental studies have been conducted to understand the behavior of the haplogranite system over crustal P-T conditions (Chappell and White, 2001; Gao et al., 2016). The role of water in granite petrogenesis is undisputed. Many authors recognize its importance in the stability field of rock-forming silicates (Puziewicz and Johannes, 1990; Castro, 2013; Scaillet et al., 2016), crystallinity-temperature profiles (e.g. Whitney, 1988), and heat distribution processes within the crust (e.g. Cao et al., 2019), thus controlling the level of emplacement (e.g. Waters and Lange, 2017) and the rate at which magmatic differentiation proceeds (Richet et al., 2006).

Moreover, the duration and rates at which feeding magmas constitute igneous bodies depend on the water content of magmatic systems, which constrains the rates at which magma extraction and evolution proceeds (Schmidt et al., 2016; Petrelli et al., 2018), near the source (e.g. Hermann and Rubatto, 2003; Diener et al., 2014) up to the final emplacement site (e.g. Schoene et al., 2012). In addition, the current school of thought understands the lithological and geochemical diversification of magmas as a result of mechanical-driven processes governed by the physics of fluid dynamics (Sparks et al., 1984; Dufek and Bachmann, 2010; among many others). Because the aforementioned processes operate at disparate rates (Petford et al., 2000) either as cyclic (e.g. Kemp and Hawkesworth, 2005; De Saint Blanquat et al., 2011), continuous (Rocha-Campos et al., 2011), or discrete events in geologic time (Martin et al., 2012), an uneven spatial and diachronous distribution of pulses in shallow intrusions, is expected (e.g. Matzel et al., 2006; Memeti et al., 2010; Scott et al., 2011; Ardill et al., 2018) (**Fig. 2.2**). Consequently, the interpretation of the geochronology of magmatic products is being re-assessed (e.g. Caricchi et al., 2016), and puts new challenges on the meaning of average pluton ages (Rodríguez et al., 2019).

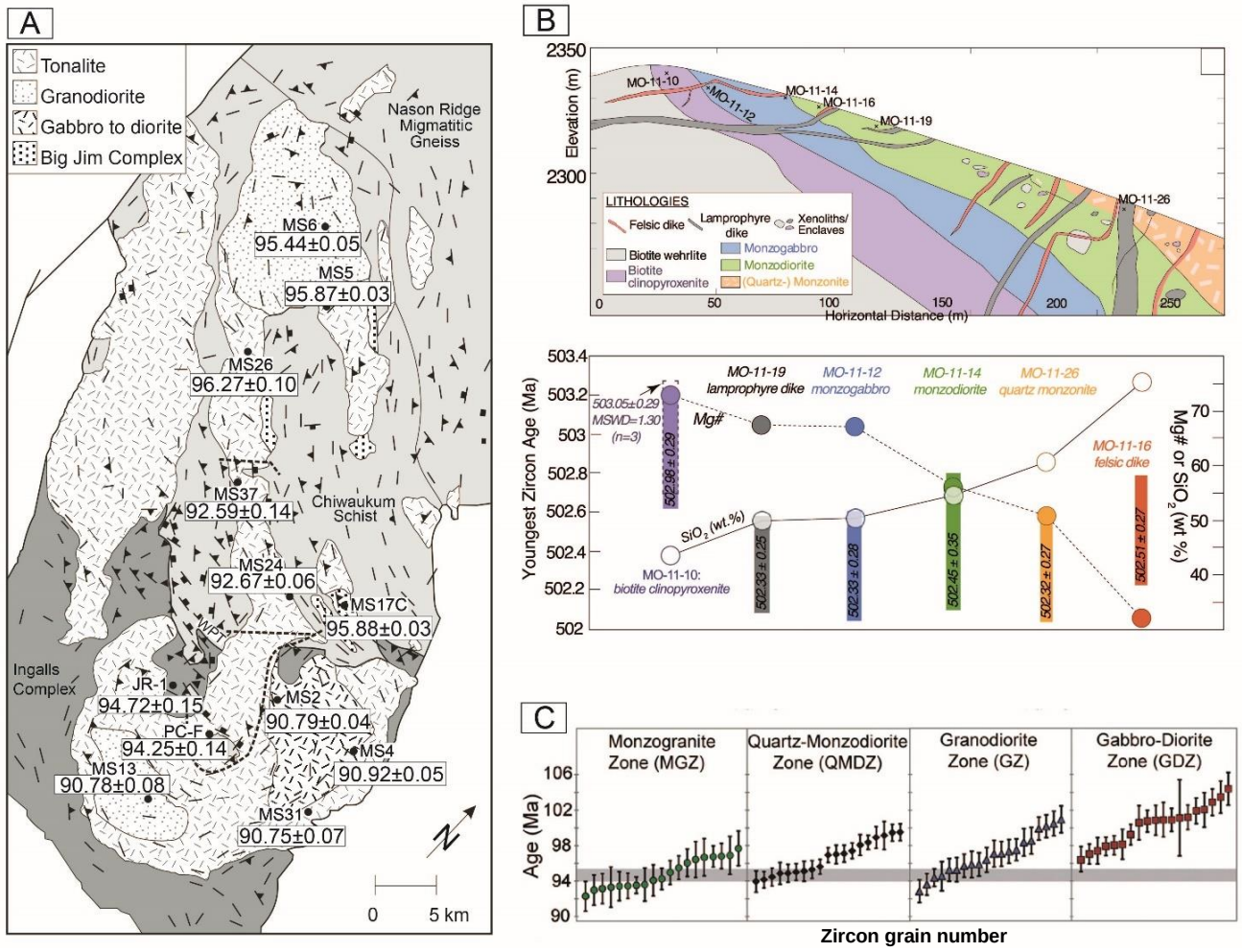

Figure 2.2.: Heterochronous distribution of U-Pb zircon ages in lithological zones of different plutons without inherited zircons from source (yet, authors discuss the probability of antecrystic entrainment from previous reservoir mushy portions). As a consequence, displayed zircon ages represent the duration of emplacement-site processes. A. Map of the Mount Stuart batholith, showing the different lithological zones (legend at the upper left inset) and their average zircon sample average age. Note that average ages of the different lithological zones have few age onlaps (within displayed errors), and represent the moment at which the different amalgamated increments took place (modified from Matzel et al., 2006) B. Cross section and U-Pb zircon ages of samples extracted from the different lithological zones of the Dariv Igneous Complex, western Mongolia. Here magmatic differentiation rates are estimated from geochronology (extracted from Schmidt et al., 2016). C. U-Pb zircon age spectra of the four different lithological zones of the composite Caleu pluton. Here, zircons date the protracted late-magmatic stage of the pluton construction, in which mush rejuvenation through syn-magmatic diking is invoked to explain such a long-lived stage (modified from Molina et al., 2015).

2.2. Geochemical insights into the interpretation of the occurrence of zircon in crustal A- and S-type magmas

Several experiments have been developed to provide geochemical conditions for the expected temperature at which zircon saturates in magmatic systems (Boehnke et al., 2013; Gervasoni et al., 2016; among others). The main results are: (1) magmas in excess of alumina (peraluminous S-type) stabilize zircons at higher temperatures in contrast with those in a deficit of alumina (particularly peralkaline A-type); and (2) increasing the zirconium content of hosting magmas may, as well, anticipate zircon saturation in cooling melts.

Despite the fact that A-type granites appear as ephemeral magma pulses (Martin et al., 2012) in Phanerozoic orogenic belts (*cf.* Windley, 1993), many of them display a wide spectrum of zircon ages, mainly product of sheer amounts of inherited zircons (Williams, 1992; Scott et al., 2011; Morales Cámera et al., 2018; Gao et al., 2019). A solid agreement holds that this type of magmatism is in close relation with mantle precursors (Kemp and Hawkesworth, 2005; Frost and Frost, 2011), concomitant with periods of tectonic relaxation and lithospheric thinning (Turner et al., 1992; Wu et al., 2002). They can result from extreme fractional crystallization of juvenile mantle magmas (Bonin, 2007), anatexis of lower crust material (Whalen et al., 1987; Eby, 1992; Landenberger and Collins, 1996), or as hybrid melts between these two end-members (e.g. Dahlquist et al., 2010). Either way, magmas formed in such conditions screen high HFSE, halogen, and low water contents at the source (Eby, 1990; Skjerlie and Johnston, 1993; Bonin, 2007), and are generated by high-temperature dehydration melting reactions (Patiño Douce, 1997; Gao et al., 2016). In terms of bulk-rock chemistry, the majority of A-type granites are peralkaline in composition (Whalen, 1987), but also they can be found as metaluminous, or even peraluminous granites (Bonin, 2007; Gao et al., 2016; Zhao et al., 2013).

Due to its peraluminousity and metasedimentary nature, magmatic reworking of xeno- and antecrystic zircon is commonly exhibited in S-type granites (e.g. Collins, 1998; Bea et al., 2006; Villaseca et al., 2007). In these granites, zircon is often found as restitic inclusions after dehydration melting of pelites and greywackes (Barbero and Villaseca, 1992; Rossi et al., 2001; Sandeman and Clark, 2002; René et al., 2008). Additionally, it may occur in minerals resulting from decompression breakdown of residual phases (Brown, 2013), and is interpreted as an early crystallizing accessory phase, sourced at residing melts saturated in zirconium (e.g. Ayers et al., 1997).

2.3. Study workflow

This study explores the meaning of the dates of zircons hosted in selected small-volume plutons of a crustal origin, with a large geochronological span at the sample scale. The unfolding thought-flow is, therefore:

The crystallization age span of dated zircons is directly proportional to the volume of magma reservoirs and rates of magma supply. Hence, small-volume igneous bodies with a large zircon age span are most probably explained by zircon inheritance from the source. Because, inheritance conditions of zircons are highly dependent on the geochemical characteristics of magmas, which correlate with the petrogenetic environment and anatectic conditions, the geochronological span of igneous bodies must be evaluated in terms of the different variables that depict each particular study case, such as partial melting P-T conditions, source geochemistry, rates of magma supply, mode of emplacement, and mush rejuvenation processes.

2.4. Geological context of the studied plutons

In the south-Central Andes, some Late Triassic plutonic bodies are related to anatexis, formed in extensional conditions (Mpodozis and Kay, 1992; Charrier et al., 2015). Bimodal magmatism is characteristic of this period (Gana, 1991; Parada, 1981; Parada, 1988; Morata et al., 2000), and forms part of a tectono-magmatic transition, from the end of Paleozoic terrane accretion to the western Gondwana margin to the initiation of the Andean orogeny in the Mesozoic (**Fig. 2.3**), namely pre-Andean and Andean cycles, respectively (Vásquez et al., 2011). Oxygen and hafnium isotope systematics in zircon show a progression from upper Paleozoic crustal-related magma sources to more mantle-like in the Triassic (Hervé et al., 2014; del Rey et al., 2016). Current models for the prevailing tectonic setting advocate to attenuated subduction in a thinned lithosphere (after the Permian compressional San Rafael orogenic phase) (Coloma et al., 2017; González et al., 2017); asthenospheric upwelling of mantle magmas could have induced crustal anatexis in some portions of the Triassic arc. Upper Triassic bimodal magmatism is recognized in the Coastal Range of Chile (ca. 31ºS) (Gana, 1991), depicted in an association of leucogranites, quartz-diorites, and gabbros, as well as aciditic and basic intercalations of volcanic products and related subvolcanic dikes (sourced at different lithospheric depths). They exhibit a wide range of initial strontium ratios ($^{87}Sr/^{86}Sr0$ values between 0.70397 and 0.71161) (Morata et al., 2000) and are emplaced in the Carboniferous to Permian accretionary prism. Farther south, also in the Coastal Range, Upper Triassic fayalite-bearing granite rocks have been identified and interpreted as anorogenic (Vásquez and Frantz, 2008). About 29-30ºS, in the Frontal Range, the same picture emerges: hosted within the Permian belt of the upper Paleozoic to Triassic Elqui-Limarí Batholith, scarce upper Triassic epizonal S-type peraluminous two-mica leucogranite plutons, A-type metaluminous Hedenbergite-bearing leucogranites, and an associated coeval mafic dike swarm (Parada et al, 1988) are recognized.

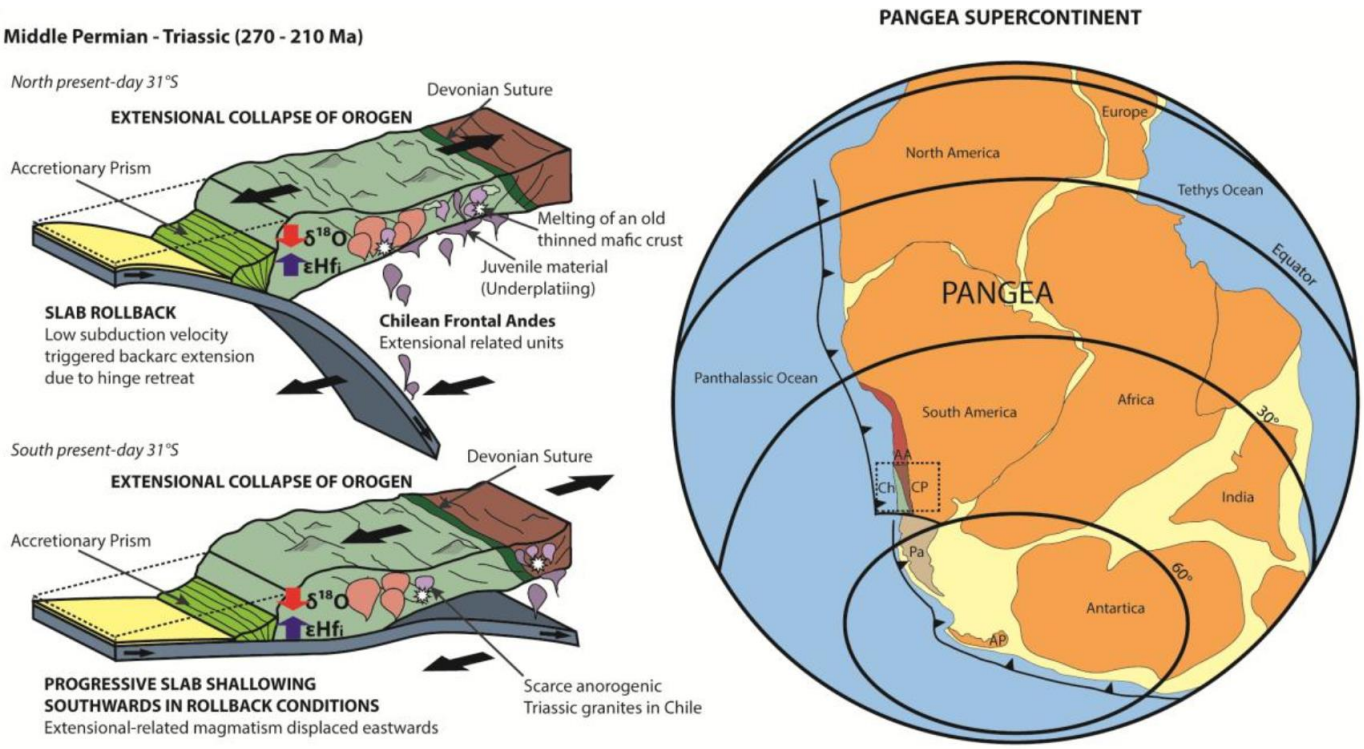

Figure 2.3: Late Paleozoic to Triassic evolution of the southwestern margin of Gondwana. Here the docking of a terrane in the Late Paleozoic is involved in crustal thickening, and a subsequent generation of collisional to post-collisional anorogenic granites, followed by orogenic collapse in the Late Triassic, characterized by bimodal magmatism. resembling an island arc setting. Extracted from del Rey et al. (2016).

2.4.1. The Elqui-Limarí batholith

According to Mpodozis and Kay (1990), the Elqui-Limarí batholith (part of the Chollay and Montosa-El Potro batholiths belt) found in the High Andes of North-Central Chile (28-31ºS) consists of two major intrusive suits (**Fig. 2.4**), the Carboniferous-Lower Permian "Elqui Superunit" (SUE) and the Permian-Triassic "Ingaguás Superunit" (SUI). The SUE comprises upper Carboniferous calc-alkaline tonalites and granodiorites, with a subduction-related geochemical signature (Guanta and Montosa Units), and Early Permian two-mica peraluminous granites of the Cochiguás and El Volcán Units, derived from partially melted metasedimentary rocks. The SUI is located roughly to the east of SUE outcrops. It consists of an association of late Permian to Triassic peraluminous shallow-level plutons, showing miarolitic cavities and graphic textures. They were assumed to be derived from a garnet-bearing thickened crust. Leucocratic granites, Bt(±Amp)-bearing granodiorites and pink hololeucocratic monzogranites constitute most of SUI volume (>80%), represented by the Los Carricitos, Chollay, and El León Units; the youngest products of this superunit are fine-grained Bt-granites and rhyolitic porphyries of the El Colorado Unit.

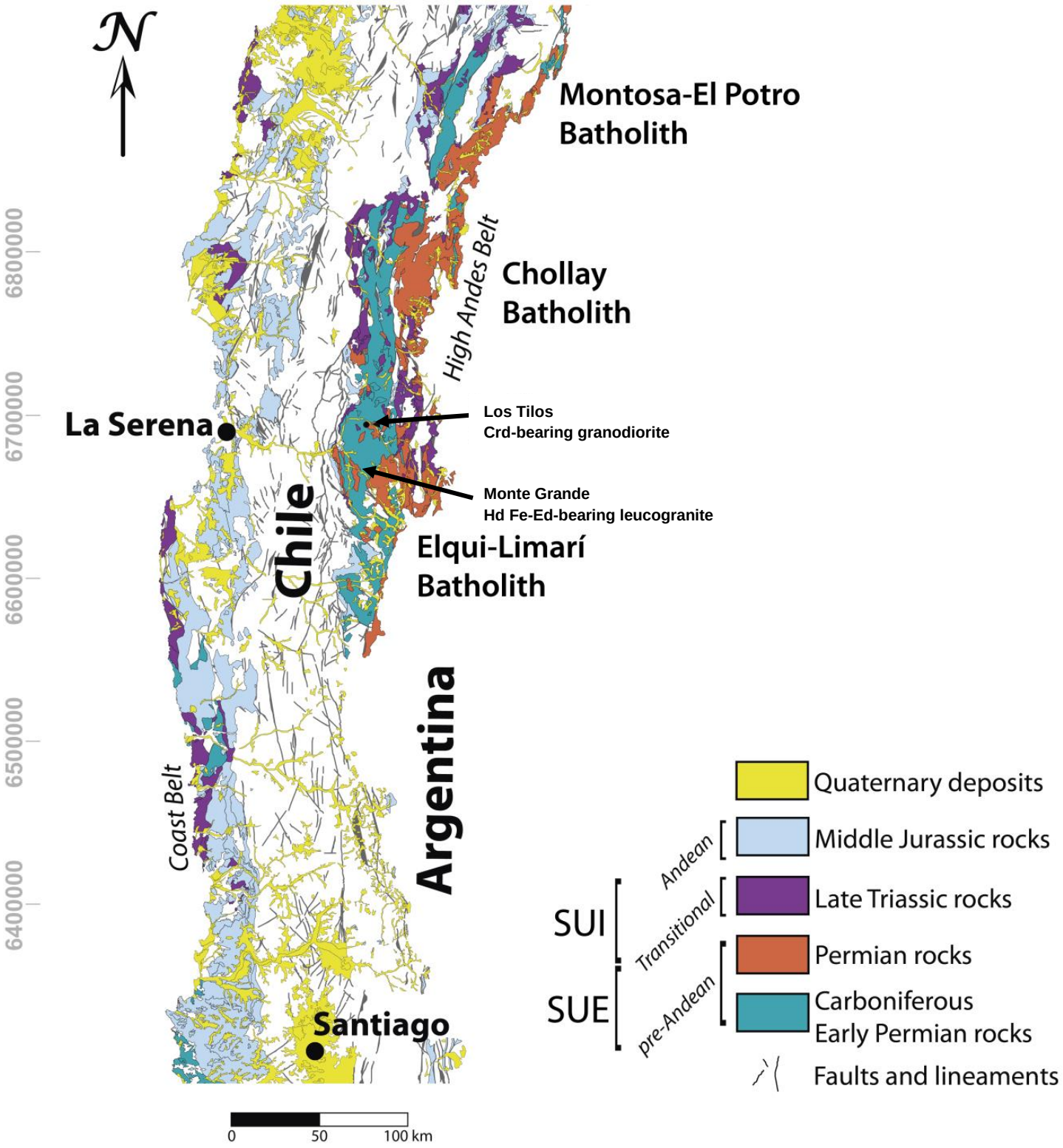

Figure 2.4. Distribution of pre-Andean, Transitional and Andean intrusives, along the Central Chile Andes. SUE and SUI stand for "Elqui Superunit" and "Ingaguás Superunit", respectively. Modified from Mapa Geológico de Chile escala 1:1.000.000 (http://portalgeomin.sernageomin.cl:6080/arcgis/rest/services).

2.4.2. Late Triassic post-orogenic plutons: the Los Tilos and Monte Grande plutons

The Los Tilos pluton is hosted within the SUE (**Fig. 2.4**). Mafic and felsic syn-plutonic dike swarms (a bimodal association), up to meter-scale dike widths, are recognized hosted in these units (Parada, 1990). A two-peak U-Pb zircon mean ages of 215 and 235 Ma is reported by Molina et al. (2020), whereas a 215.9 Ma age is reported by Hervé et al. (2014), making the Los Tilos pluton be considered as the Late Triassic "Transitional plutonism" of Central Chile (*sensu* Parada, 1990). This pluton is composed of medium K-Feldspar, plagioclase, and anhedral quartz. Titanite, apatite, and zircon are accessory phases. Large euhedral hexagonal-bipyramidal quartz (high-temperature β-quartz paramorphs; Parada, 1988; Ferreira et al., 2019) is part of centimetric cordierite-quartz-plagioclase nodules, surrounded by thin leucocratic rims (cockades); this might be associated with low-pressure biotite breakdown reactions (Barbey et al., 1999). Parada (1988) considered the composition of Los Tilos's muscovites containing Xce=0.15, obtaining a minimum crystallization pressure of 3 kb and a temperature of 670ºC for the coexisting feldspars in relatively oxidizing conditions (near the QFM+1 buffer). A local crustal influence in the generation of these magmas is suggested by zircon εHf isotopic values ranging from 0 to +3 and average $\delta^{18}O$ values of 6.4 ‰ (Hervé et al., 2014; **Fig. 2.3**).

The Monte Grande pluton is also hosted within the Guanta Unit (**Fig. 2.4**). In contrast to the Los Tilos pluton, very few mafic dikes intrude this igneous body. Oxygen isotopes in zircon display mantle-like values (in between 5 to 6 ‰ δ18O) (Hervé et al., 2014). This granite is composed of anhedral quartz, mesoperthitic hypersolvus K-feldspar, chloritized biotite, edenite, Fe-Hedenbergite, and accessory zircon, Fe-Ti oxides, allanite, and titanite (Parada, 1988). A fairly anhydrous origin and an epizonal level of emplacement for this pluton are suggested by the occurrence of nearly coeval and spatially-related rhyolitic porphyries with also hypersolvus K-feldspar and particular plagioclase zoning (Parada, 1981; 1983; 1984; 1988; 1990).

2.5. Objectives and methodologies

2.5.1. General objective

Constrain the crustal anatexis conditions and establish a conceptual model to explain the role of magma chemistry in the crystallization and preservation of zircons above the *solidus* of the late Triassic A- and S-type granites in the High Andes of Central Chile.

2.5.2. Specific objectives and methodologies

I. Recognize the geochemical characteristics and energetic requirement of anatectic products formed at different temperatures and water contents, for the Lower, Middle, and Upper Crust.

> **Methodologies:** (1) Thermodynamic modeling of isochemical pseudosections (Perple_X software; Connolly, 2005) of average crust compositions (obtained from Rudnick and Gao, 2003); (2) Compositional characterization of anatectic melts and restitic material, through mass balance (MATLAB R2017a); (3) Elaboration of relative enthalpy diagrams in the P-T space.

II. Determine whole-rock composition, and U-Pb zircon ages and geochemistry of the selected small granite bodies and identify probable mixed-population of zircons brought from their source (or elsewhere) up to the final emplacement site.

> **Methodologies:** (1) Field campaigns for lithological characterization and sampling; (2) Whole-rock geochemical data characterization (ICP-OES and ICP-MS); (3) U-Pb zircon spot ages and geochemistry (LA-ICP-MS).

III. Establish source materials, petrotectonic background, and emplacement conditions for the selected granite bodies.

> **Methodologies:** (1) Lithological characterization under the petrographic microscope; (2) Whole-rock geochemistry (IPC-OES and ICP-MS); (3) Mineral chemistry (EPMA); (4) Petrogenetic characterization in comparison with experimental petrology framework; (5) Numerical modeling (MATLAB r2017a) coupled with thermodynamic modeling (Perple_X software; Connolly, 2005) and compositional isopleths elaboration to establish formation and emplacement P-T conditions.

IV. Determine the duration of this magma pulse, identifying zircons of xenocrystic, antecrystic, and autocrystic origin (after Miller's et al. 2007 criteria).

Methodologies: (1) LA-ICP-MS U-Pb zircon geochronology of selected simples; (2) LA-ICP-MS geochemical characterization of dated zircons; (3) Cathodoluminescence imaging to identify out-of-context grains.

V. Model the timespan inherited zircons could survive, and how intensive variables (P-T-X) could influence the systematics of zircon formation.

Methodologies: (1) Implement equations of zircon crystallization kinetics (Watson, 1996) in a numerical simulation software (MATLAB R2017a); (2) Fix and couple thermodynamic models with estimated source and emplacement P-T conditions; (3) Establish the maximum timespan of zircon survival in the modeled P-T interval.

2.5.3. Analytical conditions and operating conditions

Rock samples (a total of 33) were ground and pulverized to at least 95% minus 200 mesh at the Laboratorio de Preparación de Muestras, Departamento de Geología, Universidad de Chile. Major and trace element analyses were obtained using ICP-emission spectrometry and ICP-MS, respectively, at the Activation Laboratories Lds., Ancaster, Ontario, Canada. The samples were mixed with lithium metaborate/tetraborate combined in an induction furnace, then poured into a solution of 5% nitric acid containing an internal standard and mixed continuously until completely dissolved. FeO values were determined through titration (using potassium dichromate) via cold acid digestion of ammonium metavanadate and hydrofluoric acid.

Two samples were collected for LA-ICP-MS U-Pb zircon geochronology and geochemistry (a total of 45 zircon grains). Zircon separation consisted of sample crushing and grinding followed by zircon concentration via Wilfley table, Frantz isodynamic magnetic separator, heavy liquid separation, and handpicking at Laboratorio de Preparación de Muestras, Departamento de Geología, Universidad de Chile. Cathodoluminescence images were acquired using a high-resolution Quanta 400 FEG environmental SEM connected to an Oxford INCA350 EDS and a Gatan Mono CL3+ system with 10 kV imaging conditions and 6.7 nm spot size. U-Pb isotopes and trace elements were analyzed simultaneously at the State Key Laboratory of Geological Processes and Mineral Resources, China University of Geosciences, Wuhan, using an Agilent 7500a ICP-MS apparatus coupled with a GeoLas 2005 laser ablation system with a DUV 193 nm ArF-excimer laser (MicroLas, Germany). Detailed analytical procedures and data reduction are available in Liu et al. (2010). A spot size of 32 μm was used. Argon was used as the make-up gas and mixed with the carrier gas (helium) via a T-connector before entering the ICP. Nitrogen was added to the central gas flow (Ar + He) of the Ar plasma to lower the detection limit and improve precision (Hu et al., 2008). Each analysis incorporated a background acquisition of 20–30 s (gas blank) followed by 50 s data acquisition. Zircon 91,500 was

used as a standard for mass discrimination and U-Pb isotope fractionation. The time-dependent drifts of U–Th–Pb isotopic ratios were corrected using linear interpolation (with time) for every five analyses according to the variations of standard 91,500. The preferred U–Th–Pb isotopic ratios used for 91,500 are from Wiedenbeck et al. (1995). The reproducibility of the U-Pb was evaluated by comparison with the secondary zircon standard GJ-1 (Jackson et al., 2004). Off-line integration of background and analyzed signals, time-drift correction, and quantitative calibration for trace element analyses and U-Pb dating, were performed using ICPMSDataCal (Liu et al., 2010). The uncertainties of preferred values for the external standard 91,500 were properly propagated. Concordia diagrams and weighted mean calculations were made using Isoplot/Ex_ver3 (Ludwig, 2003). Associated errors are quoted at the 1σ confidence level.

Electron microprobe analyses of major and trace elements of micas, cordierite, amphibole, pyroxene, and zircon were conducted using a JEOL JXA-8230 machine (LAMARX laboratory, FCEFyN at UNC, Argentina). A total of 181 spot analyses were performed, using a 15 kV accelerating voltage, a 10 nA current, and a 10 μm diameter beam. Reference standard materials were measured before each session for peak overlap, background, and offline corrections. Different crystals were used to perform the respective analyses, for the different elements. Micas: TAP (F, Na, Mg, Al), PETJ (K, Cl, Ca), LIF (Ti), and PETH (Si); Cordierite: TAP (Na, Mg, Al, Si), PETJ (K, Cl, Ca), LIFH (Cr, Mn, Fe, Zn); Amphibole: TAP (F, Na, Mg, Al, Si), LIF (Ti, Cr, Mn, Fe), PETH (Ca, K, Cl, Zr, Sr); Pyroxene: TAP (Na, Mg, Al, Si), PETJ (K, Ca, Ti), LIF (Zn), LIFH (Cr, Mn, Fe), PETH (Zr); Zircon: PETJ (P, Y), TAP (Al, Hf), PETH (U, Zr, Si). Results were corrected for instrumental beam-matrix effects and instrumental drift by the phi-rho-Z method (CITZAF; Armstrong et al., 2013).

2.6. Presentation and organization of this thesis

Through the development of this thesis, two scientific contributions were prepared and successfully published as Research Articles in WoS/ISI indexed journals. Another article is being prepared with the unpublished chapters of this manuscript, hence the preferred language used in this thesis is English. The introduction, geological context, and state of the art of zircon crystallization systematics and crustal granite petrogenesis are presented in the first three chapters. The fourth chapter contains results of isochemical projections of thermodynamic models for crust melting, some comments about the energetic requirements of *anatexis*, the geochemical signature of leucosomes, and implications on the inheritance of magmatic zircon in anatectic melts. The article of Molina et al. (2020) is presented in the fifth chapter and corresponds to the core of this thesis. The article of Ferreira et al. (2019) is included in **Annexes** and corresponds to a collaborative work to understand cordierite granites with different tectonics setting in Brazil, Argentina, and Chile. In this case, I was the leader of the Chilean counterpart, particularly of the Andean Late Triassic post-orogenic plutons, as well as responsible for the thermodynamic modelling. The sixth chapter of this thesis delivers general reflections concerning the conditions of crust *anatexis* and implications for the inheritance of magmatic zircon from magma sources. The seventh chapter provides a brief conclusion regarding the origin of crustal magmas in light of zircon crystallization systematics. The eighth chapter contains the **Annexes**, in which also raw results of numerical and thermodynamic models are presented graphically, and a complete list of the geochemical and geochronological data resulting from the different analyses performed here. A list of contributions related to this thesis is presented as follows:

WoS/ISI articles:

During the development of this doctoral thesis, the following articles were published.

Molina P.G., Parada M.A., Changqian Ma. 2020. Zircon inheritance from long-lived sources of Late Triassic post-orogenic plutons, High Andes, Central Chile (~30°S): Magmatic feedbacks and petrogenetic implications. Lithos. V. 370-371.

Ferreira V.P., Sial A.N., Toselli A.J., de Toselli J.R., **Molina P.G.,** Parada M.A., Celino J.J., Saavedra J. 2019. Cordierite-bearing granitic Rocks in South America: contrasting sources and conditions of formation. Journal of South American Earth Sciences. V. 92, pp. 417-434.

Articles in congresses:

Martinez A.M., Paterson S.R., Memeti V., Parada M.A., **Molina P.G**. 2018. Mantle driven Cretaceous flare-ups in Cordilleran Arcs. Boston, Massachusetts, USA

Ferreira V.P., Sial A.N., Toselli A.J., de Toselli J.R., **Molina P.G.,** Parada M.A., Celino J.J., Saavedra J. 2017. Cordierite-Bearing Granitic Rocks in South America: Contrasting Sources and Conditions of Formation. Goldschmidt Conference, Paris.

Molina P.G., Gutiérrez F.J., Payacán I.J., Parada M.A., 2016.The extent of crustal assimilation in meridional Andean silicic magmatism since Late Cretaceous: geochemical and rheological perspectives. AGU Fall Meeting 2016, San Francisco, Californa, USA.

Molina P.G., Parada M.A., Gutiérrez F.J., Chang-qian M., Yian W.L. and Yuanyuan L., 2015. Zircon chronology and geochemistry evidence of different granitoid sources and tectonic regimes in the Upper Paleozoic – Mesozoic evolution of the Central Chile Andes. 8th Hutton Symposium on Granites and Related Rocks, Florianapolis, Brazil.

CHAPTER 3. CRUSTAL MAGMAS AND ZIRCON AS A PETROGENETIC MARKER: STATE OF THE ART

Crustal melting or *anatexis*, and melt extraction, are thought to be responsible for generating a stratified-heterogeneous continental crust (Rudnick and Gao, 2003). Partial melting of the crust occurs, generally, in post-collisional tectonic settings (followed by rapid exhumation paths), and subsequent mantle upwelling (Karakas and Dufek, 2015) or adjacent to large magma reservoirs (Clark et al., 2011).

3.1. Crustal melting mechanisms

3.1.1. Heat sources

Anatexis (well above dry-granite solidus) occurs at temperatures higher than 900ºC in volatile-free melting conditions, and temperatures as low as 700ºC through volatile-saturated melting (Harley, 1998). In both cases, this implies a geothermal gradient higher than ~20º/Km (Brown, 2006), mostly at granulite facies. Partial melting is an energy-consuming process such as chemical and phase-change reactions (Nicholls and Stout, 1982; Glazner, 2007). In consequence, high temperatures (above the *solidus*) are achieved in very particular geological scenarios (Clark et al., 2011).

The following heat flow equation of Clark et al. (2011) provides a simple way to model time-dependent temperature evolution in a heterogeneous thickened crust; the authors emphasize that the temperature estimations are an overestimate, as they do not assume lateral heat flow in the crust:

$$\frac{\partial T}{\partial t} = \frac{d}{dz}\left[k(T)\frac{dT}{dz}\right] + u\frac{dT}{dz} + \frac{1}{\rho C_p}(A_{rad} + A_{mech} + A_{chem})$$

Where T is temperature, t is time, z is thickness, k is temperature-dependent thermal diffusivity (Whittington et al., 2009), C_p is the specific heat capacity, u is vertical transport velocity relative to Earth's surface (rate of burial, or exhumation if negative). A_{rad}, A_{mech} and A_{chem} are the rates of heat production per unit volume by radioactive decay, mechanical deformation, and chemical reactions (negative value if partial melting energy consumption operates), respectively.

An increase in mid-crustal temperatures, leading to *anatexis*, could be product of augmented radioactive-decay heat production (Chamberlain and Sonder, 1990) of highly incompatible element concentrations in the crust, by igneous differentiation such as U, Th, and K. These elements mainly provide radioactive decay heat production, with values of 0.1-3.0 $\mu W/m^3$ (Vilà et al., 2010). A heterogeneous distribution of heat-producing elements (assumed to be concentrated preferably in the Upper Crust, due to its felsic composition) after crustal thickening (crust stacking or homogeneous deformation) is expected (Bea, 2012).

Mechanical heating in shear zones can also contribute to raising crustal temperatures (Currie and Hyndman, 2006) reaching up to ultra-high-temperature conditions. An increasing discussion regarding the contribution of these mechanisms, which is out of the scope of Clark et al (2011) approach, to the extent of high-temperature metamorphism (e.g. Nabelek et al., 2010) is still debatable.

3.2. Water-fluxed and dehydration melting

3.2.1. Volatile-phase present melting (low-temperature *anatexis*)

Several authors invoke water (along with CO_2, S, F, etc.) as the main component changing the temperature of the beginning of melting (Ebadi and Johannes, 1991). The composition of the melts generated by *anatexis* depends on the availability of this main volatile component: water-fluxed *anatexis* produces tonalitic to trondhjemitic melts, whereas dehydration melting generates leucosomes of granitic composition (Patiño Douce and Beard, 1995; Patiño Douce, 1996).

Moreover, magmas generated by fluid-present melting will experience an increase in their density and volume decrease (hindered diapiric transport of neosome at low melt fractions until coalescence), whereas fluid-absent melting (dominated by dehydration reactions) will produce a positive density change, a decrease in system density and brittle fracture of the host (**Fig. 3.1**; Clemens and Droop, 1998).

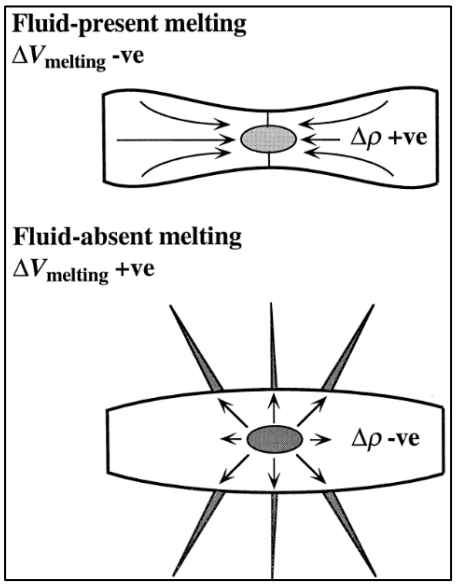

Figure 3.1: Schematic representation of the physical behaviour of a partially melted rock, under fluid-present and fluid-absent fusion. In the former condition bulk density increase, whereas in the latter the contrary occurs. Extracted from Clemens and Droop (1998).

Considering that the crystallization order of liquidus phase assemblages can change considerably with water activity (Scaillet and Pichavant, 2003), as it is a dominant component in hydrous minerals (namely amphibole, biotite, and muscovite), anatectic magmas generated under water-rich (or water-poor) conditions reflect this, accordingly. This is in strong agreement with natural observations in calc-

alkaline batholiths of the Andes, where at shallow-level emplacement conditions, water activity seems to be below saturation (meaning low initial water contents; e.g. Clemens and Vielzeuf, 1987), consistent with the textural development of eu- to subhedral early anhydrous phases before crystallizing late sub- to anhedral hydrous phases (biotite and/or amphibole), in comparison with the generation of water-saturated granotonalites in the Adamello massif in the Italian Alps (Castro, 2013; **Fig. 3.2**).

Figure 3.2: Two contrasting tonalitic rocks, one from the Cordilleran North Patagonian batholith (Argentina), and the other from the Adamello batholith (Northern Italy). In the latter, hornblende crystals are at the liquidus, whereas plagioclase stands as a late-stage phase. In contrast, the former case shows early crystallization of plagioclase, followed by amphibole, resulting in an agpaitic texture (see text for explanation).

3.2.2. Volatile-free melting (high-temperature *anatexis*)

As stated above, the water-undersaturated nature of some magmas generated in the southern Andes, suggests that there must be a more relevant mechanism rather than water-fluxed melting in the generation of anatectic granites. Patiño Douce and Johnston (1991) (among many others) recognize the role of hydrous minerals breakdown in the generation of melt (incongruent melting of biotite, amphibole, and muscovite; **Fig. 3.3**). **Table 3.1** details the generation of melt by hydrous-phase dehydration reactions along with the crystallization of peritectic phase assemblages, depending on the protolith (generally pyroxene, cordierite, garnet, aluminosilicate, and K-feldspar; Weinberg and Hasalová, 2015 and references therein).

Further, the source of infiltrated water (additional to released water by hydrous-phase breakdown reactions) in anatectic regions could come from *subsolidus* dehydration metamorphic reactions, magma differentiation (Holtz and Johaness, 1994), or advected meteoric water (Brown, 1994 and references therein).

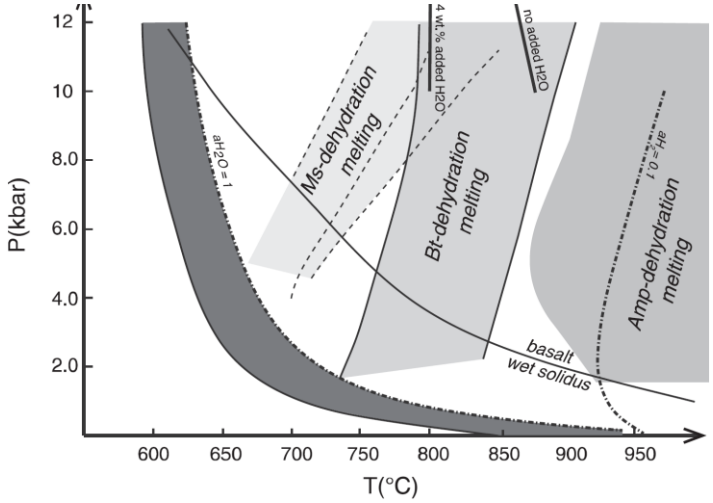

Figure 3.3: Diagram showing different temperatures of dehydration melting by muscovite, biotite, and amphibole breakdown. The different discontinuous lines represent water activities changing the solidus temperature and melting curve slopes, in the P-T space. Wet granite solidus in dark-gray area. Extracted from Weinberg and Hasalová (2015).

Table 3.1: Summary of the three main dehydration-melting reactions and their peritectic mineral assemblages (note that the peritectic minerals are, exclusively, anhydrous minerals). MP, MT, and HP stand for medium pressure, medium-temperature, and high pressure, respectively. Extracted from Weinberg and Hasalová (2015).

	Peritectic mineral	Melt composition	PT conditions	Protolith type
Ms-dehydration melting				
Ms + Pl + Qtz = Als + Kfs + melt	Als, Kfs	Kfs-rich melt	MP MT	metapelite
Bt-dehydration melting				
Bt + Als + Qtz = Grt/ Crd + Kfs + melt	Grt, Crd, Kfs	Kfs-rich melt	Crd will form at LP, Grt at HP, both at intermediate T	metapelite (no Pl)
Bt + Pl + Als + Qtz = Grt/ Crd + Kfs + melt	Grt, Crd, Kfs	Kfs + Pl in melt	Crd will form at LP, Grt at HP, both at intermediate T	metapelite
Bt + Pl + Qtz = Opx (+Cpx + Grt) + melt	Opx, Cpx, Grt (depends on rock composition)	Kfs + Pl in melt	variable, type of peritectic mineral depends on rock composition and PT	metapsammite, metagranitoids, metatonalite
Amp-dehydration melting				
Hbl + Qtz = Pl + Opx + Cpx (+Grt) + melt Hbl + Pl = Cpx (+Grt + Opx + Amp) + melt	Pl, Opx, Cpx, Grt	Pl-rich melt	variable, type of peritectic mineral depends on rock composition and PT	metabasalt K-poor/Ca-rich amphibolite

3.3. Geodynamic significance of the melting P-T paths

Depending on the tectonic setting, different pressure-temperature paths can alter the order of the different phase-breakdown melting reactions (Clemens and Droop, 1998). They may be petrographically recognized as prograde mineral decomposition, dehydration, incongruent melting textures, coronitic armoring of metamorphic prograde assemblages, and retrograde *rehydration-crystallization* (Brown, 1994) reactions (if water was not completely evacuated from the source in prograde metamorphism).

Two main types of orogenic processes, leading to decompression dehydration-melting, are recognized (**Fig. 3.4**; Thompson, 1990):

- **Clockwise pressure-temperature paths:** Generated by basin inversion/crustal thickening followed by erosional or extensional thinning, and/or lithospheric delamination with consequent orogenic collapse.
- **Counterclockwise pressure-temperature paths:** Generated by heating previous (or concomitant) to crustal thickening. This can be a product of upwelling of mantle-derived magmas (under- or intraplating) and mantle lithosphere thinning.

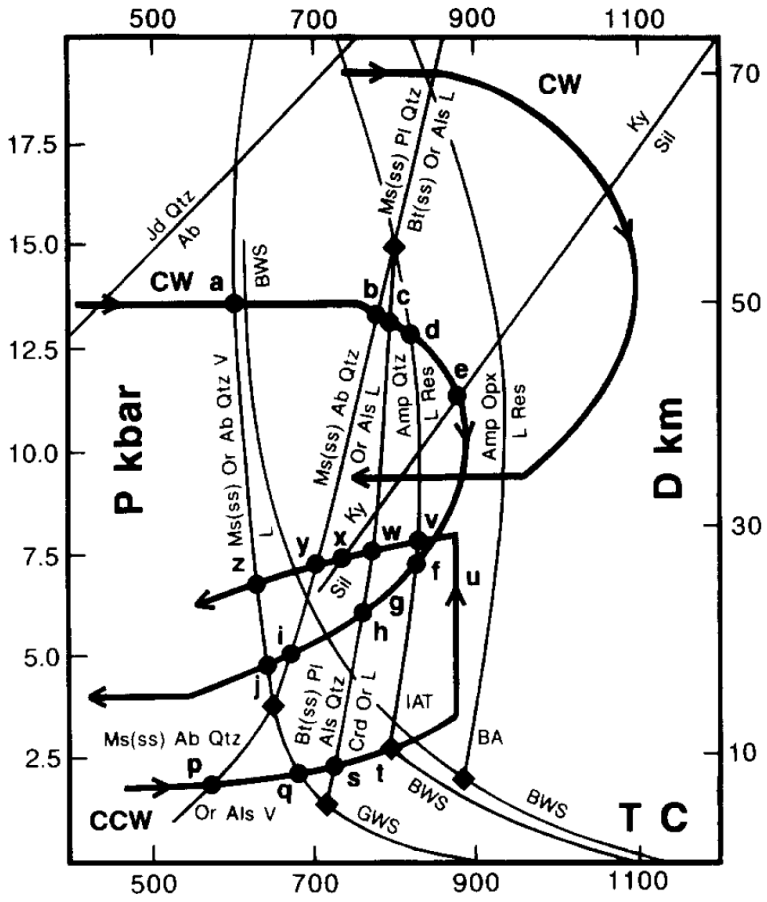

Figure 3.4: Pressure-temperature diagram showing different clockwise melting paths (**CW**) and counterclockwise paths (**CCW**). Continuous lines stand for the different reactions represented by the different mineral assemblages in each field. IAT=Island Arc Tholeiite, BA=Alkali Basalt, BWS=Basalt Wet Solidus, GWS=Granite Wet Solidus. Extracted from Brown (1994).

3.4. Melt segregation, extraction, and migration

3.4.1. Allochtonous granites

Most crustally-derived granites display petrological evidence of separation from their restitic phases at different depths (Brown, 2013). Repeated magmatic recycling of the crust leads to geochemical depletion and the formation of 'sterile' orogens; in contrast, young margins are characterized by the abundance of sediment-rich sources which are prone to generate large granitic massifs ('fertile' orogens) (Vielzeuf et al., 1990). Melt extraction and diapiric ascent to higher structural levels occur more efficiently in fluid-absent anatexis, in comparison with water-induced melting (Clemens and Droop, 1986). The coalescence of partial melts and ascent by diking operates at somewhat constrained rates (Petford et al., 2000). This is governed by the physics of fluid dynamics, in which the melt fraction of magmas is placed within maximum and minimum possible values to achieve efficient segregation (Bachmann et al., 2007); at this point, the rock behaves as an interconnected network of melt that can

segregate interstitial liquid (>5 vol.%; Sawyer, 1994) by pervasive grain-scale flow by compaction, porous flow, and channel flow through conduits (**Fig. 3.5**; Brown, 2010). Additionally, liquid interconnectivity in partially melted rocks can be reached at melt fractions as low as 2 vol.% (Wolf and Wyllie, 1991), suggesting that even at very low melt volumes magmatic liquids can be transported and extracted to the Middle and Upper Crust.

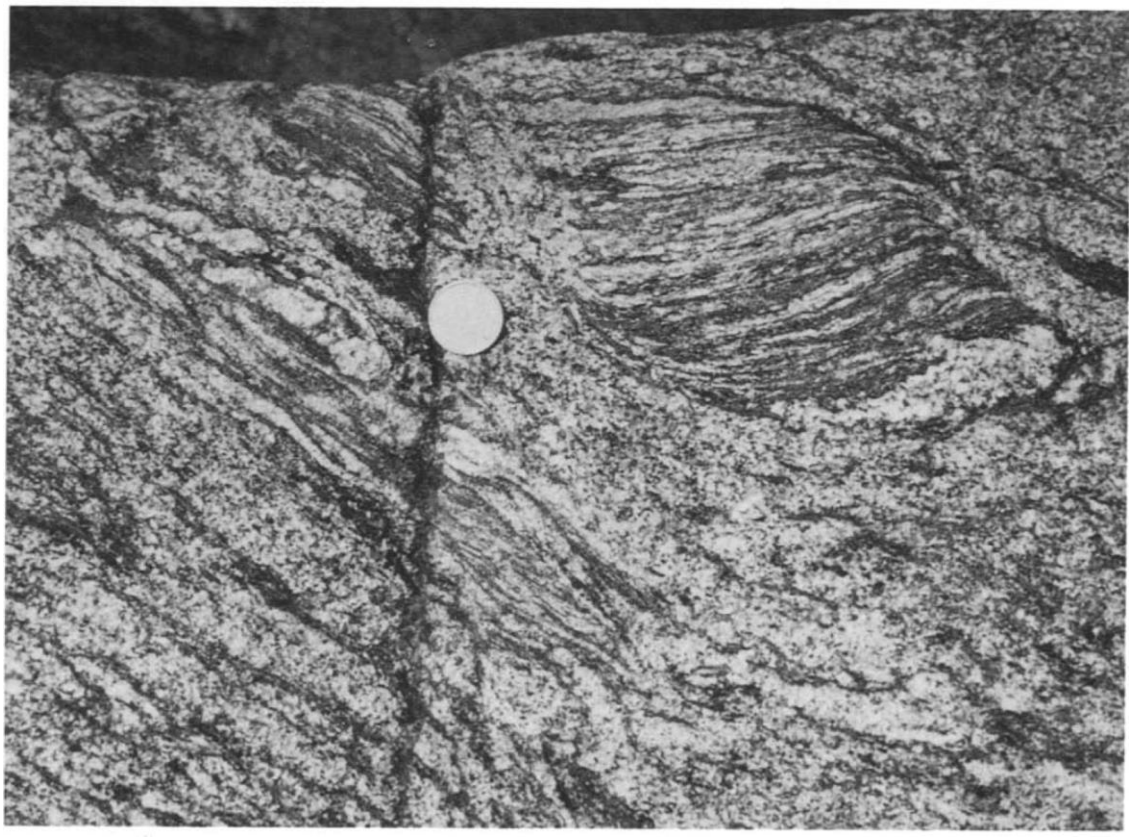

Figure 3.5: Diatexite from the St. Malo migmatite belt, northwest France. Here schlieren textures are developed surrounding stromatic fine-layered migmatite relicts (to the right of the coin). This textural difference is interpreted as different melt fraction volumes at the mesoscale, disrupting the structure of the protolith. Extracted from Brown (1994).

In subduction settings, the partially melted overriding crust may be prone to high tectonic stresses, promoting pervasive pumping of granitic melts in migmatites (Simakin and Talbot, 2001); highly intense deformation and compaction, at melt fractions as low as 5-15 vol.% (Rushmer, 1992), can facilitate this process.

The composition of the leucosome of the partially melted crust is generally less dense and less viscous than the paleosome and melanosome (Clemens and Droop, 1998). This implies that a higher buoyancy force will drive the separation of the anatectic melt with its solid residue (Sawyer et al., 2011), along

with melt migration through dilatant structures in ductile and brittle-elastic fractures at different depths in the crust (Leitch and Weinberg, 2002; Weinberg and Regenauer-Lieb, 2010).

3.4.2. Parautochthonous and autochthonous granites

Considering the generation of migmatites with melt fractions below the critical lock-up point, its migration through the crust would be majorly restricted; in-situ partial melting of host rocks (no need for neosome transport or paleosome dragging) could result in parautochthonous (**Fig. 3.6**) or autochthonous (**Fig. 3.7**) highly peraluminous granites. They can be recognized (Barbero and Villaseca, 1992), as follows: **(a)** an absence of contact aureole with adjacent metamorphic rocks; **(b)** a thermodynamic equilibrium of leucosome mineral assemblages and those of country-rock granulites; and **(c)** similar crystallization ages between anatectic granite and host metamorphic assemblages.

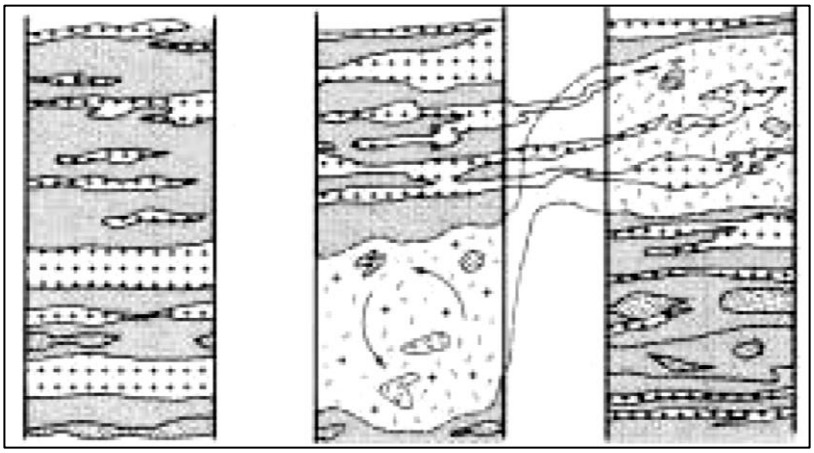

Figure 3.6: Three-stage cross section of the emplacement model for de Layos Granite, Spain, consisting in three stages, from left to right: Migmatitic event with segregation of big pools of leucogranite; Extensive convective homogenization, with a broad zone of melt fraction above the lock-up point; Melt segregation with limited ascent and near-emplacement structures. Extracted from Barbero and Villaseca (1992).

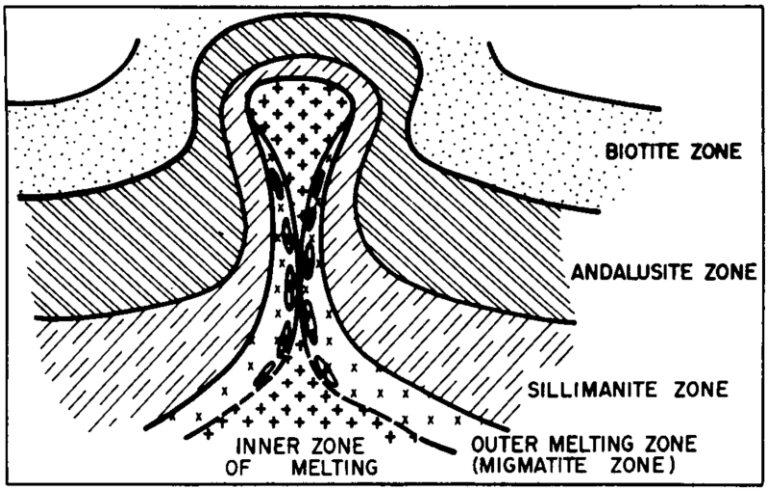

Figure 3.7: Suggested emplacement mechanism of the Cooma Granodiorite, Australia. Here a high-temperature aureole may have formed by diapiric transport, after anatexis. Partial melting of host metasedimentary rocks and transport from source to the emplacement place was short, defining a parautochthonous intrusion. Extracted from Flood and Vernon (1978).

3.5. Thermodynamic modeling and phase equilibria: Energy constraints on *anatexis*

Anatexis and assimilation are widely recognized as mechanisms responsible for magma generation in several geodynamic contexts, at different crustal levels (Brown, 2010). This supposition is backed by field observations of significant fagocitation of stopped blocks in diverse contexts (e.g. Wolak et al.,

2005), and by the fact that peraluminousity of many differentiating magma bodies increases with radiogenic isotopic and geochemical signatures (Clarke et al., 1988; Cameron et al., 1980; Spell., 1993; McCulloch et al., 1994; McBirney et al., 1987).

On the other hand, aside from mechanical processes (Marsh, 1982), some authors have questioned crust melting as a main petrogenetic process in the light of the energetic limitations of its progress (eg. Glazner, 2007). The necessary energy to dissolve xenoliths equals a vast amount of heat transferred to partially melt the host rocks. Partial melting of disaggregated rocks could be a mechanism to support assimilation because the energy requirements are less compared to ubiquitous melting of the wall-rock (Clarke et al., 1988; Beard et al., 2005).

The energy requirements to evaluate the intensity of crust melting can be evaluated by a) graphical analysis to visualize crystallinity and compositional changes, in terms of isenthalpic diagrams at a fixed pressure, derived from magma mixing and assimilation, b) energy-constrained numerical modeling of open-system processes such as magma replenishment, assimilation, and fractional crystallization and c) precise host-rock phase equilibria pseudosections, and rheological changes, given a proper adiabatic decompression path.

(a) The following equations provided by Ussler and Glazner (1992), are based on the work of Nicholls and Stout (1982), who calculated the heat effects balance for rock assimilation, and crystallization of magmas, considering different initial compositions and the enthalpy difference between the initial and final states of a magmatic system, as follows:

$$H'(T) = H(T)_{magma} - H(T_0)_{solid}$$

where $H(T)_{magma}$ is the enthalpy of the magma at the temperature of interest, and $H(T_0)_{solid}$ the standard state enthalpy for a fully crystallized magma at 1.0 bar at a given temperature. Therefore $H'(T)$ is the energy required for the magma to raise its temperature from T_0 to T.

Assuming magma as a mixture of crystals+liquid (and correspondingly their enthalpy requirements to raise the temperature), the above equation can be rewritten as:

$$H'(T) = H(T)_{crystals} + H(T)_{liquid} - H(T_0)_{solid}$$

By definition:

$$H(T)_{crystals} = \sum_i w_i \int_{T_0}^{T} C_{p,i} dT$$

Where w_i is the weight fraction of the mineral *i* in the magma, $C_{p,i}$ the specific heat capacity [J/g K] of mineral *i* at constant pressure, and T_0 the reference temperature. Additionally:

$$H(T)_{liquid} = \sum_j w_j \left\{ \int_{T_0}^{T} C_{p,j} dT + \Delta H_j^f + \int_{T_{f,j}}^{T} \Delta C_{p,j} dT \right\}$$

Where w_j is the calculated weight fraction of the normative mineral *j* in the magma, $C_{p,j}$ the specific heat capacity of the mineral j [J/g K] at constant pressure, ΔH_j^f the enthalpy of fusion of mineral *j* at 1 bar [J/g], and $\Delta C_{p,j}$ the specific heat capacity difference between the calculated normative mineral *j* in its molten and solid-state [J/g K].

Later, Glazner (2007) analyzed the extent of xenolith incorporation in natural systems, through the graphical analysis of enthalpy-composition diagrams of magma mixing and assimilation processes, highlighting the role of increasing magma crystallinity along with heat-consumption processes (magma mixing and partial melting), as a major obstacle on the incorporation of wall-rock (**Fig. 3.8**).

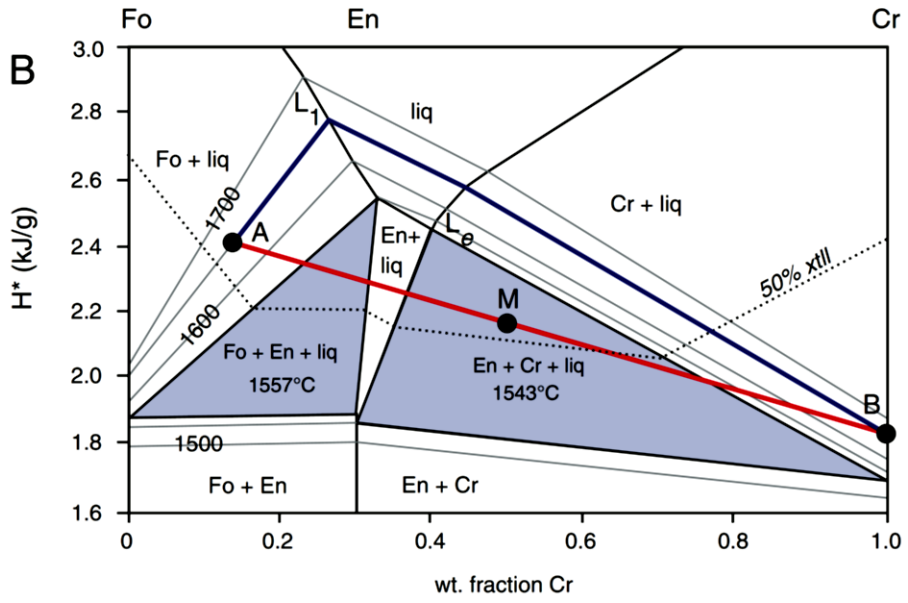

Figure 3.8: Enthalpy-composition (H-X) diagram for the system Mg_2SiO_4-SiO_2 (Fo-En-Qtz). Cristobalite (Cr) represents the Qtz endmember. This example represents a 1:1 mixture, of a mafic magma incorporating the same amount (wt.%) of silica. Isothermal mixture paths are no isenthalpic; this condition requires as much as 0.4 kJ/g enthalpy addition to maintain the temperature at a fixed value. Isenthalpic mixing results in a lower temperature, due to heat requirements to partially melt Cr. Extracted from Glazner (2007).

(b) Open-system magmatic processes have been numerically modeled. Spera and Bohrson (2001) integrated a mass-balanced isobaric crystallization and fusion heat of the different phases involved in magma recharge, down-with-temperature crystallization, and wall rock incorporation. Their results contribute to a better understanding of the geochemical and isotopic signature of the expected mixture, at a given temperature (Bohrson and Spera, 2003). The extraction of just a fraction of the generated anatectic melts was also considered in this calculation, by the introduction of an

"extraction efficiency factor" as later proposed by Gelman et al. (2014) among others. Borhson and Spera (2007) provided a computational algorithm to model this phenomenon. Mass, thermal and compositional outcomes can be obtained for the magma reservoir, igneous cumulates, mafic enclaves, and the produced anatectic melt (which could be compared to, for example, coalescence of migmatitic leucosomes in anatectic terranes), forming parautochthonous igneous bodies, as hypothesized for the petrogenesis of the Layos Granite, Hercynian Complex of Toledo, Spain (Barbero and Villaseca 1992).

(c) Multicomponent phase equilibria isochemical PT projections (pseudosections) can be attained using the Perple_X software programmed by Connolly (2005). This tool provides a complete thermodynamic data set, including the one from Holland and Powell (1998), in which solution models for a vast number of phases are calibrated and incorporated into calculations. Gibbs free energy minimization procedures are computed by compositional space discretization; the determination of the exact solid solution is bypassed to save computational resources, therefore each phase composition is expressed discretely, by a sum of "pseudocomponents". Results can be visualized as a phase diagram in the PT space. System properties such as specific volume, density, entropy, enthalpy, specific heat, volumetric fraction of any phase, etc. can be retrieved at a given point, or even following an arbitrary path; for example, melting phase relations for an adiabatic decompression path were calculated by Connolly (2005), for a -dry- average mantle composition (**Fig. 3.9**).

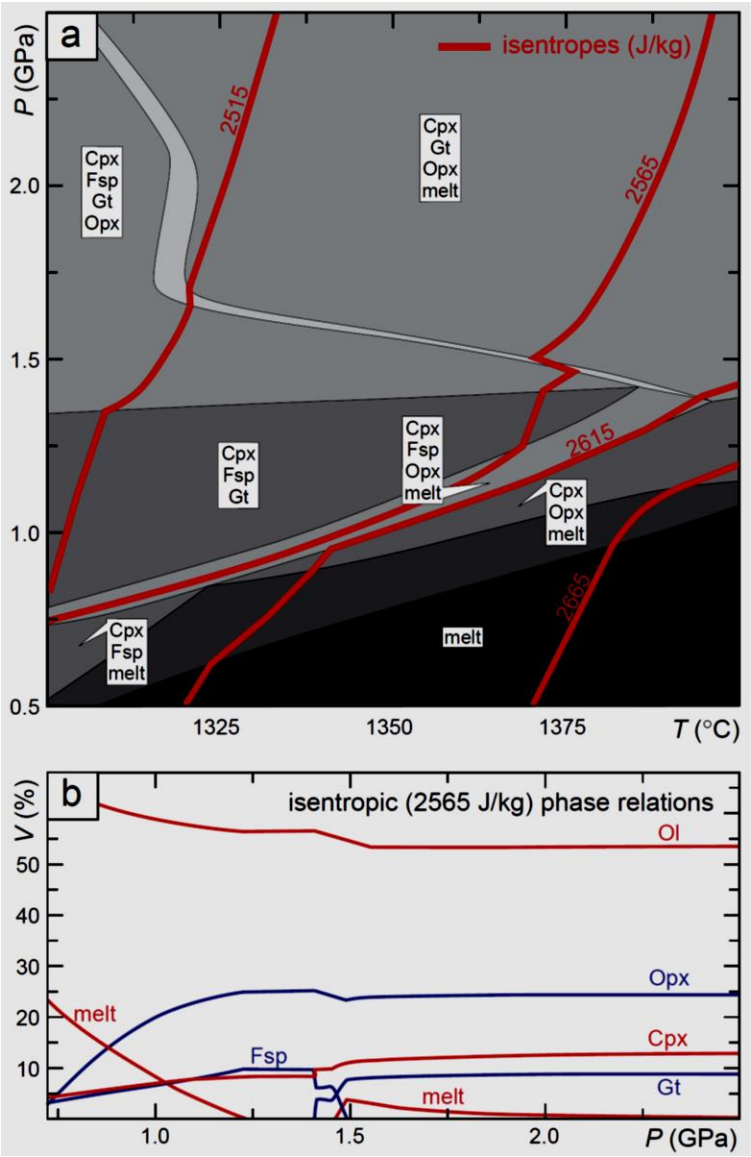

Figure 3.9: Here the 2565 J/kg isentrope was chosen arbitrarily, to visualize volumetric phase relations at a given adiabatic decompression path in **(b)**. Note that different mineral assemblages label each stability field in **(a)**. Phase transformation and melting reactions in **(a)** are accompanied by energy requirement differences (inflection points in red curves representing isentropes). Extracted from Connolly (2005).

3.6. Zircon as a petrogenetic marker

The latter sections display the different mechanisms by which crust can be melted, which are the possible chemical and mineralogical outcomes, and how does high (or low) temperature anatexis occur. The duration of source melting and magma emplacement timescales are usually inferred using U-Pb zircon dating (e.g. Bhattcharya et al., 2018). In some of these studies, zircon inheritance is revealed (e.g. Scott et al., 2011), but still lack a thorough assessment of the meaning obtained age, provided an estimation for the budget of inherited grains (Siégel et al., 2017).

3.6.1. Crystallization ages

A clue mineral phase in geochronology provided the U-Th-Pb isotopic system behavior, and the high uranium concentration in zircon (Hoskin and Schaltegger, 2003). Almost every rock in the Earth's evolutionary history can be dated with this method, as the ^{238}U-^{235}Pb half-life decay constant is sufficiently long to register zircon crystallization before 4 Ga (e.g. Xing et al., 2014).

3.6.2. Crystallization temperatures

The titanium content in zircons increases along with temperature estimates, leading to well-calibrated zircon thermometry equations (Watson et al., 2006), later revisited to account for variations in silica and titanium activities of magmas (Ferry and Watson, 2007), as follows:

$$log(Ti_{Zrn}) = (5.711 \pm 0.072) - \frac{(4800 \pm 86)}{T(K)} - \log(a_{SiO2}) + \log(a_{TiO2})$$

Ti_{Zrn} corresponds to the titanium concentration (ppm) in zircon, and $T(K)$ the zircon crystallization temperature.

Similarly, for a wider range of magma compositions, zircon saturation/dissolution temperatures have been obtained through experimental melt-phase equilibria, considering the melt composition and its zirconium content (Gervasoni et al., 2016):

$$ln(D_{Zr}) = 4.29 \pm 0.34 - (1.35 \pm 0.1)\ln(G) - (0.0056 \pm 0.0002) * T(°C)$$

Where $D_{Zr}=Zr_{solid}/Zr_{melt}$ (considering Zr_{solid}=496,000 ppm in zircon) and the G parameter of the melt $G=(3Al_2O_3+SiO_2)/(Na_2O+K_2O+CaO+MgO+FeO)$ in molar proportions, resulting in T(°C), the zircon saturation temperature.

It is expected that strongly peraluminous magmas (high G values) form zircons early in their evolution (Miller et al., 2003), whereas older zircons could reflect the initial stages of magma generation through anatexis (Kelsey et al., 2008).

3.6.3. Zircon host-rock characterization

Different types of zircon hosting rocks can be identified through their trace element budget (Belousova et al., 2002; Grimes et al., 2015; Kirkland et al., 2015; Chapman et al., 2016). Furthermore, O and Hf isotopes can be used coupled (Bolhar et al., 2008) or independently (Hawkesworth and Kemp, 2006), to reveal the origin of zircons and possible crustal recycling processes.

3.6.4. Magma oxidation state

Cerium (Ce) along with Europium (Eu) are divalent elements, +3/+4 and +2/+3 valences, respectively. The strong partitioning of tetravalent Ce compared to adjacent trivalent REE (La and Pr) results in positive geochemical anomalies in magmatic zircons, and is used to quantify the oxidation state of zircon-forming melts (Ballard et al., 2002; Trail et al., 2011; Burnham and Berry 2012; Trail et al., 2012; Zou et al., 2019) (**Fig. 3.10**).

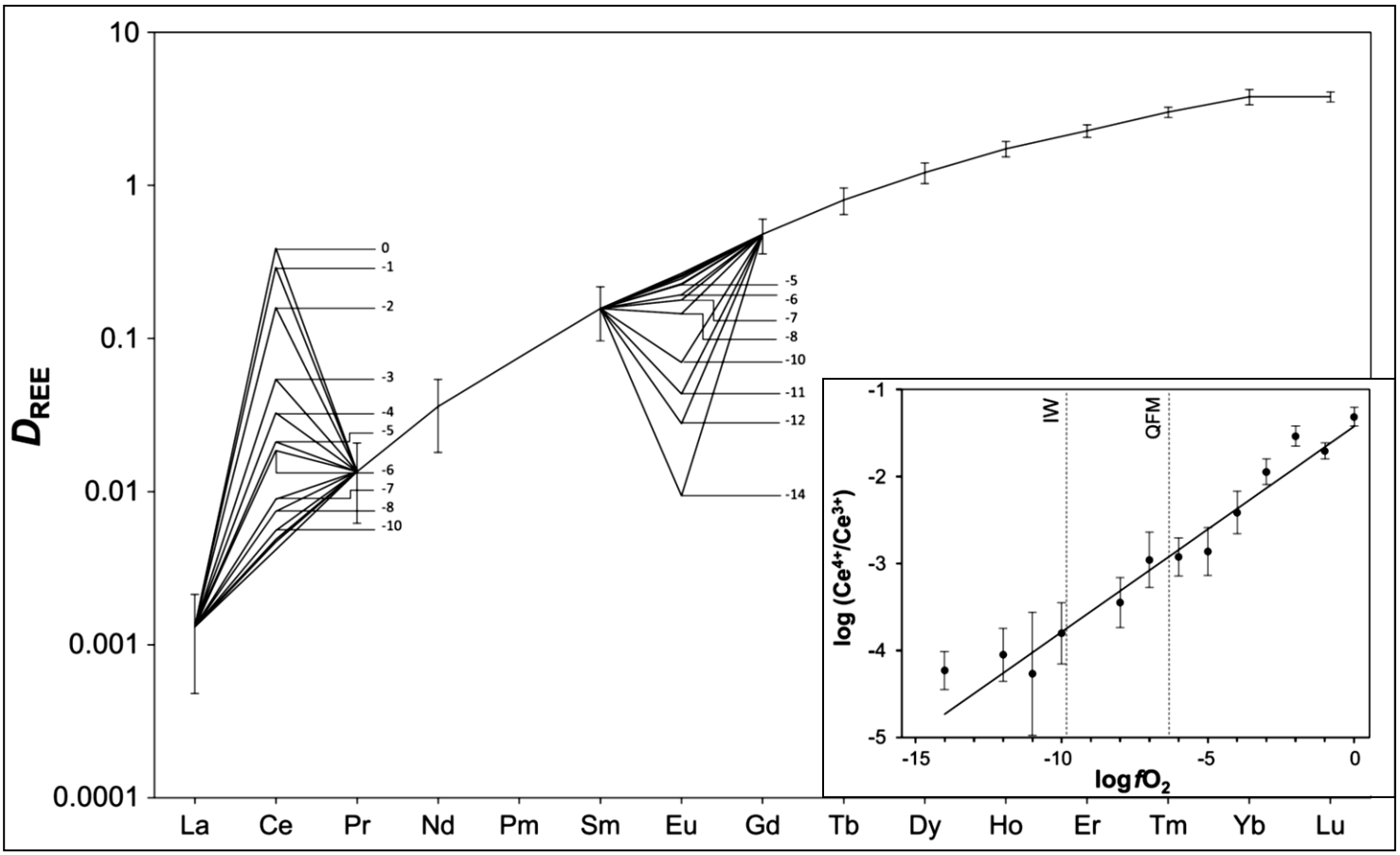

Figure 3.10: REE partitioning in zircon (determined by LA-ICP-MS) and associated logfO_2 values (numbers in anomaly apex). Inset shows the cerium anomaly magnitude and related magma oxidation state and mineral redox buffers. Modified from Burnham and Berry (2012).

3.6.5. Zircon as a petrogenetic tracer

Chemical variations in zircon are used as differentiation indexes, to unravel different petrogenetic processes such as fractional crystallization, partial melting**,** and/or magma mixing (**Fig. 3.11**):

- **Increase of the Hf content, Yb/Gd, Sm/La, and Ce/Sm ratios with differentiation:** Product of Apatite (Wark and Miller, 1993), titanite, and/or allanite (Castiñeiras et al., 2010; Reid et al., 2011) fractionation (e.g. Claiborne et al., 2010b).
- **Decrease of the Th/U and Zr/Hf ratios with differentiation:** Due to zircon, titanite, amphibole, clinopyroxene, and/or garnet crystallization, previous or along-with zircon formation (Wang et al., 2010).

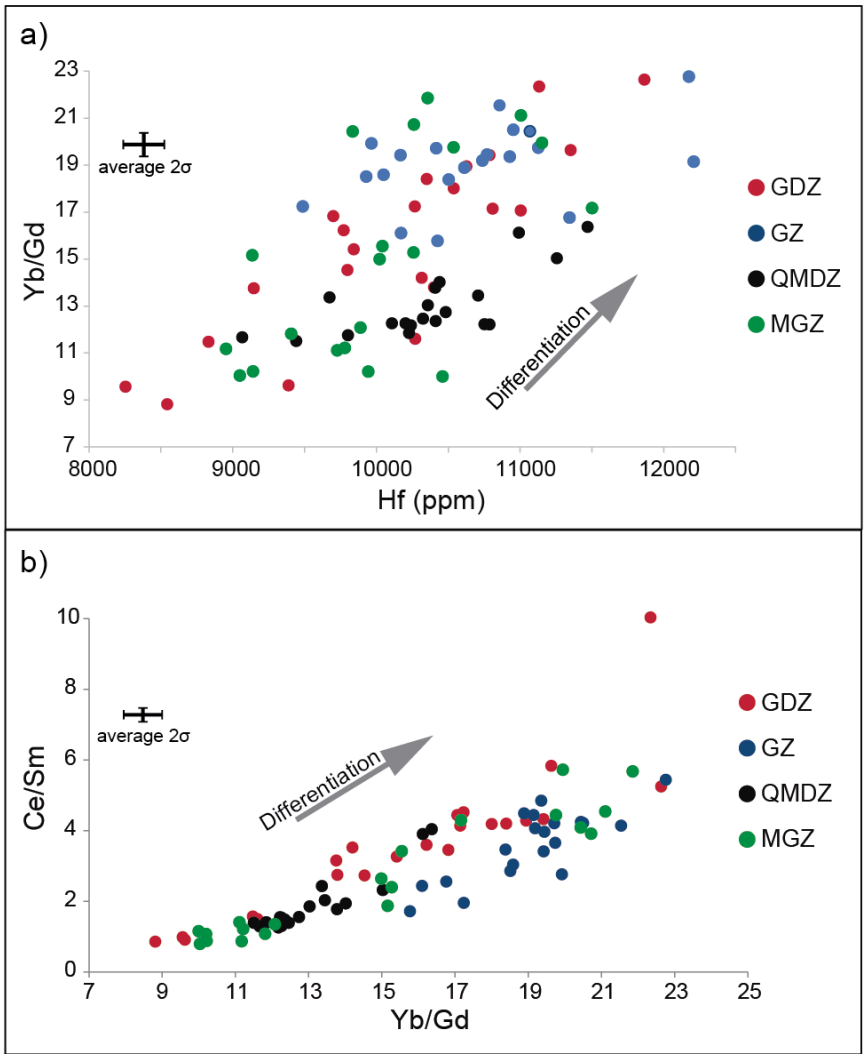

Figure 3.11: Zircon LA-ICP-MS analyses obtained from co-genetic rocks from the Upper Cretaceous Caleu Pluton, Central Chile (GDZ, GZ, QMDZ, and MGZ stand for gabbro, granodiorite, quartz-monzodiorite and monzogranitic lithologies, respectively) (Molina et al., 2015 unpublished data).

CHAPTER 4. THERMODYNAMIC MODELING OF CRUST ANATEXIS: RESULTS AND DISCUSSIONS

To properly characterize the geochemical signature of crustal magmas, and address the energetic requirements of anatexis at different depths, thermodynamic modeling (PerpleX software; Connelly, 2005) of at different P-T-X_{H2O} conditions was performed based on the CFMASHN (Lower Crust) and KCFMASH (Middle and Upper Crust) components systems, and represented as isochemical pseudosections (with variable initial water content). The visualization of isenthalpic curves on the P-T space provides a powerful tool to evaluate the relative energy between two system states, and therefore the feasibility of the crust to partially melt or be assimilated (as suggested by Ussler and Glazner, 1992). Intensive variables, the system crystallinity (vol.%), residual melt, and solid residue compositions, were retrieved in the whole modeled range.

Average Lower, Middle, and Upper Crust compositions were used in modeled pseudosections of isochemical systems, and correspond to those suggested by Rudnick and Gao (2003). The different magmatic phases were modeled considering solution models provided for orthopyroxene, biotite, garnet, clinopyroxene, chlorite, olivine, silicate melt, spinel, and chloritoid (Holland and Powell, 1998); amphibole (Wei and Powell, 2003); mica (Auzanneau and Schmidt, 2010); plagioclase (Newton et al., 1980); clinohumite (Duffy and Greenwood, 1979); and ideal talc, cordierite, antigorite, and brucite. Magma residue composition was calculated by mass balance as follows:

$$Res_i^{PT}(wt.\%) = \frac{Prot_i - (Liq_i^{PT} * Liq_{wt}^{PT})/100}{1 - \frac{Liq_{water}^{PT}}{100} - \frac{Liq_{wt}^{PT}}{100}}$$

where Res_i^{PT} corresponds to the solid residue composition i (component in weight percent), $Prot_i$ the protolith composition, Liq_i^{PT} the composition of the residual liquid at any given PT condition, Liq_{water}^{PT} the amount of exsolved water (wt.%), and Liq_{wt}^{PT} the amount of liquid (in wt.%). Residue composition, on the P-T space, was computed with MATLAB software (R2017a).

4.1. Crust anatexis conditions under variable water content

According to the simulations provided here, melting of the crust at temperatures near and below 600°C was not achieved (**Annexes**), whereas anatexis in the Middle-Upper crust interphase was obtained (up to *ca.* 30% melt volume) at temperatures near 700°C and water contents above 1 wt.% (**Fig. 4.1**). Dry (volatile phase-absent) melting at temperatures near 800°C does not occur in the lower crust, while eutectic conditions are achieved in the middle and upper crust in the same conditions (**Fig. 4.2**). A minimum of >2 wt.% H_2O is necessary to partially melt the lower crust at 800°C. A thermal perturbation of 900°C surpasses the *solidus* of the crust in all cases, at any depth. It is important to note that, at a given initial H_2O content, isothermal decompression paths are characterized by somewhat constant crystallinities (**Fig 4.1** and **Fig. 4.2**), followed by water exsolution and subsequent *eutectic* crystallization.

Residual liquids within the *efficient melt extraction window* defined by Dufek and Bachmann (2010) (magmas with a 30 to 50 vol. % of melt phase) are found in the middle crust at 700°C, just above 3 wt.% H_2O contents (**Fig. 4.1**). Contrastingly, at 800°C, similar water contents are needed to equilibrate magmas within these crystallinities, but at the base of the crust. Melt extraction could only occur in the Middle and Upper Crust in water-undersaturated conditions at 800ºC (**Fig. 4.2**).

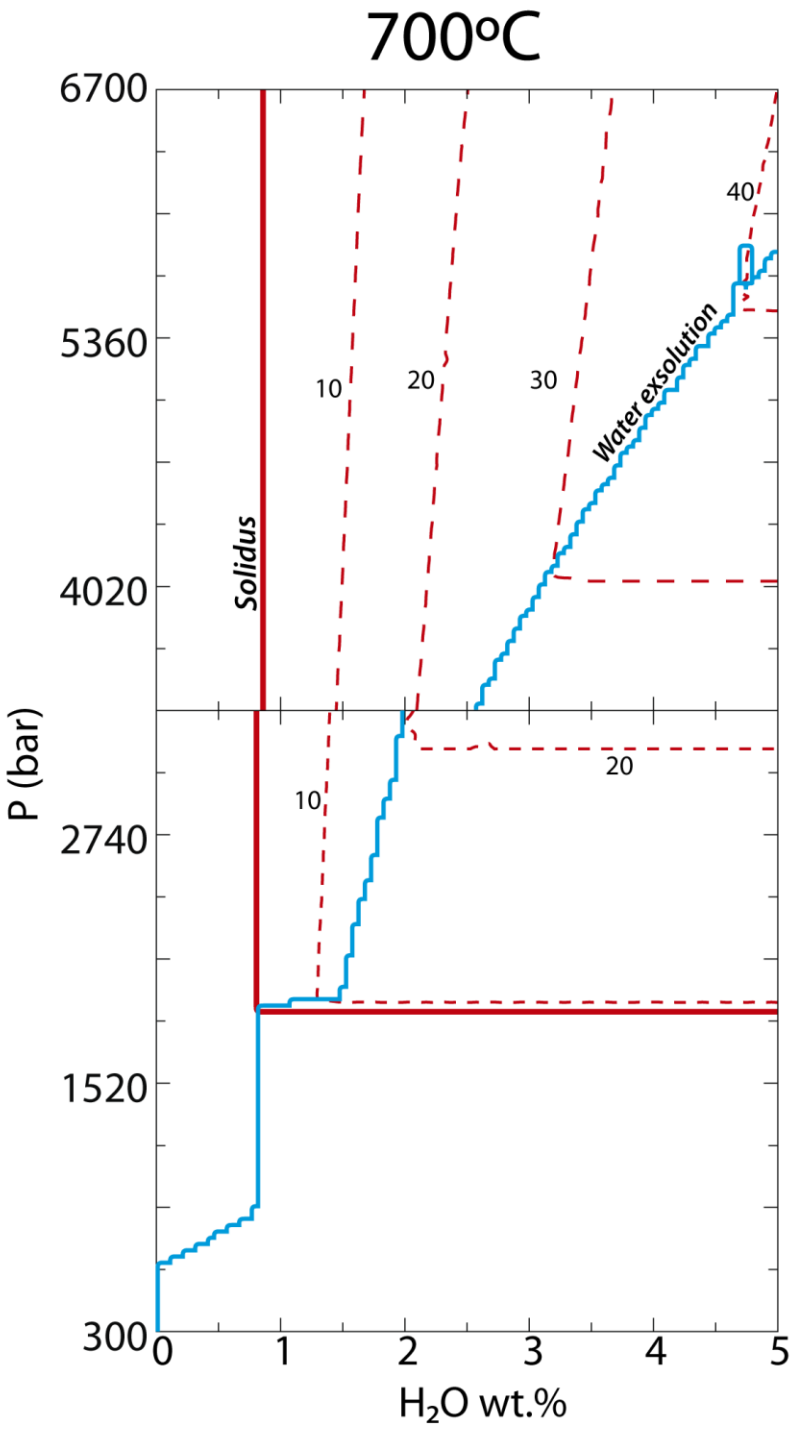

Figure 4.1: Simplification of modeled isochemicals pseudosectons for the upper and middle crust (at 700ºC). Lower crust pseudosection was omitted because of the absence of melt phase at this temperature The thick red line is the solidus whereas thin discontinuous red lines correspond to melt fractions (in vol.%). Water exsolution is represented by the thick blue line (exsolution of a volatile phase is expected at lower pressures than the dividing line). It is interesting to note that the slopes melt fraction curves change when water saturation is reached, following eutectic crystallization of modeled magmas.

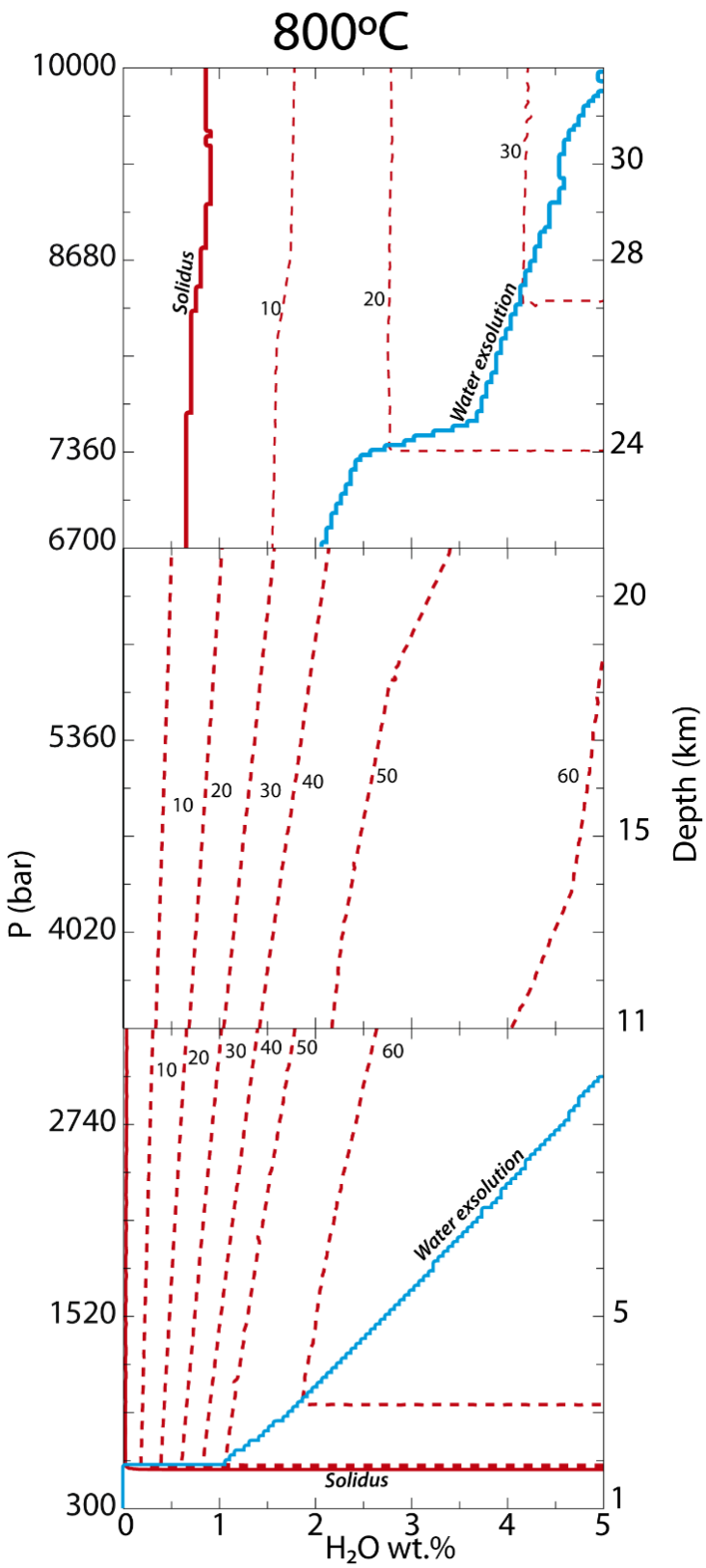

Figure 4.2: Simplification of modeled isochemical pseudosections for the entire crust (at 800ºC). Here, only the lower crust could exist at temperatures below the *solidus* in dry conditions (below 1 wt.% H_2O). Water exsolution was not achieved in the Middle Crust. Same legend as in **Figure 4.1.**

4.2. Energy requirement for crustal anatexis under variable water content

The simulations provided in the former section were used as a framework to display the relative energetic states of magmas at different P-T-X_{H2O} conditions. As purpose to understand the heat requirements to achieve crust *anatexis* and possible adiabatic ascent paths, the models of isochemical projections above 700ºC were considered. As a rule, greater energetic requirements are needed to sustain magmatic systems with high melt fractions and water contents at constant temperatures. This is a consequence of the different enthalpy values necessary for the dissolution and melting of participant minerals (Ussler and Glazner, 1992). In the modeled haplogranitic system, the obtained enthalpy differences between almost completely crystallized magmas and partially molten rocks (30 vol.% melt) of 0.2 kJ/g are in concordance with those obtained by Glazner (2007) for mixtures in the system Mg_2SiO_4-SiO_2. Also, the adiabatic ascent of magmas is feasible and could induce melting by decompression in water-undersaturated conditions but, accordingly, with a mild increase in dissolved water (**Fig. 4.3**). This is a consequence of the slope of the isenthalpic envelopes, which get farther from *solidus* as melts approach the surface, following the *adiabat* curves (Clemens, 2003).

The energetic barriers that might preclude anatexis take place as temperature increases, as a consequence of the energy consumption of the metamorphic reactions (Thompson and Connolly, 1995. The conditions for ultra-high temperature metamorphism are greatly impeded to a larger extent when metapelites are affected in comparison with refractory granitic crust (Schron et al., 2018), and are achieved generally in highly mature 'sterile' orogens (Vielzeuf et al., 1990). Under this analysis, a foreign heat supply is -again invoked- to surpass the energetic requirements to achieve *anatexis* of common crustal rocks. This is elucidated by the emplacement of the ubiquitous Late Triassic to Early Jurassic mafic dikes in the Elqui-Limarí Batholith (Elqui Dike Swarm), which is recognized by Parada (1988) as a possible precursor and/or trigger to partially melt the crust in a thinned lithosphere context (e.g. Karakas and Dufek,2015). Nevertheless, crustal thickening by vertical stacking of granitic blocks is recognized as a major energy contributor (by radiogenic heat production coming from the decay of ^{40}K, ^{230}Th, ^{235}U, and ^{238}U) to achieve anatexis in collisional to post-collisional settings (Bea, 2012).

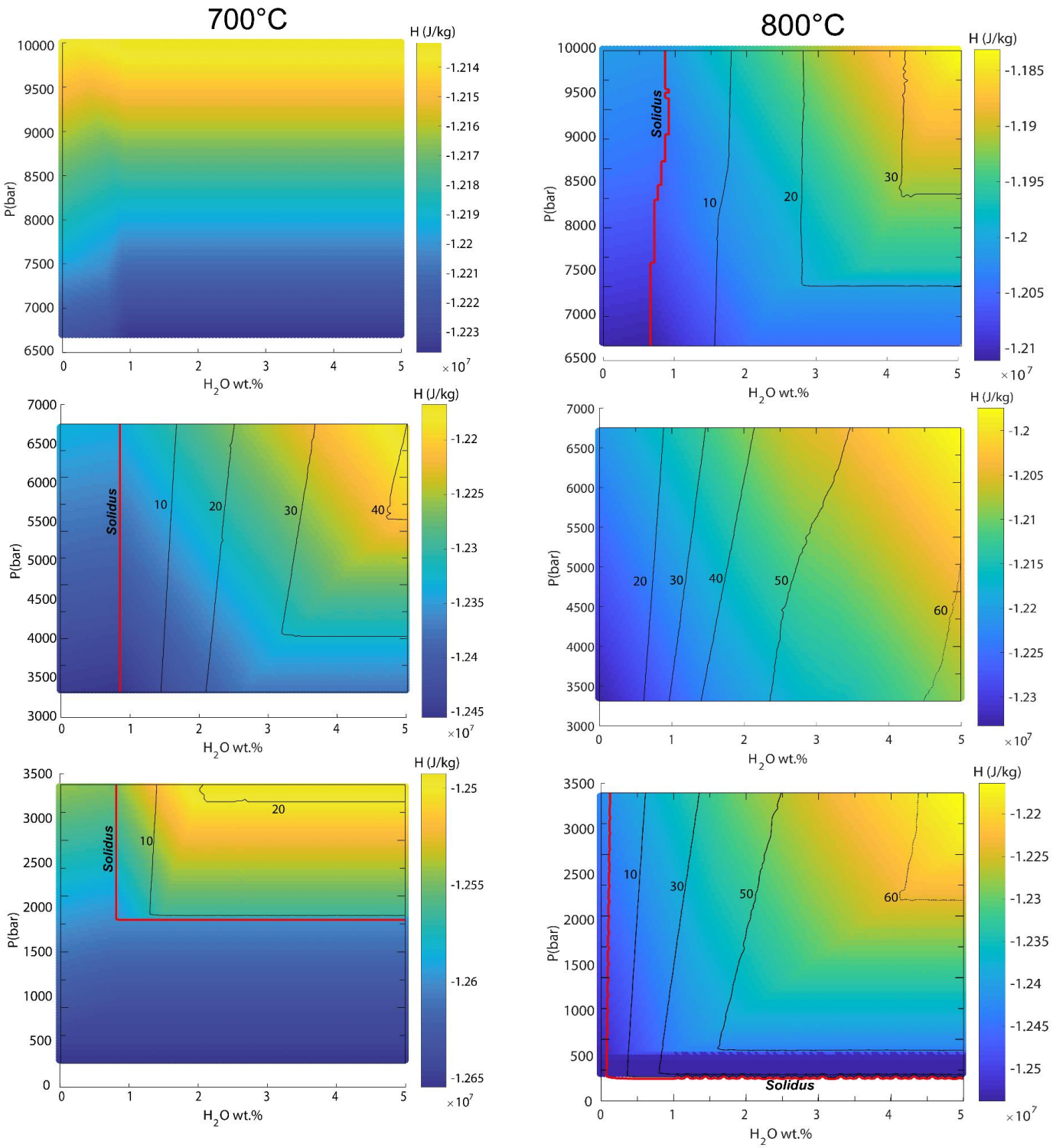

Figure 4.3: Simplified isochemical pseudosections for the Lower, Middle, and Upper Crust (at different water contents in weight percent) at temperatures of 700°C (left) and 800°C (right). Magma crystallinity (numbered thin black lines represent vol. % melt phase) and *solidus* (shown as thick red line) is projected in each diagram. Relative enthalpy states are indicated in scaled bars with colors.

4.3. Crust melting under water-saturated conditions and implications on the stability of entrained zircon grains

For simplicity, the composition of the leucosome portion of partially melted crust rocks was calculated under water-saturated conditions. The initial whole-rock compositions suggested by Rudnick and Gao (2003), for the Lower (10 to 6.7 kbar), Middle (6.7 to 3.5 kbar), and Upper (3.5 to 0.3 kbar) Crust sections, and following the above thermodynamic solution models within the KCFMASH components system, are considered in this thermodynamic simulation. The water-saturated *solidii* temperatures obtained here, reach values as low as *ca.* 600°C, whereas a maximum *solidus* temperature of 750°C is reached near the surface (**Fig. 4.5**). Melts formed within the *extraction efficiency window* (in the range of 30 to 50 melt vol.%) suggested by Dufek and Bachmann (2010), are only found just slightly above *solidus* temperatures (<650°C) at Middle crustal levels. However, the generation of melt with the same crystallinities can be obtained at temperatures as high as 750° C and 850° C in the Upper and Lower Crust, respectively (**Fig. 4.4**).

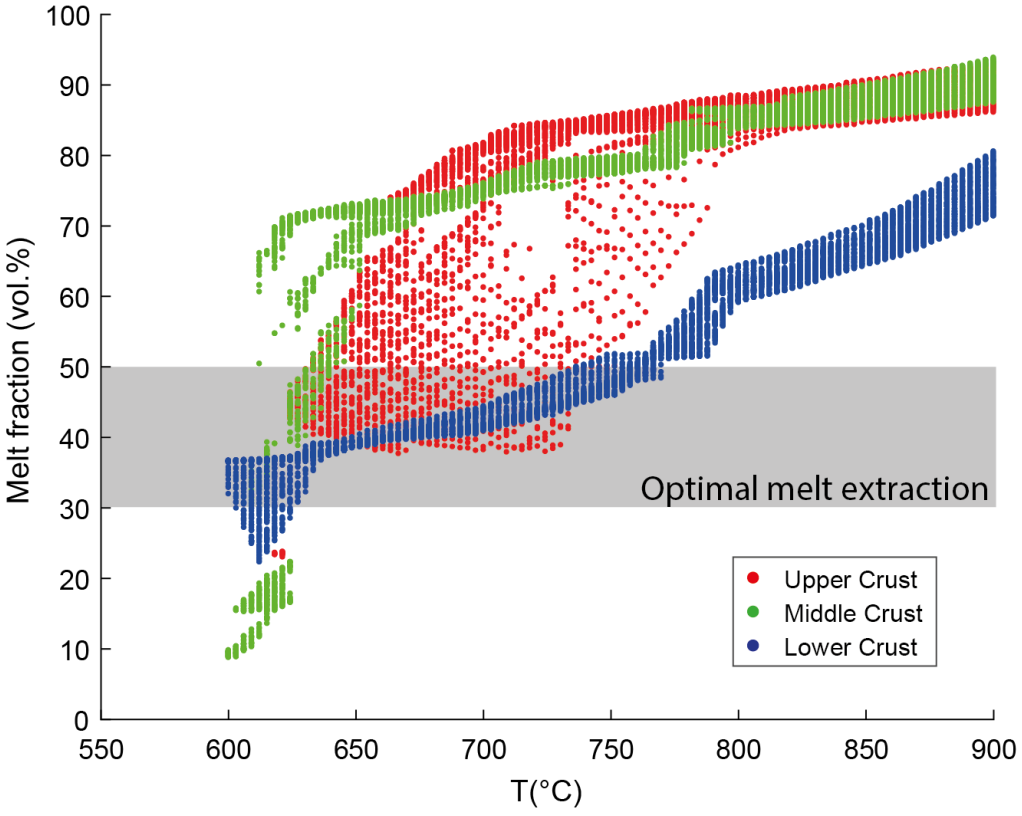

Figure 4.4: Variations of melt fraction (vol.%) versus temperature, obtained from the thermodynamic models of water-saturated melting presented here. The variability of melt fractions of anatectic magmas formed in the Upper Crust is explained by the negative slope of the *solidus* curve in the P-T space (compared with that of the Middle and Lower Crust), as magmas approach the surface (full range of melt fraction profiles in **Annexes**). *Optimal melt extraction window* after Dufek and Bachmann (2010).

The composition of the near-*eutectic* anatectic melts shows high values of SiO_2, Na_2O, and K_2O (wt.%), and low CaO (wt.%), compared with those obtained at higher temperatures. The Al_2O_3 content of modeled melt compositions shows minimum values (between 10 to 11 wt.%) at around 700°C, irrespective of the resulting crystallinity and depth of the crustal melting (**Annexes**). The Fe-index shows a consistent decrease with increasing temperature; values above 0.8 are bracketed within 650°-750°C, 650°- 800°C, and 650°-850°C, for the Upper, Middle, and Lower Crust, respectively. These values can be ascribed to magmas formed in a thinned lithosphere setting, as suggested by Frost and Frost (2011).

Anatexis of the Middle and Upper Crust cannot be achieved solely by a conductive geotherm of 15°/km, yet higher geotherm values (25° to 45°/km) can be responsible for melting of the Middle Crust (**Fig. 4.5**). In this geodynamic context, a perturbed geotherm as high as 35°/km can be achieved by the intrusion of mafic dike swarms within the lower crust (Dufek and Bergantz, 2005), or by augmented heat flow conduction in back-arc settings (Curie and Hyndman, 2006).

Results indicate that peraluminous melts (ASI index values above 1.0) are generated -preferably- at depths within the Lower Crust (at equivalent pressures within 6.7 to10 kbar) (**Fig. 4.5**), and -generally- at higher temperatures than metaluminous and peralkaline melts (**Fig. 4.6**). Contrastingly, the thermodynamic models of melting presented here, show that the amount of excess in alumina and alkalis indicate no correlation with pressure (**Annexes**). This finding is backed by observations made by Whalen et al. (1987) who proposed that crustal-related A-type granites are not only associated with anatexis of charnokitic lower crust (*cf.* Landenberger and Collins, 1996). A-type granitic magmas can also be formed by low pressure (P<4 kbar) dehydration melting of calc-alkaline granites at temperatures above 900°C, if any mechanism of thermal perturbation exists (*ie*. advection of hot mafic magmas into high crustal levels; Patiño Douce, 1997).

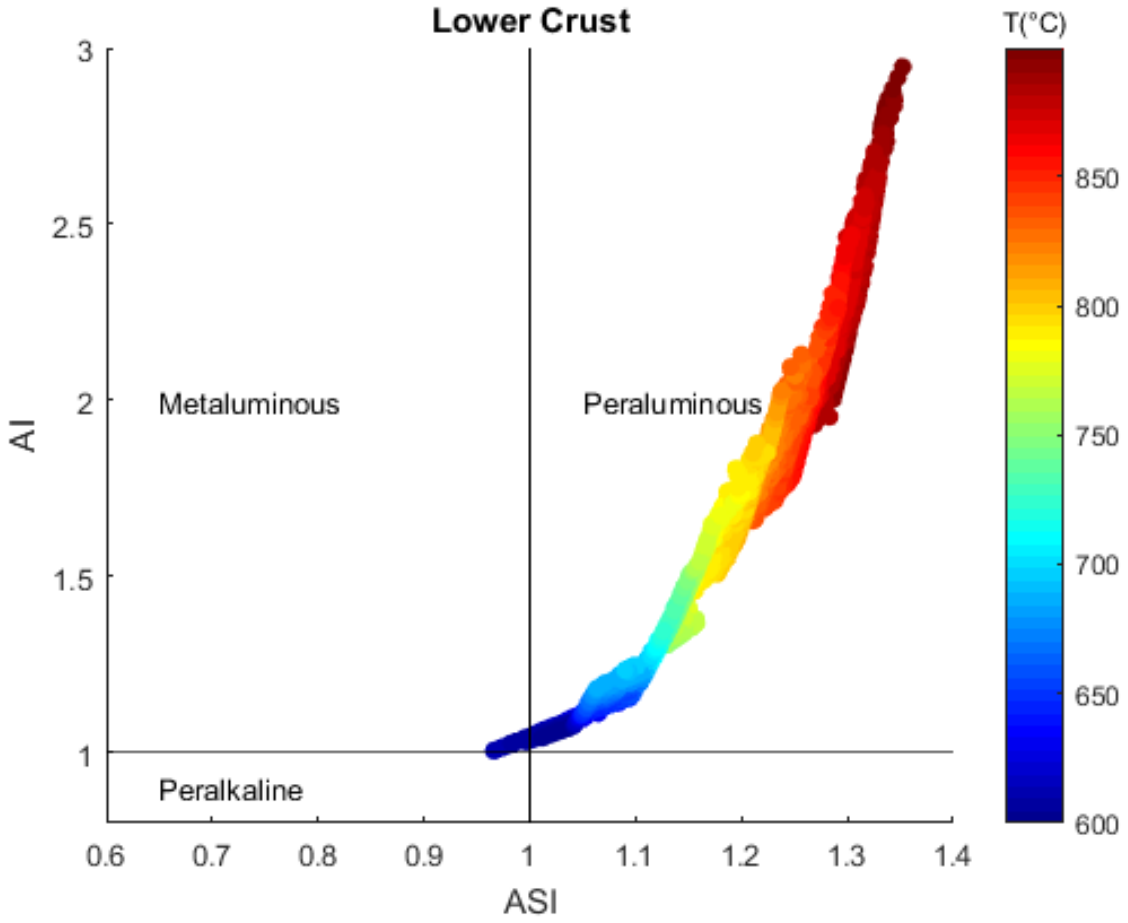

Figure 4.5: Thermodynamic models of crust anatexis for the Lower Crust (KCFMASH components system), under water-saturated conditions. ASI vs AI values after the formulation of Frost and Frost (2011). Anatectic melts show a strong peraluminous character in comparison with a few fractions of metaluminous and peralkaline melts generated near the *eutectic* temperatures (see **Fig. 4.4**).

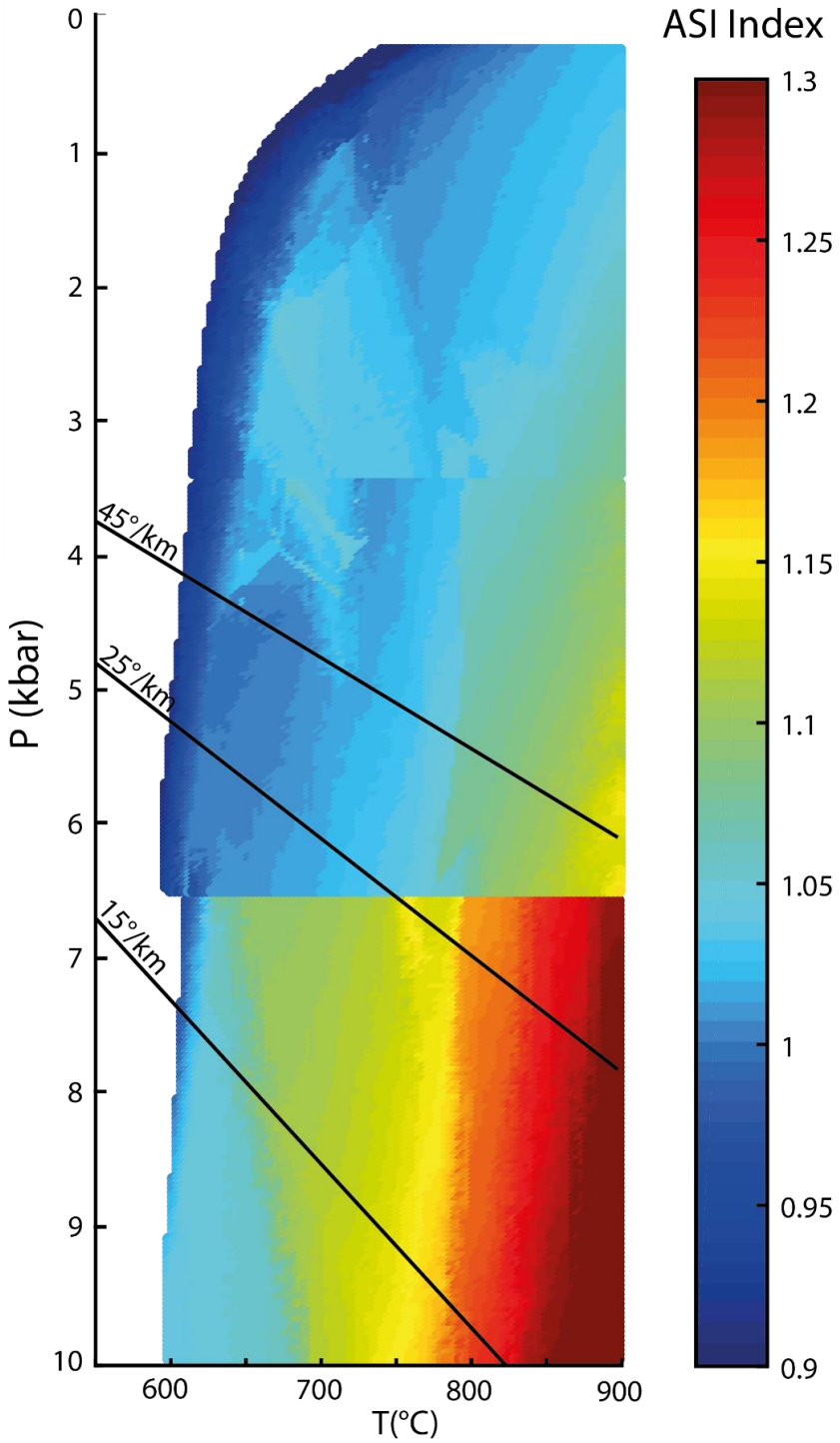

Figure 4.6: Thermodynamic models of crust anatexis (KCFMASH components system), under water-saturated conditions. Values for the composition of the Lower, Middle, and Upper Crust are those suggested by Rudnick and Gao (2003). Solid black lines represent different geotherms and correspond to those suggested by Thompson (1999) for a steady-state Standard Continent geotherm(15°/km), and perturbed geotherms due to the underplating of mafic magmas at the base of the crust in an extending lithosphere setting (Lachenbruch and Sass, 1978): that typical for the Basin and Range (25°/km) setting, and that expected for the Battle Mountain High (45°/km). Colorbar represents modeled ASI index as defined by Frost and Frost (2011).

The temperatures at which zircons saturate in the *anatectic* leucosome were obtained following the equation provided by Gervasoni et al. (2016), utilizing the composition of liquids obtained from the isochemical thermodynamic models, and the calculated Zr (ppm) concentrations in residual liquids. The latter was obtained assuming perfect incompatibility with bulk mineral assemblage, under equilibrium crystallization. The initial Zirconium concentration was considered equal to that proposed by Rudnick and Gao (2003), for whole-rock compositions of each crustal level, these values are 193, 149, and 68 (ppm) for the Upper, Middle, and Lower Crust, respectively. Magmas with temperatures below calculated Zircon Saturation Temperature, may form new cores and/or stabilize entrained zircon grains, independently of their multiple origins (*cf.* Miller et a., 2007). The model results indicate that zircons are only stable in melts formed in the Middle and Lower Crust at temperatures below 700°C, whereas zircon would crystallize (in a zirconium-saturated magmatic environment) from melts in the Upper Crust at temperatures as high as 800°C, near the surface (**Fig. 4.7**).

The above results provide new insights regarding the interpretation of the U-Pb zircon ages of crust-related plutons. Plutons formed by dehydration melting of the Lower Crust might have a significant amount of inherited zircon cores (Miller et al., 2000) most probably favored by rapid magma ascent and crystallization at a higher structural level (Bhattacharya et al., 2018), therefore common in allochthonous granites (see **Section 3.4**). Crust-related autochtonous granites emplaced in the Middle and Upper crust might reflect in-situ crystallization of zircons, yet fluid-absent anatexis in the shallow crust (Brown, 2013), must be related to anomalously high geotherms, and with the recognition of peripheral migmatitic structures adjacent to plutons (e.g. Flood and Vernon, 1978). Interpretations of U-Pb zircon geochronological data of deep-formed crustal granites can be understood if the melts at the source are saturated in zirconium, and subject to rapid extraction that allows for preserving inherited restitic zircons (Ayres et al., 1997; Clemens, 2003; Bea 2006;). This inference is consistent with that proposed by Diener et al. (2014) who claim that high melt production rates during crustal *anatexis*, followed by fast magma ascent, would be responsible for the high abundance of inherited zircons, leading to complex patterns in the basement U-Pb zircon ages (e.g. Bea et al., 2007; Molina et al., 2020).

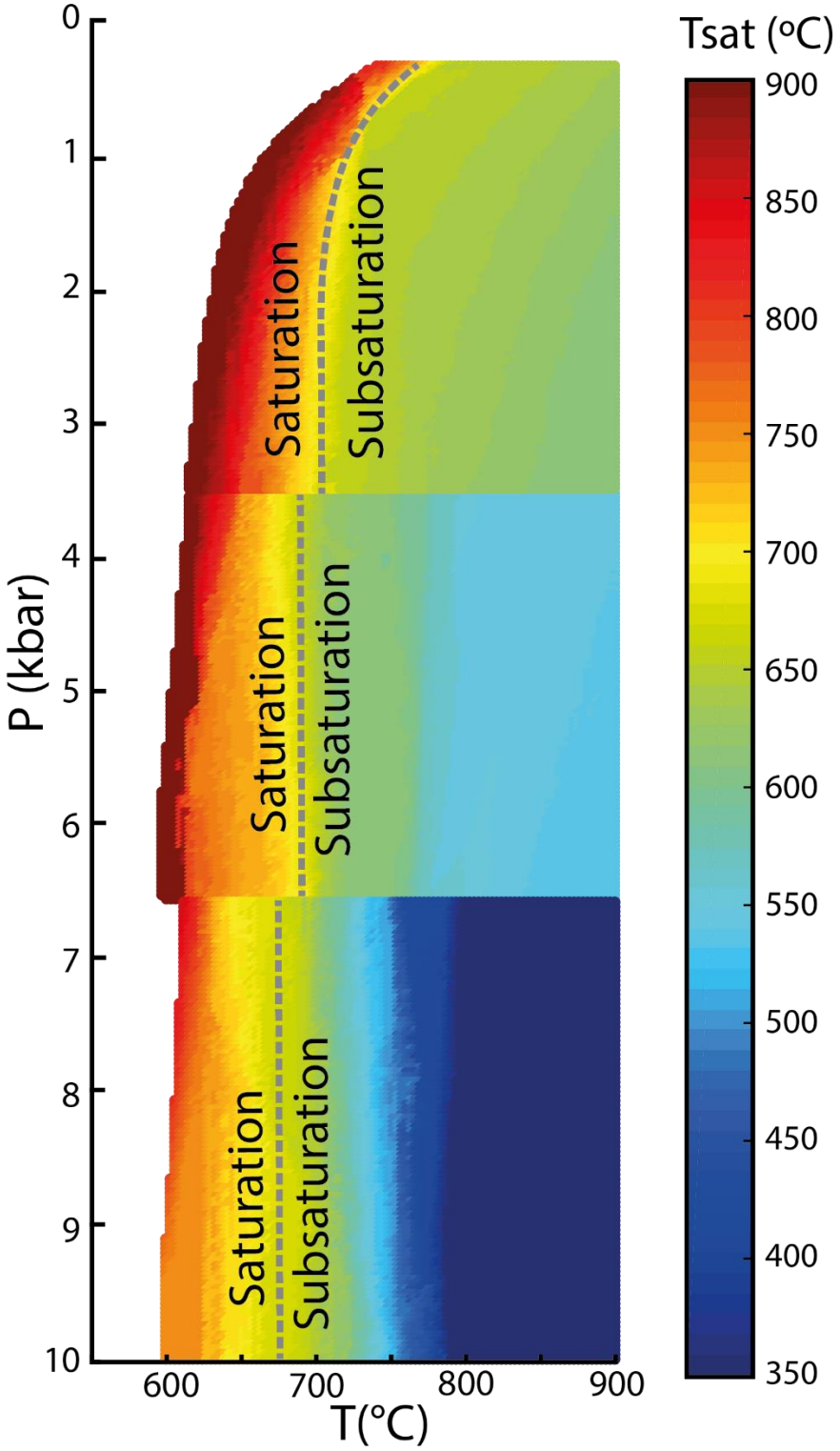

Figure 4.7: Thermodynamic models for crust anatexis (see main text for model details). The right-side color bar represents the calculated zircon saturation temperature (Tsat) (Gervasoni et al., 2016). A system temperature below Tsat holds a magmatic environment that would stabilize entrained zircon grains and/or generate new zircon cores, whereas higher-than-saturation magma temperatures characterize liquids that will eventually dissolve inherited zircon cores.

CHAPTER 5. ZIRCON INHERITANCE FROM THE SOURCES OF THE STUDIED LATE TRIASSIC PLUTONS (PUBLISHED IN LITHOS)

Lithos 370–371 (2020) 105662

Contents lists available at ScienceDirect

Lithos

journal homepage: www.elsevier.com/locate/lithos

Research Article

Zircon inheritance from long-lived sources of Late Triassic post-orogenic plutons, High Andes, Central Chile (~30°S): Magmatic feedbacks and petrogenetic implications

Pablo G. Molina [a,*], Miguel A. Parada [a], Changqian Ma [b]

[a] Departamento de Geología, Centro de Excelencia en Geotermia de los Andes (CEGA), Universidad de Chile, Plaza Ercilla 803, Santiago, Chile
[b] State Key Laboratory of Geological Processes and Mineral Resources, China University of Geosciences, Wuhan, People's Republic of China

ARTICLE INFO

Article history:
Received 28 November 2019
Received in revised form 22 June 2020
Accepted 25 June 2020
Available online 30 June 2020

Keywords:
Zircon inheritance
Post-orogenic
Thermodynamic modeling
S-type granite
Ferroan granite

ABSTRACT

A comprehensive understanding of the magmatic system evolution and petrogenetic environment is crucial for the correct interpretation of magmatic zircon age spectra. In the Central Andes, a protracted Late Paleozoic period of collisional to post-collisional magmatism was followed by Late Triassic emplacement of post-orogenic plutons and associated mantle precursors. Some of these magma products are crowded with inherited zircons with a large age span at the sample scale (>25 Myr). This work deals with two contrasting inheritance-rich plutons: the peraluminous cordierite-bearing Los Tilos pluton (LTp) and the peralkaline hypersolvus Ferro-edenite/hedenbergite-bearing Monte Grande pluton (MGp). Both plutons were derived from melting of the crust: the peraluminous S-type granite represents derivation from mixed materials, whereas the peralkaline A-type leucogranite embodies nearly eutectic melts enriched in incompatible elements. Rapid cooling of entrained assemblages suggests that segregation and subsequent ascent was rapid, following emplacement-site isobaric cooling at ca. 3.5 and 2 kbar, for LTp and MGp respectively. Most zircons were inherited; their disparate chemistry originates from contrasting sources, unveiling an open-system behavior.

The effects of variations in magma temperature, emplacement pressure, and water content were evaluated in light of zircon entrainment and dissolution potential, within a thermodynamically consistent framework. Relatively dry magmas (<3 H_2O wt%) readily preserve inherited zircons whereas similar size intrusions in excess of water most probably dissolve zircons in less than 12 kyr. In this geological context, early zircon armoring and source enrichment is vital to enhance zircon preservation at high temperatures.

We suggest that the large age span observed in zircon samples of both plutons reflects a long-lived source that fed arc-related granites in the Early to Middle Triassic, culminating in the Late Triassic with the final extraction of highly enriched crustal melts, in a post-orogenic context. Dry high-silica (>75 SiO_2 wt%) magmatic flare-ups, in extensional settings, fulfill the inheritance requisites presented here. Contrastingly, a broad zircon age span in large calc-alkaline batholiths emplaced at similar depths, reflect not source processes but rather magmatic erosion, crystal armoring and recycling of previous magma batches, and a complex crystallization history, spanning the whole duration of batholith construction.

1. Introduction

Zircon, being one of the most resistant minerals to dissolution at high temperatures, is used in many ways to disentangle distinct pluton-forming processes and their duration (Siégel et al., 2017). The age intervals displayed by zircons found in intrusions of variable size vary from tens of thousands to millions of years (e.g., Michel et al., 2008; Miller et al., 2007; Paterson et al., 2016). The fact that magmatic zircon inheritance has been recognized in many plutons formed and emplaced in different petrogenetic contexts (e.g., Bea et al., 2007; Casquet et al., 2014; Paterson et al., 2016), supports the idea that the 'crystallization' age of plutons must be carefully addressed, by a thorough understanding of the magmatic environment (Miller et al., 2007). In the past decades, a direct linkage between magmatic liquid composition and zircon saturation temperature has been explored and established (Boehnke et al., 2013; Gervasoni et al., 2016; Watson and Harrison, 1983). Among the conclusions: (1) peraluminous magmas stabilize zircons at higher temperatures than peralkaline ones; and (2) increasing the zirconium content of magmas hasten zircon saturation in cooling melts. Magmas derived from crustal materials modulate these two geochemical variables in the source (Bea, 1996; Patiño Douce, 1999; Scaillet et al., 2016), and its fertility, in such, varies in time and

* Corresponding author.
E-mail addresses: pamolina@ing.uchile.cl (P.G. Molina), maparada@ing.uchile.cl (M.A. Parada), cqma@cug.edu.cn (C. Ma).

https://doi.org/10.1016/j.lithos.2020.105662
0024-4937/

space (Farner and Lee, 2017). Therefore, care must be taken in interpreting the crystallization history of plutons with abundant inherited zircons (Miller et al., 2003; Rodríguez et al., 2019). So far, just a glimpse of the weight of the disparate factors that drive granite generation, differentiation and emplacement processes, is understood in terms of zircon inheritance, preservation and growth (e.g., Bea et al., 2007; Bhattacharya et al., 2018; Kelsey et al., 2008; Watson, 1996).

This work is focused on two coeval plutons of contrasting nature, crowded with inherited zircons: a peraluminous granite (two-mica and cordierite-bearing), and a peralkaline hypersolvus leucogranite (iron-rich pyroxene-bearing). Both were emplaced during the Late Triassic in a post-orogenic context (Casquet et al., 2014) and are now exposed in the Present-day High Andes of Central Chile (~30°S). We aim to demonstrate: (1) early zircon crystallization in the source is related to particular petrotectonic contexts; (2) the composition of zircons can be used to reveal contrasting source materials and magmatogenic processes; and (3) the systematics of zircon inheritance, preservation and growth delivers insights to evaluate magma evolution and emplacement depth, in wet and dry environments (e.g., Miller et al., 2014). For this, we provide a novel approach to envision the nature of the magma source and emplacement conditions, assessing the timescales of zircon preservation and growth, based on geothermobarometric calculations, thermodynamic modeling and existing petrogenetic grid constraints.

2. Geological setting

In Central Chile, A-type granites characterize Late Triassic plutonism and mark a tectonic change between the Late Paleozoic and the initiation of the Andean regime in the Mesozoic (Oliveros et al., 2018; Parada, 1990). The Late Paleozoic to Triassic igneous rocks of the South-Central Andes were emplaced after the San Rafael orogeny

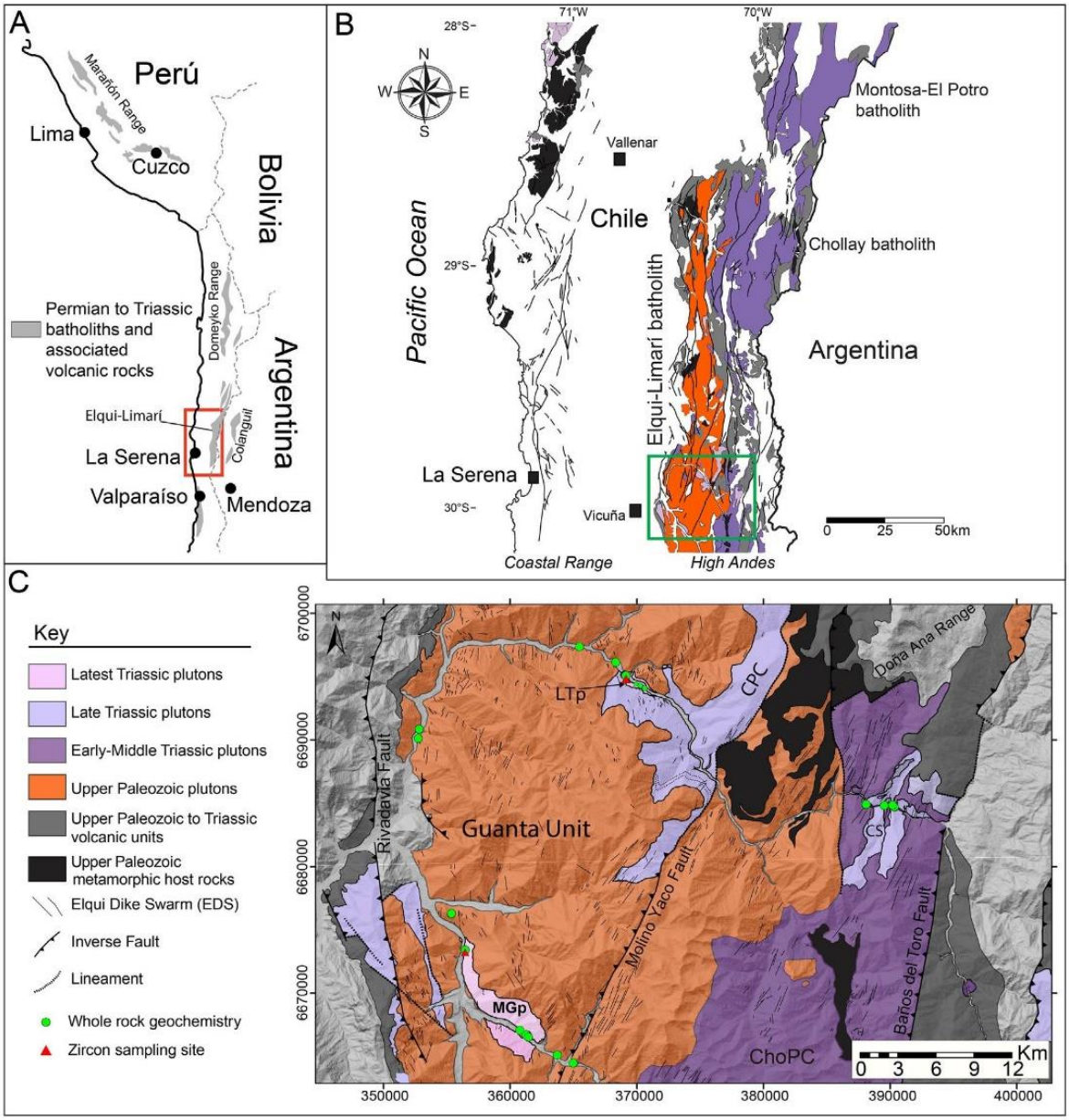

Fig. 1. A. Distribution of the Permian to Triassic belts in the Andes (modified from Hervé et al., 2014). The red rectangle indicates the location of the Elqui-Limarí batholith. B. The regional-scale geological map highlights the main Upper Paleozoic to Triassic units (after Coloma et al., 2017). The green rectangle corresponds to the study area. C. A simplified geological map showing the main units in the study area. Background shading represents topographic relief. Los Tilos pluton (LTp) and Monte Grande pluton (MGp) shown in pink; CPC: Los Carricitos Plutonic Complex; ChoPC: Chollay Plutonic Complex: CS: Colorado Syenogranties. Geological map modified after Parada, 1988 and Murillo et al. (2017). All coordinates presented as UTM, datum WGS 1984. (For interpretation of the references to colour in this figure legend, the reader is referred to the web version of this article.)

(Upper Carboniferous-Permian) and comprise several N-S trending batholiths (Fig. 1A) exposed along Perú, Chile and Argentina (Hervé et al., 2014 and references therein). In Chile, these batholiths are displayed as two coeval *en echelon* belts that crop out in the High Andes and Coastal Ranges, north of 38°S (Parada, 1990). In the High Andes belt, host rocks are represented by a few scattered basic, quartzo-feldspathic and calc-silicate metamorphic roof pendants (Fig. 1B, C) of Devonian to Carboniferous age (Coloma et al., 2017). In turn, the Coastal belt was emplaced within the Late Paleozoic metamorphic accretionary prism basement (Vásquez and Franz, 2008), which records the onset of the subduction in the Early Carboniferous (Creixell et al., 2016). The two belts are unconformably overlain by Triassic mafic and felsic volcanic rocks and Early Jurassic shallow marine back-arc limestones and sandstones (Coloma et al., 2017 and references therein).

Oxygen and hafnium isotopes systematics in zircon show a progression of source rocks, from Upper Paleozoic crustal sources to more mantle-like in the early Mesozoic (del Rey et al., 2016; Hervé et al., 2014), with a progressively increasing juvenile (Sr—Nd) component towards the Cretaceous (Parada, 1990). Current geodynamic models for the Triassic proto-Andean margin, advocate for attenuated-subduction below a thinned lithosphere combined with transtensional tectonics (Espinoza et al., 2019), in a slab rollback setting (Coloma et al., 2017; del Rey et al., 2016; González et al., 2017). In this period, relaxation of the upper plate accommodated asthenospheric upwelling, ascent, and injection of mantle magmas (Parada, 1990); activity that could have induced lower crustal anatexis (Casquet et al., 2014). Mantle magmas are portrayed by the regional-scale intrusion of the contemporaneous 'Elqui Dike Swarm' (henceforth EDS), which in some locations have mutual cross-cutting relations with the Late Triassic plutons (González et al., 2017).

Late Triassic bimodal magmatism is recognized in both belts (González et al., 2017; Vásquez and Franz, 2008). This plutonism is scant and crops out as small, scattered plutons (Parada, 1990; Fig. 1B). In the Coastal Range, this magmatism is depicted in an association of leucogranites, quartz-diorites and gabbros, as well as intercalated felsic and mafic volcanic products and related dikes (sourced at different lithospheric depths) with a wide range of initial strontium ratios between 0.704 and 0.712 (Morata et al., 2000). In the High Andes belt, at about 28–30°S, the main Late Triassic lithologies are within-plate granite plutons and associated contemporaneous bimodal volcanic rocks (basalts and high-silica rhyolites), displaying $^{87}Sr/^{86}Sr_i$ and εNd values around ~0.705 and ~ −1, respectively (González et al., 2017). These rocks are hosted within the Upper Paleozoic to Triassic Elqui-Limarí, Chollay, and Montosa-El Potro batholiths (Fig. 1B). Conversely, the older rocks of the EDS show similar $^{87}Sr/^{86}Sr_i$ ratios to those of the contemporaneous granites (~0.705) but exhibit higher εNd values (around 2.0 to 2.9). The dike magmas are interpreted as derived from an enriched mantle source (Creixell et al., 2009). The youngest magma pulse occurred in the Elqui-Limarí batholith, just before the arc 'jumped' to the present-day Coastal Range (ca. 100 km west) in the Late Triassic (Coloma et al., 2017) and before the establishment of an incipient island arc setting in the Jurassic (Rossel et al., 2013). Most of the batholith was deformed and exposed after the Cretaceous, in a style similar to that of the Laramide Province of North America (Moscoso and Mpodozis, 1988).

3. Methodology

A total of 33 rock samples were ground and pulverized to at least 95% minus 200 mesh at the Laboratorio de Preparación de Muestras, Departamento de Geología, Universidad de Chile. Major and trace element analyses were obtained using ICP-emission spectrometry and ICP-MS, respectively, at the Activation Laboratories Lds., Ancaster, Ontario, Canada. The samples were mixed with lithium metaborate/tetraborate combined in an induction furnace, then poured into a solution of 5% nitric acid containing an internal standard and mixed continuously until completely dissolved. FeO values were determined through titration (using potassium dichromate) via cold acid digestion of ammonium metavanadate and hydrofluoric acid.

Two samples were collected for LA-ICP-MS U—Pb zircon geochronology and geochemistry (a total of 45 zircon grains). Zircon separation consisted of sample crushing and grinding followed by zircon concentration via Wilfley table, Frantz isodynamic magnetic separator, heavy liquid separation, and handpicking at Laboratorio de Preparación de Muestras, Departamento de Geología, Universidad de Chile. Cathodoluminescence images were acquired using a high-resolution Quanta 400 FEG environmental SEM connected to an Oxford INCA350 EDS and a Gatan Mono CL3+ system with 10 kV imaging conditions and 6.7 nm spot size. U—Pb isotopes and trace elements were analyzed simultaneously at the State Key Laboratory of Geological Processes and Mineral Resources, China University of Geosciences, Wuhan, using an Agilent 7500a ICP-MS apparatus coupled with a GeoLas 2005 laser-ablation system with a DUV 193 nm ArF-excimer laser (MicroLas, Germany). Detailed analytical procedures and data reduction are available in Liu et al. (2010). A spot size of 32 μm was used. Argon was used as the make-up gas and mixed with the carrier gas (helium) via a T-connector before entering the ICP. Nitrogen was added into the central gas flow (Ar + He) of the Ar plasma to lower the detection limit and improve precision (Hu et al., 2008). Each analysis incorporated a background acquisition of 20–30 s (gas blank) followed by 50 s data acquisition. Zircon 91,500 was used as standard for mass discrimination and U—Pb isotope fractionation. The time-dependent drifts of U–Th–Pb isotopic ratios were corrected using a linear interpolation (with time) for every five analyses according to the variations of standard 91,500. The preferred U–Th–Pb isotopic ratios used for 91,500 are from Wiedenbeck et al. (1995). The reproducibility of the U—Pb was evaluated by comparison with the secondary zircon standard GJ-1 (Jackson et al., 2004). Off-line integration of background and analyzed signals, time-drift correction and quantitative calibration for trace element analyses and U—Pb dating, were performed using ICPMSDataCal (Liu et al., 2010). The uncertainties of preferred values for the external standard 91,500 were properly propagated. Concordia diagrams and weighted mean calculations were made using Isoplot/Ex_ver3 (Ludwig, 2003). Associated errors are quoted at the 1σ confidence level.

Electron microprobe analyses of major and trace elements of micas, cordierite, amphibole, pyroxene, and zircon were conducted using a JEOL JXA-8230 machine (LAMARX laboratory, FCEFyN at UNC, Argentina). Spot analyses were performed using a 15 kV accelerating voltage, a 10 nA current, and a 10 μm diameter beam. Reference standard materials were measured before each session for peak overlap, background and offline corrections. Different crystals were used to perform the respective analyses, for the different elements. Micas: TAP (F, Na, Mg, Al), PETJ (K, Cl, Ca), LIF (Ti) and PETH (Si); Cordierite: TAP (Na, Mg, Al, Si), PETJ (K, Cl, Ca), LIFH (Cr, Mn, Fe, Zn); Amphibole: TAP (F, Na, Mg, Al, Si), LIF (Ti, Cr, Mn, Fe), PETH (Ca, K, Cl, Zr, Sr); Pyroxene: TAP (Na, Mg, Al, Si), PETJ (K, Ca, Ti), LIF (Zn), LIFH (Cr, Mn, Fe), PETH (Zr); Zircon: PETJ (P, Y), TAP (Al, Hf), PETH (U, Zr, Si). Results were corrected for instrumental beam-matrix effects and instrumental drift by the phi-rho-Z method (CITZAF; Armstrong et al., 2013).

4. Results

4.1. Field and petrographic characteristics

The Los Tilos pluton (referred hereafter as 'LTp') is a ca. 16 km^2, tabular (Fig. 2A), heterogeneous fine to medium grain granodiorite body. LTp corresponds to the youngest plutons of the Middle to Late Triassic calc-alkaline Los Carricitos Plutonic Complex (CPC; Murillo et al., 2017) and is composed of medium-grained Bt + Amp-bearing granodiorites and granites, and coarse grain and Px + Amp-bearing diorites and tonalites. The CPC was emplaced within tonalites of the Early Permian

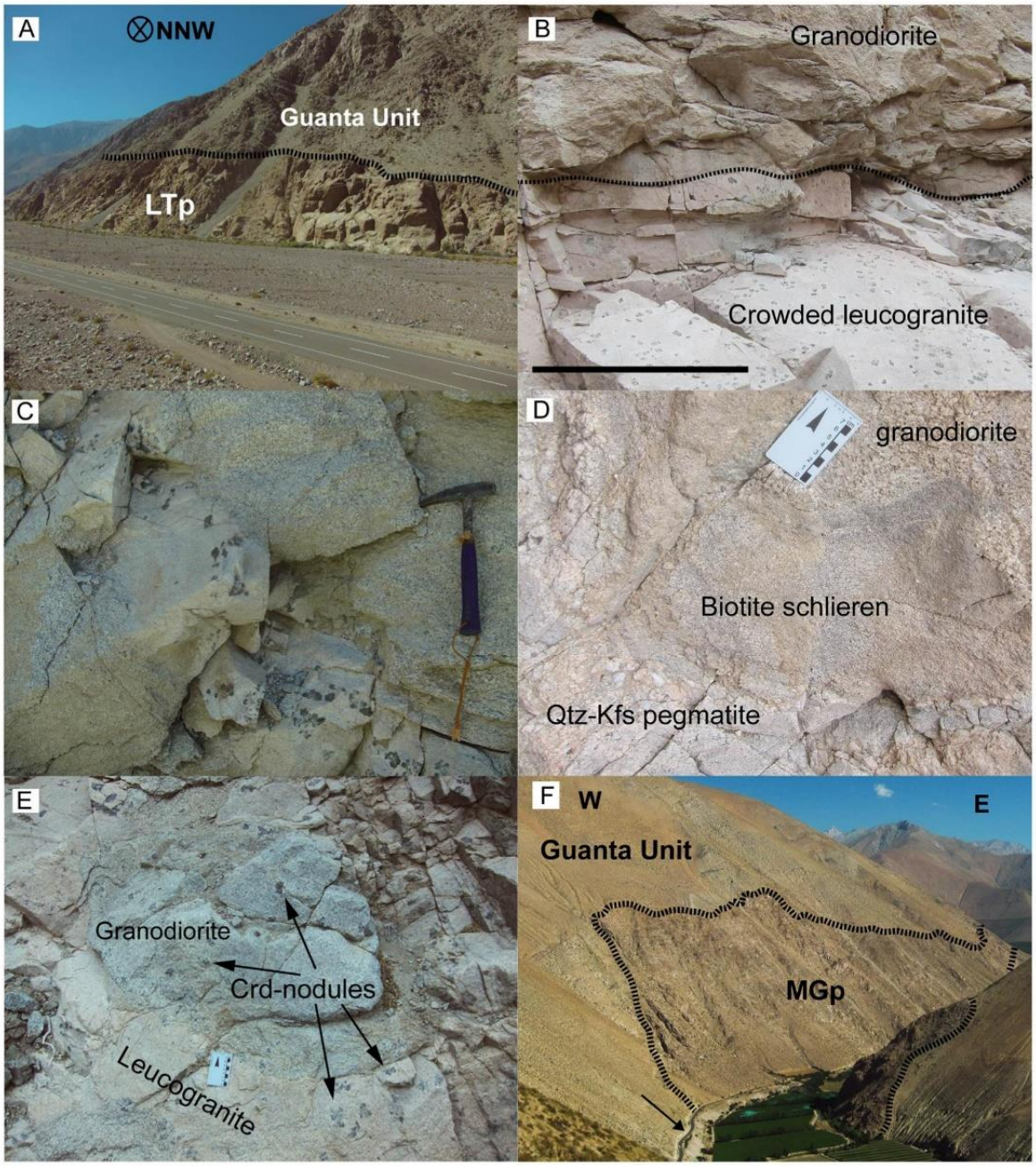

Fig. 2. Field photographs: A. Photo of LTp taken near the eastern tip of the pluton. Note the flat roof geometry. B. Nodule-crowded leucocratic zone. Scale equals 1 m. C. Nodule-bearing leucocratic dike. D. Biotite-bearing schlieren band in the main LTp granodiorite, at the edge of a Qtz-Kfs pegmatite. E. Scattered Crd-nodules among mingled granodiorite and leucogranite. Amorphous nodules display ca. 1 cm leucocratic rims. F. Panoramic view of MGp: a vertical-bounded tabular geometry is envisaged. Arrow indicates road to scale.

Guanta Unit (Murillo et al., 2017; Fig. 2A). LTp is characterized by peculiar dark-colored cordierite-quartz-plagioclase nodules (Fig. 2B, C, E). This feature is not exclusive to this pluton and can be found in other granodiorite units within CPC. The Crd-Qtz-Plg nodules also occur as well-formed ellipses, as amorphous clusters (Fig. 2C), and as scarce angular nodules. These clusters are surrounded by 0.5–3.0 cm wide leucocratic rims composed of anhedral Kfs-Qtz intergrowths (Fig. 2E). The nodules are scattered throughout the pluton and are locally concentrated (>20 nodules/m^2) in meter-sized areas (Fig. 2B), or in fine-grained *syn*-plutonic leucocratic dikes (Fig. 2B, C, E). Cuspate schlieren bands rich in mafic minerals (mostly biotite) are found in association with internal contacts surrounding the outer limit of nodule-bearing leucocratic zones and Qtz-Kfs pegmatites (Fig. 2D).

The mineralogy of LTp consists of anhedral quartz (~45 vol%), subhedral zoned plagioclase (~30 vol%) with partially sericitized cores rimmed by albite overgrowths, weakly perthitic subhedral K-feldspar (~20 vol%), subhedral biotite (~5 vol%) with subtle chloritization, and minor interstitial white mica (<1 vol%). Magnetite and ilmenite are included in, or almost completely replace, biotite. Zircon, apatite, xenotime, monazite, and magmatic epidote are accessory phases. The nodules lack biotite and are composed of subhedral polycrystalline quartz (~25 vol%), bipyramidal (beta-quartz paramorphs) quartz (~10 vol%), and highly zoned and partially sericitized plagioclase (~15 vol%) displaying sieve texture and slight fragmentation (Fig. 3A). These minerals are embedded in pinitized pseudomorphs of poikilitic cordierite (~50 vol%; Fig. 3A). In the less pinitized grains, polysynthetic twinning, and replacement by yellowish brown-green micaceous pinite along 5–20 μm width cracks, in grain interfaces and radiating perpendicular to mineral boundaries occur (Fig. 3B). Opaque minerals (magnetite-ilmenite), zircon, apatite, monazite, and xenotime are accessory phases;

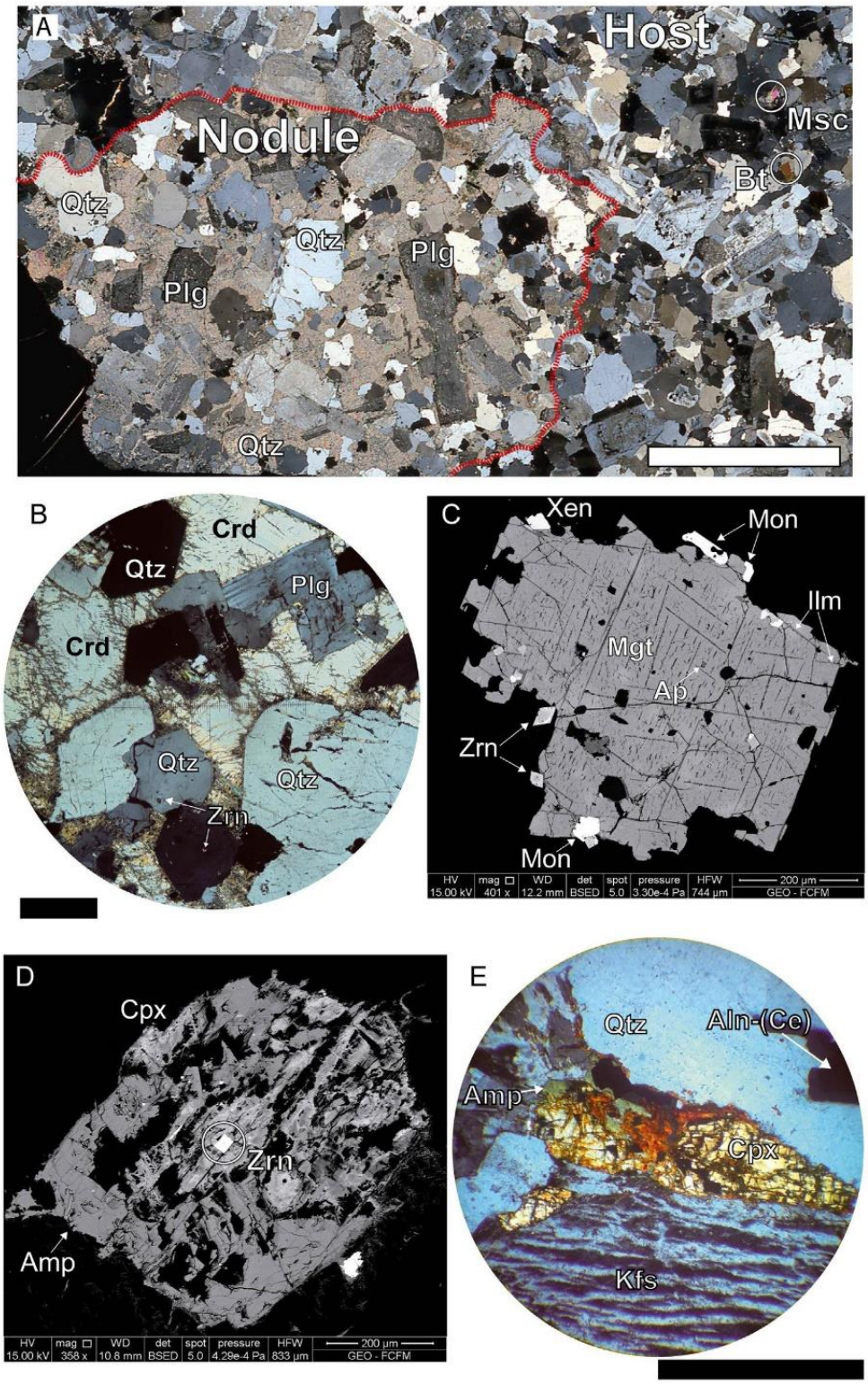

Fig. 3. A. LTp: Crossed polars wide-angle photomicrograph. Red discontinuous line delimits roughly the border of the Crd-Qtz-Plg nodule. Note the strong pinitization affecting interstitial cordierite. B. LTp: Crossed polars photomicrograph showing partially pinitized cordierite (along cracks and in grain interphases); zircon is found as inclusions in β-Qtz paramorphs. C. LTp: SEM-BSE image showing a magnetite crystal (with ilmenite lamellae); clustered with monacite, zircon, apatite and xenotime (LTp). D. MGp: SEM-BSE image showing uralitized clinopyroxene with included euhedral zircon (<15 μm). E. MGp: Photomicrograph of partially uralitized clinopyroxene, perthitic feldspar, and allanite-(Ce). One millimiter black bar for scale (excluding C and D which have its own scale). (For interpretation of the references to colour in this figure legend, the reader is referred to the web version of this article.)

they are found as closely related grains (Fig. 3C), but also as isolated inclusions in cordierite and bipyramidal quartz grains.

The Monte Grande pluton (referred hereafter as 'MGp') was also emplaced in the Guanta Unit. It consists of a medium-grained, homogeneous, hypersolvus leucogranite. This pluton is similar to LTp in having a tabular shape, but displays nearly vertical bounding contacts, resembling alkaline epizonal ring dikes (e.g., Nardi and Bonin, 1991) and cone-shaped intrusions (Fig. 1C; Fig. 2F). Using the maximum diameter in satellite plan-view, its areal extent should cover at most ~65km^2 (but no less than ~10km^2).

The mineralogy of MGp consists of mesoperthitic hypersolvus alkali feldspar (~45 vol%) together with subhedral quartz (~45 vol%), and lesser amounts of fine-grained, boxy, cellular plagioclase with interpenetrating polysynthetic twinning (~5 vol%). Quartz and K-feldspar grains form an irregular mosaic; albitic plagioclase mantles K-feldspar or fills intergranular spaces. Mafic minerals (~4 vol%) include clinopyroxene strongly replaced by iron oxides and amphiboles (Fig. 3D, E), and interstitial, xenomorphic amphibole. Pristine, euhedral allanite-(Ce) (~1 vol %) is generally found in contact with opaques (Fig. 3E). Equant zircon crystals occur as inclusions in clinopyroxene (Fig. 3D) or scattered within Kfs-Qtz intergrowths. The mineral assemblage of MGp resembles the miaskitic varieties of alkaline rocks (Marks et al., 2011).

4.2. Whole-rock geochemistry and source affinity

The geochemical characterization of the studied plutons is based on 33 new analyses and complemented with 223 analyses of Triassic igneous units collected elsewhere in the High Andes segment, available in the literature (Coloma et al., 2017; Creixell et al., 2009; González et al., 2017; Murillo et al., 2017; Parada, 1988). Rocks of LTp and MGp are among the most siliceous Triassic units presented here, with SiO_2 contents of ~74–76 wt%. In contrast, whole-rock compositions of Crd-Qtz-Plg nodules show lower values (ca. 70 wt%). The Fe_2O_3/FeO ratios vary from average values of 2.06 in LTp, 0.31 in nodules, and 0.94 in MGp. The MnO content of LTp and MGp is low and fairly similar (within 0.02 and 0.04 wt%), while nodules show higher contents (between 0.27 and 0.35 wt%). The MgO contents decrease from 0.27 in LTp to 0.07 in MGp, whereas the nodules exhibit values up to 1.76 wt%. All other elements bear similar quantities (Supplementary Material).

The aluminum-saturation index (Fig. 4A), defined as molecular Al/(Ca-1.67P + Na + K), place LTp within mildly peraluminous granites field (1.02 average), while MGp is in the peralkaline field (0.92 average). Also, MGp rocks classify as ferroan, similar to numerous Late Triassic granite plutons (>70 SiO_2 wt%) (Fig. 4B). All samples from MGp and LTp's Crd-nodules (and few other Triassic igneous rocks) display Ga/Al ratios (Whalen et al., 1987) that are compatible with A-type granites (Fig. 4C) formed in a within-plate setting (Fig. 4D). Some of them display a derivation from continental or underplated crustal sources formed in post-collisional environments (Fig. 4C, inset). MGp resembles the field of metaluminous A-type granites ('MAGS') and experimental melts resulting from a direct fusion of greywackes (Fig. 4F; Patiño Douce, 1999).

Chondrite-normalized REE patterns show no significant difference between Crd-Qtz-Plg nodules and their host granite (LTp), whereas the MGp rocks contain higher REE concentrations (Fig. 4E). Almost all samples display similar, negative europium anomalies, bracketed between $(Eu/Eu^*)_N$ values of 0.22 and 0.56. Multi-element diagrams show resemblance between the OIB-like EDS, LTp, and Crd-nodules, with exception of Sr, P, and Ti contents. MGp, in turn, shows the higher degree of REE and HFSE enrichment of all units used for comparison (Fig. 4G). With exception of EDS, a subduction component in the origin of the studied magmas is envisaged due to the ubiquitous Nb—Ta, Sr—P, and Ti troughs and high LILE and Pb concentrations (cf. González et al., 2017).

4.3. Zircon morphology, U—Pb dating, and regional age correlations

A total of 45 LA-ICP-MS zircon analyses are reported here (Supplementary Material). The obtained $^{206}Pb/^{238}U$ dates display mostly concordant ages (43 out of 45 analyses are above 95% concordance) and are bracketed between ca. 240 and 210 Ma. A bimodal age distribution, with peaks around ca. 235 (Ladinian-Carnian) and 215 Ma (Norian) is observed in the Los Tilos cordierite-bearing granite, whereas a relatively continuous age spectrum (data concentrated towards older ages) is shown by zircons of the Monte Grande hypersolvus leucogranite (Fig. 5A). The younger zircon age peak observed in the LTp is similar to that zircon U—Pb SHRIMP rim ages (average 215.6 ± 1.9 Ma) reported by Hervé et al. (2014) in the same pluton. Contrasting zircon morphologies are revealed by cathodoluminescence images: grains from the Los Tilos pluton are smaller and have higher aspect ratios than those from the Monte Grande pluton. In general, zircon grains of LTp display fairly concordant rim overgrowths and internal discontinuities over seemingly distinct cores. In contrast, most zircon grains of MGp are partially resorbed, depicting clear discontinuities within internal overgrowths, although some grains contain homogeneous cores (Supplementary Material). Some older zircon ages are restricted to the inner portion of analyzed grains of both plutons, as expected in populations with a significant fraction of inherited cores from the source (Bea et al., 2007; Miller et al., 2003).

The magmatic pulse that gave rise to LTp and MGp marked the end of a long-lived Permian to Triassic arc evolution (Hervé et al., 2014; Coloma et al., 2017; Fig. 5B (3)). The most prominent age peaks of LTp and MGp (Norian) are equivalent to that observed in nearly contemporaneous back-arc basin lavas and pyroclastic deposits (Fig. 5B (2)) and epizonal syenogranites (Fig. 5B (4)). The older age peaks (Ladinian-Carnian) correlate with zircon ages of Triassic rhyolites (Fig. 5B (1); Murillo et al., 2017) formed in a rift phase recognized in the southwestern margin of Gondwana (Espinoza et al., 2019).

4.4. Mineral composition and magmatic affinity

4.4.1. Zircon

Characterization of Mgp and LTp zircon compositions was obtained from LA-ICP-MS data along with 38 EPMA analyses (complete data set in Supplementary Material). Chondrite-normalized REE patterns of analyzed zircons show an increase in concentrations from La to Lu, positive Ce and negative Eu anomalies (Fig. 6A) These patterns, along with Th/U ratios mostly above 0.5, suggest a magmatic affinity (Siégel et al., 2017). Zircons from LTp have lower total REE concentrations than those from MGp, and a distinctively less-pronounced europium anomaly (inset in Fig. 6A). Zircons from the two plutons show similar Ce anomalies (inset in Fig. 6A) and zircon grains from LTp display a narrow range of REE contents (except for lanthanum), compared with the scattered values of MGp zircons. The Ti content of zircons is bracketed between 1 and 8 (ppm) and is slightly higher in LTp (inset in Fig. 6A). Zircons of both plutons have similar Hf and P contents in the range of 7000–18,000 (ppm) and 0–3500 (ppm), respectively (Fig. 6B). Yttrium concentration in MGp zircons, reach values as high as ca. 16,000 (ppm), whereas LTp zircons are below ca. 9000 (ppm) (Fig. 6B). Zircon grains from nodules share the same geochemical fingerprint as their host granite (see Fig. 6 for detailed caption). Using the tectono-magmatic discrimination diagram of Grimes et al. (2015), zircon grains from MGp fall within the mantle-zircon array, encompassed by the ocean-island affinity field (Fig. 6C), while those from LTp plot in the continental arc-type field; which is consistent with the juvenile components in the formation of MGp's zircons, and supracrustal components in the formation of zircons of LTp (Hervé et al., 2014).

4.4.2. Cordierite

A total of 21 EPMA analyses were made on cordierite (data set in Supplementary Material) from the cordierite-bearing nodules of LTp (recalculations on the basis of 18 oxygen atoms). Cordierite compositions display values of octahedrally coordinated and channel site cations consistent with a magmatic origin (Pereira and Bea, 1994), with Mg/(Fe + Mn + Mg) ratios between 0.45 and 0.51, and Ca + K + Na (channel site cations) contents between 0.1 and 0.21 (Fig. 7A). Similarly, the MnO (wt%) contents in cordierites (between 1.56 and 1.86) are indicative of an igneous origin from a peraluminous magma (Dahlquist et al., 2005). The high sodium contents (between 0.09 and 0.22 a.p.f.u.) are among the highest found in cordierite-bearing granites of South America (Ferreira et al., 2019), An inversely-correlated linear trend exists between octahedral versus tetrahedral site cation contents (Fig. 7A).

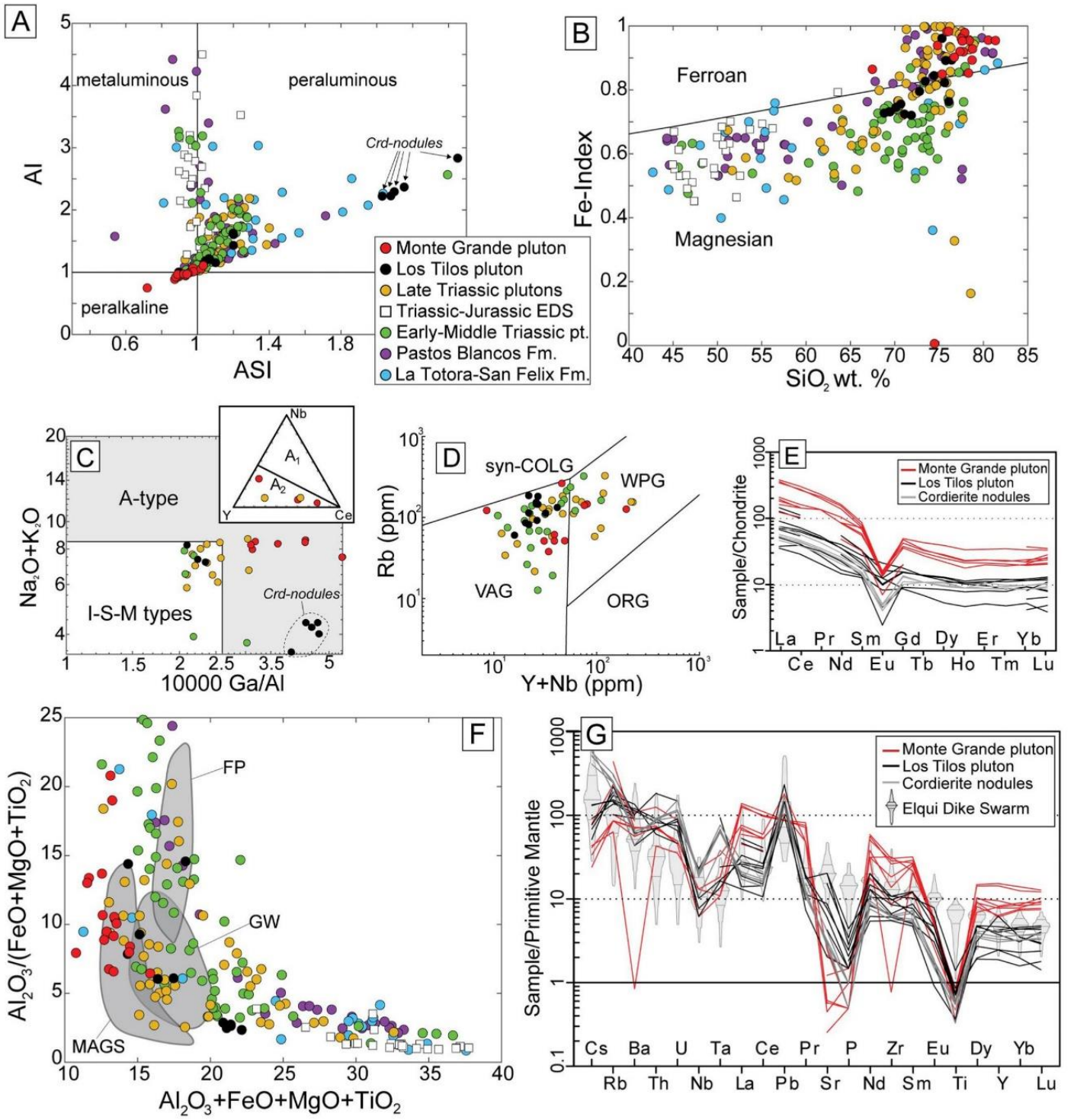

Fig. 4. Whole-rock geochemistry: A. Alkalinity index AI = Al/(Na + K) versus aluminum saturation index ASI = Al/(Ca-1.67P + Na + K). B. SiO_2 versus Fe-index = (FeO + 0.9Fe_2O_3)/(FeO + 0.9Fe_2O_3 + MgO). A and B after Frost and Ronald Frost (2011). C. A-type granite discrimination diagram (after Whalen et al., 1987), A-type granites in gray field. Inset shows the A-type granites subdivision (Eby, 1992): A_1 represents derivation from a OIB-like source, whereas A_2 post-collisional crustal magmas. D. Tectonic discrimination diagram after Pearce et al. (1984). E. Whole rock chondrite-normalized REE patterns (normalization values after Anders and Grevesse, 1989). F. Composition fields of experimental melts obtained from distinct protoliths (Patiño Douce, 1999). MAGS: metaluminous A-type granites: GW: greywackes; FP: felsic pelites. G. Multi-element diagram (normalization values after McDonough and Sun, 1995). Elqui Dique Swarm (EDS) data in background.

This trend is nearly parallel to that expected by the coupled substitution $^{Ch}Na^{+} + {}^{IV}(Mg^{2+},Fe^{2+}) = {}^{Ch}\square + {}^{IV}Al^{3+}$ (Schreyer, 1965).

4.4.3. Micas

Twenty four biotites and 17 white micas of LTp were analyzed (data set in Supplementary Material). The Al_2O_3 and MgO contents in biotite range from 16.2 to 18.0 (wt%), and from 7.9 to 9.0 (wt%), respectively, which correspond to ca. 3 Al to 2 Mg a.p.f.u. (recalculated on the basis of 22 oxygen atoms), consistent with a peraluminous granite affinity (Nachit et al., 1985) (Fig. 7B). A mild inverse correlation between total Al (a.p.f.u.) and Mg (a.p.f.u) is roughly consistent with the siderophyllitic substitution (inset on Fig. 7B). The Mg# of biotites

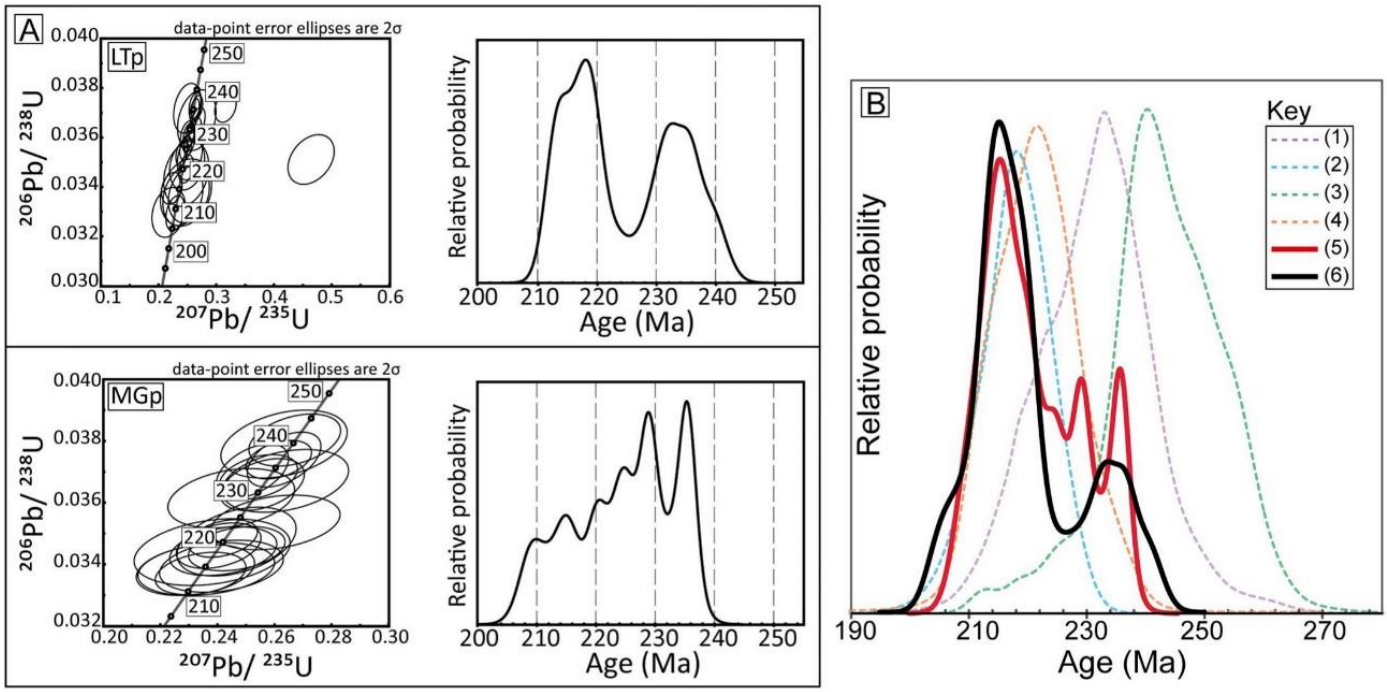

Fig. 5. U—Pb Zircon geochronology: A. LA-ICP-MS data obtained from the peraluminous Los Tilos pluton (LTp) and the peralkaline Monte Grande pluton (MGp). B. Regional-scale correlation of U—Pb ages reported elsewhere (Hervé et al., 2014; Coloma et al., 2017; Murillo et al., 2017). Contemporaneous batholith coverage: intermediate to acidic continental-marine volcanic products represented by the Pastos Blancos Formation (1), and the La Totora and San Felix Formations (2). Triassic arc-root: gabbros to granodiorites of the Chollay Plutonic Complex, ChoPC (3), and within-plate granites of the bimodal Colorado Syenogranites (4). The Monte Grande (5) and Los Tilos (6) age spectra are results from this study plus published data (Hervé et al., 2014).

(calculated as Mg# = Mg/(Mg + Fe) in a.p.f.u.) is constrained between 0.39 and 0.43. White micas can be classified mainly as muscovite (X_{mus} between 0.71 and 0.79), and are characterized by a very low celadonite component ($X_{Al\text{-}Ce} < 0.05$; Fig. 7B). The Si contents of white micas are bracketed between 6.08 and 6.32 a.p.f.u. Following the Miller et al. (1981) criteria, nearly half of the analyzed muscovites fall within the 'Primary Mica Field' (inset on Fig. 7B).

4.4.4. Amphibole

A total of 46 pseudomorphic (replacing pyroxene) and 20 xenomorphic (interstitial) MGp amphibole analyses were made (data set in Supplementary Material). According to the Leake et al. (1997) classification, all amphiboles correspond to Ferro-edenite (Fig. 7C). Following the Locock (2014) procedure, the recalculated chemistry of amphiboles (on the basis of 24 oxygen atoms) yields total Al (a.p.f.u.) contents between 0.9 and 1.2, whereas total Ti spans 0.021 to 0.216 (a.p.f.u.). Total A-site occupancy (sum of Na^A and K^A ions) present values mostly above 0.5 (between 0.29 and 0.73; 0.64 avg.). Fe/(Fe + Mg) ratios are between 0.96 and 0.98, corresponding to iron-rich amphiboles formed in low fO_2 magmas (Anderson and Smith, 1995). Calculated Fe^{2+}/Fe^{3+} ratios (disregarding outliers) place pseudomorphic amphiboles within the 12.7 and 21.3 interval (17.2 avg.), whereas xenomorphic amphiboles show higher values between 13.7 and 28.9 (21.1 avg.). A well-correlated inverse relationship between $Aliv^T+(Na + K)^A$ versus Si^T (a.p.f.u.) indicates the edenitic substitution as a controlling mechanism of cationic exchange (Fig. 7C).

4.4.5. Pyroxene

A total of 35 MGp's pyroxene analyses are presented here (data set in Supplementary Material). Pyroxene nomenclature and cation site occupancy (structural formulae on the basis of 6 oxygens) after Morimoto (1988). Ferric iron abundance was estimated from charge balance (Droop, 1987; Lindsley, 1983). Pyroxenes of MGp classify as hedenbergite and ferrohedenbergite (Fig. 7D) and are tightly clustered between Wo(40.5–45.5), En(0.3–5.5), and Fs(52.1–59.2). The occupancy of the M1 site is mainly dominated by Fe^{2+}, averaging ca. 0.9 a.p.f.u., whereas R^{3+} cations ($Fe^{3+}+Ti^{3+}+Al^{3+}+Cr^{3+}$) average 0.05 a.p.f.u. Additionally, the M2 site is almost completely filled by Ca^{2+} and Fe^{2+} cations, averaging 0.8 and 0.1 a.p.f.u., respectively, whereas Fe^{2+}/Mg^{2+} ratios average 38.5. A fairly good (R^2 ~ 0.72) linear correlation between R^{3+} cations (M1 site) and Na^+ (M2 site) is observed (Fig. 7D); this trend is also correlated with total Fe^{2+}/Fe^{3+} ratios in clinopyroxene.

The origin of the studied iron-rich Cpx of MGp deserves some explanation. Pyroxenes display $X^{FeO}_{Cpx}/X^{MgO}_{Cpx}$ (in mole fraction) values from 9.5 to 193.1 (average ~ 24, ignoring data outliers). Considering that published K^{Px-Liq}_{dFe-Mg} partitioning is mostly in the 0.23 to 0.27 range (e.g., Putirka, 1999), the predicted liquid $X^{FeO}_{Liq}/X^{MgO}_{Liq}$ ratios are lower than those required for equilibrium with the host MGp, (Fig. 8). Hence, a direct crystallization from their host-rock MGp is very unlikely. Also, based on the remarkably high (ca. 450 ± 0.7 $Å^3$, 2σ) calculated unit-cell volumes (using the Nimis, 1999, Eq. (2); Supplementary Material), and their geochemical fingerprint (low R^{3+}, Al^{IV}, and Ti cations, and high Fe#), MGp's pyroxenes share a marked affinity with clinopyroxenes associated with tholeiitic to alkaline magmas (Dal Negro et al., 1989).

5. Discussion

5.1. Magma geothermobarometry and kinetic implications

A proper estimation of the titanium and silica activity is necessary for a correct application of the Ti-in-Zrn thermometer (Ferry and Watson, 2007). Because the titanium content of the studied zircons is remarkably low (mostly <6 ppm; inset on Fig. 6A), the calculated crystallization temperatures may result in very low values and therefore contradict the assumption of a magmatic origin (Siégel et al., 2017). Rutile saturation thermometry results in near-solidus temperatures for

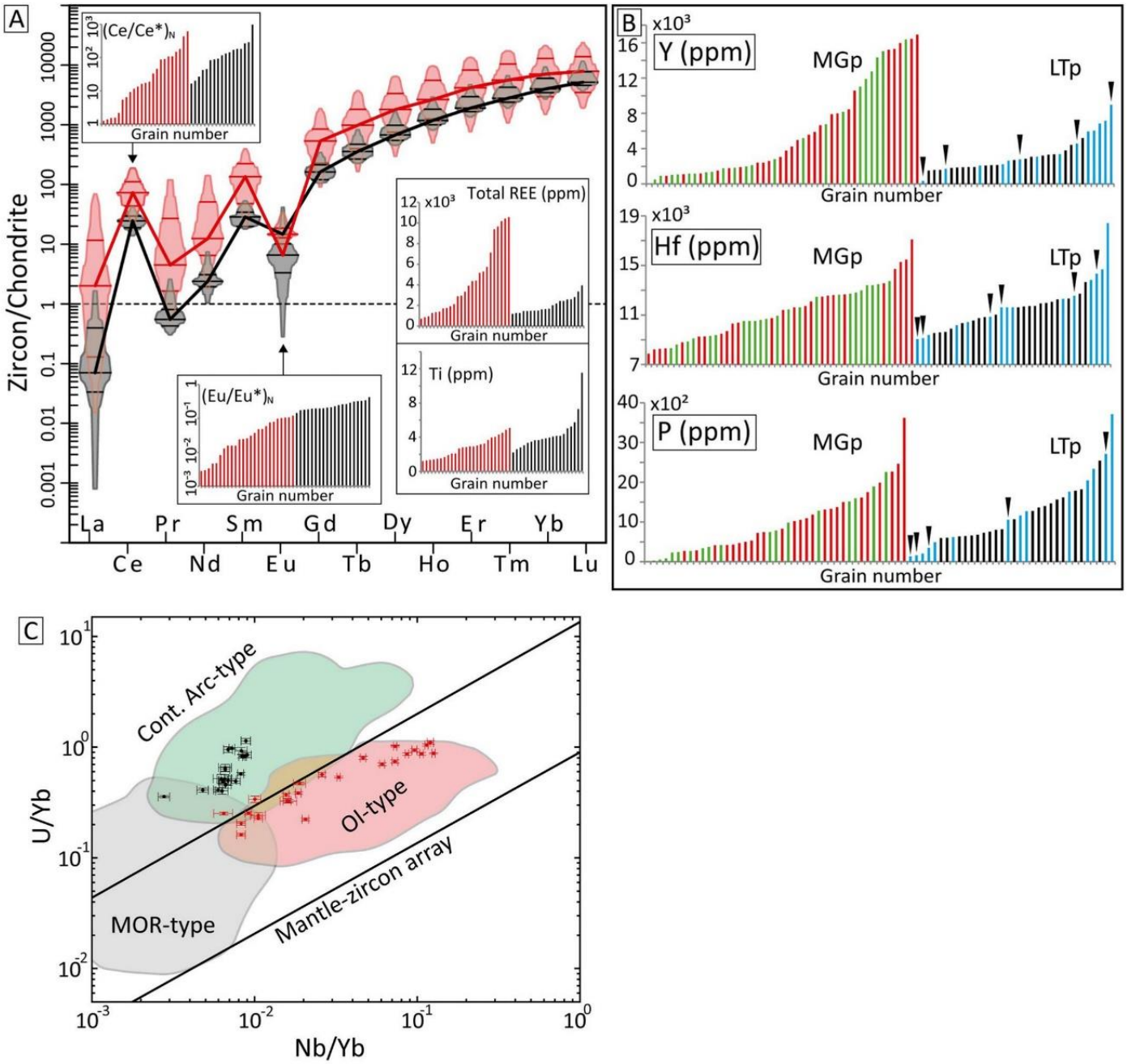

Fig. 6. Zircon chemistry: Black and red colors correspond to LTp and MGp LA-ICP-MS analyses, respectively. A. Chondrite-normalized (normalization values after Anders and Grevesse, 1989) zircon REE contents are displayed in violin-plot diagrams. Each 'violin' represents the data distribution of the measured elements. Dividing lines correspond to the different quartiles. Cerium anomaly calculated as $Ce/\sqrt{(La*Pr)}$. Total REE calculated as the sum of all REE, excluding Ce and Eu. B. Elemental concentration histograms (LA-ICP-MS and EPMA). Green and blue bars correspond to EPMA data of zircons of MGp and LTp, respectively. Zircon grains included in Crd-Qtz-Plg nodules are indicated by black triangles above some bars of LTp. C. Tectono-magmatic discrimination diagram after Grimes et al. (2015). Error bars are 1σ. (For interpretation of the references to colour in this figure legend, the reader is referred to the web version of this article.)

LTp and MGp (<750 °C) (Fig. 4B), suggesting that early crystallization of Ti-bearing phases is unlikely (Supplementary Material). The values of the activity of TiO_2 in rutile-undersaturated magmas may be probably around ~0.5 for out-of-context zircons (Schiller and Finger, 2019). We assume $aTiO_2 = 0.5$ as a maximum, and $aSiO_2 = 1$ reflecting ubiquitous quartz. Hence, the resulting Ti-in-zircon temperatures (after Ferry and Watson, 2007) are a minimum, in the 670 to 760 °C range (Table 1).

5.1.1. Los Tilos pluton

Magmatic cordierites form close to the peraluminous granite solidus at pressures between 4 and 5 kbar, or as a near-liquidus phase at or below 2 kbar (Scaillet et al., 2016). The observed chemical trend of LTp cordierites (Fig. 7A) highlights the importance of a temperature-controlled cation exchange. In fact, channel-site sodium incorporation in cordierite is accomplished by charge balance (Bertoldi et al., 2004), and is inversely correlated to temperature, holding no dependence with pressure variations. Two different Na-in-Crd thermometer calibrations (Mirwald, 1986; Tropper et al., 2018 resulted in calculated crystallization temperatures around 500–600 °C (Table 1). The experiments conducted by Tropper et al. (2018) reveal that cordierites formed from rapid crystallization could contain very high sodium contents and thus yield low calculated temperatures, due to the low Si—Al

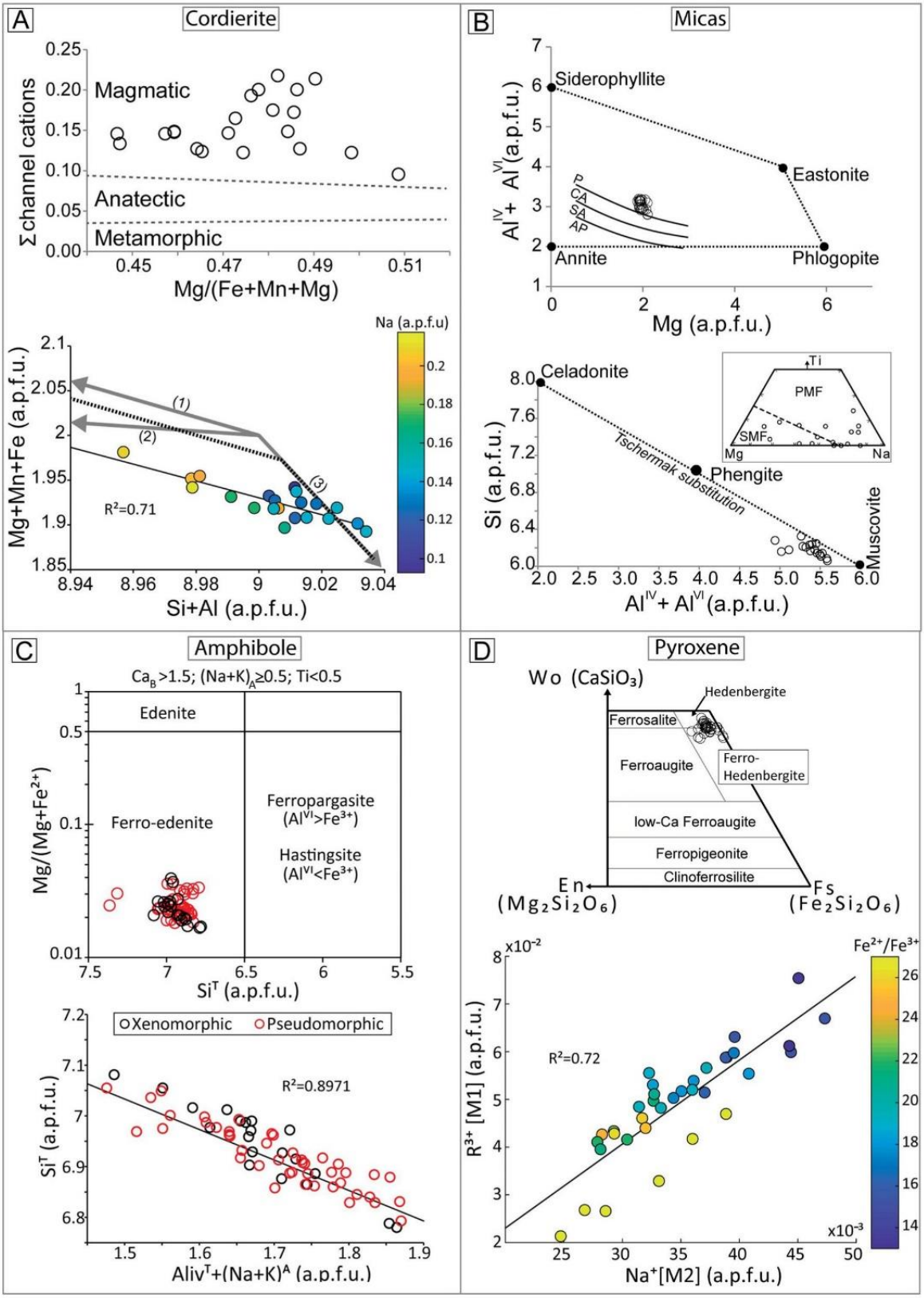

Fig. 7. EPMA mineral chemistry: A. Above: Cordierite discrimination diagram after Pereira and Bea (1994). Below: Octahedral (Mg + Mn + Fe) versus tetrahedral (Si + Al) diagram highlighting the typical cation exchange vectors found in natural cordierites (Bertoldi et al., 2004 and references therein): (1) $^{Ch}Na^{+}+{}^{IV}(Mg^{2+},Fe^{2+}) = {}^{Ch}\square + {}^{IV}Al^{3+}$, (2) $^{Ch}Na^{+}+{}^{IV}Be^{2+} = {}^{Ch}\square + {}^{IV}Al^{3+}$, (3) $^{Ch}Na^{+}+{}^{VI}Li^{+} = {}^{Ch}\square + {}^{VI}Mg^{2+}$. B. Above: Modified affinity diagram of Nachit et al. (1985); P=Peraluminous, CA = Calc-alkaline, SA = Subalkaline, AP = Alkaline and Peralkaline. Below: White mica classification diagram showing the celadonite, phengite and muscovite endmembers. Inset shows white mica discrimination diagram, after Miller et al. (1981). Primary and secondary mica fields separated by discontinuous line, labeled PMF and SMF, respectively. C. Above: Amphibole classification diagram after Leake et al. (1997), Y-axis at logarithmic scale. Below: Diagram representing the edenite exchange $Si^{T} + \square^{A} \leftrightarrow Al^{T} + (Na + K)^{A}$. Best fit linear interpolation of data in straight black line. D. Above: Pyroxene classification after Morimoto (1988). Below: Trivalent M1-site cations ($Fe^{3+}+Ti^{3+}+Al^{3+}+Cr^{3+}$) versus Na^{+} at the M2 site.

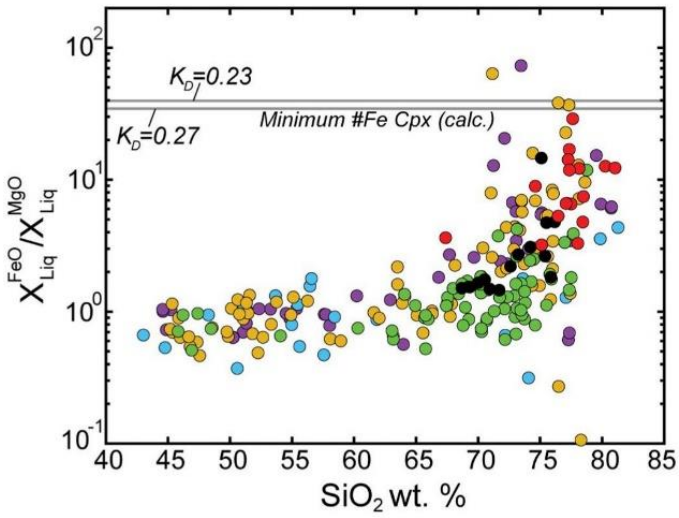

Fig. 8. Pyroxene-liquid equilibrium test: Observed liquid FeO/MgO ratios (mole fraction from whole-rock geochemistry) compared with calculated liquid in equilibrium (horizontal gray lines) with the less iron-rich pyroxenes analyzed (Kd values are from Putirka, 1999). Same symbols as in Fig. 4.

structural ordering achieved, a reflection of disequilibrium conditions. In the same way, the β-quartz paramorph crystals in LTp's Crd-nodules can be associated with rapid cooling, owing to the almost instantaneous β- to α-quartz transition at crustal levels (Ferreira et al., 2019).

Black and white micas provide distinct information about crystallization conditions (Table 1). Experiments involving biotite in equilibrium with peraluminous melts show that their stability field covers a wide temperature range, up to ca. 850 °C (Scaillet et al., 2016). Also, higher crystallization temperatures are displayed in biotites with greater Mg# (René et al., 2008). The observed range of #Mg in LTp biotites (0.39 to 0.43) places its crystallization temperature between 750 and 800 °C. White micas with low Si a.p.f.u. (celadonitic component) are formed at lower pressures than those with higher Si content (Massonne and Schreyer, 1987); therefore, muscovites of LTp can be placed roughly at pressures lower than ~4 kbar (Fig. 7B). Petrographically, muscovites from LTp appear to be a near-solidus phase and crystallized from late-stage deuteric reactions (Parada, 1988). Low-celadonite muscovite (Fig. 7B) in equilibrium with peraluminous granitic melt (in the absence of aluminosilicates) crystallize near the solidus (<680 °C), at pressures >3.5 kbar (Anderson and Rowley, 1981; Scaillet et al., 2016; Table 1).

5.1.2. Monte Grande pluton

Emplacement pressure conditions of MGp were calculated using the of Mutch et al. (2016) geobarometer, which is suitable for near-solidus granitic magmas, displaying values around 1.75 to 2.25 kbar. Assuming the maximum anorthite component of $X_{An} < 0.1$ for late-stage plagioclase as an upper boundary (Parada, 1988), the later conditions are consistent with those obtained using the method of Holland and Blundy (1994), this is 650 ± 25(1σ) °C and 2.2 ± 0.3(1σ) kbar (Table 1). The obtained temperatures are also near the solidus of peralkaline granites (Scaillet et al., 2016).

Geothermometry of MGp's iron-rich pyroxenes (Putirka, 2008, eq. 32d) display temperatures ranging from ca. 980 to 1060 (°C) (Table 1), at K^{Px-Liq}_{dFe-Mg} values (Putirka, 2008, eq. 35) in the 0.22–0.24 range, consistent with those ratios considered in the equilibrium test shown above (Fig. 8). Because of its presumably foreign origin (see Section 4.4), the crystallization temperatures of the clinopyroxenes are likely related to its original environment, not the temperature of MGp's magmas. Furthermore, based on calculated Fe—Mg partitioning between the M1 and M2 sites (Nimis, 1999), the intracrystalline equilibrium temperature (Dal et al., 1982, eq. 14) of these pyroxenes is between ca. 890 and 1000 (°C) (Table 1); these high temperatures are considered to be derived from very rapid cooling magmas and could equate the temperature at which entrainment took place. Based on the fact that the abundance of R^{3+} cations (a.p.f.u.) in the M1 site is inversely correlated to M1-O2 (Å) bonding distances, and hence crystallization pressures (Dal Negro et al., 1982), the observed geochemical trend of MGp's pyroxenes screens a more reduced environment at depth, than those formed/equilibrated shallower (Fig. 7D).

5.2. Thermodynamic framework

As discussed above, zircon grains formed in a magmatic environment (Section 4.4), and may bear a significant amount of inherited grains (Section 4.3). This assumption must be tested, for which we provide a two-fold approach: (1) We use the Siégel et al. (2017)

Table 1
LTp and MGp mineral geothermobarometric estimates.

	Peraluminous Los Tilos pluton							
	Cordierite			Biotite		Muscovite		Zircon
Ref.	Mirwald (1986)	Tropper et al. (2018)		Scaillet et al. (2016)	René et al. (2008)	Scaillet et al. (2016)	Anderson and Rowley (1981)	Ferry and Watson (2007)
Method	Lin. Interp.*	Exp. (cal. W)	Exp. (cal. SP5)	Experimental	#Mg	Experimental	Chemographic	Eq. 15+
Ave. T (°C) [1σ]	450 [95]	515 [68]	555 [87]	<850	750–800	<680	<650	728 [38]
P (kbar)	–	–	–	–	–	>3.5	>3.3	–

	Peralkaline Monte Grande pluton				
	Amphibole		Pyroxene		Zircon
Ref.	Mutch et al. (2016)	Holland and Blundy (1994)	Putirka (2008)	Dal et al. (1982)	Ferry and Watson (2007)
Method	Experimental	Th. Model (Cal. B)**	Eq. 32d***	Eq. 14****	Eq. 15+
Ave. T (°C) [1σ]	–	650 [25]	976–1059	856 [10.3]	688 [38]
P (kbar)	2.0 [0.2]	2.2 [0.3]	–	–	–

* Linear interpolation of Mirwald (1986) experiments: T(°C) = (6250–20,000*Na(a.p.f.u.))/7.
** Geothermobarometry using the Hbl-Plg Holland and Blundy (1994) method by iteration. Spreadsheet provided by Lawford Anderson (http://www.minsocam.org/msa/rim/RiMG069/RiMG069_Ch04_hbld_plag_thermo-jla.xls).
*** The obtained pyroxene crystallization temperature range was obtained assuming any crustal pressure (from 1 to 10 kbar).
**** Intracrystalline Fe—Mg equilibration temperature.
\+ Ti-in-Zrn crystallization temperatures (Ferry and Watson, 2007) assuming $aSiO_2 = 1$ and $aTiO_2 \sim 0.5$.

recommendations to identify possible out-of-context crystals; and (2) the petrogenetic scenario will be reviewed in light of zircon dissolution estimates (e.g., Bea et al., 2007; Tapster et al., 2016) within a thermodynamically constrained framework, to explore the magmatic feedbacks on the inheritance potential of the studied plutons.

To complement the P-T estimates presented here, we develop a set of isochemical thermodynamic models using Perple_X software (ver. 6.8.6). These models are then used to determine the potential for zircon to dissolve at or enroute its emplacement site. The modeled isochemical projections (CKFMASHNT components system) on the P-T space, so-called pseudosections (Connolly, 2005), were used to obtain the composition of the different phases, and their volumetric and weight fractions. The modeled mineral structural formulae were then compared to measured compositions (Section 4.4), based on numerical conditional iterations (software MATLAB R2017a) to attain a 'probability of match', as follows:

$$\left(PM_j^i\right)_{PT} = \frac{\#\left(X_{Obs_j}{}^i\right)_{PT}}{K_j}, \quad : \quad 100 * \frac{\left| X_{Obs_i}{}^j - \left(X_{Mod_i}{}^j\right)_{PT} \right|}{X_{Obs_i}{}^j} \leq Tolerance \qquad (1)$$

Where PM is the probability of match, X_{Obs} (a.p.f.u.) the measured composition, X_{Mod} (a.p.f.u.) the modeled composition, K the total number of performed analyses. Variable i is the specified element, and j the phase of interest. In other words, at a given PT condition, the probability of match equals the number of analyses that satisfy the inequality at the right side of Eq. (1) (a compositional departure below a given tolerance), divided by the total number of performed analyses. Extending this definition to more than one chemical component, and assuming statistical independence:

$$\left(PM_j^{C1,C2\ldots}\right)_{PT} = \prod_{i=1}^{N} \left(PM_j^i\right)_{PT} \qquad (2)$$

This is the multiplication of the different probabilities of match for each component i, with N the total number of considered components, namely C1, C2, C3, and so on.

The performed thermodynamic simulations are in good agreement with the geothermobarometric estimations presented in Section 5.1. (Fig. 9). Enough evidence of high undercooling in both plutons (see above), implies that residual/restitic phases (if any) should not suffer major dissolution. In this regard, the absence of garnet in LTp, and biotite compositions constrain LTp crystallization below 4 kbar, at ca. 750 (°C); thus biotite is a *liquidus* phase, susceptible to be transported in the magmatic system (within HMF crystallinities; Fig. 9A, D). In turn, white micas appear above the lock-up threshold of crystalline mushes (Dufek and Bachmann, 2010), therefore its compositional match reflects crystallization at the emplacement site (ca. 3.5 kbar and 650 °C). The analyzed cordierites in nodules were reproduced at pressures below 3 kbar and temperatures between 750 and 850 °C (Fig. 9B, E). Near solidus MGp amphiboles are stable below ca. 690 °C and 3 kbar (Fig. 9C, F).

5.3. Zircon inheritance: From source to emplacement

5.3.1. The origin of zircon

Most zircon chemistry of both plutons does not resemble that observed in crystallization from a cooling evolving melt (cf. Claiborne et al., 2010; Molina et al., 2015; Fig. 10A), and show a significant deviation from lattice strain models (LSM) failing to support a clear in-situ origin (Zou et al., 2019; Fig. 10D). Hence, the anomalously large age span observed (Fig. 5) indicates that most zircons were probably inherited. Furthermore, zircon age and titanium contents (and equivalent crystallization temperatures) show no correlation (Fig. 10C), and as a general tendency, the older studied zircon grains thus crystallized from more evolved magmas than those of the younger age peak (inset in Fig. 10C). Moreover, the greater REE and yttrium contents of MGp's zircons compared to those of LTp (Fig. 6), is best explained by enrichment of the environment, not magmatic differentiation (Fig. 10B). All of this suggests that most of the studied zircons were inherited and formed in an open magmatic system once changes in melt chemistry reached zircon saturation at a somewhat constant temperature.

The disparity in yttrium contents of zircons of LTp and MGp (Fig. 6 and Fig. 10B) reflects compositional differences in the forming melts. These chemical differences could be ascribed to contrasting behavior of accessory minerals in the primary hosting magmas (Wark and Miller, 1993). For example, the large allanite-(Ce) crystals and the absence of monazite in MGp could be a product of monazite destabilization at the source by the effect of increasing Ca in the magma residue (Montel, 1993). This could also explain the large LREE dispersion, REE enrichment, and prominent Eu anomalies in MGp zircons (Fig. 6A).

5.3.2. A model for the preservation of inherited zircons: Setup and rationale

A high fraction of inherited grains will lead to an overestimation of whole-rock zircon saturation temperatures (Miller et al., 2003; Siégel et al., 2018). We provide a first-order correction for the Zr (ppm) content of hosting rocks, by subtracting the observed 'inherited' zircon domain (reference cathodoluminescence images from this study and from Hervé et al., 2014) from total zirconium of whole-rock geochemical analyses, by mass balance. The average volume fraction (assuming a prolate ellipsoid geometry) of zircon cores in LTp and MGp display values of ca. 0.35 and 0.30, corresponding to average corrected contents of ca. 50 (77 uncorrected) and 125 (180 uncorrected) whole-rock Zr (ppm), respectively. The thermodynamic models presented above (Section 5.2) were used as a framework to provide the minimum Zr (ppm) content expected in interstitial liquids in equilibrium with inherited zircons, prior to full crystallization (using the Gervasoni et al., 2016 formulation). This evaluation was performed within the obtained emplacement pressure interval for each pluton between 3.5 and 4 kbar for LTp, and 1.5 to 2.5 kbar for MGp (see Section 5.1 and Table 1). A magma water content of up to 6 wt% was used because this value equates to the maximum amount of dissolved water expected in granitic magmas emplaced at high crustal levels (between 2 and 4 kbar), near their water-saturated solidii (Holtz et al., 2001).

Because only scarce (<5 vol%) phenocrysts are found in the homogeneous -highly silicic- MGp leucogranite, and considering that its whole-rock geochemistry resembles pure crustal melts obtained experimentally (see Section 4.2), its composition is thought to represent a nearly eutectic liquid. Conversely, LTp is heterogeneous (schlieren bands, straight and cuspate-border felsic dikes, and variations in nodule abundance; see Section 4.1 and Fig. 2) suggesting that these peraluminous magmas might have carried significant restitic material from source region (cf. Patiño Douce, 1999) and/or had subtle pre- and *syn*-emplacement history of crystallization. Since both plutons lack aplites or felsic veinlets, which can be attributable to late-stage residual liquid evacuation/redistribution, we assume equilibrium crystallization at the emplacement site. We consider that MGp and LTp zircon entrainment took place near the magma sources, where their respective geochemical fingerprints were acquired (Fig. 6C; Fig. 10). An upper limit of ~850 (°C) equates the maximum calculated temperature both carrier magmas could have reached before zircon entrainment (Table 1) and is consistent with the temperature range in which biotite dehydration melting occurs (Weinberg and Hasalová, 2015), leaving peritectic cordierite as a melting byproduct. This temperature estimate is also within the intracrystalline equilibration temperatures of the rapidly cooled entrained MGp's clinopyroxenes (Section 5.1, Table 1).

At a given water content, high-temperature magmas (low crystallinity) require higher dissolved zirconium to preserve zircons than low-temperature magmas (high crystallinity) (Fig. 11). Conversely, zircons are readily preserved in magmas with lower H_2O (wt%) contents due to the appearance of early *liquidus* assemblages, which favor zirconium accumulation in the residual melt (Fig. 11). It is interesting to note that

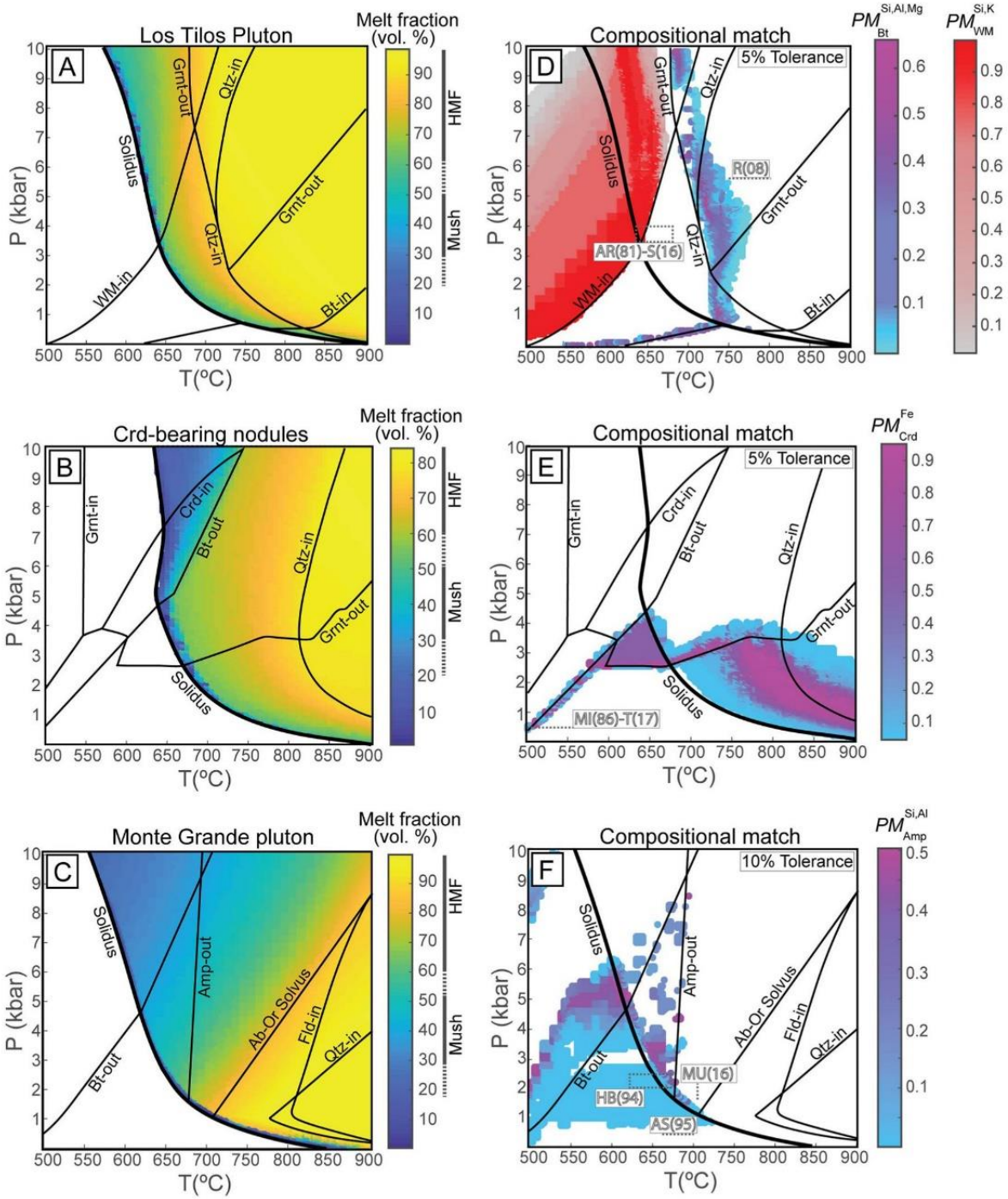

Fig. 9. Perple_X (Connolly J., 2005) isochemical pseudosections: P-T projections in the CKFMASHNT component system on a 200 × 200 grid. Left row represents the main reactions depicting the apparition of the different phases of interest and melt fraction (vol% melt) of the magma system. HMF: High melt fraction magmas, below the lock-up point. Mush: Interconnected frame of crystals (Dufek and Bachmann, 2010). Right row: colour-coded probability of match 'PM' according to Eq. (1) and Eq. (2) (see Section 5.2 for details). Black discontinuous lines/rectangles plot the geothermobarometric estimates (Section 5.1) after: AR (Anderson and Rowley, 1981); R (René et al., 2008); S (Scaillet et al., 2016); MI (Mirwald, 1986); T (Tropper et al. (2018)); HB (Holland and Blundy, 1994); MU (Mutch et al., 2016).

except for MGp at water saturation (Fig. 11B), neither of both magmas should stabilize inherited zircons at low crystallinities unless the magmas held higher degrees of Zr (ppm) enrichment at their early stage. This caveat is an aspect to consider because: (1) melting of an HFSE-rich source and/or low degrees of partial melting (Pearce and Norry, 1979) are, most probably, the main factors controlling the zirconium budget of Triassic rocks of the batholith (Fig. 12A); and (2) if we consider that at some point mechanical separation of zircon took place, a substantial amount of solids is expected to be left behind in the residue after extraction, hence lowering the Zr (ppm) content of carrier magmas (Fig. 12B) in comparison to those that saturated zircon in their early stage (Miller et al., 2003).

To estimate the maximum preservation time of entrained zircons we use the three-dimensional dissolution/growth model of Watson (1996):

$$\frac{dr}{dt}x10^{17} = -U\left(\frac{1.25x10^{10}}{r}\right)e^{\left(-\frac{28380}{T}\right)} + 7.24x10^{8}e^{\left(-\frac{23280}{T}\right)} \quad (3)$$

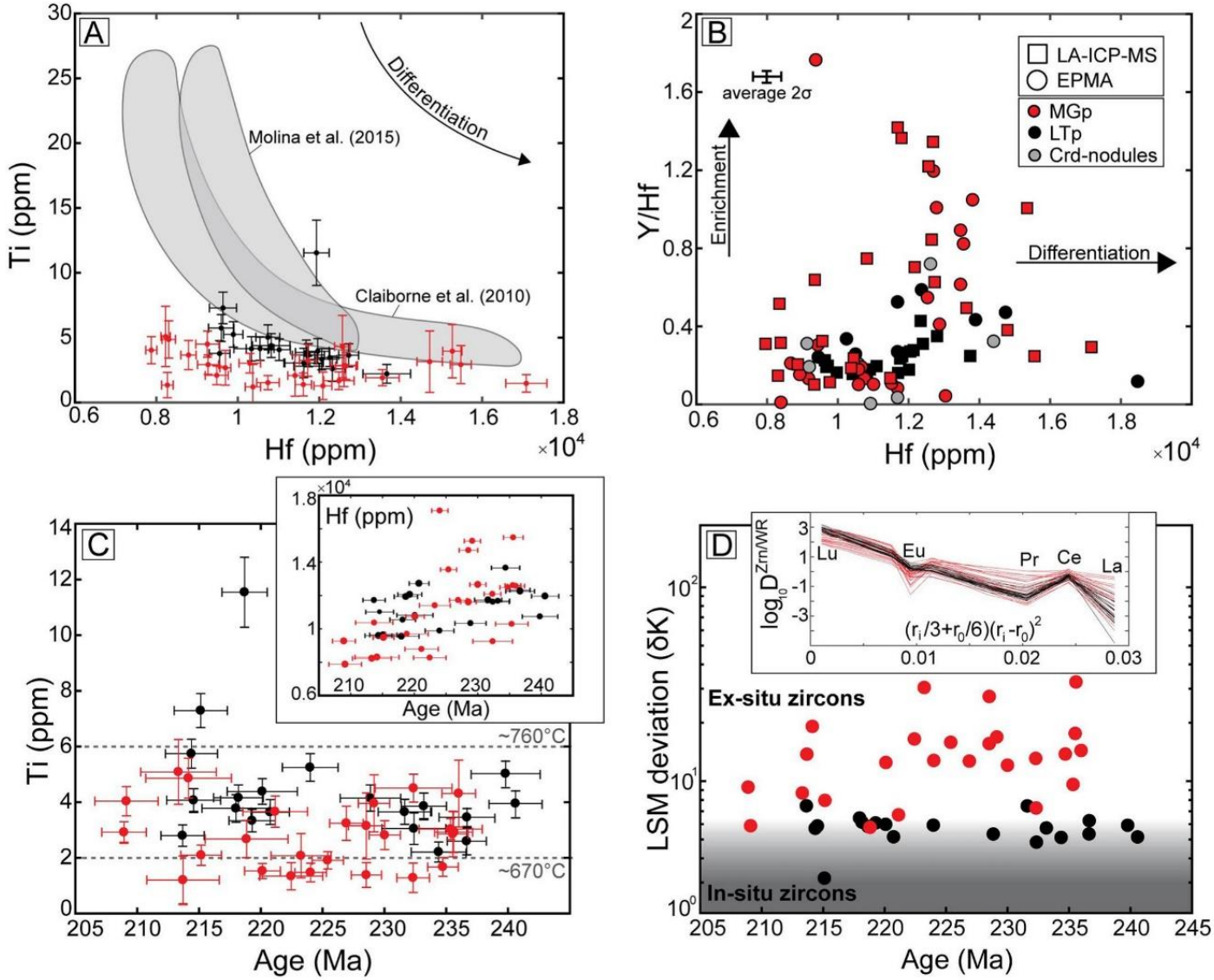

Fig. 10. Chemistry of inherited zircons: A. Hafnium versus titanium (ppm) diagram highlighting down-with-temperature differentiation. Ti and Hf error bars are at 2σ B. Enrichment versus differentiation plot. C. Age (Ma) versus titanium content of zircons. Calculated Ti-in-Zrn temperatures after (Ferry and Watson, 2007) assuming $aTiO_2 \sim 0.5$ and $aSiO_2 = 1$ (see Section 5.1). Age error bars are at 1σ. D. Age (Ma) versus lattice strain model deviation (δK) for analyzed zircons (Zou et al., 2019); higher values represent a bigger departure from ideal crystallographic REE substitution. Inset shows the lattice-strain parameter for zircons of both samples, normalized to the average whole-rock REE contents of each pluton.

With $\frac{dr}{dt}$ in cm/s the dissolution/growth rate, r the crystal radius in cm, T the absolute temperature, and U the degree of Zr(ppm) deficit/excess. The latter variable was parameterized as a function of magma temperature, through a third order interpolation of the plot in Fig. 11, as follows:

$$U(ppm) = f(T) = A + B(T) + C(T)^2 + D(T)^3 - RefZr(ppm) \quad (4)$$

Values A, B, C, and D are coefficients (listed in Table 2), and RefZr the Zr (ppm) content of the modeled rock. The rationale behind this parametrization relies on the fact that inherited zircons crystallized in an open system (Fig. 10), without other mineral assemblages controlling its chemical evolution (cf. Grimes et al., 2015); this implies that the degree of Zr (ppm) deficit/excess was not buffered (i.e. infinite melt reservoir) and rather was most likely controlled by processes near the source (e.g., Clemens and Stevens, 2012). Nonetheless, if we consider a reservoir with limited volume (closed system), the gradual dissolution of zircons will further increase Zr(ppm) concentration of the residual liquids (Watson, 1996), therefore reducing the magma's potential to dissolve zircon grains at high temperatures (values of U would decrease at a greater rate). In this scenario, the formation of new overgrowths at low temperatures (when zircon saturation is reached) will be progressively hampered by zirconium exhaustion, leading to lower growth rates than in an infinite melt volume reservoir (e.g., Bea et al., 2007). As a consequence, the model of preservation of inherited grains presented here (open magmatic system) is the worst-case scenario and thus places boundaries on all other variables considered in modeling (magma water content, pressure, cooling rates, zircon initial radius (r_0), and reservoir Zr content).

5.3.3. Magmatic feedbacks on the preservation and growth of zircons: Petrogenetic implications

The magma cooling rates considered here are those obtained by Nabelek et al. (2012) for the intrusion of an H_2O-bearing granitic magma as a single pulse in the upper crust, this is ~ −0.005°/yr. This value is similar to that calculated by Bea et al. (2007) for zircon-crowded sills (<3 kbar) below 850 °C, and with those suggested by Watson (1996) for magmas rapidly segregated from source after the thermal peak, with interaction with mafic dikes at the emplacement site. Latent heat released by extensive crystallization would contribute

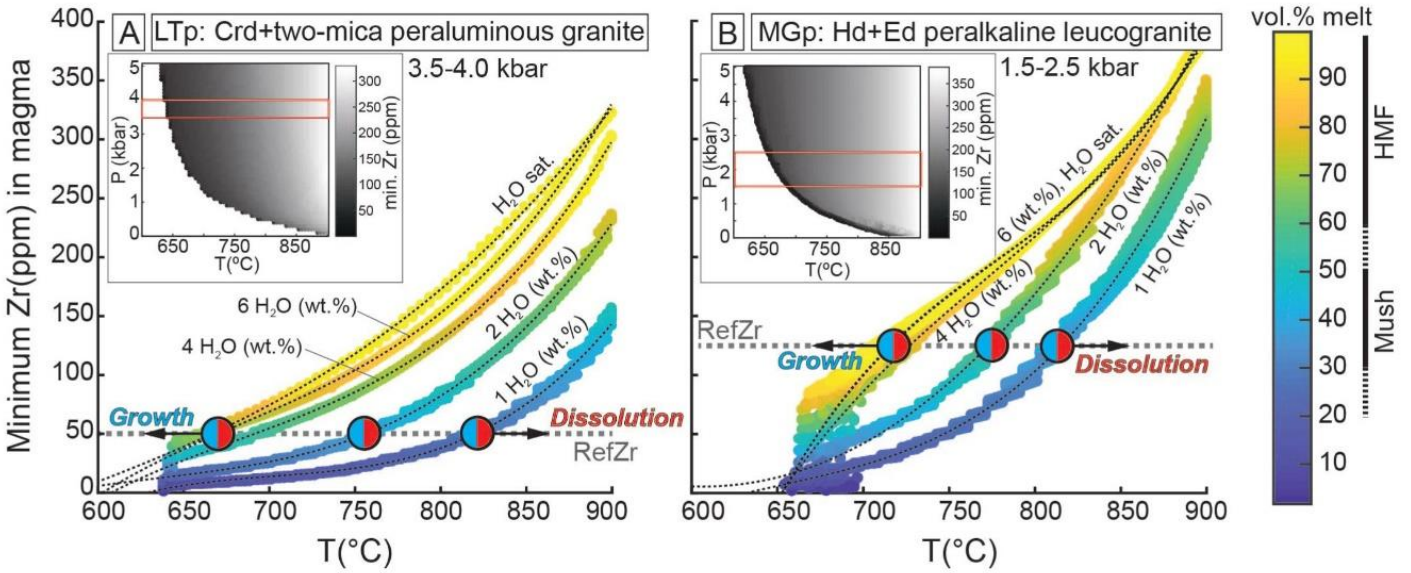

Fig. 11. Temperature versus calculated minimum zirconium (ppm) content in modeled magmas: Gray discontinuous line equates the parameter RefZr (zirconium (ppm) content in the studied plutons), for LTp and MGp (letters A and B, respectively). Inset shows the minimum zirconium content expected in the P-T space to stabilize zircons (for simplicity, only water saturated models are shown in insets). Bicolor circle is the point at which entrained zircons become stable(blue)/unstable(red). Red rectangle in inset is the obtained emplacement pressure for each pluton. Colour bar represents the melt fraction (vol% melt) present in the modeled magma. Black discontinuous curve interpolates results (polynome constants listed on Table 2). (For interpretation of the references to colour in this figure legend, the reader is referred to the web version of this article.)

to buffer the magma temperature near its terminal stage. Hence, solid productivity (grams of solid per degrees celsius) and cooling rates (°/yr) would vary in time as the magmas crystallize (Morse, 2011). Consequently, new zircon overgrowths are prone to be formed over inherited cores when zircon saturated magmas approach their solius, at their protracted late-stage (Miller et al., 2007; Molina et al., 2015). This approach is a simplification of cooling rate models of magmas emplaced in the upper crust, which consider conductive cooling and insulation to the surroundings by the effect of temperature-dependent thermal diffusivity, and within-reservoir heat and mass advection (e.g., Molina et al., 2015), among other processes. Nevertheless, this model highlights the importance of magma composition (peraluminous versus peralkaline), water magma content, and emplacement pressure, in the estimated timespan in which entrained zircons will spend before (dissolution) and after (growth) zircon saturation in the melt is reached.

Our model indicates that zircon grains will be readily preserved in water-undersaturated magmas at high pressure (Fig. 13). Under more 'wet' conditions, zircon grains will not survive in carrier magmas for more than 12 kyr in any of the considered pressures (1 to 5 kbar). However, the dissolution of zircon grains could be prevented if they are armored (e.g., Bea, 1996) by early crystallizing assemblages (Qtz-Kfs or Bt-Kfs at temperatures above 780 °C in MGp and LTp, respectively; Fig. 13), as seen in various small (<25 μm) euhedral zircon grains in

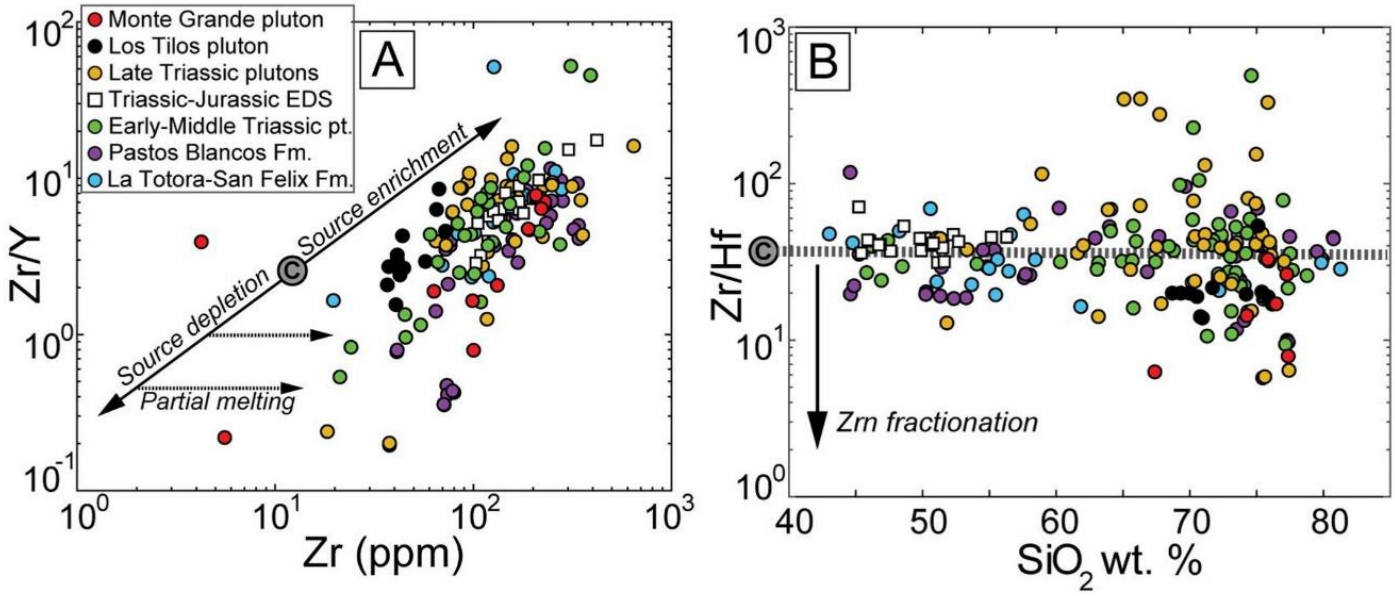

Fig. 12. A. Whole rock HFSE diagram (after Pearce and Norry, 1979), showing the geochemical behavior of enrichment/depletion in a chondritic source (letter C in gray circle) and different degrees of partial melting (increasing to the right). B. Whole rock Zr/Hf ratios highlighting the effect of zircon fractionation compared to chondritic ratio (letter C in gray circle) (after Bea et al., 2006).

Table 2
Minimum zirconium (ppm) contents of modeled magmas (at equivalent emplacement pressure ranges), as a function of temperature T (in Celsius degrees). A, B, C and D are the third-degree polynome constants obtained from interpolation of Fig. 11 plot (see Section 5.3.2.).

	Unit	minZr(ppm) = f(T) = $A^*T^3 + B^*T^2 + C^*T + D$			
		A	B	C	D
3.5–4.0 kbar	LTp (H_2O sat)	1/268434	−0.0062	3.9335	−936.1
	LTp (1 H_2O)	1/71797	−0.0294	20.7513	−4900.3
	LTp (2 H_2O)	1/108743	−0.0176	11.3441	−2468.7
	LTp (4 H_2O)	1/75812	−0.0270	18.9388	−4502.9
	LTp (6 H_2O)	1/73485	−0.0280	19.7776	−4743.0
1.5–2.5 kbar	MGp (H_2O sat)	1/28213	−0.0826	65.1855	−17,218.0
	MGp (1 H_2O)	1/64576	−0.0304	20.1603	−4525.4
	MGp (2 H_2O)	1/563157	1/1271	−2.9118	1086.0
	MGp (4 H_2O)	1/47702	−0.0484	38.5363	−10,347.0
	MGp (6 H_2O)	1/29077	−0.0801	63.2708	−16,728.0

association with monazite, xenotime, apatite, and magnetite (Fig. 3C) in LTp, and among some -remarkably small (<15 μm radius)- well preserved zircon grains included in pyroxene antecrysts in MGp (Fig. 3D).

The geological setting of both Late Triassic plutons, their geochemical affinity, and the resultant mineralogy, place the studied Late Triassic magmas in a within-plate context (González et al., 2017), similar to the late- to post-orogenic magmatism (Nardi and Bonin, 1991), best represented by LTp (mixed source) and MGp (high temperature lower crustal melts), respectively (Fig. 14). The high degree of incompatible-element enrichment agrees with the idea that extraction of magmas in a thinned crust may represent remarkably evolved (highly silicic) parcels of melts evacuated from the source region and is consistent with the bimodal character of the Late Triassic magmatism (Farner and Lee, 2017).

The very high silica content of MGp and some of the highly differentiated contemporaneous rhyolites (Fig. 4), together with the presence of hypersolvus alkali feldspar (Martin and Bonin, 1976) and the near-eutectic amphibole crystallization indicate shallow emplacement depth (ca. 2 kbar), and that the initial water content of primary magmas

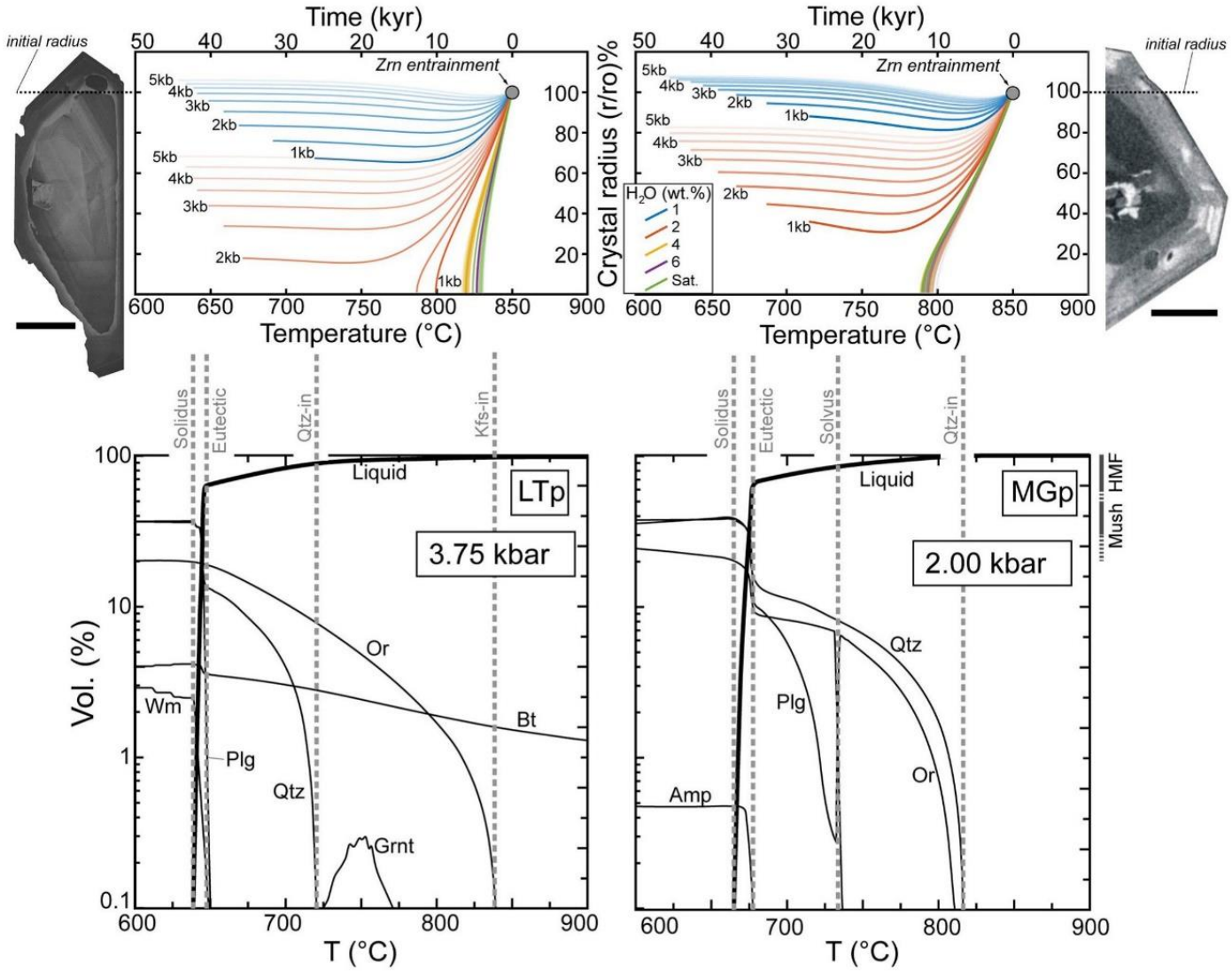

Fig. 13. Time-dependent spherical dissolution/growth models of zircons: Numbers along each curve are different emplacement pressures (in kbar). Liquidus temperature and modal volume % of each crystallizing phase (which may armor zircon inclusions; see Section 5.3.3.) is shown below (for simplicity, only water-saturated models are shown). Wet magmas (H_2O wt% >4) do not preserve zircons longer than 12 kyr. Reference cathodoluminescence images for each model are scaled to match the y-axis crystal radius % (black bar scale equals 50 μm).

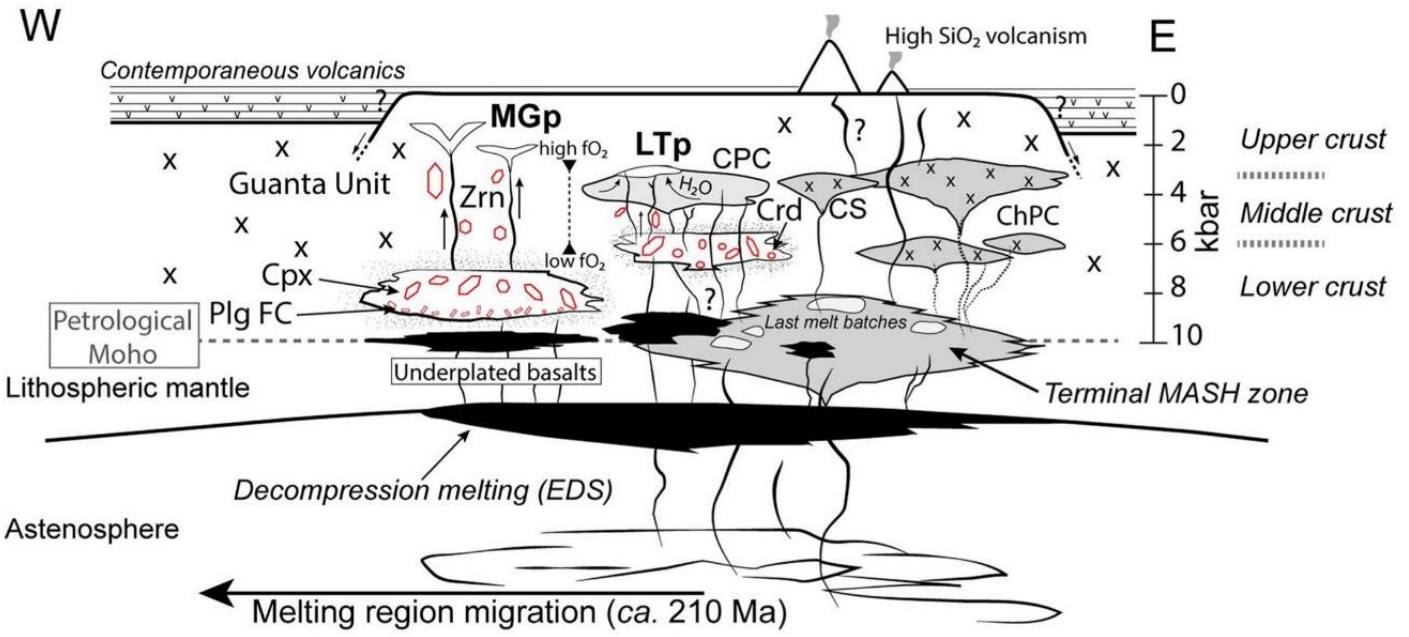

Fig. 14. A crustal-scale model for the Late Triassic magmatism, High Andes, Central Chile: Contemporaneous volcanics are the La Totora, San Felix and Pastos Blancos Fm. Petrological Moho depth after González et al. (2017). Most Triassic magma products were fed by a long-lived MASH zone in a volcanic arc setting; slab rollback and subsequent melting region migration (ca. 210 Ma) terminates magmatic activity in the batholith. Cordierite and clinopyroxene were entrained and rapidly cooled. Decompression melting, underplated basalts and EDS (dikes not shown) may be the main heat source to produce melting of the crust. CPC: Early to Middle Triassic Chollay Plutonic Complex; CPC: Late Triassic Los Carricitos Plutonic Complex; CS: Late Triassic Colorado Syenogranites; EDS: Elqui Dike Swarm (not shown). Horizontal distances and size of reservoirs are not to scale.

was low (Castro, 2013), dry enough to permit magma ascent through the middle crust without 'freezing' at water saturation (Waters and Lange, 2017). On the other side, early biotite in LTp indicates that the water content of this magmas was somewhat higher than in MGp. In fact, magmas that formed LTp should not have had less dissolved water than that at saturation of a haplogranite system at 850 °C and ca. 4 kbar (>3 H_2O wt%; Holtz et al., 2001). Water saturation at the emplacement site of LTp is inferred by the occurrence of pegmatites within late-stage segregates (Fig. 2D). Extensive crystallization in a narrow temperature range by attainment of water saturation in LTp probably occurred in less than ~22 kyr (Petrelli et al., 2018, eq. 6), at this moment, latent-heat released by crystallization will offset cooling by water exsolution (Richet et al., 2006). In this time interval, the cooling rate at the very late-stage of LTp might have been even lower than assumed, perhaps explaining why some observed zircon overgrowth rims are larger than modeled (Fig. 13). Our results indicate that different water contents of forming magmas may give insights to understand the different age distribution of zircons in both plutons (e.g., Miller et al., 2014; Supplementary Material): a continuous crystallization of zircon in a dry magma (MGp) contrasts zircon crystallization in a wet magma, which took place in its early and late stages, resulting in a bimodal age distribution (LTp) (Fig. 5A). The dissolution of entrained zircons was probably mitigated by the short time magmas spent at high melt fractions, preceding necessarily fast segregation and ascent (Diener et al., 2014) as evidenced by the rapid cooling of entrained assemblages near the source of LTp (peritectic cordierite and quartz) and MGp (iron-rich clinopyroxene), respectively (see Section 5.1).

6. Conclusions

The Late Triassic magmatism located in the High Andes of Central Chile (~30°S), represents the last magma pulse of the Elqui-Limarí Batholith before the arc migrated ~100 km west, to the Present-day Coastal Range. This pulse is characterized by the emplacement of some particular plutons in a post-orogenic extensional setting: the peraluminous Crd-bearing Los Tilos pluton (LTp) and the peralkaline hypersolvus Hd + Ed-bearing Monte Grande pluton (MGp). Both plutons were formed by melting of the crust caused by heat from basalt underplating and intraplating (Elqui Dike Swarm). These magmas were rapidly segregated and emplaced at different crustal levels, reflecting their contrasting water contents at their sources: ca. 3.5 and 2 kbar, for LTp and MGp respectively. LTp's magmas seem to represent a mixture of mantle and crustal materials whereas MGp's could represent pure crustal melts of anorogenic affinity. The large age span and geochemical characteristics of zircons suggest that most of them were inherited from an open-system heterogeneous source. Zircon crystallization at the source was most likely driven by zirconium enrichment, not temperature variations. Whole-rock geochemistry might reflect mechanical separation of early zircon, left as a residue at deeper crustal levels when segregation took place. Zircon dissolution potential of the respective carrier magmas was modeled, indicating that water content and pressure play a major role in the preservation of inherited zircons. Water-undersaturated magmas will readily preserve zircon grains, because of their high liquidus temperatures leading to efficient zirconium accumulation in residual melts (MGp). Instead, wet magmas dissolve zircons in less than 12 kyr, unless armored by early crystallizing minerals and/or favorably allowed to grow by induction of late-stage temperature buffering by water-saturation (LTp).

We suggest that the large age span (>25 Myr) observed in zircon samples of both plutons reflects a long-lived source that fed arc-related granites in the Early to Middle Triassic, culminating in the Late Triassic with the rapid extraction of highly enriched crustal melts. The magmatic conditions revealed in this study are optimal for preserving inherited zircons. Dry high-silica (>75 SiO_2 wt%) magmatic flare-ups, closely associated with extensional settings (Waters and Lange, 2017), match the inheritance requisites presented here. Contrastingly, a broad zircon age span in large calc-alkaline batholiths emplaced at similar depths, reflect not source processes but rather magmatic erosion, crystal armoring and recycling of previous magma batches, and a complex crystallization history, spanning the whole duration of batholith construction (e.g., Paterson et al., 2016).

Declaration of Competing Interest

The authors declare that they have no known competing financial interests or personal relationships that could have appeared to influence the work reported in this paper.

Acknowledgments

This research was supported by funds of the Andean Geothermal Centre of Excellence (CEGA), CONICYT-FONDAP project 15090013. The authors are indebted to Calvin Barnes, Scott Paterson, Cristóbal Ramírez de Arellano, Sebastián Herrera, and two anonymous reviewers for their constructive comments, text editing, suggestions, and fruitful discussions that greatly improved this work; and also would like to thank F. Colombo, M. Demartis, A. Guereschi and S. Verdecchia for EPMA assistance at LAMARX, UNC, Argentina. A collaborative work between PGM and MAP at the University of Chile and Changqian Ma, Jianwei Li, and Liu Yuanyuan at China University of Geosciences, Wuhan, is acknowledged. PGM thanks the CONICYT Ph.D. grant 21150905.

Appendix A. Supplementary data

Supplementary data to this article can be found online at https://doi.org/10.1016/j.lithos.2020.105662.

References

Anders, E., Grevesse, N., 1989. Abundances of the elements: meteoric and solar. Geochim. Cosmochim. Acta 53, 197–214.

Anderson, J.L., Rowley, M.C., 1981. Synkinematic intrusion of peraluminous and associated metaluminous granitic magmas, Whipple Mountains, California. Can. Mineral. 19, 83–101.

Anderson, J.L., Smith, D.R., 1995. The effects of temperature and fO2 on the Al-in-hornblende barometer. Am. Mineral. 80, 549–559. https://doi.org/10.2138/am-1995-5-614.

Armstrong, J.T., Donovan, J., Carpenter, P., 2013. CALCZAF, TRYZAF and CITZAF: the use of multi-correction-algorithm programs for estimating uncertainties and improving quantitative X-ray analysis of difficult specimens. Proceed. Microscopy Microanal. v19, 812–813.

Bea, F., 1996. Controls on the trace element composition of crustal melts. Special Paper 315: The Third Hutton Symposium on the Origin of Granites and Related Rocks, pp. 33–41. https://doi.org/10.1130/0-8137-2315-9.33.

Bea, F., Montero, P., Ortega, M., 2006. A LA-ICP-MS evaluation of Zr reservoirs in common crustal rocks: implications for Zr and Hf geochemistry, and zircon-forming Processes. The Canadian Mineralogist 44 (3), 693–714.

Bea, F., Montero, P., González-Lodeiro, F., Talavera, C., 2007. Zircon Inheritance reveals exceptionally fast crustal magma generation processes in central iberia during the cambro-ordovician. J. Petrol. 48, 2327–2339. https://doi.org/10.1093/petrology/egm061.

Bertoldi, C., Proyer, A., Garbe-Schönberg, D., Behrens, H., Dachs, E., 2004. Comprehensive chemical analyses of natural cordierites: Implications for exchange mechanisms. Lithos 78, 389–409. https://doi.org/10.1016/j.lithos.2004.07.003.

Bhattacharya, S., Kemp, A.I.S., Collins, W.J., 2018. Response of zircon to melting and metamorphism in deep arc crust, Fiordland (New Zealand): implications for zircon inheritance in cordilleran granites. In Contributions to Mineralogy and Petrology. 173. https://doi.org/10.1007/s00410-018-1446-5.

Boehnke, P., Watson, E.B., Trail, D., Harrison, T.M., Schmitt, A.K., 2013. Zircon saturation re-revisited. Chem. Geol. 351, 324–334.

Casquet, C., Hervé, F., Pankhurst, R.J., Baldo, E., Calderón, M., Fanning, C.M., Rapela, C.W., Dahlquist, J., 2014. The Mejillonia suspect terrane (Northern Chile): Late Triassic fast burial and metamorphism of sediments in a magmatic arc environment extending into the early Jurassic. Gondwana Res. 25 (3), 1272–1286. https://doi.org/10.1016/j.gr.2013.05.016.

Castro, A., 2013. Tonalite–granodiorite suites as cotectic systems: A review of experimental studies with applications to granitoid petrogenesis. Earth Sci. Rev. 124, 68–95. https://doi.org/10.1016/j.earscirev.2013.05.006.

Claiborne, L.L., Miller, C.F., Wooden, J.L., 2010. Trace element composition of igneous zircon: a thermal and compositional record of the accumulation and evolution of a large silicic batholith, Spirit Mountain, Nevada. Contrib. Mineral. Petrol. 160, 511–531. https://doi.org/10.1007/s00410-010-0491-5.

Clemens, J.D., Stevens, G., 2012. What controls chemical variation in granitic magmas? Lithos 134–135, 317–329. https://doi.org/10.1016/j.lithos.2012.01.001.

Coloma, F., Valin, X., Oliveros, V., Vásquez, P., Creixell, C., Salazar, E., Ducea, N., 2017. Geochemistry of Permian to Triassic igneous rocks from northern Chile (28o-30o15'S): Implications on the dynamics of the proto-Andean margin. Andean Geol. 44, 147–178.

Connolly, J.A.D., 2005. Computation of phase equilibria by linear programming: A tool for geodynamic modeling and its application to subduction zone decarbonation. Earth Planet. Sci. Lett. 236, 524–541. https://doi.org/10.1016/j.epsl.2005.04.033.

Creixell, C., Parada, M.Á., Morata, D., Roperch, P., Arriagada, C., 2009. The genetic relationship between mafic dike swarms and plutonic reservoirs in the Mesozoic of Central Chile (30°-33°45′S): Insights from AMS and geochemistry. Int. J. Earth Sci. 98, 177–201. https://doi.org/10.1007/s00531-007-0240-9.

Creixell, C., Oliveros, V., Vásquez, P., Navarro, J., Vallejos, D., Valin, X., Godoy, E., Ducea, M., 2016. Geodynamics of late Carboniferous–early Permian forearc in North Chile (28°30′–29°30′S). J. Geol. Soc. Lond. 173, 757–772. https://doi.org/10.1144/jgs2016-010.

Dahlquist, J.A., Rapela, C.W., Baldo, E.G., 2005. Petrogenesis of cordierite-bearing S-type granitoids in Sierra de Chepes, Famatinian orogen, Argentina. J. S. Am. Earth Sci. 20, 231–251. https://doi.org/10.1016/j.jsames.2005.05.014.

Dal Negro, A., Manoli, S., Secco, L., Piccirillo, E.M., 1989. Megacrystic clinopyroxenes from Victoria (Australia): crystal chemical comparisons of pyroxenes from high and low pressure regimes. Eur. J. Mineral. 1, 105–121.

Dal, Negro A., Carbonin, S., Molin, G.M., Cundari, A., Piccirillo, E.M., 1982. Intracrystalline cation distribution in natural clinopyroxenes of tholeiitic, transitional, and alkaline basaltic rocks. In: Saxena, S.K. (Ed.), Advances in Physical Geochemistry. Advances in Physical Geochemistry. vol 2. Springer, New York, NY.

del Rey, A., Deckart, K., Arriagada, C., Mart?nez, F., 2016. Resolving the paradigm of the late Paleozoic-Triassic Chilean magmatism: Isotopic approach. Gondwana Res. 37, 172–181. https://doi.org/10.1016/j.gr.2016.06.008.

Diener, J.F.A., White, R.W., Hudson, T.J.M., 2014. Melt production, redistribution and accumulation in mid-crustal source rocks, with implications for crustal-scale melt transfer. Lithos 200–201 (1), 212–225. https://doi.org/10.1016/j.lithos.2014.04.021.

Droop, G.T.R., 1987. A general equation for estimating Fe3+ concentration in ferromagnesian silicates and oxides from microprobe analyses, using stoichiometric criteria. Mineral. Mag. 51, 431–435.

Dufek, J., Bachmann, O., 2010. Quantum magmatism: Magmatic compositional gaps generated by melt-crystal dynamics. Geology 38, 687–690. https://doi.org/10.1130/G30831.1.

Eby, G.N., 1992. Chemical Subdivision of the A-Type Granitoids: Petrogenetic and Tectonic Implications. https://doi.org/10.1130/0091-7613(1992)020<0641.

Espinoza, M., Montecino, D., Oliveros, V., Astudillo, N., Vásquez, P., Reyes, R., Celis, C., González, R., Contreras, J., Creixell, C., Martínez, A., 2019. The synrift phase of the early Domeyko Basin (Triassic, northern Chile): Sedimentary, volcanic, and tectonic interplay in the evolution of an ancient subduction-related rift basin. Basin Res. 31, 4–32. https://doi.org/10.1111/bre.12305.

Farner, M.J., Lee, C.T.A., 2017. Effects of crustal thickness on magmatic differentiation in subduction zone volcanism: A global study. Earth Planet. Sci. Lett. 470, 96–107. https://doi.org/10.1016/j.epsl.2017.04.025.

Ferreira, V.P., Sial, A.N., Toselli, A.J., de Toselli, J.R., Molina, P.G., Parada, M.A., Celino, J.J., Saavedra, J., 2019. Cordierite-bearing granitic rocks in South America: Contrasting sources and conditions of formation. J. S. Am. Earth Sci. 92, 417–434. https://doi.org/10.1016/j.jsames.2019.03.022.

Ferry, J.M., Watson, E.B., 2007. New thermodynamic models and revised calibrations for the Ti-in-zircon and Zr-in-rutile thermometers. Contrib. Mineral. Petrol. 154 (4), 429–437. https://doi.org/10.1007/s00410-007-0201-0.

Frost, C.D., Ronald Frost, B., 2011. On ferroan (A-type) granitoids: their compositional variability and modes of origin. J. Petrol. 52 (1), 39–53. https://doi.org/10.1093/petrology/egq070.

Gervasoni, F., Klemme, S., Rocha-Júnior, E.R.V., Berndt, J., 2016. Zircon saturation in silicate melts: a new and improved model for aluminous and alkaline melts. Contrib. Mineral. Petrol. 171 (3), 1–12. https://doi.org/10.1007/s00410-016-1227-y.

González, J., Oliveros, V., Creixell, C., Velásquez, R., Vásquez, P., Lucassen, F., 2017. The Triassic magmatism and its relation with the Pre-Andean tectonic evolution: Geochemical and petrographic constrains from the High Andes of north Central Chile (29°30′ – 30°S). J. S. Am. Earth Sci. https://doi.org/10.1016/j.jsames.2017.12.009.

Grimes, C.B., Wooden, J.L., Cheadle, M.J., John, B.E., 2015. "Fingerprinting" tectonomagmatic provenance using trace elements in igneous zircon. Contrib. Mineral. Petrol. 170, 1–26. https://doi.org/10.1007/s00410-015-1199-3.

Hervé, F., Fanning, C.M., Calderón, M., Mpodozis, C., 2014. Early Permian to Late Triassic batholiths of the Chilean Frontal Cordillera (28 ° – 31 ° S): SHRIMP U – Pb zircon ages and Lu – Hf and O isotope systematics. Lithos 184–187, 436–446. https://doi.org/10.1016/j.lithos.2013.10.018.

Holland, T., Blundy, J., 1994. Non-ideal interactions in calcic amphiboles and their bearing on amphibole-plagioclase thermometry. Contrib. Mineral. Petrol. 116, 433–447. https://doi.org/10.1007/BF00310910.

Holtz, F., Johannes, W., Tamic, N., B. H., 2001. Maximum and minimum water contents of granitic melts: a reexamination and implications. Lithos 56, 1–14.

Hu, Z.C., Gao, S., Liu, Y.S., Hu, S.H., Chen, H.H., Yuan, H.L., 2008. Signal enhancement in laser ablation ICP-MS by addition of nitrogen in the central channel gas. J. Anal. At. Spectrom. 23, 1093–1101.

Jackson, S.E., Pearson, N.J., Griffin, W.L., Belousova, E.A., 2004. The application of laser ablation inductively coupled plasma-mass spectrometry to in situ U–Pb zircon geochronology. Chem. Geol. 211 (1–2), 47–69.

Kelsey, D.E., Clark, C., Hand, M., 2008. Thermobarometric modelling of zircon and monazite growth in melt-bearing systems: examples using model metapelitic and metapsammitic granulites. J. Metamorph. Geol. 26 (2), 199–212. https://doi.org/10.1111/j.1525-1314.2007.00757.x.

Leake, B.E., Woolley, A.R., Arps, C.E.S., Birch, W.D., Gilbert, M.C., Grice, J.D., Hawthorne, F.C., Kato, A., Kisch, H.J., Krivovichev, V.G., Linthout, K., Laird, J., Maresch, W.V., Nickel, E.H.,

Rock, N.M.S., Smith, D.C., Stephenson, N.C.N., Ungaretti, L., Whittaker, E.J.W., Youzhi, G., 1997. Nomenclature of amphiboles: Report of the Subcommittee on Amphiboles of the International Mineralogical Association, Commission on New Minerals and Mineral Names. Mineral. Mag. 61, 295–321.
Lindsley, D.H., 1983. Pyroxene thermometry. Am. Mineral. 68, 477–493.
Liu, Y., Hu, Z., Zong, K., Gao, C., Gao, S., Xu, J., Chen, H., 2010. Reappraisement and refinement of zircon U–Pb isotope and trace element analyses by LA-ICP-MS. Chin. Sci. Bull. 55 (15), 1535–1546.
Locock, A.J., 2014. An Excel spreadsheet to classify chemical analyses of amphiboles following the IMA 2012 recommendations. Comput. Geosci. 62, 1–11. https://doi.org/10.1016/j.cageo.2013.09.011.
Ludwig, K.R., 2003. Isoplot/EX Version 3.0, a Geochronological Toolkit for Microsoft Excel. 4. Berkeley Geochronology Center Special Publication, p. 73.
Marks, M.A.W., Hettmann, K., Schilling, J., Frost, B.R., Markl, G., 2011. The mineralogical diversity of alkaline igneous rocks: critical factors for the transition from miaskitic to agpaitic phase assemblages. J. Petrol. 52, 439–455. https://doi.org/10.1093/petrology/egq086.
Martin, R.F., Bonin, B., 1976. Water and magma genesis: the association hypersolvus granite-subsolvus granite. Can. Mineral. 14, 228–237.
Massonne, H.J., Schreyer, W., 1987. Phengite geobarometry based on the limiting assemblage with K-feldspar, phlogopite, and quartz. Contrib. Mineral. Petrol. 96, 212–224. https://doi.org/10.1007/BF00375235.
McDonough, W.F., Sun, S.-s., 1995. The composition of the Earth. Chemical Geology 120 (3–4), 223–253. https://doi.org/10.1016/0009-2541(94)00140–4.
Michel, J., Baumgartner, L., Putlitz, B., Schaltegger, U., Ovtcharova, M., 2008. Incremental growth of the Patagonian Torres del Paine laccolith over 90 k.y. Geology 36, 459–462.
Miller, C.F., Stoddard, E.F., Bradfish, L.J., Dollase, W.A., 1981. Composition of plutonic mucovite: genetic implications. Can. Mineral. 19, 25–34.
Miller, C.F., McDowell, S.M., Mapes, R.W., 2003. Hot and cold granites: Implications of zircon saturation temperatures and preservation of inheritance. Geology 31, 529–532. https://doi.org/10.1130/0091-7613(2003)031<0529:HACGIO>2.0.CO;2.
Miller, J.S., Matzel, J.E.P., Miller, C.F., Burgess, S.D., Miller, R.B., 2007. Zircon growth and recycling during the assembly of large, composite arc plutons. J. Volcanol. Geotherm. Res. 167, 282–299. https://doi.org/10.1016/j.jvolgeores.2007.04.019.
Miller, C.F., Frazier, W.O., Carley, T., Claiborne, L., Padilla, A., Dylan, T., Gualda, G., 2014. Zr/Sr ratios distinguish cool & wet from cold & dry magmatic suites. 2014 GSA Annual Meeting. Vancouver, British Columbia, Canada.
Mirwald, P.W., 1986. Ist cordierit ein geothermometer? Fortschritte der Mineralogie 64/1, 119.
Molina, P.G., Parada, M.A., Gutiérrez, F.J., Ma, C., Li, J., Yuanyuan, L., Reich, M., Aravena, A., Gutiérrez, F.J., Ma, C., Li, J., Yuanyuan, L., Reich, M., Aravena, A., 2015. Protracted late magmatic stage of the Caleu pluton (Central Chile) as a consequence of heat redistribution by diking: Insights from zircon data and thermal modeling. Lithos 227. https://doi.org/10.1016/j.lithos.2015.04.008.
Montel, J.M., 1993. A model for monazite/melt equilibrium and application to the generation of granitic magmas. Chem. Geol. 110 (1–3), 127–146. https://doi.org/10.1016/0009-2541(93)90250-M.
Morata, D., Aguirre, L., Oyarzún, M., Vergara, M., 2000. Crustal contribution in the genesis of the bimodal Triassic volcanism from the Coastal Range, Central Chile. Rev. Geol. Chile 27 (1), 83–98. https://doi.org/10.5027/andgeoV27n1-a06.
Morimoto, N., 1988. Nomenclature of pyroxenes. Forschr. Miner. 66 (2), 237–252.
Morse, S.A., 2011. The fractional latent heat of crystallizing magmas. Am. Mineral. 96, 682–689. https://doi.org/10.2138/am.2011.3613.
Moscoso, R., Mpodozis, C., 1988. Estilos Estructurales en el Norte Chico de Chile (28°-31°S), Regiones de Atacama y Coquimbo. Rev. Geol. Chile 15 (2), 151–166.
Murillo, I., Velásquez, R., Creixell, C., 2017. Geología de las áreas Guanta-Los Cuartitos y Paso de Vacas Heladas, regiones de Atacama y Coquimbo, Servicio Nacional de Geología y Minería. Carta Geológica de Chile, Serie Geología Básica vols. 192e193 map scale 1:100.000.
Mutch, E.J.F., Blundy, J.D., Tattitch, B.C., Cooper, F.J., Brooker, R.A., 2016. An experimental study of amphibole stability in low-pressure granitic magmas and a revised Al-in-hornblende geobarometer. Contrib. Mineral. Petrol. 171, 1–27. https://doi.org/10.1007/s00410-016-1298-9.
Nabelek, P.I., Hofmeister, A.M., Whittington, A.G., 2012. The influence of temperature-dependent thermal diffusivity on the conductive cooling rates of plutons and temperature-time paths in contact aureoles. Earth Planet. Sci. Lett. 317–318, 157–164. https://doi.org/10.1016/j.epsl.2011.11.009.
Nachit, H., Razafimahefa, N., Stussi, J.M., Carron, J., 1985. Composition chimique des biotites et typologie magmatique des granitoides. Comptes Rendus de l'Académie des Sciences Paris 301, 813–817.
Nardi, L.V.S., Bonin, B., 1991. Post-orogenic and non-orogenic alkaline granite associations: the Saibro intrusive suite, southern Brazil - A case study. Chem. Geol. 92 (1–3), 197–211. https://doi.org/10.1016/0009-2541(91)90056-W.
Nimis, P., 1999. Clinopyroxene geobarometry of magmatic rocks. Part 2. Structural geobarometers for basic to acid, tholeiitic and mildly alkaline magmatic systems. pp. 62–74.
Oliveros, V., González, J., Espinoza Vargas, M., Vásquez, P., Rossel, P., Creixell, C., Sepúlveda, F., Bastias, F., 2018. The Early Stages of the Magmatic Arc in the Southern Central Andes. , pp. 165–190. https://doi.org/10.1007/978-3-319-67774-3_7.
Parada, M.A., 1988. Pre-Andean peralumious and metaluminous leucogranitoid suites in the high Andes of Central Chile. J. S. Am. Earth Sci. 1, 211–221.
Parada, M.A., 1990. Granitoid plutonism in central Chile and its geodynamic implications. A review. GSA Special paper, p. 104.
Paterson, S.R., Memeti, V., Mundil, R., Zák, J., 2016. Repeated, multiscale, magmatic erosion and recycling in an upper-crustal pluton: Implications for magma chamber dynamics and magma volume estimates. Am. Mineral. 101 (10), 2176–2198. https://doi.org/10.2138/am-2016-5576.
Patiño Douce, A.E., 1999. What do experiments tell us about the relative contributions of crust and mantle to the origin of granitic magmas? Geological Society. 168. Special Publications, London, pp. 55–75. https://doi.org/10.1144/GSL.SP.1999.168.01.05 1
Pearce, J.A., Norry, M.J., 1979. Petrogenetic implications of Ti, Zr, Y, and Nb variations in volcanic rocks. Contrib. Mineral. Petrol. 69 (1), 33–47. https://doi.org/10.1007/BF00375192.
Pearce, J. a, Harris, N.B.W., Tindle, A.G., 1984. Trace element distribution diagrams for the tectonic interpretation of granitic rocks. J. Petrol. 25 (4), 956–983. https://doi.org/10.1093/petrology/25.4.956.
Pereira, M.D., Bea, F., 1994. Cordierite-producing reactions in the Pefia Negra complex, Avila batholith, Central Spain: the key role of cordierite in low-pressure anatexis. Can. Mineral. 32, 763–780.
Petrelli, M., El Omari, K., Spina, L., Le Guer, Y., La Spina, G., Perugini, D., 2018. Timescales of water accumulation in magmas and implications for short warning times of explosive eruptions. Nat. Commun. 9 (1). https://doi.org/10.1038/s41467-018-02987-6.
Putirka, K., 1999. Clinopyroxene + liquid equilibria to 100 kbar and 2450 K. Contrib. Mineral. Petrol. 135, 151–163. https://doi.org/10.1007/s004100050503.
Putirka, K.D., 2008. Thermometers and Barometers for Volcanic Systems. Rev. Mineral. Geochem. 69, 61–120. https://doi.org/10.2138/rmg.2008.69.3.
René, M., Holtz, F., Luo, C., Beermann, O., Stelling, J., 2008. Biotite stability in peraluminous granitic melts: Compositional dependence and application to the generation of two-mica granites in the south Bohemian batholith (Bohemian Massif, Czech Republic). Lithos 102 (3–4), 538–553. https://doi.org/10.1016/j.lithos.2007.07.022.
Richet, P., Hovis, G., Whittington, A., 2006. Water and magmas: thermal effects of exsolution. Earth Planet. Sci. Lett. 241 (3–4), 972–977. https://doi.org/10.1016/j.epsl.2005.10.015.
Rodríguez, N., Díaz-Alvarado, J., Fernández, C., Fuentes, P., Breitkreuz, C., Tassinari, C.C.G., 2019. The significance of U–Pb zircon ages in zoned plutons: the case of the Flamenco pluton, Coastal Range batholith, northern Chile. Geosci. Front. 10 (3), 1073–1099. https://doi.org/10.1016/j.gsf.2018.06.003.
Rossel, P., Oliveros, V., Ducea, M.N., Charrier, R., Scaillet, S., Retamal, L., Figueroa, O., 2013. The early Andean subduction system as an analog to island arcs: evidence from across-arc geochemical variations in northern Chile. Lithos 179, 211–230.
Scaillet, B., Holtz, F., Pichavant, M., 2016. Experimental constraints on the formation of silicic magmas. Elements 12 (2), 109–114. https://doi.org/10.2113/gselements.12.2.109.
Schiller, D., Finger, F., 2019. Application of Ti-in-zircon thermometry to granite studies: problems and possible solutions. Contrib. Mineral. Petrol. 174, 51. https://doi.org/10.1007/s00410-019-1585-3.
Schreyer, W., 1965. Synthetische und natürliche Cordierite I: Mischkristallbildung synthetischer Cordierite und ihre Gleichgewichtsbeziehungen. Neues Jb. Mineral. Monat. 103, 35–79.
Siégel, C., Bryan, S.E., Allen, C.M., Gust, D.A., 2017. Use and abuse of zircon-based thermometers: A critical review and a recommended approach to identify antecrystic zircons. Earth Sci. Rev. 176 (February 2017), 87–116. https://doi.org/10.1016/j.earscirev.2017.08.011.
Tapster, S., Condon, D.J., Naden, J., Noble, S.R., Petterson, M.G., Roberts, N.M.W., ... Smith, D.J., 2016. Rapid thermal rejuvenation of high-crystallinity magma linked to porphyry copper deposit formation; evidence from the Koloula Porphyry Prospect, Solomon Islands. Earth and Planetary Science Letters 442, 206–217. https://doi.org/10.1016/j.epsl.2016.02.046.
Tropper, P., Wyhlidal, S., Haefeker, U.A., Mirwald, P.W., 2018. An experimental investigation of Na incorporation in cordierite in low P/high T metapelites. Mineral. Petrol. 112, 199–217. https://doi.org/10.1007/s00710-017-0522-2.
Vásquez, P., Franz, G., 2008. The Triassic Cobquecura Pluton (Central Chile): an example of a fayalite-bearing A-type intrusive massif at a continental margin. Tectonophysics 459, 66–84. https://doi.org/10.1016/j.tecto.2007.11.067.
Wark, D.A., Miller, C.F., 1993. Accessory mineral behavior during differentiation of a granite suite: monazite, xenotime and zircon in the Sweetwater Wash pluton, southeastern California, U.S.A. Chem. Geol. 110 (1–3), 49–67. https://doi.org/10.1016/0009-2541(93)90247-G.
Waters, L.E., Lange, R.A., 2017. Why aplites freeze and rhyolites erupt: Controls on the accumulation and eruption of high-SiO 2 (eutectic) melts. Geology 45, 1019–1022. https://doi.org/10.1130/G39373.1.
Watson, E.B., 1996. Dissolution, growth and survival of zircons during crustal fusion: kinetic principals, geological models and implications for isotopic inheritance. Trans. R. Soc. Edinb. Earth Sci. 87 (1–2), 43–56. https://doi.org/10.1017/S0263593300006465.
Watson, E.B., Harrison, T.M., 1983. Zircon saturation revisited: temperature and composition effects in a variety of crustal magma types. Earth Planet. Sci. Lett. 64, 295–304.
Weinberg, R.F., Hasalová, P., 2015. Water-fluxed melting of the continental crust: A review. Lithos 212–215, 158–188. https://doi.org/10.1016/j.lithos.2014.08.021.
Whalen, J.B., Currie, K.L., Chappell, B.W., 1987. A-type granites: geochemical characteristics, discrimination and petrogenesis. Contrib. Mineral. Petrol. 95 (4), 407–419. https://doi.org/10.1007/BF00402202.
Wiedenbeck, M., Allé, P., Corfu, F., Griffin, W.L., Meier, M., Oberli, F., Quadt, A.V., Roddick, J.C., Spiegel, W., 1995. Three natural zircon standards for U–Th–Pb, Lu–Hf, trace element and REE analyses. Geostand. Newslett. 19 (1), 1–23.
Zou, X., Qin, K., Han, X., Li, G., Evans, N.J., Li, Z., Yang, W., 2019. Insight into zircon REE oxybarometers: A lattice strain model perspective. Earth Planet. Sci. Lett. 506, 87–96. https://doi.org/10.1016/j.epsl.2018.10.031.

CHAPTER 6. COEXISTENCE OF A- AND S-TYPE PLUTONS DURING THE CONSTRUCTION OF THE LATE TRIASSIC CENTRAL CHILE ANDES BASEMENT: FINAL CONSIDERATIONS

6.1. Source materials, petrogenetic conditions and tectonic implications

This work depicts the formation of two coeval contrasting granites (S-type and A-type granite plutons), nearly emplaced at a similar depth, in a thinned lithosphere setting. The geochemical contrast is consistent with the explanation of a resulting difference in the typology of granites, as a consequence of source heterogeneities in the context of post-collisional magmatism (Clemens, 2003). The peraluminous S-type Los Tilos pluton would represent derivation from crustal sources but mixed with enriched-mantle materials, represented by the coeval mafic dyke swarm (Elqui Dike Swarm: EDS; Creixell et al., 2009), which would also act as crustal melting precursors. This observation agrees with petrogenetic models proposed by numerous authors (e.g. Villaseca et al., 1998; Clark et al., 2011; Frost and Frost, 2011), who recognize the participation of juvenile magmas in the formation of peraluminous melts. A mixture of peritectic minerals resulting from the fusion of metasedimentary sources, together with leucosome liquids, provides an explanation for the geochemical characteristics of peraluminous magmas (Patiño Douce, 1999). The particular case of the peraluminous Los Tilos pluton (LTp) would correspond to restitic material dragged from the source that rapidly cooled at the emplacement site (3.5 to 4.0 kbar) giving rise to cordierite and β-quartz paramorphs (see **Annexes**). Similarly, the hypersolvus leucogranite (MGp) displays integration of anatectic byproducts in ascending melts (hedenbergite), emplaced and cooled rapidly at shallow levels (1.5 to 2.5 kbar). On the other hand, the geochemical signature of MGp reveals anorogenic geochemical characteristics consistent with derivation from melting of the crust that probably undergone long periods of high heat flow, in a tectonic context of continent-continent collision or island-arc magmatism (Eby, 1992). The emplacement of juvenile mantle magmas (EDS) might be also responsible for the high temperatures achieved during the formation of MGp melts (by volatile-phase absent anatexis) but, in contrast to LTp, without chemical interaction with mafic precursors, therefore representing 'pure' anatectic melts (*cf.* Patiño Douce, 1999).

The pre-Andean granitic basement, located in this segment of the Andes, which is mainly formed by Late Paleozoic granitoids, is believed to be exhumed since the Late Triassic - Jurassic (Hervé et al., 2014; Jensen, 1984), because of extensional conditions analog to that of the Laramide Province of North America (Moscoso and Mpodozis, 1988). These extensional conditions might have facilitated the ascent of mantle magmas through the crust (Karakas and Dufek, 2015), giving rise to the emplacement of the Elqui Limarí Dike Swarm and the studied plutons. The high temperatures achieved to produce *anatexis* of the Paleozoic granitic basement can also be explained by the thinning

of the lithosphere (Currie and Hyndman, 2006); this is a geodynamic characteristic of the southwestern Gondwana margin during the Early Mesozoic (e.g. Espinoza et al., 2019) as an analog to an island-arc setting (Rossel et al., 2013). This setting is thought to be a consequence of post-collisional orogenic collapse processes after the San Rafael orogeny (Kleinman and Japas, 2009). The thermal relaxation of the resulting thickened orogen, together with rapid exhumation of rocks of the newly-formed orogenic front (*cf.* Hervé et al., 2014), could have been accompanied by *anatexis* of the lower crust up to 25 vol. % melt fractions, provided an external supply of heat (Thompson, 1999; **Fig. 4.3**). This would happen after a period of incubation equivalent to the magmatic gap between the western (Elqui Complex) and eastern (Ingaguás Complex) parts of the Elqui Limarí Batholith.

The intense and protracted Upper Paleozoic arc magmatism (Martin et al., 1999), was followed by a waning stage of igneous activity and arc *loci* shift to the west in the Late Triassic to Early Jurassic (Coloma et al., 2017). Similarly, Zentilli et al. (2018) discuss that the mineralization of the Eocene-Oligocene belt of porphyry type Cu-Mo deposits located in northern Chile (20°-27°S), occurred also at the culminating stage of vigorous protracted igneous activity before quiescence. These igneous products were also emplaced in the same -narrow- strip of crust occupied by Late Triassic plutons, therefore suggesting that magma emplacement and ascent occurred by the utilization of the same crustal discontinuities, inherited from pre-Andean structures related to the opening of Upper Paleozoic to Triassic marginal basins in south western Gondwana (e.g. Franzese and Spalletti, 2001).

The anorogenic affinity and high enrichment in HFSE of some of the Late Triassic plutons (Vásquez and Frantz, 2008; González et al., 2017; Molina et al., 2020) can be interpreted by two, non-excluding, petrogenetic scenarios (*cf.* Frost and Frost, 2011). Namely, the subduction-related component and the *anatectic* component of formed magmas, respectively: (1) Extraction of the last melt batches available asthenospheric source region after uninterrupted arc magmatism since the Carboniferous (del Rey et al., 2016). The A-type geochemical features are interpreted as a result of the extraction and ascent of highly silicic magmas (representative of the very last melt fractions) in thinned lithosphere contexts (Farner and Lee, 2017). (2) Anatexis of a more refractory crust as the orogen became increasingly hotter, by decomposition of hydrated phases (Vielzeuf et al., 1990; Schorn et al., 2016), could generate A-type granites resulting from low degrees of high-temperature partial melting (e.g. Kemp and Hawkesworth, 2005). These scenarios may also explain the isotopic signature variations of rocks of the Elqui-Limarí batholith, from more radiogenic Upper Paleozoic rocks with εNd between 0 and -5, and $^{87}Sr/^{86}Sr$ between 0.705 and 0.710, to less radiogenic Late Triassic rocks with εNd around 0, and $^{87}Sr/^{86}Sr$ between 0.704 and 0.707 (*cf.* González et al., 2017).

6.2. Understanding the preservation of inherited zircons in the studied magmatic systems

U-Pb ages of zircon crystallization are generally used to determine dates of pluton emplacement (e.g. Ratschbacher et al., 2018); its validity and interpretation are discussed in light of the different petrogenetic processes that might provide mixed signals of zircon ages (Siégel et al., 2017). Their understanding is generally supported by complex thermal models (**Chapter 2**), which in turn depend on a large number of physical variables to achieve geologically-reasonable results. This work attains a thorough understanding of the factors that drive zircon crystallization and preservation, and up to which extent they share a reciprocal relationship with the tectonomagmatic context in which magmas are formed (see **Figure 1.1**, **Section 4.3**, and **Chapter 5**), therefore contributes to a better understanding of the timescales of pluton construction, rates of magma generation, and source P-T conditions and materials.

The preservation of inherited zircon cores depends on the availability of H_2O during crustal melting, and the degree of zirconium enrichment at a given temperature (Watson, 1996). Inherited zircon grains commonly come from inclusions of large silicate crystals of the source, thus armored from chemical dissolution (Chen and Williams, 1990). However, dehydration melting (water-absent melting) of the crust, which has a high *liquidus* temperature and a wide range of eutectic temperatures (Holtz et al., 2001), is commonly accompanied by the liberation of zircon inclusions after the breakdown of hosting hydrated mafic silicates. The new silicates formed from the melt could be, in turn, prone to enclose peritectic phases (eg. zircon) (Rossi et al., 2002). All these situations could generate zircons with complex zonation textures and variable compositions, which are far from easy interpretation. On the other hand, magmas formed by water-induced melting are not always suitable to preserve inherited zircons due to their low solidus temperatures and narrow eutectic temperature range.

A relation between zircon inheritance and depth of magma emplacement appears to exist because of the magma cooling rate. The critical crystallinities (crystallinities above 70 vol.%) achieved by magmas *en route* to their emplacement level depend on the cooling rates, confining pressure (Waters and Lange, 2017), and cooling derived from volatile exsolution (Richet et al., 2006), among other factors. Deep magmas trapped by host-rock anisotropies and/or rheological barriers while ascending will slowly cool (Gelman et al., 2013), and could maintain conditions above zircon saturation temperatures for long periods, which are less adequate to preserve inherited zircon cores. Contrastingly, magmas emplaced at shallow crustal levels without apparent structural barriers (for example those emplaced in non-orogenic settings; Rogers and Greenberg, 1990), will most likely present inherited zircon grains. In this case, the zircon crystals carried by melts formed at the source

region could be affected by dissolution unless high ascent velocities of magmas took place as expected in a thinned, and tectonically-relaxed, lithosphere (Petford, 2000).

The studied zircons show contrasting chemistry and are interpreted to be formed at the source (see **Chapter 5**), related to different hosting parental magmas (Chapman et al., 2016). These geochemical characteristics mimic the composition of the partially melted material, which happens to be heterogeneous (e.g. Hansmann and Oberli, 2004). As a conclusion, the geochemistry of inherited grains displays compelling evidence to identify primary magmas in equilibrium with early zircon (e.g. Gao et al., 2016). Consequently, crustal heterogeneities, such as those expected in margins composed of amalgamated terranes, could be screened by means of detailed studies of zircons formed in magmas resulting from crust anatexis.

CHAPTER 7. CONCLUSIONS

The conditions by which *anatexis* occurs are thoroughly addressed in this work, using a novel approach in which the stability field of zircon is placed to constrain the thermodynamic and kinetic conditions for the generation of *anatectic* magmas, in a thinned lithosphere environment.

Two contrasting and coeval plutons, emplaced in the High Andes of Central Chile (~30°S), which are indicative of crustal melting in the Late Triassic, were selected. This igneous activity is represented by the Monte Grande pluton (MGp) and Los Tilos pluton (LTp), which are A- and S-type granitoids, respectively. MGp has a marked anorogenic signature (Ga/Al values above 0.0025, Y+Nb>45, and a generalized enrichment in HFSE). In turn, LTp stands as a geochemically peraluminous cordierite-bearing granodiorite, with clear evidence of rapid cooling of peritectic phases formed through *anatexis*. These plutons pierce the root of the upper Paleozoic arc and are emplaced at a shallow structural level (<3.5 kbar). As a consequence, the studied rocks develop agpaitic and hypersolvus assemblages, together with textures ascribed to *subsolidus* reactions of metastable minerals formed at depth.

Zircon grains found in the studied plutons formed in the Lower Crust and were preserved in source melts during arc activity that lasted more than *ca.* 30 Ma. The geochemical signature of these zircons reveals a heterogeneous source, with mixed signals of continental and island arc affinities. The modeled composition of the peraluminous melt of migmatized crust, in water-saturated conditions, shows a strong dependence on the temperature of *anatexis*. In fact, peraluminous anatectic melts are common in the Lower Crust, whereas temperatures above *ca.* 700°C are needed to form melts of this composition, in the Middle and Upper Crust. Yet, zircon grains entrained in melts formed in the Lower and Middle Crust are prone to be dissolved unless the primary anatectic melts were highly enriched in zirconium or extracted rapidly. Magmas formed in convergent plate boundaries, in tectonic compression, represent igneous media with a high dissolution potential, therefore zircon crystallization will most probably occur after the acquisition of critical effective viscosities, at their final emplacement site.

In this study case, the thermodynamic and kinetic models for the efficient preservation of inherited zircons carried in *anatectic* melts, formed as a consequence of high-temperature (~900°C) dehydration melting, indicate that rapid extraction from source and emplacement (reaching the *solidus* in less than 12 kyr) took place. The thermal conditions to accomplish *anatexis* could be achieved by the combined effects of augmented radioactive-decay heat production after crustal thickening (San Rafael orogenic phase), heat advection by the intrusion of a mafic dike swarm (Elqui Dike Swarm), the achievement of high temperatures by the maturation of a ‘sterile’ orogen by

protracted arc activity, or increased heat flow by tectonic relaxation in a back-arc setting. An energetic addition of 0.2 kJ/g is required to partially melt the crust, up to melt fractions within the *efficient extraction crystallinity window* (between crystallinities of 50 to 70 vol.%). The adiabatic ascent of water-undersaturated melts (<3 wt.% H_2O) could have easily occurred by the utilization of melt pathways inherited from existing crustal discontinuities, resulting from previous tectonic stages. A fast ascent of formed magmas is needed to prevent *eutectic* freezing when water saturation by decompression occurs. These conditions ensure the preservation of entrained minerals such as those formed from crystallizing magmas and/or those peritectic phases resulting from crust *anatexis*.

BIBLIOGRAPHY

Annen, C., 2009. From plutons to magma chambers: Thermal constraints on the accumulation of eruptible silicic magma in the upper crust. Earth Planet. Sci. Lett. 284, 409–416.

Aravena, A., Gutiérrez, F.J., Parada, M.A., Payacán, Í., Bachmann, O., Poblete, F., 2017. Compositional zonation of the shallow La Gloria pluton (Central Chile) by late-stage extraction/redistribution of residual melts by channelization: Numerical modeling. Lithos 284–285, 578–587.

Ardill, K., Paterson, S., Memeti, V., 2018. Spatiotemporal magmatic focusing in upper-mid crustal plutons of the Sierra Nevada arc. Earth Planet. Sci. Lett. 498, 88–100.

Armstrong, J.T., Donovan, J., Carpenter, P., 2013. CALCZAF, TRYZAF and CITZAF: the use of multi-correction-algorithm programs for estimating uncertainties and improving quantitative X-ray analysis of difficult specimens. Proceed. Microscopy Microanal. v19, 812–813

Auzanneau, E., Schmidt, M.W., Vielzeuf, D., D Connolly, J.A., 2010. Titanium in phengite: A geobarometer for high temperature eclogites. Contrib. to Mineral. Petrol. 159, 1–24. https://doi.org/10.1007/s00410-009-0412-7

Ayres, M., Harris, N.B.W., Vance, D., 1997. Possible Constraints on Anatectic Melt Residence Times from Accessory Mineral Dissolution Rates: An Example from Himalayan Leucogranites. Mineral. Mag. 61, 29–36.

Ayres, M., Harris, N.B.W., Vance, D., 1997. Possible Constraints on Anatectic Melt Residence Times from Accessory Mineral Dissolution Rates: An Example from Himalayan Leucogranites. Mineral. Mag. 61, 29–36. https://doi.org/10.1180/minmag.1997.061.404.04

Bachmann, O., Miller, C.F., de Silva, S.L., 2007. The volcanic-plutonic connection as a stage for understanding crustal magmatism. J. Volcanol. Geotherm. Res. 167, 1–23.

Bacon, C.R., Lowenstern, J.B., 2005. Late Pleistocene granodiorite source for recycled zircon and phenocrysts in rhyodacite lava at Crater Lake, Oregon. Earth Planet. Sci. Lett. 233, 277–293.

Ballard, J.R., Palin, M.J., Campbell, I.H., 2002. Relative oxidation states of magmas inferred from Ce(IV)/Ce(III) in zircon: application to porphyry copper deposits of northern Chile. Contrib. to Mineral. Petrol. 144, 347–364.

Barbero, L. Villaseca, C., 1992. The Layos Granite, Hercynian Complex of Toledo (Spain): an example of parautochthonous restite-rich granite in a granulitic area 127–0.8.

Barbey, P., Marignac, C., Montel, J.M., Macaudière, J., Gasquet, D., Jabbori, J., 1999. Cordierite growth textures and the conditions of genesis and emplacement of crustal granitic magmas: the Velay granite complex (Massif Central, France). J. Petrol. 40, 1425–1441.

Bea, F., 2012. The sources of energy for crustal melting and the geochemistry of heat-producing elements. Lithos 153, 278–291.

Bea, F., Montero, P., González-Lodeiro, F., Talavera, C., 2007. Zircon Inheritance Reveals Exceptionally Fast Crustal Magma Generation Processes in Central Iberia during the Cambro-Ordovician. J. Petrol. 48, 2327–2339.

Bea, F., Montero, P., Ortega, M., 2006. A LA-ICP-MS evaluation of Zr reservoirs in common crustal rocks: implications for Zr and Hf geochemistry, and zircon-forming processes. Can. Mineral. 44, 693–714.

Beard, J.S., Ragland, P.C., and Crawford, M.L., 2005, Reactive bulk assimilation: A model for crust-mantle mixing in silicic magmas: Geology, v. 33, p. 681–684.

Bhattacharya, S., Kemp, A.I.S., Collins, W.J., 2018. Response of zircon to melting and metamorphism in deep arc crust, Fiordland (New Zealand): implications for zircon inheritance in cordilleran granites, Contributions to Mineralogy and Petrology. Springer Berlin Heidelberg.

Boehnke, P., Watson, E.B., Trail, D., Harrison, T.M., Schmitt, A.K., 2013. Zircon saturation re-revisited. Chemical Geology 351, 324–334.

Bohrson, W. A., and F. J. Spera, 2007. Energy-Constrained recharge, Assimilation, and Fractional Crystallization (EC-RAxFC): A Visual Basic computer code for calculating trace element and isotope variations of open-system magmatic systems, Geochem. Geophys. Geosyst.

Bohrson, W.A., Spera, F.J., 2003. Energy-constrained open-system magmatic processes IV: Geochemical, thermal and mass consequences of energy constrained recharge, assimilation and fractional crystallization (EC-RAFC). Geochemistry, Geophys. Geosystems 4.

Bolhar R, Weaver SD, Palin JM, Cole JW, Paterson LA (2008) Systematics of zircon crystallization in the Cretaceous Separation Point suite, New Zealand, using U/Pb isotopes, REE and Ti geothermometry. Contrib Mineral Petrol 156:133–160

Bonin, B., 2007. A-type granites and related rocks: Evolution of a concept, problems and prospects. Lithos 97, 1–29.

Broderick, C., Wotzlaw, J.F., Frick, D.A., Gerdes, A., Ulianov, A., Günther, D., Schaltegger, U., 2015. Linking the thermal evolution and emplacement history of an upper-crustal pluton to its lower-crustal roots using zircon geochronology and geochemistry (southern Adamello batholith, N. Italy). Contrib. to Mineral. Petrol. 170, 1–17.

Brown, M., 1994. The generation, segregation, ascent and emplacement of granite magma: the migmatite-to-crustally-derived granite connection in thickened orogens. Earth Sci. Rev. 36, 83–130.

Brown, M., 2001. Crustal Melting and Granite Generation: key issues. Phys. Chem. Earth. v26, p.201-212.

Brown, M., 2010. Melting of the continental crust during orogenesis: The thermal, rheological, and compositional consequences of melt transport from lower to upper continental crust. Can. J. Earth Sci. 47, 655–694.

Brown, M., 2013. Granite: From genesis to emplacement. Bull. Geol. Soc. Am. 125, 1079–1113.

Burnham, A.D., Berry, A.J., 2012. An experimental study of trace element partitioning between zircon and melt as a function of oxygen fugacity. Geochim. Cosmochim. Acta 95, 196–212.

C.J. Wei, R. Powell., 2003. Phase relations in high-pressure metapelites in the system KFMASH (K2O–FeO–MgO–Al2O3–SiO2– H2O) with application to natural rocks, Contrib. Mineral. Petrol. 145: 301–315.

Cameron M., Bagby W.C., Cameron K.L., 1980. Petrogenesis of voluminous mid-Tertiary ignimbrites of the Sierra Madre Occidental, Chihuahua, Mexico. Contributions of Mineralogy and Petrology, v74, p 271-284.

Cao, W., Lee, C.T.A., Yang, J., Zuza, A. V., 2019. Hydrothermal circulation cools continental crust under exhumation. Earth Planet. Sci. Lett. 515, 248–259.

Casquet, C., Hervé, F., Pankhurst, R.J., Baldo, E., Calderón, M., Fanning, C.M., Rapela, C.W., Dahlquist, J., 2014. The Mejillonia suspect terrane (Northern Chile): Late Triassic fast burial and metamorphism of sediments in a magmatic arc environment extending into the Early Jurassic. Gondwana Res. 25, 1272–1286.

Castiñeiras, P., García, F.D., Barreiro, J.G., 2010. REE-assisted U-Pb zircon age (SHRIMP) of an anatectic granodiorite: Constraints on the evolution of the A Silva granodiorite, Iberian allochthonous complexes. Lithos 116, 153–166.

Castro, A., 2013. Tonalite–granodiorite suites as cotectic systems: A review of experimental studies with applications to granitoid petrogenesis. Earth-Science Rev. 124, 68–95.

Chamberlain CP, Sonder LJ (1990) Heat- producing elements and the thermal and baric patterns of metamorphic belts. Science 250: 763-769

Chapman, J.B., Gehrels, G.E., Ducea, M.N., Giesler, N., Pullen, A., 2016. A new method for estimating parent rock trace element concentrations from zircon. Chem. Geol. 439, 59–70.

Chappell, B.W., White, J.R., 2001. Two contrasting granite types: 25 years later Two contrasting granite types: 25 years later 489–499.

Charrier, R., Ramos, V.A., Tapia, F., Sagripanti, L., 2015. Tectono-stratigraphic evolution of the Andean Orogen between 31 and 37°S (Chile and Western Argentina). Geol. Soc. London, Spec. Publ. 399, 13–61.

Chen, Y.D., Williams, I.S., 1990. Zircon inheritance in mafic inclusions from Bega batholith granites, southeastern Australia: An ion microprobe study. J. Geophys. Res. 95, 17787.

Cherniak, D.J., Watson, E.B., 2001. Pb diffusion in zircon. Chemical Geology 172, 5–24.

Cherniak, J., Hanchar, M., Watson, B., 1997. Diffusion of tetravalent cations in zircon 383–390.

Claiborne, L.L., Miller, C.F., Wooden, J.L., 2010. Trace element composition of igneous zircon: a thermal and compositional record of the accumulation and evolution of a large silicic batholith, Spirit Mountain, Nevada. Contrib. to Mineral. Petrol. 160, 511–531.

Clark, C., Fitzsimons, I.C.W., Healy, D., Harley, S.L., 2011. How does the continental crust get really hot? Elements 7, 235–240.

Clarke, D.B., Henry, A.S., and White, M.A., 1998, Exploding xenoliths and the absence of “elephants’ graveyards” in granite batholiths: Journal of Structural Geology, v. 20, p. 1325–1343.

Clemens, J.D., 2003. S-type granitic magmas - petrogenetic issues, models and evidence. Earth-Science Rev. 61, 1–18.

Clemens, J.D., Droop, G.T.R., 1998. Fluids, P-T paths and the fates of anatectic melts in the Earth's crust. Lithos 44, 21–36.

Clemens, J.D., Vielzeuf, D., 1987. Constraints on melting and magma production in the crust. Earth Planet. Sci. Lett. 86, 287–306.

Collins, W.J., 1998. Evaluation of petrogenetic models for Lachlan Fold Belt granitoids: Implications for crustal architecture and tectonic models. Aust. J. Earth Sci. 45, 483–500.

Coloma, F., Valin, X., Oliveros, V., Vásquez, P., Creixell, C., Salazar, E., Ducea, N., 2017. Geochemistry of Permian to Triassic igneous rocks from northern Chile (28o-30o15'S): Implications on the dynamics of the proto-Andean margin. Andean Geology 44, 147–178.

Connolly, J.A.D., 2005. Computation of phase equilibria by linear programming: A tool for geodynamic modeling and its application to subduction zone decarbonation. Earth Planet. Sci. Lett. 236, 524–541.

Creixell, C., Parada, M.Á., Morata, D., Roperch, P., Arriagada, C., 2007. The genetic relationship between mafic dike swarms and plutonic reservoirs in the mesozoic of central chile (30°–33°45′S): insights from AMS and geochemistry. Int. J. Earth Sci. 98, 177–201.

Curie, C.A., Hyndman, R.D., 2006. The thermal structure of subduction zone back arcs. J. Geophys. Res. Solid Earth 111, 1–22.

Dahlquist, J.A., Alasino, P.H., Eby, G.N., Galindo, C., Casquet, C., 2010. Fault controlled Carboniferous A-type magmatism in the proto-Andean foreland (Sierras Pampeanas, Argentina): Geochemical constraints and petrogenesis. Lithos 115, 65–81.

De Saint Blanquat, M., Horsman, E., Habert, G., Morgan, S., Vanderhaeghe, O., Law, R., Tikoff, B., 2011. Multiscale magmatic cyclicity, duration of pluton construction, and the paradoxical relationship between tectonism and plutonism in continental arcs. Tectonophysics 500, 20–33.

del Rey, A., Deckart, K., Arriagada, C., Martínez, F., 2016. Resolving the paradigm of the late Paleozoic-Triassic Chilean magmatism: Isotopic approach. Gondwana Research 37, 172–181.

Diener, J.F.A., White, R.W., Hudson, T.J.M., 2014. Melt production, redistribution and accumulation in mid-crustal source rocks, with implications for crustal-scale melt transfer. Lithos 200–201, 212–225.

Dufek, J., Bachmann, O., 2010. Quantum magmatism: Magmatic compositional gaps generated by melt-crystal dynamics. Geology 38, 687–690.

Dufek, J., Bergantz, G.W., 2005. Lower crustal magma genesis and preservation: A stochastic framework for the evaluation of basalt-crust interaction. J. Petrol. 46, 2167–2195. https://doi.org/10.1093/petrology/egi049

Duffy C.J., Greenwood H.J.,1979. *Phase-equilibria in the system MgO-MgF_2-SiO_2-H_2O*. American Mineralogist **64**:1156-74

Ebadi, A., Johannes, W., 1991. Beginning of melting and compo- sition of first melts in the system Qz–Ab–Or–H O–CO .22 Contrib. Mineral. Petrol. 106, 286–295.

Eby, G.N., 1990. The A-type granitoids: A review of their occurence and chemical characteristics and speculations on their petrogenesis. Lithos 26, 115–134.

Eby, G.N., Eby, G.N., 1992. Chemical subdivision of the A-type granitoids: Petrogenetic and tectonic implications.

Espinoza, M., Montecino, D., Oliveros, V., Astudillo, N., Vásquez, P., Reyes, R., Celis, C., González, R., Contreras, J., Creixell, C., Martínez, A., 2019. The synrift phase of the early Domeyko Basin (Triassic, northern Chile): Sedimentary, volcanic, and tectonic interplay in the evolution of an ancient subduction-related rift basin. Basin Res. 31, 4–32.

Farner, M.J., Lee, C.T.A., 2017. Effects of crustal thickness on magmatic differentiation in subduction zone volcanism: A global study. Earth Planet. Sci. Lett. 470, 96–107.

Ferreira, V.P., Sial, A.N., Toselli, A.J., de Toselli, J.R., Molina, P.G., Parada, M.A., Celino, J.J., Saavedra, J., 2019. Cordierite-bearing granitic rocks in South America: Contrasting sources and conditions of formation. Journal of South American Earth Sciences 92, 417–434.

Ferry, J.M., Watson, E.B., 2007. New thermodynamic models and revised calibrations for the Ti-in-zircon and Zr-in-rutile thermometers. Contrib. to Mineral. Petrol. 154, 429–437.

Flood, R.H., Vernon, R.H., 1978. The Cooma Granodiorite, Australia: An example of in situ crustal anatexis? Geology 6, 81–84.

Flood, R.H., Vernon, R.H., 1978. The Cooma Granodiorite, Australia: An example of in situ crustal anatexis? Geology 6, 81–84. https://doi.org/10.1130/0091-7613(1978)6<81:TCGAAE>2.0.CO;2

Franzese, J.R., Spalletti, L.A., 2001. Late triassic- Early jurassic continental extension in SouthWestern Gondwana: Tectonic segmentation and pre-break-up rifting. J. South Am. Earth Sci. 14, 257–270.

Frost, C.D., Ronald Frost, B., 2011. On ferroan (A-type) granitoids: Their compositional variability and modes of origin. J. Petrol. 52, 39–53.

Gana, P., 1991. Magmatismo bimodal del Triásico Superior-Jurásico inferior, en la Cordillera de la Costa, provincias de Elqui y Limarí, Chile. Revista Geológica de Chile. 18, 55-67.

Gao, P., Zheng, Y.F., Zhao, Z.F., 2016. Distinction between S-type and peraluminous I-type granites: Zircon versus whole-rock geochemistry. Lithos 258–259, 77–91.

Gao, P., Zheng, Y.F., Zhao, Z.F., 2016. Experimental melts from crustal rocks: A lithochemical constraint on granite petrogenesis. Lithos 266–267, 133–157.

Gao, W., Wang, Z., Li, L., Tan, Y., 2019. Petrogenesis and tectonic implications of Triassic A-type granites in southeastern China: insights from zircon U–Pb–Hf isotopic and whole-rock geochemical compositions of the Luoguyan and Guiyantou granites in northwestern Fujian Province. Int. Geol. Rev. 61, 224–239.

Gelman, S.E., Deering, C.D., Bachmann, O., Huber, C., Gutiérrez, F.J., 2014. Identifying the crystal graveyards remaining after large silicic eruptions. Earth Planet. Sci. Lett. 403, 299–306.

Gelman, S.E., Gutiérrez, F.J., Bachmann, O., 2013. On the longevity of large upper crustal silicic magma reservoirs. Geology 41, 759–762.

Gervasoni, F., Klemme, S., Rocha-Júnior, E.R.V., Berndt, J., 2016. Zircon saturation in silicate melts: a new and improved model for aluminous and alkaline melts. Contrib. to Mineral. Petrol. 171, 1–12.

Gervasoni, F., Klemme, S., Rocha-Júnior, E.R.V., Berndt, J., 2016. Zircon saturation in silicate melts: a new and improved model for aluminous and alkaline melts. Contrib. to Mineral. Petrol. 171, 1–12.

Glazner, A.F., 2007. Thermal limitations on incorporation of wall rock into magma. Geology 35, 319–322.

Glazner, A.F., Bartley, J.M., Coleman, D.S., Gray, W., Taylor, R.Z., 2004. Are plutons assembled over millions of years by amalgamation from small magma chambers? GSA Today 14, 4.

Gómez-Tuena, A., Cavazos-Tovar, J.G., Parolari, M., Straub, S.M., Espinasa-Pereña, R., 2018. Geochronological and geochemical evidence of continental crust 'relamination' in the origin of intermediate arc magmas. Lithos 322, 52–66.

González, J., Oliveros, V., Creixell, C., Velásquez, R., Vásquez, P., Lucassen, F., 2017. The Triassic magmatism and its relation with the Pre-Andean tectonic evolution: Geochemical and petrographic constrains from the High Andes of north central Chile (29°30′ – 30°S). J. South Am. Earth Sci.

González, J., Oliveros, V., Creixell, C., Velásquez, R., Vásquez, P., Lucassen, F., 2017. The Triassic magmatism and its relation with the Pre-Andean tectonic evolution: Geochemical and petrographic constrains from the High Andes of north central Chile (29°30′ – 30°S). J. South Am. Earth Sci.

Gutiérrez, F., Parada, M.A., 2010. Numerical modeling of time-dependent fluid dynamics and differentiation of a shallow basaltic magma chamber. J. Petrol. 51, 731–762.

Hansmann, W., Oberli, F., 2004. Zircon inheritance in an igneous rock suite from the southern Adamello batholith (Italian Alps). Contrib. to Mineral. Petrol. 107, 501–518.

Harley SL (1998) On the occurrence and characterization of ultrahigh-tempera- ture metamorphism. In: Treloar PJ, O'Brien PJ (eds) What Drives Metamorphism and Metamorphic Reactions? Geological Society of London Special Publication 138, pp 81-107

Hawkesworth, C.J., Kemp, a. I.S., 2006. Using hafnium and oxygen isotopes in zircons to unravel the record of crustal evolution. Chem. Geol. 226, 144–162.

Hermann, J., Rubatto, D., 2003. Relating zircon and monazite domains to garnet growth zones: Age and duration of granulite facies metamorphism in the Val Malenco lower crust. J. Metamorph. Geol. 21, 833–852.

Hervé, F., Fanning, C.M., Calderón, M., Mpodozis, C., 2014. Early Permian to Late Triassic batholiths of the Chilean Frontal Cordillera (28° – 31°S): SHRIMP U – Pb zircon ages and Lu – Hf and O isotope systematics. Lithos 184–187, 436–446.

Holland T., Powell R., 1998. An internally consistent thermodynamic data set for phases of petrological interest, J. Meta- morph. Geol. 16 (1998) 309–343.

Holtz, F., Johannes, W., 1994. Maximum and minimum water contents of granitic melts: implications for chemical and physical properties of ascending magmas. Lithos 32, 149–159.

Holtz F, Johannes W, Tamic N, B.H., 2001. Maximum and minimum water contents of granitic melts: a reexamination and implications. Lithos 56, 1–14.

Hoskin, P.W.O., Schaltegger, U., 2018. The composition of zircon and igneous and metamorphic petrogenesis. Zircon 27–62.

Huber, C., Bachmann, O., Manga, M., 2009. Homogenization processes in silicic magma chambers by stirring and mushification (latent heat buffering). Earth Planet. Sci. Lett. 283, 38–47.

Jackson, S.E., Pearson, N.J., Griffin, W.L., Belousova, E.A., 2004. The application of laser ablation inductively coupled plasma-mass spectrometry to in situ U–Pb zircon geo- chronology. Chem. Geol. 211 (1–2), 47–69.

Jensen, O.L., 1984. Andean tectonics related to geometry of subducted Nazca plate: Discussion and reply. Geological Society of America Bulletin. v.95, p: 877-880.

Karakas, O., Dufek, J., 2015. Melt evolution and residence in extending crust: Thermal modeling of the crust and crustal magmas. Earth Planet. Sci. Lett. 425, 131–144.

Kelsey, D.E., Clark, C., Hand, M., 2008. Thermobarometric modelling of zircon and monazite growth in melt-bearing systems: Examples using model metapelitic and metapsammitic granulites. J. Metamorph. Geol. 26, 199–212.

Kemp, A.I.S., Hawkesworth, C.J., 2005. Generation and Secular Evolution of the Continental Crust. The crust: treatise on geochemistry 3, 349.

Kemp, A.I.S., Whitehouse, M.J., Hawkesworth, C.J., Alarcon, M.K., 2005. A zircon U-Pb study of metaluminous (I-type) granites of the Lachlan Fold Belt, southeastern Australia: Implications for the high/low temperature classification and magma differentiation processes. Contrib. to Mineral. Petrol. 150, 230–249.

Kleiman, L.E., Japas, M.S., 2009. The Choiyoi volcanic province at 34°S–36°S (San Rafael, Mendoza, Argentina): Implications for the Late Palaeozoic evolution of the southwestern margin of Gondwana. Tectonophysics 473, 283–299.

Lachenbruch AH., Sass J.H., 1978. Models of an extending lithosphere and heat flow in the Basin and Range province. Geological Society of America, Memoir 152, 209-150.

Landerberger, B., Collins, W.J., 1996. Derivation of A-type granites from a dehydrated charnokitic lower crust, evidence from Chaelundi Complex, eastern Australia. J. Petrol. 37, 145–170.

Leitch, A.M., Weinberg, R.F., 2002. Modelling granite migration by mesoscale pervasive £ ow 200, 131–146.

Liu, Y., Hu, Z., Zong, K., Gao, C., Gao, S., Xu, J., Chen, H., 2010. Reappraisement and refine- ment of zircon U–Pb isotope and trace element analyses by LA-ICP-MS. Chin. Sci. Bull. 55 (15), 1535–1546.

Ludwig, K.R., 2003. Isoplot/EX Version 3.0, a Geochronological Toolkit for Microsoft Excel. 4. Berkeley Geochronology Center Special Publication, p. 73.

Lustrino, M., Wilson, M., 2007. The circum-Mediterranean anorogenic Cenozoic igneous province. Earth-Science Reviews. 81, 1-65.

Mamani, M., Wörner, G., Sempere, T., 2010. Geochemical variations in igneous rocks of the Central Andean orocline (13°S to 18°S): Tracing crustal thickening and magma generation through time and space. Bull. Geol. Soc. Am. 122, 162–182.

Marsh, B.D., 1982, On the mechanics of igneous diapirism, stoping, and zone melting: American Journal of Science, v. 282, p. 808–855.

Marsh, J.H., Stockli, D.F., 2015. Zircon U-Pb and trace element zoning characteristics in an anatectic granulite domain: Insights from LASS-ICP-MS depth profiling. Lithos 239, 170–185.

Martin, M.W., Clavero R, J., Mpodozis M, C., 1999. Late Paleozoic to Early Jurassic tectonic development of the high Andean Principal Cordillera, El Indio Region, Chile (29–30°S). J. South Am. Earth Sci. 12, 33–49.

Martin, R.F., Sokolov, M., Magaji, S.S., 2012. Punctuated anorogenic magmatism. Lithos 152, 132–140.

Matzel, J.E.P., Bowring, S.A., Miller, R.B., 2006. Time scales of pluton construction at differing crustal levels: Examples from the Mount Stuart and Tenpeak intrusions, North Cascades, Washington. Bull. Geol. Soc. Am. 118, 1412–1430.

McBirney, A.R., Taylor, H.P., and Armstrong, R.L., 1987, Paricutin re-examined: A classic example of crustal assimilation in calc-alkaline magma: Contributions to Mineralogy and Petrology, v. 95, p. 4–20,

McCulloch M.T., Kyser T.K., Woodhead J.D., Kinsley L., 1994. Pb−Sr−Nd−O isotopic constraints on the origin of rhyolites from the Taupo Volcanic Zone of New Zealand: evidence for assimilation followed by fractionation from basalt. Contributions to mineralogy and Petrology. V 155, p 303-312.

Memeti, V., Paterson, S., Matzel, J., Mundil, R., Okaya, D., 2010. Magmatic lobes as “snapshots” of magma chamber growth and evolution in large, composite batholiths: An example from the Tuolumne intrusion, Sierra Nevada, California. Geol. Soc. Am. Bull. 122, 1912–1931.

Menand, T., Annen, C., Blanquat, M. de Saint, 2015. Rates of magma transfer in the crust: Insights into magma reservoir recharge and pluton growth. Geology 43, 199–202.

Miller, C.F., Hatcher, R.D., Ayers, J.C., Coath, C.D., Harrison, T.M., 2000. Age and zircon inheritance of eastern blue ridge plutons, southwestern North Carolina and northeastern Georgia, with implications for magma history and evolution of the southern appalachian orogen. Am. J. Sci. 300, 142–172. https://doi.org/10.2475/ajs.300.2.142

Miller, C.F., McDowell, S.M., Mapes, R.W., 2003. Hot and cold granites: Implications of zircon saturation temperatures and preservation of inheritance. Geology 31, 529–532.

Miller, J.S., Matzel, J.E.P., Miller, C.F., Burgess, S.D., Miller, R.B., 2007. Zircon growth and recycling during the assembly of large, composite arc plutons. J. Volcanol. Geotherm. Res. 167, 282–299.

Molina, P.G., Parada, M.A., Gutiérrez, F.J., Ma, C., Li, J., Yuanyuan, L., Reich, M., Aravena, A., Gutiérrez, F.J., Ma, C., Li, J., Yuanyuan, L., Reich, M., Aravena, A., 2015. Protracted late magmatic stage of the Caleu pluton (central Chile) as a consequence of heat redistribution by diking: Insights from zircon data and thermal modeling. Lithos 227.

Molina, P.G., Parada, M.A., Ma, C., 2020. Zircon inheritance from long-lived sources of Late Triassic post-orogenic plutons, High Andes, Central Chile (~30°S): Magmatic feedbacks and petrogenetic implications. Lithos 370–371, 105662.

Morales Cámera, M.M., Dahlquist, J.A., Ramacciotti, C.D., Galindo, C., Basei, M.A.S., Zandomeni, P.S., Macchioli Grande, M., 2018. The strongly peraluminous A-type granites of the Characato suite (Achala batholith), Sierras Pampeanas, Argentina: Evidence of Devonian-Carboniferous crustal reworking. J. South Am. Earth Sci. 88, 551–567.

Morata, D.; Aguirre, L.; Oyarzún, M.; Vergara, M. 2000. Crustal contribution in the genesis of the bimodal Triassic volcanism from the Coastal Range, central Chile. Revista Geológica de Chile 27 (1): 83-98.

Moscoso, R., Mpodozis, C., 1988. Estilos Estructurales en el Norte Chico de Chile (28°-31°S), Regiones de Atacama y Coquimbo. Rev. Geológica Chile 15, 151–166.

Mpodozis, C., Kay, S., 1990. Provincias Magmáticas ácidas y evolución tectónica de Gondwana: Andes Chilenos (28-31°S).

Murillo, I., Velásquez, R., Creixell, C., 2017. Geología de las áreas Guanta-Los Cuartitos y Paso de Vacas Heladas, regiones de Atacama y Coquimbo, Servicio Nacional de Geología y Minería. In: Carta Geológica de Chile, Serie Geología Básica, vols. 192e193 map scale 1:100.000.

Nabelek PI, Whittington AG, Hofmeister AM (2010) Strain-heating as a mecha- nism for partial melting and ultrahigh temperature metamorphism in conver- gent orogens: Implications of temperature-dependent thermal diffusivity and rheology. Journal of Geophysical Research 115: B12417.

Namur, O., Humphreys, M.C.S., Holness, M.B., 2014. Crystallization of interstitial liquid and latent heat buffering in solidifying gabbros: Skaergaard intrusion, Greenland. J. Petrol. 55, 1389–1427.

Nicholls, J., Stout, M.Z., 1982. Heat effects of assimilation, crystallisation and vesiculation in magmas. Contrib. to Mineral. Petrol. 81, 328–339.

Noble, S.R., Searle, M.P., 1995. Age of crustal melting and leucogranite formation from U-Pb zircon and monazite dating in the western Himalaya, Zanskar, India. Geology 23, 1135–1138.

Oliveros, V., González, J., Espinoza Vargas, M., Vásquez, P., Rossel, P., Creixell, C., Sepúlveda, F., Bastias, F., 2018. The Early Stages of the Magmatic Arc in the Southern Central Andes 165–190.

Ortiz, M., Merino, R., 2015. Geología de las áreas Río Chollay - Matancilla y Cajón del Encierro. Regiones de Atacama y Coquimbo, Servicio Nacional de Geología y Minería. In: Carta Geológica de Chile, Serie Geología Básica, pp. 175e176 map scale 1:100.000.

Parada, M.A., 1981. Lower Triassic alkaline granites of Central Chile (30???S) in the high-Andean Cordillera. Geologische Rundschau 70, 1043–1053.

Parada, M.A., 1883. Crystallization conditions of epizonal leucogranite plutons in the light of compositional zoning of plagioclase, high andes (30o S), Chile. Revista Geológica de Chile 43–54.

Parada, M.A., 1984. La asociacion de granitos subsolvus e hipersolvus del pluton Monte Grande (chile 30 0 s) y el desarrollo de sus pertitas. Revista Geologica de Chile 23, 69–77.

Parada, M.A. 1988. Pre-Andean peralumious and metaluminous leucogranitoid suites in the high Andes of central Chile. Journal of South American Earth Sciences 1: 211-221.

Parada, M.A., 1990. Granitoid plutonism in central Chile and its geodynamic implications; A review. GSA Special paper 104.

Paterson, S., Memeti, V., Mundil, R., Zák, J., 2016. Repeated, multiscale, magmatic erosion and recycling in an upper-crustal pluton: Implications for magma chamber dynamics and magma volume estimates. Am. Mineral. 101, 2176–2198.

Paterson, S., Tobisch, O., 1988. Using pluton ages to date regional deformations: Problems with commonly used criteria. Geology, v.16, p. 1108-1111.

Patiño Douce, A.E., Beard, J.S., 1995. Dehydration melting of biotite gneiss and quartz amphibolite from 3 to 15 kbar. J. Petrol. 36, 707–738.

Patiño Douce A.E., 1996. Effects of pressure and H20 content on the compositions of primary crustal melts. Trans- actions of the Royal Society of Edinburgh." Earth Sciences, 87, 11 21.

Patiño Douce, A.E., 1997. Generation of metaluminous A-type granites by low-pressure melting of calc-alkaline granitoids. Geology 25, 743–746.

Patiño Douce, A.E., 1999. What do experiments tell us about the relative contributions of crust and mantle to the origin of granitic magmas? Geol. Soc. London, Spec. Publ. 168, 55–75.

Patiño Douce, A.E., Johnston, A.D. 1991. Phase equilibria and melt productivity in the pelitic system: implications for the origin of peraluminous granitoids and aluminous granulites. Contributions to Mineralogy and Petrology, 107, 202-218.

Petford, N., Cruden, A., McCaffrey, K., Vigneresse, J., 2000. Granite magma formation, transport and emplacement in the Earth's crust. Nature 669–673.

Petrelli, M., El Omari, K., Spina, L., Le Guer, Y., La Spina, G., Perugini, D., 2018. Timescales of water accumulation in magmas and implications for short warning times of explosive eruptions. Nat. Commun. 9.

Puziewicz, J., Johannes, W., 1990. Experimental study of a biotite-bearing granitic system under water-saturated and water-undersaturated conditions. Contrib. to Mineral. Petrol. 104, 397–406.

R.C. Newton, T.V. Charlu, O.J. Kleppa., 1980. Thermochemistry of the high structural state plagioclases, Geochem. Cosmochim. Acta 44: 933–941.

Ratschbacher, B.C., Brenhin Keller, C., Schoene, B., Paterson, S.R., Lawford Anderson, J., Okaya, D., Putirka, K., Lippoldt, R., 2018. A new workflow to assess emplacement duration and melt residence time of compositionally diverse magmas emplaced in a sub-volcanic reservoir. J. Petrol. 59, 1787–1810.

Reid, M.R., Vazquez, J. a., Schmitt, A.K., 2010. Zircon-scale insights into the history of a Supervolcano, Bishop Tuff, Long Valley, California, with implications for the Ti-in-zircon geothermometer. Contrib. to Mineral. Petrol. 161, 293–311.

René, M., Holtz, F., Luo, C., Beermann, O., Stelling, J., 2008. Biotite stability in peraluminous granitic melts: Compositional dependence and application to the generation of two-mica granites in the South Bohemian batholith (Bohemian Massif, Czech Republic). Lithos 102, 538–553.

Richet, P., Hovis, G., Whittington, A., 2006. Water and magmas: Thermal effects of exsolution. Earth Planet. Sci. Lett. 241, 972–977.

Rocha, B.C., Moraes, R., Möller A., Cioffi, C.R., Jercinovic, M.J., 2016. Timing of anatexis and melt crystallization in the Socorro–Guaxupé Nappe, SE Brazil: Insights from trace element composition of zircon, monazite and garnet coupled to U—Pb geochronology. Lithos 277, pp. 337-355.

Rocha-Campos, A.C., Basei, M.A., Nutman, A.P., Kleiman, L.E., Varela, R., Llambias, E., Canile, F.M., da Rosa, O. de C.R., 2011. 30million years of Permian volcanism recorded in the Choiyoi igneous province (W Argentina) and their source for younger ash fall deposits in the Paraná Basin: SHRIMP U-Pb zircon geochronology evidence. Gondwana Res. 19, 509–523.

Rodríguez, N., Díaz-Alvarado, J., Fernández, C., Fuentes, P., Breitkreuz, C., Tassinari, C.C.G., 2019. The significance of U–Pb zircon ages in zoned plutons: the case of the Flamenco pluton, Coastal Range batholith, northern Chile. Geosci. Front. 10, 1073–1099.

Rogers, J.J.W., Greenberg, J.K., 1990. Late-Orogenic, Post-Orogenic, and Anorogenic Granites: Distinction by Major-Element and Trace-Element Chemistry and Possible Origins. J. Geol. 98, 291–309.

Rossel, P., Oliveros, V., Ducea, M.N., Charrier, R., Scaillet, S., Retamal, L., Figueroa, O., 2013. The Early Andean subduction system as an analog to island arcs: Evidence from across-arc geochemical variations in northern Chile. Lithos 179, 211–230.

Rossi, J.N., Toselli, A.J., Saavedra, J., Sial, A.N., Pellitero, E., Ferreira, V.P., 2002. Common Crustal Source for Contrasting Peraluminous Facies in the Early Paleozoic Capillitas Batholith, NW Argentina. Gondwana Res. 5, 325–337.

Rudnick, R.L., Gao, S., 2003. 3.01 - Composition of the Continental Crust. Treatise on Geochemistry 1, 1–64.

Rushmer, T., 1992. The chemical and rheological changes in amphibolite during partial melting: Experimental results between 8 and 18 kbar. Terra Abstracts, Abstract supplement to Terra Nova, 4: 40.

Salazar, E., Coloma, F., Creixell, C., 2013. Geología del área El Tránsito - lagunillas, Región de Atacama, Servicio Nacional de Geología y Minería. In: Carta Geológica de Chile, Serie Geología Básica, vol 149 map scale 1:100.000.

Sandeman, H.A., Clark, A.H., 2003. Glass-rich, Cordierite–Biotite Rhyodacite, Valle Ninahuisa, Puno, SE Peru: Petrological Evidence for Hybridization of 'Lachlan S-type' and Potassic Mafic Magmas. J. Petrol. 44, 355–385.

Sawyer, E.W., 1994. Melt segregation in the continental crust. Geology 22, 1019–1022.

Sawyer, E.W., Cesare, B., and Brown, M., 2011, When the continental crust melts: Elements, v. 7, p. 229–234.

Scaillet, B., Holtz, F., Pichavant, M., 2016. Experimental constraints on the formation of silicic. Elements 12, 109–114.

Scaillet, B., Pichavant, M., 2003. Experimental constraints on volatile abundances in arc magmas and their implications for degassing processes. In: Oppenheimer, C., Pyle, D.M., Barclay, J. (Eds.), Volcanic Degassing: Special Publications. Geological Society, London, pp. 23–52.

Schmidt, M.W., Bucholz, C.E., Sambuu, O., Eddy, M.P., Jagoutz, O., Bowring, S.A., 2016. Constraining the time scales of magmatic differentiation with U-Pb zircon geochronology. Geology 45, 11–14.

Schoene, B., Schaltegger, U., Brack, P., Latkoczy, C., Stracke, A., Günther, D., 2012. Rates of magma differentiation and emplacement in a ballooning pluton recorded by U-Pb TIMS-TEA, Adamello batholith, Italy. Earth Planet. Sci. Lett. 355–356, 162–173.

Schorn, S., Diener, J.F.A., Powell, R., Stüwe, K., 2016. Thermal buffering in the orogenic crust. 46, 1–8.

Scott, J.M., Palin, J.M., Cooper, A.F., Sagar, M.W., Allibone, A.H., Tulloch, A.J., 2011. From richer to poorer: Zircon inheritance in Pomona Island Granite, New Zealand. Contrib. to Mineral. Petrol. 161, 667–681.

Scott, J.M., Palin, J.M., Cooper, A.F., Sagar, M.W., Allibone, A.H., Tulloch, A.J., 2011. From richer to poorer: Zircon inheritance in Pomona Island Granite, New Zealand. Contrib. to Mineral. Petrol. 161, 667–681.

Siégel, C., Bryan, S.E., Allen, C.M., Gust, D.A., 2017. Use and abuse of zircon-based thermometers: A critical review and a recommended approach to identify antecrystic zircons. Earth-Science Rev. 176, 87–116.

Siegel, K., Williams-Jones, A.E., van Hinsberg, V.J., 2017. The amphiboles of the REE-rich A-type peralkaline Strange Lake pluton – fingerprints of magma evolution. Lithos 288–289, 156–174.

Simakin A., Talbot C., 2001. Tectonic pumping of pervasive granitic melts. Tectonophysics 332, 387-402.

Skjerlie, K.P., Johnston, A.D., 1993. Fluid-absent melting behavior of an F-rich tonalitic gneiss at mid-crustal pressures: Implications for the generation of anorogenic granites. J. Petrol. 34, 785–815.

Spalletti, L.A., Limarino, C.O., 2017. The Choiyoi magmatism in south western Gondwana: implications for the end-permian mass extinction - a review. Andean Geol. 44, 328.

Sparks R.S.J., Huppert.E., H., Turner, J.S, 1984. The fluid dynamics of evolving magma chambers. Phil. Trans. R. Soc. London. 310, p. 511-534.

Spell, T.L., Kyle, P.R., Thirlwall, M.F., and Campbell, A., 1993, Isotopic and geochemical constraints on the origin and evolution of postcollapse rhyolites in the Valles Caldera, New Mexico: J. Geophys. Res., v. 98, p. 19,723-19,739.

Spera, F.J., Bohrson, W.A., 2001. Energy-Constrained Open-System Magmatic Processes I: General Model and Energy-Constrained Assimilation and Fractional Crystallization (EC-AFC) Formulation. J. Petrol. 42, 999–1018.

T.J.B. Holland, R. Powell., 1998. An internally consistent thermodynamic data set for phases of petrological interest, J. Meta- morph. Geol. 16: 309–343.

Thompson A.B. 1999. Some time-space relationships for crustal melting and granitic intrusion at various depths. In Understanding Granites: Integrating New and Classical Techniques. Castro A., Fernández C., and Vigneresse J.L. eds. Geological Society Special Publication No. 168.

Thompson, A.B.A.B., Connolly, J.A.D.D., 1995. Melting of the continental crust: Some thermal and petrological constraints on anatexis in continental collision zones and other tectonic settings. J. Geophys. Res. Solid Earth 100, 15565–15579. https://doi.org/10.1029/95JB00191

Trail, D., Bruce Watson, E., Tailby, N.D., 2012. Ce and Eu anomalies in zircon as proxies for the oxidation state of magmas. Geochim. Cosmochim. Acta 97, 70–87.

Trail, D., Watson, E.B., Tailby, N.D., 2011. The oxidation state of Hadean magmas and implications for early Earth's atmosphere. Nature 480, 79–82.

Turner, S.P., Foden, J.D., Morrison, R.S., 1992. Derivation of some A-type magmas by fractionation of basaltic magma: An example from the Padthaway Ridge, South Australia. Lithos 28, 151–179.

Ussler, W., Glazner, A.F., 1992. Graphical analysis of enthalpy-composition relationships in mixed magmas. J. Volcanol. Geotherm. Res. 51, 23–40.

Vásquez, P., Franz, G., 2008. The Triassic Cobquecura Pluton (Central Chile): An example of a fayalite-bearing A-type intrusive massif at a continental margin. Tectonophysics 459, 66–84.

Vásquez, P., Glodny, J., Franz, G., Frei, D., Romer, R.L., 2011. Early Mesozoic Plutonism of the Cordillera de la Costa (34°–37°S), Chile: Constraints on the Onset of the Andean Orogeny. The Journal of Geology 119, 159–184.

Vielzeuf, D., Clemens J.D., Pin C., Moinet E., 1990.Granites, granulites, and crustal differentiation. In Granulites Crustal Evolution.

Vilà M, Fernández M, Jiménez-Munt I (2010) Radiogenic heat production vari- ability of some common lithological groups and its signifi cance to litho- spheric thermal modeling. Tectonophysics 490: 152-164

Villaseca, C., Barbero, L., Rogers, G., 1998. Crustal origin of Hercynian peraluminous granitic batholiths of central Spain: petrological, geochemical and isotopic (Sr, Nd) constraints. Lithos 43, 55–79.

Villaseca, C., Orejana, D., Paterson, B.A., 2007. Zr-LREE rich minerals in residual peraluminous granulites, another factor in the origin of low Zr-LREE granitic melts? Lithos 96, 375–386.

Wang, X., Griffin, W.L., Chen, J., 2010. Hf contents and Zr/Hf ratios in granitic zircons. Geochemical

Wark, D.A., Miller, C.F., 1993. Accessory mineral behavior during differentiation of a granite suite: monazite, xenotime and zircon in the Sweetwater Wash pluton, southeastern California, U.S.A. Chem. Geol. 110, 49–67.

Waters, L.E., Lange, R.A., 2017. Why aplites freeze and rhyolites erupt: Controls on the accumulation and eruption of high-SiO 2 (eutectic) melts. Geology 45, 1019–1022.

Watson, E.B., 1996. Dissolution, growth and survival of zircons during crustal fusion: kinetic principals, geological models and implications for isotopic inheritance. Trans. R. Soc. Edinb. Earth Sci. 87, 43–56.

Watson, E.B., Harrison, T.M., 1983. Zircon saturation revisited: temperature and composi- tion effects in a variety of crustal magma types. Earth and Planetary Science Letters 64, 295–304.

Watson, E.B., Wark, D.A., Thomas, J.B., 2006. Crystallization thermometers for zircon and rutile. Contrib. to Mineral. Petrol. 151, 413–433.

Weinberg, R.F., and Regenauer-Lieb, K., 2010, Ductile fractures and magma migration from source: Geology, v. 38, p. 363–366.

Weinberg, R.F., Hasalová, P., 2015. Water-fluxed melting of the continental crust: A review. Lithos 212–215, 158–188.

Whalen, J.B., Currie, K.L., Chappell, B.W., 1987. A-type granites: geochemical characteristics, discrimination and petrogenesis. Contrib. to Mineral. Petrol. 95, 407–419.

Whitney, J.A., 1988. The origin of granite: The role and source of water in the evolution of granitic magmas. Geol. Soc. Am. Bull. 100, 1886–1897.

Whittington, A.G., Hofmeister, A.M., Nabelek, P.I., 2009. Temperature-dependent thermal diffusivity of the Earth's crust and implications for magmatism. Nature 458, 319–321.

Wiedenbeck, M., Allé, P., Corfu, F., Griffin, W.L., Meier, M., Oberli, F., Quadt, A.V., Roddick, J.C., Spiegel, W., 1995. Three natural zircon standards for U–Th–Pb, Lu–Hf, trace element and REE analyses. Geostand. Newslett. 19 (1), 1–23.

Williams, I.S., 1992. Some observations on the use of zircon U-Pb geochronology in the study of granitic rocks. Trans. R. Soc. Edinb. Earth Sci. 83, 447–458.

Windley, B.F., 1993. Proterozoic anorogenic magmatism and its orogenic connections: Fermor Lecture 1991. J. Geol. Soc. London. 150, 39–50.

Wolak, J., Blevins, M., Krueger, R.J., Martin, D.M., Zimmerman, N., and Yoshinobu, A.S., 2004, Field constraints on magma, host rock, and xenolith rheology during pluton emplacement: Geological Society of America Abstracts with Programs, v. 36, no. 4, p. 70.

Wolak, J., Yoshinobu, A.S., and Barnes, C.G., 2005, Xenoliths, foliations and folds in a big tank fi lled by many small increments: Geological Society of America Abstracts with Programs, v. 37, no. 4, p. 71.

Wolf M., Wyllie P., 1991. Dehydration-melting of solid amphibolite at 10 kbar: Textural development, liquid interconnectivity and applications to the segregation of magmas. Mineralogy and Petrology. 44, 151-179.

Wu, F. yuan, Sun, D. you, Li, H., Jahn, B. Ming, Wilde, S., 2002. A-type granites in northeastern China: Age and geochemical constraints on their petrogenesis. Chem. Geol. 187, 143–173.

Xing, G.F., Wang, X.L., Wan, Y., Chen, Z.H., Jiang, Y., Kitajima, K., Ushikubo, T., Gopon, P., 2014. Diversity in early crustal evolution: 4100 Ma zircons in the Cathaysia Block of southern China. Sci. Rep. 4, 1–8.

Zentilli, M., Maksaev, V., Boric, R., Wilson, J., 2018. Spatial coincidence and similar geochemistry of Late Triassic and Eocene–Oligocene magmatism in the Andes of northern Chile: evidence from the MMH porphyry type Cu–Mo deposit, Chuquicamata District. Int. J. Earth Sci. 107, 1097–1126.

Zhao, K.D., Jiang, S.Y., Chen, W.F., Chen, P.R., Ling, H.F., 2013. Zircon U-Pb chronology and elemental and Sr-Nd-Hf isotope geochemistry of two Triassic A-type granites in South China: Implication for petrogenesis and Indosinian transtensional tectonism. Lithos 160–161, 292–306.

Zou, X., Qin, K., Han, X., Li, G., Evans, N.J., Li, Z., Yang, W., 2019. Insight into zircon REE oxy-barometers: A lattice strain model perspective. Earth Planet. Sci. Lett. 506, 87–96.

ANNEXES

A. Models of isochemical pseudosections in the KCFMASH system at a 600ºC temperature

Lower Crust

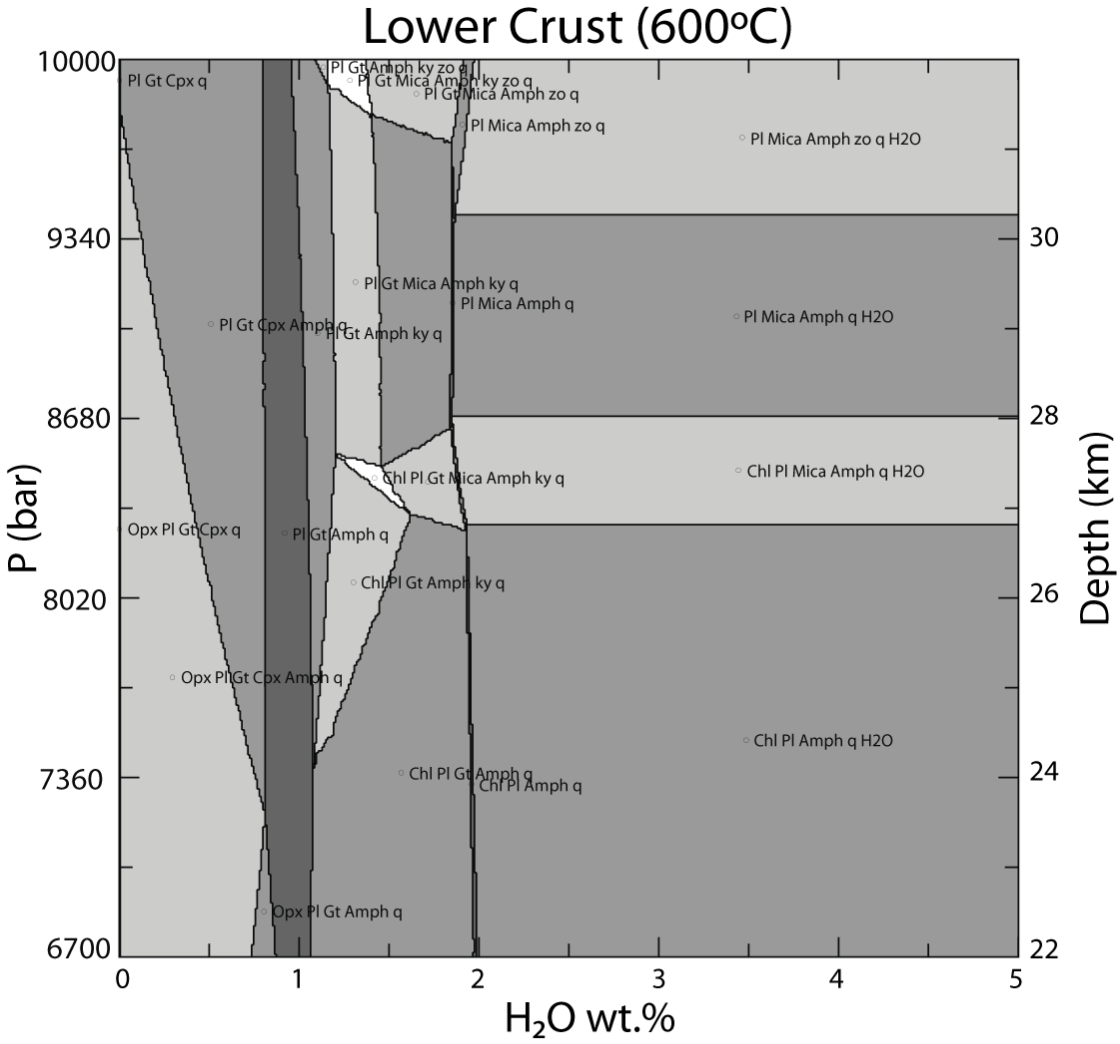

Middle Crust

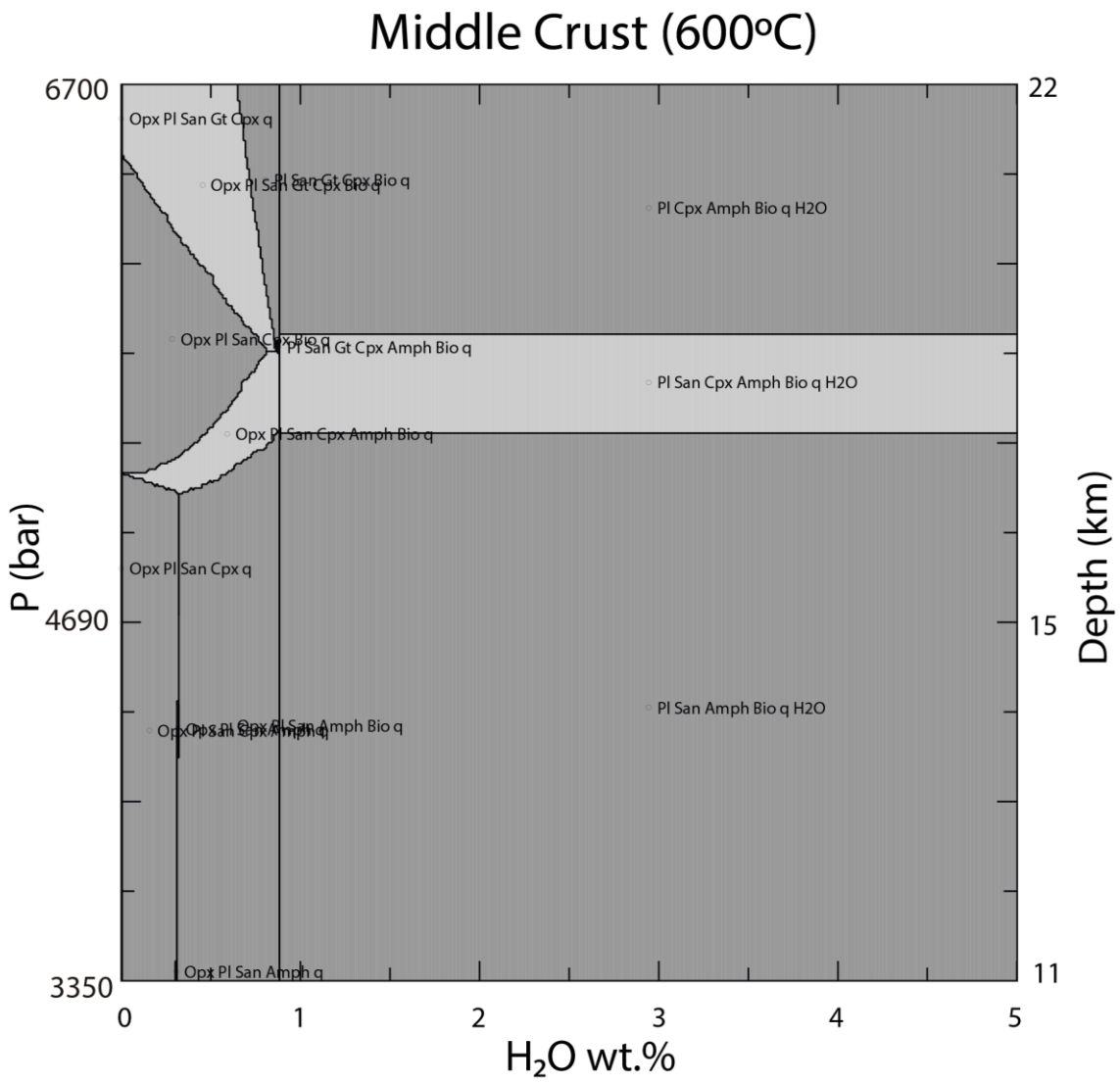

Upper Crust

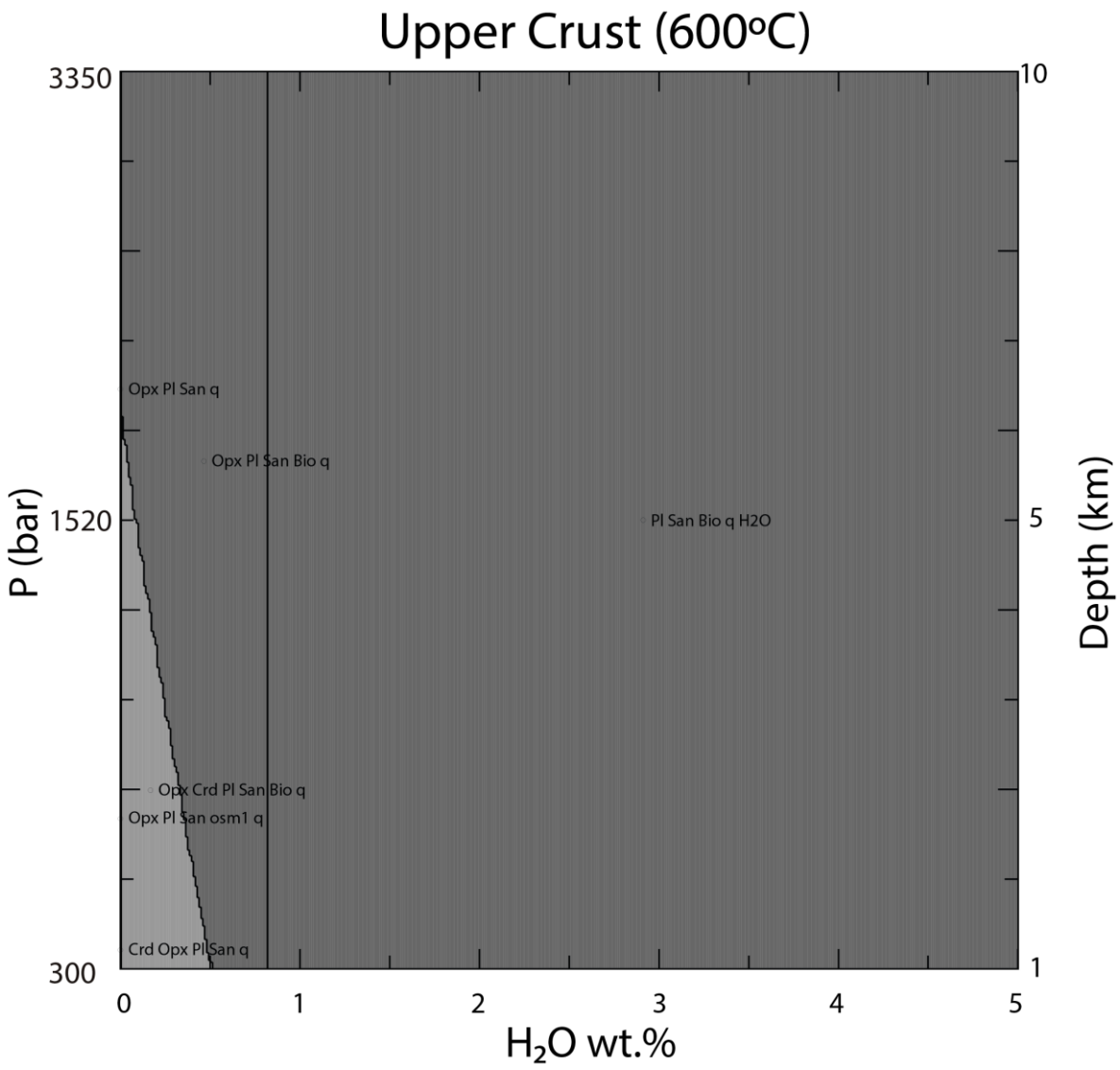
Upper Crust (600ºC)
3350
1520
300
P (bar)
10
5
1
Depth (km)
Opx Pl San q
Opx Pl San Bio q
Pl San Bio q H2O
Opx Crd Pl San Bio q
Opx Pl San osm1 q
Crd Opx Pl San q
0
1
2
3
4
5
H2O wt.%

B. Melt fraction of crustal magmas

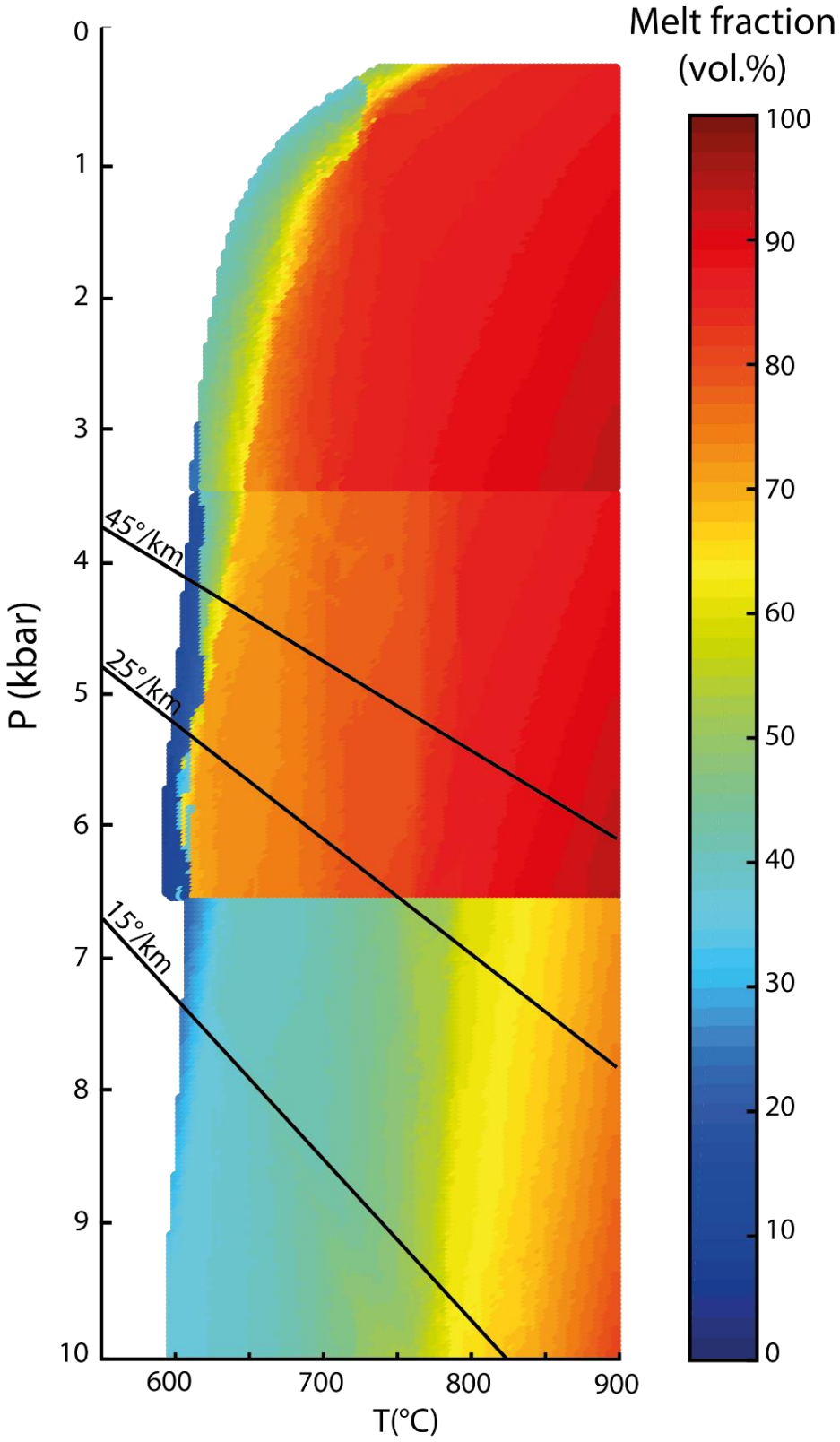

C. Modeled composition of anatectic melts

Upper Crust

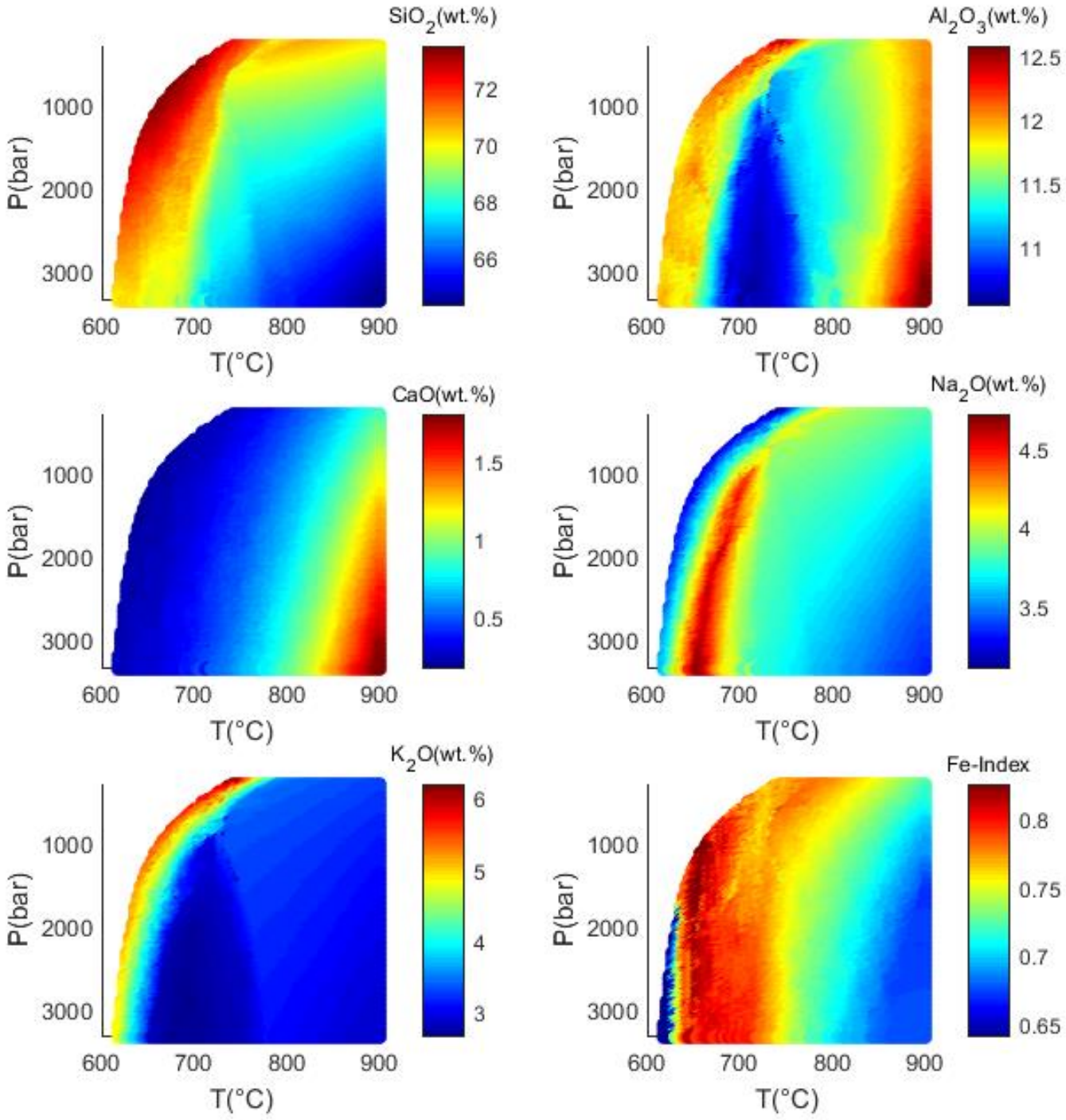

Middle Crust

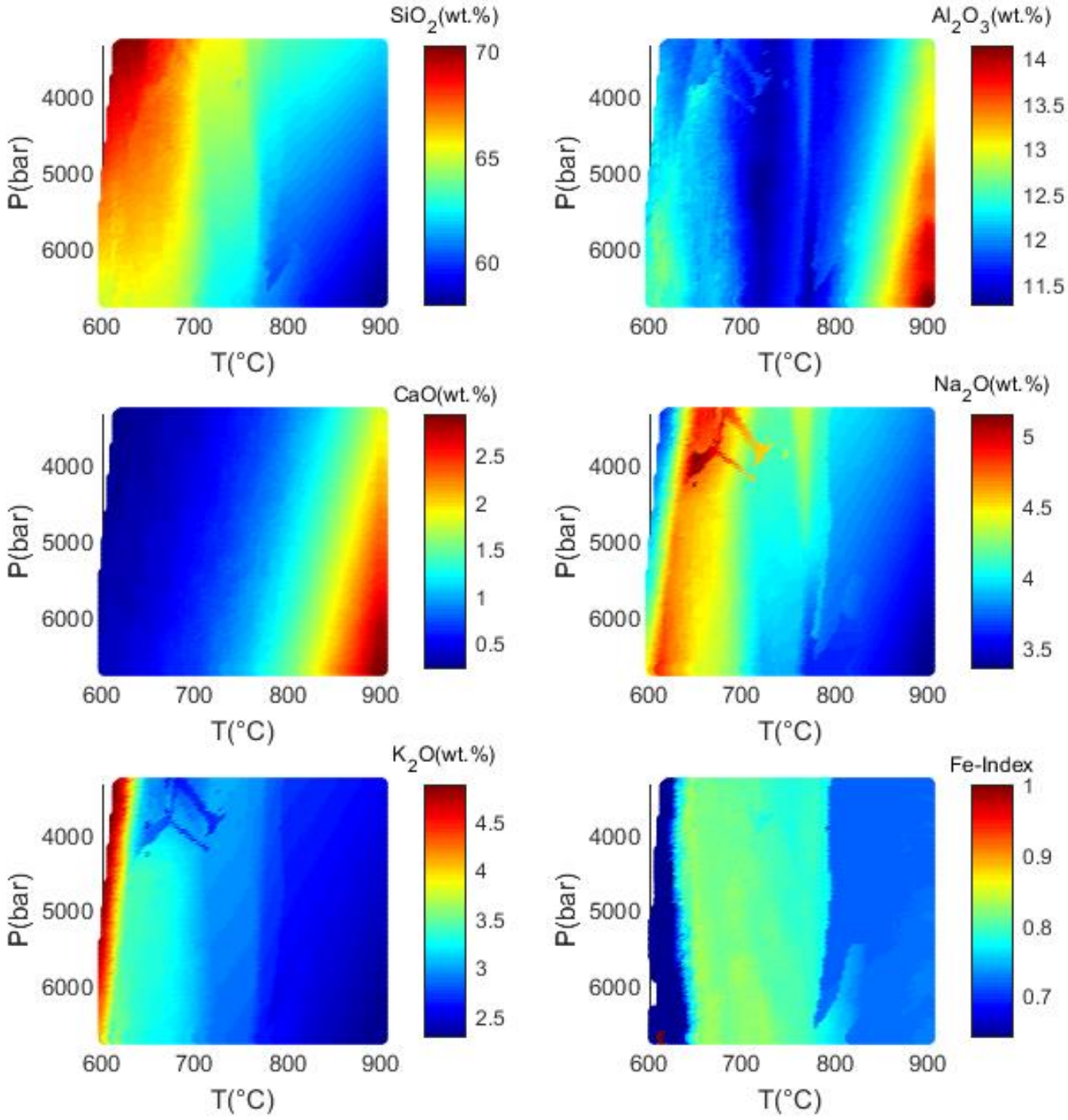

Lower Crust

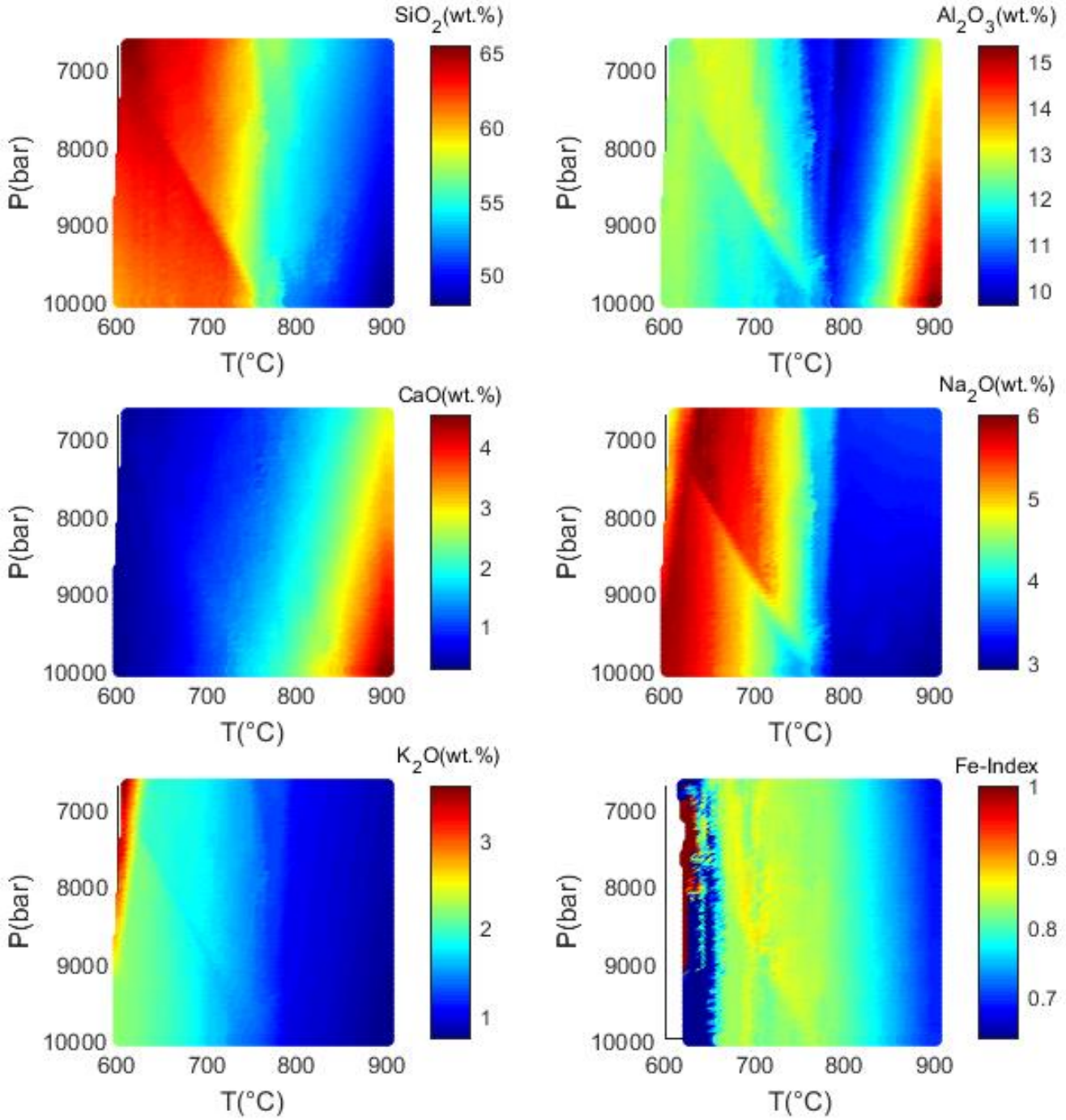
SiO2(wt.%)
65
60
55
50
Al2O3(wt.%)
15
14
13
12
11
10
CaO(wt.%)
4
3
2
1
Na2O(wt.%)
6
5
4
3
K2O(wt.%)
3
2
1
Fe-Index
1
0.9
0.8
0.7
P(bar)
7000
8000
9000
10000
T(°C)
600
700
800
900

D. Modeled ASI vs AI indexes

Pressure-sensitive models: Upper Crust

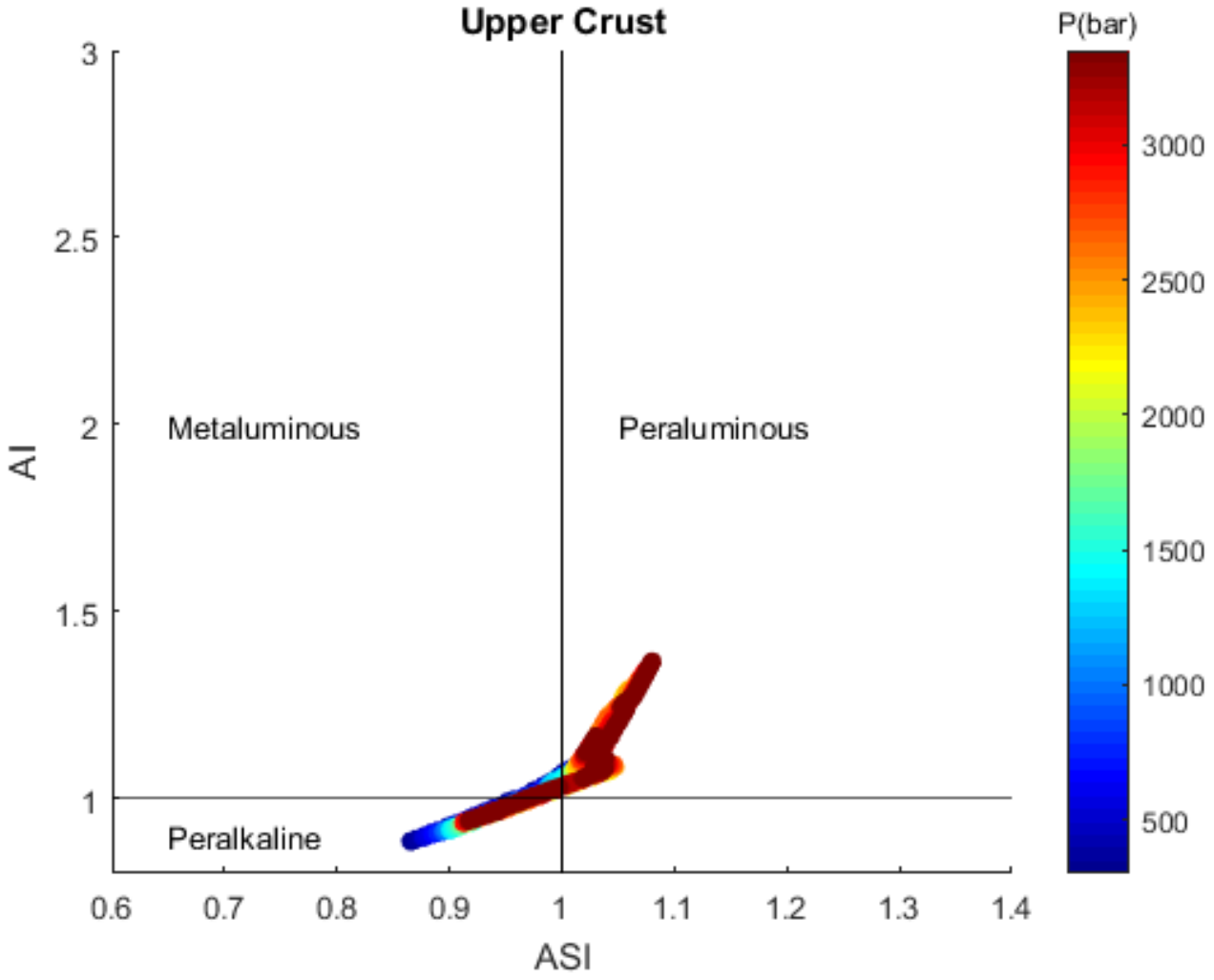

Pressure-sensitive models: Middle Crust

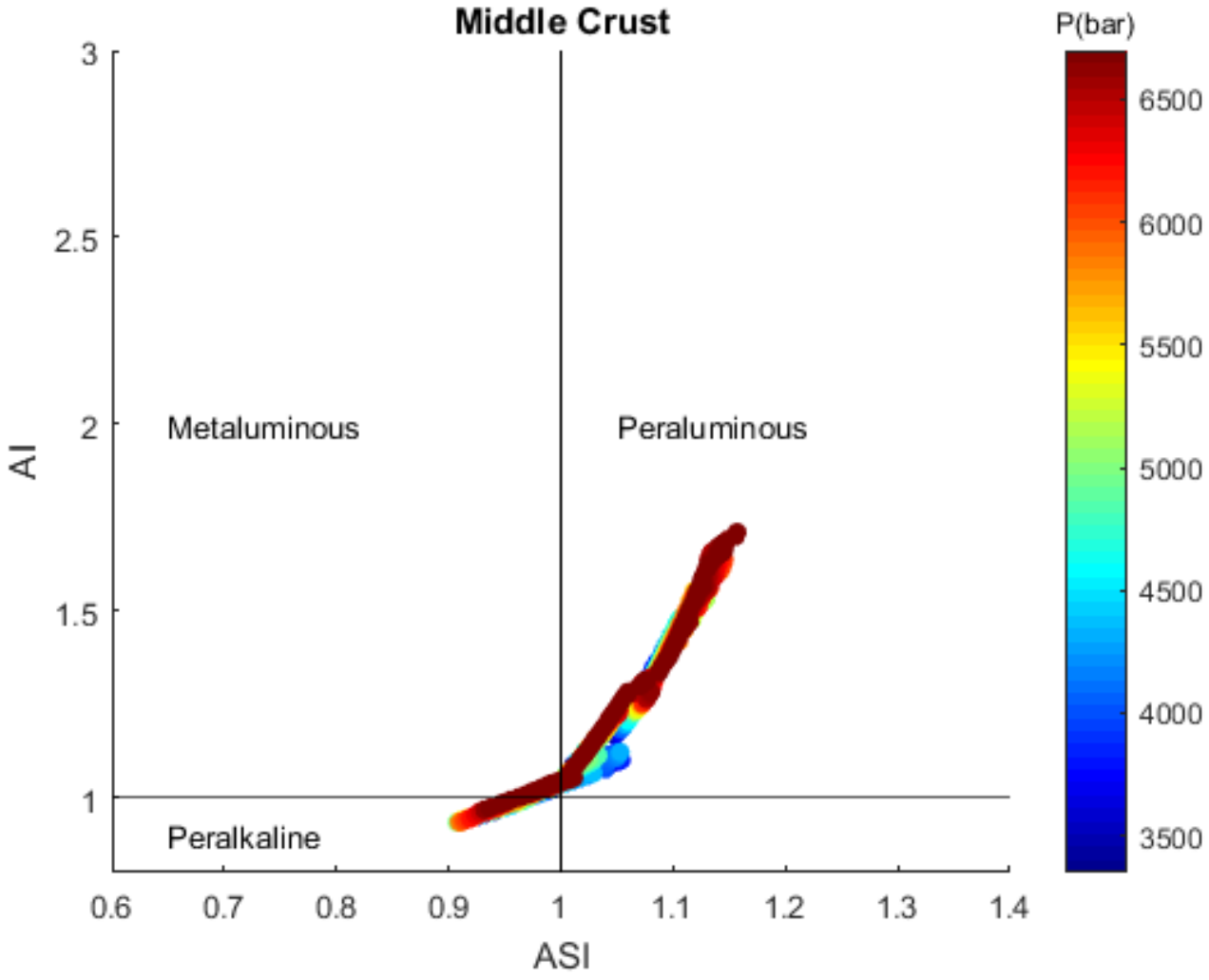

Pressure-sensitive models: Lower Crust

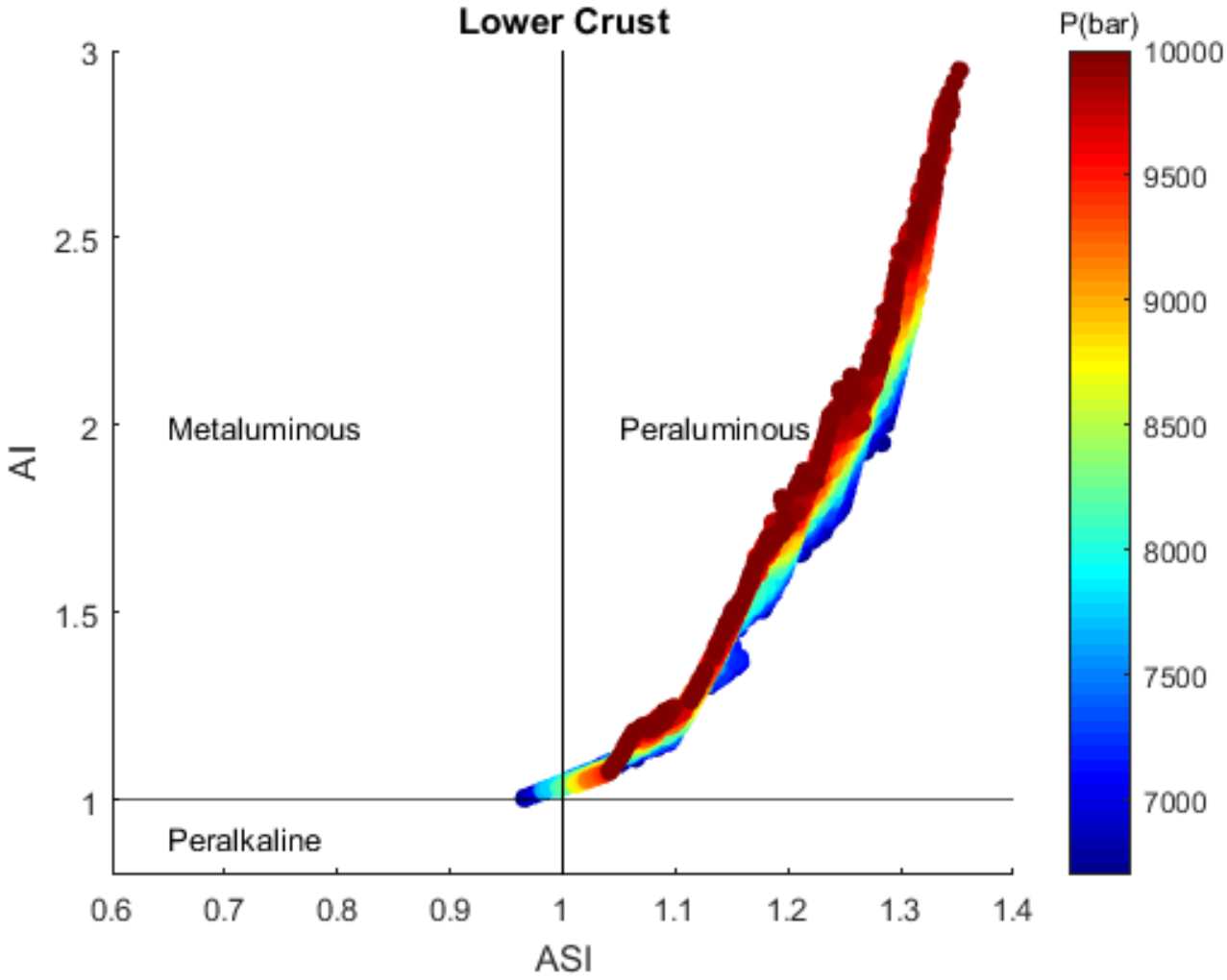

Temperature-sensitive models: Upper Crust

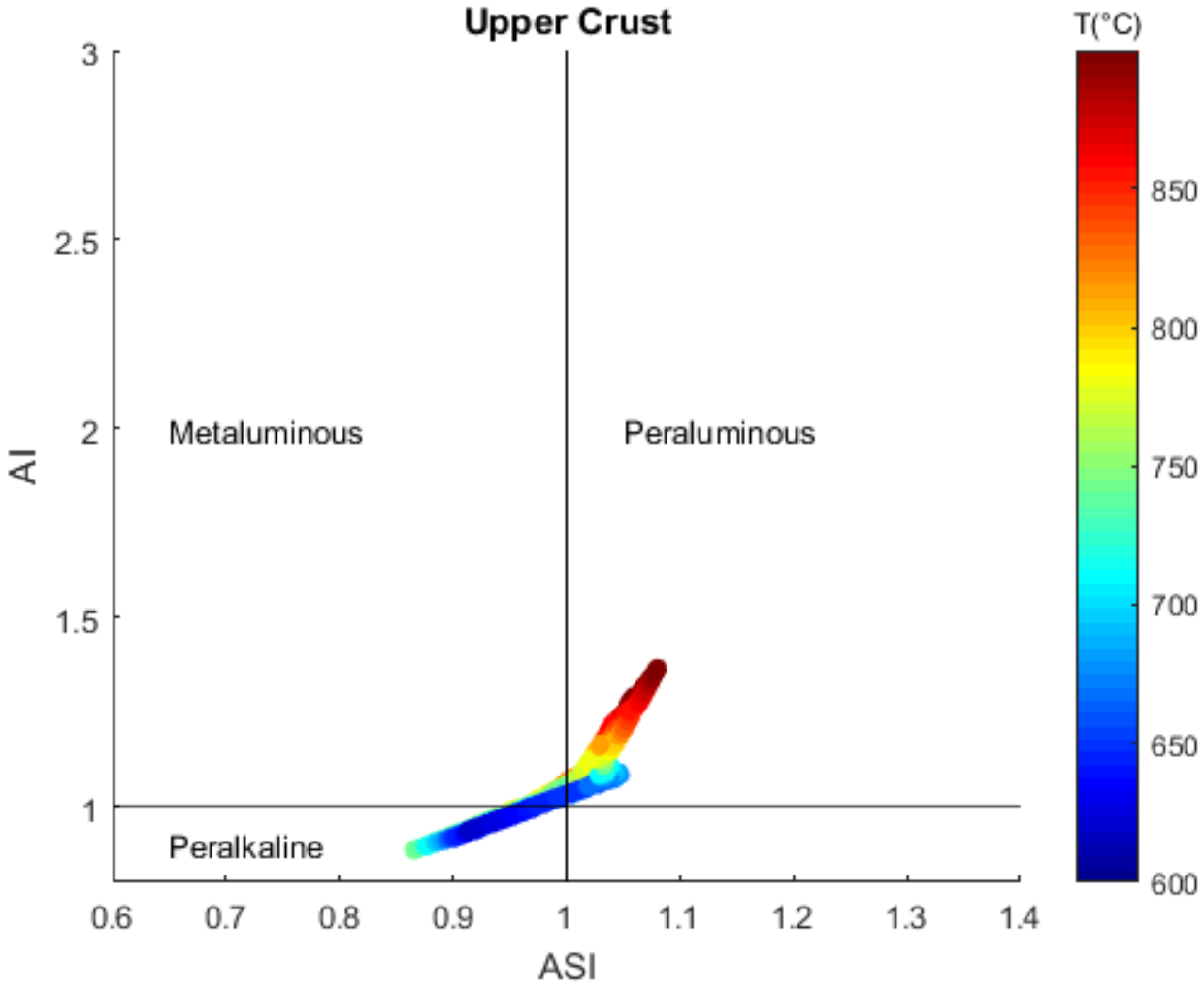

Temperature-sensitive models: Middle Crust

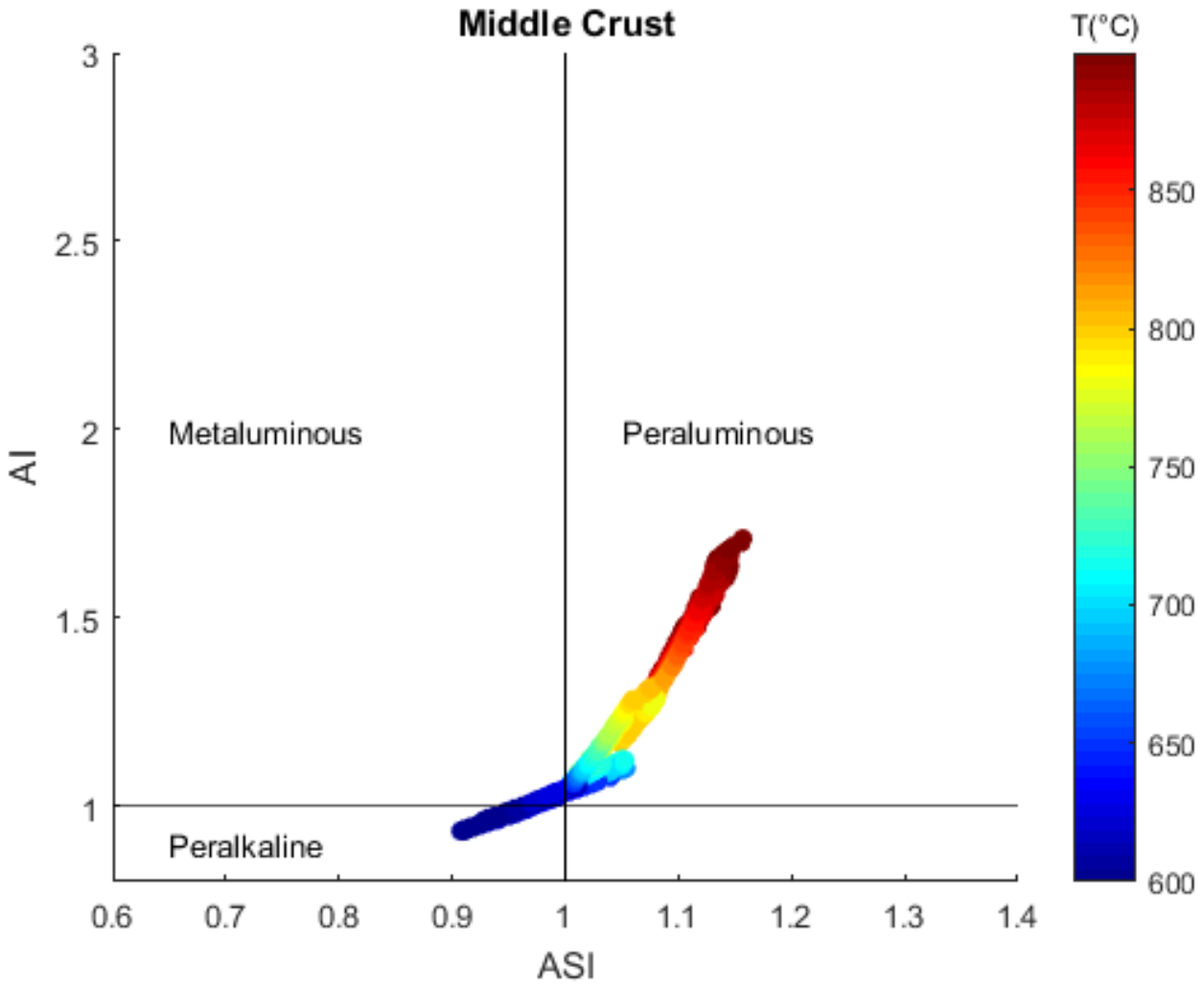

Temperature-sensitive models: Lower Crust

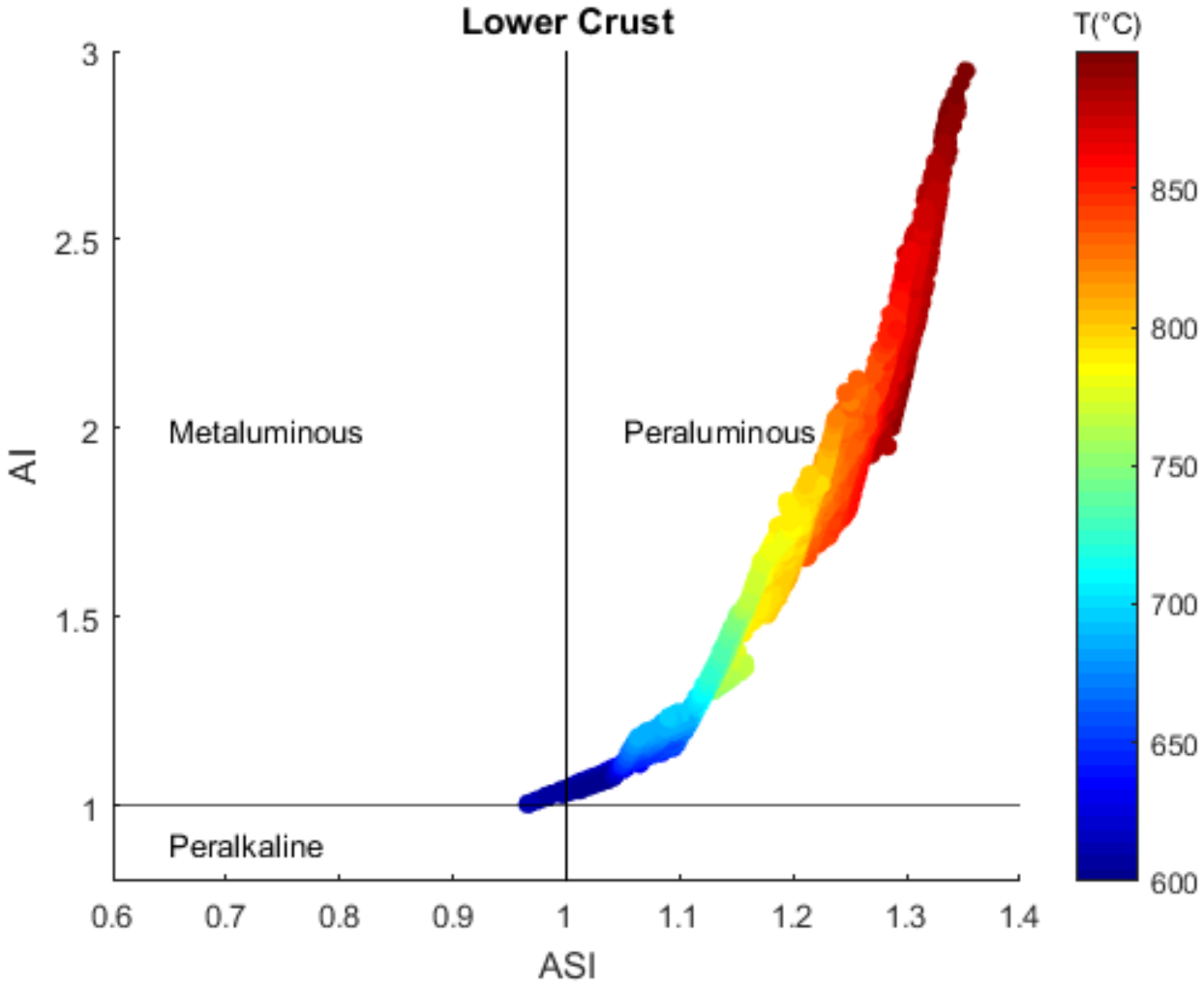

E. Whole-rock geochemistry

Samples UTM Coordinates (WGS84)

Sample	E	N	Altitude (masl.)	Unit	Lithology
PTPM02	369161	6695060	1277	Los Tilos pluton	Granite
PTPM03	370285	6694417	1324	Elqui Dike Swarm	Mafic dike
PTPM04	370285	6694417	1324	Colorado Sienogranites	Sienogranite dike
PTPM05	370462	6694336	1318	Colorado Sienogranites	Sienogranite dike
PTPM06	370550	6694172	1313	Elqui Dike Swarm	Mafic dike
PTPM07A	361238	6666739	1356	Monte Grande pluton	Leucogranite
PTPM07B	361438	6666548	1365	Monte Grande pluton	Leucogranite
PTPM09	364984	6664500	1560	Elqui Dike Swarm	Mafic dike
PTPM2-01	355339	6676252	1411	Colorado Sienogranites	Sienogranite dike
PTPM2-02	355374	6676317	1427	Elqui Dike Swarm	Mafic dike
PTPM2-03	352816	6690866	961	Colorado Sienogranites	Sienogranite dike
PTPM2-04A	369406	6694731	1286	Los Tilos pluton	Crd nodule
PTPM2-04B	369406	6694731	1286	Los Tilos pluton	Crd nodule
PTPM2-04C	369406	6694731	1286	Los Tilos pluton	Crd nodule
PTPM2-04D	369406	6694731	1286	Los Tilos pluton	Crd nodule
PTPM2-04E	369406	6694731	1286	Los Tilos pluton	Crd nodule
PTPM2-05	370461	6694335	1308	Los Tilos pluton	Granite
PTPM2-06	390345	6684712	1998	Elqui Dike Swarm	Mafic dike
PTPM2-07	390323	6684732	2012	Colorado Sienogranites	Sienogranite dike
PTPM2-08	390323	6684732	2012	Elqui Dike Swarm	Mafic dike
PTPM2-09	390185	6684861	1967	Colorado Sienogranites	Sienogranite dike
PTPM2-10	389546	6684847	1973	Colorado Sienogranites	Coarse sienogranite
PTPM2-11	388100	6684928	1910	Piuquenes granite (ChPC)	Biotite granite
PTPM2-12	388100	6684928	1910	Elqui Dike Swarm	Mafic dike
HA-10	365465	6697365	1314	Elqui Dike Swarm	Mafic dike
HA-01	356462	6673443	1047	Monte Grande pluton	Leucogranite
HA-15	369128	6695084	1248	Los Tilos	Granite
HA-04	360976	6666841	1108	Monte Grande pluton	Leucogranite
HA-02	356462	6673443	1047	Elqui Dike Swarm	Mafic dike
HA-06	363727	6665122	1487	Elqui Dike Swarm	Mafic dike
HA-11	365465	6697365	1314	Elqui Dike Swarm	Mafic dike
HA-14	368326	6696142	1246	Elqui Dike Swarm	Mafic dike

Major elements

Sample	Unit	Lithology		SiO2	TiO2	Al2O3	Fe2O3	FeO	FeOt (calc)	MgO	CaO	MnO	Na2O	K2O	P2O5	H2O+	H2O-	LOI	Total
			Units	**wt.%**	**wt.%**	**wt.%**	**wt.%**	**wt.%**	**wt.%**	**wt.%**	**wt.%**	**wt.%**	**wt.%**	**wt.%**	**wt.%**	**wt.%**	**wt.%**	**wt.%**	**wt.%**
			Detection limit	**0.01**	**0.001**	**0.01**	**0.01**	**0.1**		**0.01**	**0.01**	**0.001**	**0.01**	**0.01**	**0.01**	**0.1**	**0.1**		
			Analysis method	**FUS-ICP**	**FUS-ICP**	**FUS-ICP**	**FUS-ICP**	**TITR**		**FUS-ICP**	**FUS-ICP**	**FUS-ICP**	**FUS-ICP**	**FUS-ICP**	**FUS-ICP**	**H2O+**	**GRAV**	**FUS-ICP**	
PTPM02	Los Tilos pluton	Granite		74.25	0.149	12.86	1.06	0.9	1.85	0.34	1.15	0.035	3.91	3.26	0.05	0.4	0.2	0.71	98.674
PTPM03	Elqui Dike Swarm	Mafic dike		53.37	0.846	17.1	2.54	4.2	6.49	4.58	4.9	0.116	4.26	2.21	0.2			5.2	99.522
PTPM04	Colorado Sienogranites	Sienogranite dike		67.55	0.418	14.62	1	2.4	3.30	1.62	3.45	0.227	5.14	1.32	0.1				97.845
PTPM05	Colorado Sienogranites	Sienogranite dike		72.34	0.224	13.53	0.9	1.3	2.11	0.56	1.42	0.056	3.89	3.24	0.05			2.23	99.74
PTPM06	Elqui Dike Swarm	Mafic dike		62.07	0.561	17.12	0.83	3.2	3.95	2.5	3.91	0.181	4.26	1.56	0.1			3.45	99.742
PTPM07A	Monte Grande pluton	Leucogranite		75.68	0.148	11.85	1.28	1.3	2.45	0.04	0.39	0.038	3.65	4.82	< 0.01	0.2	0.1	0.21	99.406
PTPM07B	Monte Grande pluton	Leucogranite		75.88	0.12	11.56	1.01	1	1.91	0.03	0.35	0.029	3.52	4.73	< 0.01	0.1	0.1	0.25	98.479
PTPM09	Elqui Dike Swarm	Mafic dike		49.8	1.621	16.78	2.7	5.8	8.23	6.62	9.03	0.139	3.11	0.98	0.28			2.51	99.37
PTPM2-01	Colorado Sienogranites	Sienogranite dike		71.08	0.385	13.16	0.69	1.2	1.82	0.13	2.41	0.028	3.83	3.58	0.09	0.8	0.2	2.82	99.403
PTPM2-02	Elqui Dike Swarm	Mafic dike		45.9	2.064	15.52	3.66	6.9	10.19	6.45	7.41	0.251	3.08	1.36	0.25			6.71	99.555
PTPM2-03	Colorado Sienogranites	Sienogranite dike		70.41	0.078	11.7	0.06	2.5	2.55	0.85	3.83	0.063	3.86	2.85	< 0.01			3.26	99.461
PTPM2-04A	Los Tilos pluton	Crd nodule		69.37	0.065	14.95	1.14	3.7	4.73	1.74	0.35	0.289	0.86	3.52	0.01	2.7	0.5	3.29	99.284
PTPM2-04B	Los Tilos pluton	Crd nodule		70.57	0.093	14.77	1.12	3.6	4.61	1.49	0.47	0.272	1.26	3.12	0.02	2.4	0.4	2.88	99.665
PTPM2-04C	Los Tilos pluton	Crd nodule		68.73	0.114	14.43	1.77	4	5.59	2.1	0.46	0.284	1.03	2.97	0.02	3	0.4	3.34	99.248
PTPM2-04D	Los Tilos pluton	Crd nodule		70.04	0.108	14.67	1.33	3.8	4.00	1.71	0.44	0.307	1.28	2.94	0.01	2.4	0.4	3.12	99.755
PTPM2-04E	Los Tilos pluton	Crd nodule		71.74	0.123	14.72	0.53	4.1	4.58	1.78	0.61	0.346	1.25	2.2	0.02	1.7	0.3	2.46	99.879
PTPM2-05	Los Tilos pluton	Granite		76.21	0.073	12.6	0.89	0.3	1.1	0.13	0.56	0.02	3.75	4.49	0.03	0.1	<0,1	0.69	99.743

PTPM2-06	Elqui Dike Swarm	Mafic dike		51.37	1.714	15.65	5.72	3.3	8.45	4.11	6	0.156	4.33	1.76	0.56			4.97	99.64
PTPM2-07	Colorado Sienogranites	Sienogranite dike		73.54	0.355	13.07	0.92	0.9	1.73	0.14	0.96	0.037	4.49	3.16	0.06	0.7	0.1	1.51	99.142
PTPM2-08	Elqui Dike Swarm	Mafic dike		46.72	1.622	16.7	4.14	6.2	9.93	8.71	6.65	0.202	2.38	0.89	0.18	4	0.3	5.23	99.624
PTPM2-09	Colorado Sienogranites	Sienogranite dike		76.1	0.171	12.43	0.54	0.9	1.39	0.1	0.3	0.038	4.06	3.94	0.02	0.4	<0,1	0.71	99.309
PTPM2-10	Colorado Sienogranites	Coarse sienogranite		73.39	0.256	13.24	0.36	1.8	2.12	0.29	0.74	0.042	4.56	3.85	0.05	0.4	<0,1	1.05	99.628
PTPM2-11	Piuquenes granite (ChPC)	Biotite granite		74.23	0.212	12.95	0.52	1.3	1.77	0.41	0.87	0.054	3.67	3.89	0.06	0.3	<0,1	0.97	99.136
PTPM2-12	Elqui Dike Swarm	Mafic dike		52.7	1.134	15.32	2.63	4.5	6.87	6.08	5.34	0.142	4.16	1.67	0.18			4.61	98.466
HA-10	Elqui Dike Swarm	Mafic dike		56.30	0.76	17.30	2.77	3.32	5.81	2.73	4.72	0.08	4.01	2.87	0.56			3.73	99.15
HA-01	Monte Grande pluton	Leucogranite		76.50	0.11	11.90	0.48	0.88	1.31	0.14	0.73	0.03	4.00	4.32	0.01			0.57	99.67
HA-15	Los Tilos	Granite		75.90	0.14	12.80	0.81	0.40	1.13	0.35	1.06	0.03	3.86	3.47	0.03			0.73	99.58
HA-04	Monte Grande pluton	Leucogranite		77.30	0.15	11.50	0.74	1.04	1.71	0.07	0.41	0.03	3.43	4.52	0.01			0.41	99.608
HA-02	Elqui Dike Swarm	Mafic dike		51.50	1.50	15.20	3.43	6.84	9.93	5.77	8.13	0.14	3.13	0.38	0.21			3.46	99.69
HA-06	Elqui Dike Swarm	Mafic dike		52.30	1.80	17.10	0.20	5.52	5.67	6.62	7.20	0.18	3.57	1.44	0.40			3.32	99.65
HA-11	Elqui Dike Swarm	Mafic dike		50.80	1.70	17.10	2.80	6.44	8.96	5.29	7.71	0.20	3.74	1.85	0.30			1.78	99.71
HA-14	Elqui Dike Swarm	Mafic dike		46.83	1.37	16.00	3.03	6.28	9.01	9.38	8.96	0.18	2.40	1.04	0.27			4.11	99.85

Trace elements

Sample	Unit	Lithology		Cs	Rb	Ba	Th	U	Nb	Ta	Pb	Sr	Zr	Y	Hf	Sc	Ni	Cr	Zn	Co
			Units	**ppm**	**ppm**	**ppm**	**ppm**	**ppm**	**ppm**	**ppm**	**ppm**	**ppm**	**ppm**	**ppm**	**ppm**	**ppm**	**ppm**	**ppm**	**ppm**	**ppm**
			Detection limit	**0.5**	**2**	**2**	**0.1**	**0.1**	**1**	**0.1**	**5**	**2**	**2**	**1**	**0.2**	**1**	**20**	**20**	**30**	**1**
			Analysis method	**FUS-MS**	**FUS-MS**	**FUS-ICP**	**FUS-MS**	**FUS-MS**	**FUS-MS**	**FUS-MS**	**FUS-MS**	**FUS-ICP**	**FUS-ICP**	**FUS-ICP**	**FUS-MS**	**FUS-MS**	**FUS-MS**	**FUS-MS**	**FUS-MS**	**FUS-MS**
PTPM02	Los Tilos pluton	Granite		1.9	81	788	7.2	1.3	5	0.5	21	151	69	17	2.3	4	< 20	160	40	2
PTPM03	Elqui Dike Swarm	Mafic dike		3	47	1610	3.5	1	3	0.2	22	953	94	14	2.5	16	50	20	100	25
PTPM04	Colorado Sienogranites	Sienogranite dike		0.6	34	321	6.7	1.6	3	0.4	22	267	86	10	2.2	7	< 20	< 20	180	8
PTPM05	Colorado Sienogranites	Sienogranite dike		1.1	95	741	11.5	2.4	6	0.7	22	279	116	18	3	4	< 20	100	40	3
PTPM06	Elqui Dike Swarm	Mafic dike		4.2	63	291	1.9	0.4	3	0.2	70	473	96	9	2.4	10	< 20	50	130	12
PTPM07A	Monte Grande pluton	Leucogranite		0.7	51	456	5.9	0.9	4	0.4	13	12	317	35	6.7	3	< 20	< 20	80	< 1
PTPM07B	Monte Grande pluton	Leucogranite		0.5	51	365	5.7	0.9	4	0.4	13	11	298	27	6.4	2	< 20	120	60	< 1
PTPM09	Elqui Dike Swarm	Mafic dike		< 0.5	40	199	1.1	0.3	5	0.3	8	364	170	24	3.8	27	100	150	100	34
PTPM2-01	Colorado Sienogranites	Sienogranite dike		3	117	752	7.4	1.5	7	0.8	7	145	173	27	4.3	6	< 20	< 20	< 30	4
PTPM2-02	Elqui Dike Swarm	Mafic dike		2.1	61	373	0.4	0.1	5	0.3	78	284	179	30	4.1	33	100	160	230	43
PTPM2-03	Colorado Sienogranites	Sienogranite dike		1.3	73	170	11	2.1	15	1.2	6	68	118	95	5	6	< 20	80	70	3
PTPM2-04A	Los Tilos pluton	Crd nodule		11.8	184	591	7.3	2.3	7	1.4	20	54	64	15	2.1	3	< 20	< 20	100	4
PTPM2-04B	Los Tilos pluton	Crd nodule		10.6	152	418	6.4	3	12	2.4	25	63	58	14	2	7	< 20	180	110	4
PTPM2-04C	Los Tilos pluton	Crd nodule		8.5	145	377	7.1	2.2	13	2.5	25	57	64	13	2.1	4	< 20	110	140	3
PTPM2-04D	Los Tilos pluton	Crd nodule		10.9	144	375	6.9	1.9	13	2.3	20	61	64	14	2.1	5	< 20	< 20	120	3
PTPM2-04E	Los Tilos pluton	Crd nodule		12.6	112	287	7.2	2.3	14	2.8	< 5	81	66	18	2	4	< 20	190	50	3
PTPM2-05	Los Tilos pluton	Granite		1.6	113	283	5.4	1.8	4	0.6	20	40	57	18	2.2	3	30	130	< 30	< 1

PTPM2-06	Elqui Dike Swarm	Mafic dike		2.7	58	237	3.6	1	10	0.7	25	335	252	27	5.7	21	40	60	120	21
PTPM2-07	Colorado Sienogranites	Sienogranite dike		4.9	110	631	9.7	2.4	11	1	15	81	317	36	7.6	6	< 20	90	< 30	1
PTPM2-08	Elqui Dike Swarm	Mafic dike		6.4	67	178	1.5	0.2	2	0.1	10	351	134	25	3.3	35	160	200	160	46
PTPM2-09	Colorado Sienogranites	Sienogranite dike		2.4	131	609	15.9	3.6	7	0.8	15	40	149	23	4.3	4	< 20	90	< 30	1
PTPM2-10	Colorado Sienogranites	Coarse sienogranite		5	161	579	14.2	2.4	9	0.9	18	57	251	28	6.3	5	< 20	< 20	50	
PTPM2-11	Piuquenes granite (ChPC)	Biotite granite		3.8	126	843	11.1	0.9	5	0.6	27	169	110	15	3.1	4	< 20	100	40	2
PTPM2-12	Elqui Dike Swarm	Mafic dike		9.1	89	352	3.7	0.9	5	0.4	< 5	382	145	18	3.4	18	110	130	80	30
HA-10	Elqui Dike Swarm	Mafic dike		1.89	103	1257	15.1	3.53	11.1	0.75	11.0	743	302	19.9	6.64	10.7	13.6	15.7	52.1	7.16
HA-01	Monte Grande pluton	Leucogranite		1.64	140	707	9.92	1.73	14.9	1.23	26.7	48.7	142	61.2	5.90	2.51	0.94	1.73	66.5	0.91
HA-15	Los Tilos	Granite		2.72	91.2	746	6.53	1.49	6.61	0.62	19.9	119	88.8	19.8	3.08	4.33	0.52	2.13	20.9	2.02
HA-04	Monte Grande pluton	Leucogranite		0.86	51.2	471	5.43	0.98	8.52	0.67	12.8	11.3	272	40.6	7.29	3.16		0.82	64.5	0.39
HA-02	Elqui Dike Swarm	Mafic dike		3.80	8.68	88.5	0.73	0.24	6.88	0.53	4.27	429	105	20.5	2.71	24.1	108	122	95.0	43.8
HA-06	Elqui Dike Swarm	Mafic dike		0.80	67.6	320	2.36	0.44	6.82	0.47	13.7	515	206	27.1	4.36	27.3	69.5	121	96.5	32.0
HA-11	Elqui Dike Swarm	Mafic dike		3.52	68.9	612	0.63	0.49	3.97	0.26	5.37	310	138	26.0	3.31	27.7	44.7	99.5	136	31.9
HA-14	Elqui Dike Swarm	Mafic dike		1.71	15.8	465	2.89	0.75	12.0	0.82	4.26	410	126	20.5	3.08	26.4	173	381	75.9	40.9

Sample	Unit	Lithology		V	La	Ce	Pr	Nd	Sm	Eu	Gd	Tb	Dy	Ho	Er	Tm	Yb	Lu	Be	Ga
			Units	**ppm**	**ppm**	**ppm**	**ppm**	**ppm**	**ppm**	**ppm**	**ppm**	**ppm**	**ppm**	**ppm**	**ppm**	**ppm**	**ppm**	**ppm**	**ppm**	**ppm**
			Detection limit	**5**	**0.1**	**0.1**	**0.05**	**0.1**	**0.1**	**0.05**	**0.1**	**0.1**	**0.1**	**0.1**	**0.1**	**0.05**	**0.1**	**0.01**	**1**	**1**
			Analysis method	**FUS-MS**	**FUS-MS**	**FUS-MS**	**FUS-MS**	**FUS-MS**	**FUS-MS**	**FUS-MS**	**FUS-MS**	**FUS-MS**	**FUS-MS**	**FUS-MS**	**FUS-MS**	**FUS-MS**	**FUS-MS**	**FUS-MS**	**FUS-MS**	**FUS-MS**
PTPM02	Los Tilos pluton	Granite		10	21.4	43.9	4.84	16.1	3.5	0.58	3.1	0.5	3.1	0.6	1.8	0.27	1.9	0.29	1	16
PTPM03	Elqui Dike Swarm	Mafic dike		170	15.3	31.7	4.07	17.1	4	1.33	3.5	0.5	2.8	0.5	1.5	0.22	1.4	0.22	1	19
PTPM04	Colorado Sienogranites	Sienogranite dike		44	18.4	35.2	3.79	13.9	2.5	0.78	2.1	0.3	1.8	0.3	1	0.15	1	0.16	2	19
PTPM05	Colorado Sienogranites	Sienogranite dike		18	33.7	66	6.92	24.6	4.4	0.73	3.5	0.5	3	0.6	1.7	0.26	1.8	0.27	3	17
PTPM06	Elqui Dike Swarm	Mafic dike		75	11.2	22.3	2.64	10.6	2.2	0.81	1.9	0.3	1.7	0.3	0.9	0.13	0.9	0.14	3	19
PTPM07A	Monte Grande pluton	Leucogranite		< 5	88.9	184	20.5	73.1	12.8	0.87	8.4	1.2	6.9	1.3	3.8	0.55	3.9	0.61	2	20
PTPM07B	Monte Grande pluton	Leucogranite		< 5	80.4	166	17.9	62.7	10.8	0.75	7.1	1	5.4	1	3.2	0.47	3.3	0.52	2	19
PTPM09	Elqui Dike Swarm	Mafic dike		204	12.4	30.5	4.04	18.8	4.6	1.57	4.8	0.8	4.7	0.9	2.7	0.38	2.5	0.39	1	19
PTPM2-01	Colorado Sienogranites	Sienogranite dike		32	33.5	68.9	7.63	28.2	5.9	1.1	5.1	0.8	4.8	0.9	2.7	0.43	2.9	0.45	2	18
PTPM2-02	Elqui Dike Swarm	Mafic dike		253	9.4	25.3	3.74	18	5.1	1.8	5.7	0.9	5.6	1.1	3.2	0.48	3.2	0.48	2	20
PTPM2-03	Colorado Sienogranites	Sienogranite dike		7	9.8	35.1	6	31.7	14.3	0.27	17.4	3	18.1	3.4	9.3	1.3	8.6	1.29	5	19
PTPM2-04A	Los Tilos pluton	Crd nodule		5	13.5	28.4	3.19	11.8	2.7	0.29	2.6	0.4	2.6	0.5	1.5	0.23	1.6	0.26	89	37
PTPM2-04B	Los Tilos pluton	Crd nodule		< 5	11	23.5	2.65	9.4	2.2	0.23	2	0.4	2.4	0.5	1.4	0.22	1.4	0.23	194	34
PTPM2-04C	Los Tilos pluton	Crd nodule		6	12.7	26.5	2.97	10.9	2.3	0.28	2	0.4	2.3	0.5	1.4	0.22	1.4	0.22	145	36
PTPM2-04D	Los Tilos pluton	Crd nodule		7	12.5	27	3.01	10.7	2.1	0.25	2.2	0.4	2.4	0.5	1.4	0.21	1.4	0.23	135	35
PTPM2-04E	Los Tilos pluton	Crd nodule		8	17.8	35	3.87	13.7	2.9	0.28	2.7	0.4	2.7	0.5	1.7	0.24	1.6	0.25	244	31
PTPM2-05	Los Tilos pluton	Granite		< 5	8.4	17.6	1.85	6.7	1.9	0.14	2	0.4	2.7	0.6	1.7	0.29	2	0.32	2	14
PTPM2-06	Elqui Dike Swarm	Mafic dike		188	31.5	71.1	8.91	38.3	8.2	2.45	7.1	1	5.6	1.1	2.8	0.41	2.8	0.44	2	21

PTPM2-07	Colorado Sienogranites	Sienogranite dike		16	40.6	88	10.4	40.2	8.2	1.64	7.2	1.1	6.7	1.3	3.9	0.61	4	0.63	3	15
PTPM2-08	Elqui Dike Swarm	Mafic dike		234	9.3	23.6	3.39	16.1	4.5	1.81	5	0.8	5	1	2.9	0.42	2.7	0.42	5	20
PTPM2-09	Colorado Sienogranites	Sienogranite dike		7	32.9	65.5	7.02	24.9	4.9	0.47	4.1	0.7	4.1	0.8	2.5	0.39	2.7	0.43	3	15
PTPM2-10	Colorado Sienogranites	Coarse sienogranite		11	35.4	73.1	8.15	30.8	6.4	0.89	5.2	0.9	5	1	2.9	0.44	3	0.46	3	18
PTPM2-11	Piuquenes granite (ChPC)	Biotite granite		15	29.4	59.3	6.58	24.2	4.6	0.83	3.7	0.5	2.7	0.5	1.5	0.24	1.6	0.24	2	15
PTPM2-12	Elqui Dike Swarm	Mafic dike		136	16.3	34.7	4.16	16.5	3.8	1.34	3.6	0.6	3.6	0.7	2.1	0.31	2.1	0.31	1	17
HA-10	Elqui Dike Swarm	Mafic dike		103	81.4	153	18.7	71.2	11.1	3.08	8.10	0.90	4.05	0.66	1.92	0.25	1.54	0.24	2.01	20.8
HA-01	Monte Grande pluton	Leucogranite		5.09	48.8	98.1	12.1	47.3	10.2	0.75	9.82	1.57	9.52	1.88	5.47	0.85	5.46	0.82	4.08	23.1
HA-15	Los Tilos	Granite		7.36	17.8	40.4	4.55	16.2	3.10	0.56	3.02	0.51	3.18	0.64	1.94	0.30	1.91	0.31	0.98	15.2
HA-04	Monte Grande pluton	Leucogranite		2.56	84.0	161	19.0	69.5	11.7	0.90	9.44	1.23	6.72	1.27	3.77	0.57	3.61	0.58	1.63	19.1
HA-02	Elqui Dike Swarm	Mafic dike		181	6.29	15.9	3.04	15.6	4.14	1.43	4.03	0.65	3.85	0.72	2.05	0.31	1.86	0.29	0.91	18.6
HA-06	Elqui Dike Swarm	Mafic dike		204	18.9	48.5	6.48	27.8	5.71	1.84	5.66	0.85	5.14	0.99	2.76	0.41	2.55	0.38	1.38	19.1
HA-11	Elqui Dike Swarm	Mafic dike		221	8.56	20.7	3.62	17.3	4.31	1.68	4.74	0.75	4.73	0.94	2.71	0.36	2.23	0.35	1.45	21.7
HA-14	Elqui Dike Swarm	Mafic dike		211	13.6	33.6	4.48	19.7	4.25	1.45	4.16	0.64	3.85	0.74	2.09	0.31	1.99	0.29	0.91	18.2

F. Mineral chemistry

Electron Microprobe Analysis data (Pyroxene)

Unit	Lithology	Point	SiO2	TiO2	Al2O3	Cr2O3	FeO	MnO	MgO	CaO	Na2O	ZnO	ZrO2
MGp	Leucogranite	PTPM07A_z3a-Px01	47.460	0.118	0.304	0.000	31.660	0.795	0.134	18.960	0.361	0.183	0.038
MGp	Leucogranite	PTPM07A_z3a-Px02	47.100	0.115	0.301	0.017	32.030	0.838	0.130	18.410	0.395	0.000	0.000
MGp	Leucogranite	PTPM07A_z3a-Px04	47.360	0.043	0.313	0.001	31.850	0.713	0.163	18.800	0.433	0.259	0.043
MGp	Leucogranite	PTPM07A_z3a-Px05	47.510	0.159	0.287	0.000	31.080	0.812	0.549	18.710	0.403	0.044	0.022
MGp	Leucogranite	PTPM07A_z3a-Px06	46.860	0.101	0.269	0.011	30.350	0.737	0.772	18.660	0.397	0.048	0.000
MGp	Leucogranite	PTPM07A_z3c-Px11	46.770	0.154	0.283	0.005	30.670	0.696	0.482	18.770	0.371	0.238	0.022
MGp	Leucogranite	PTPM07A_z3c-Px12	47.870	0.058	0.310	0.011	31.030	0.749	0.830	18.940	0.392	0.221	0.000
MGp	Leucogranite	PTPM07A_z3c-Px13	49.360	0.052	0.107	0.016	30.020	0.761	0.715	20.400	0.314	0.185	0.108
MGp	Leucogranite	PTPM07A_z3c-Px14	47.530	0.087	0.206	0.011	30.610	0.772	0.578	19.090	0.549	0.096	0.113
MGp	Leucogranite	PTPM07A_z3c-Px15	47.670	0.072	0.248	0.000	30.760	0.821	0.765	18.890	0.413	0.170	0.011
MGp	Leucogranite	PTPM07A_z3c-Px16	47.460	0.078	0.235	0.000	30.370	0.623	0.650	19.110	0.402	0.000	0.016
MGp	Leucogranite	PTPM07A_z3c-Px17	47.950	0.068	0.180	0.032	30.310	0.703	0.710	18.800	0.330	0.011	0.000
MGp	Leucogranite	PTPM07A_z4-Px18	48.190	0.104	0.282	0.007	30.430	0.725	0.717	18.740	0.412	0.118	0.000
MGp	Leucogranite	PTPM07A_z4-Px19	47.880	0.042	0.284	0.000	30.990	0.714	0.734	19.170	0.429	0.233	0.049
MGp	Leucogranite	PTPM07A_z4-Px20	47.830	0.123	0.296	0.000	30.450	0.730	0.851	19.070	0.351	0.125	0.000
MGp	Leucogranite	PTPM07A_z4-Px21	47.930	0.101	0.259	0.000	30.390	0.741	0.703	19.210	0.508	0.166	0.000
MGp	Leucogranite	PTPM07A_z4-Px22	46.990	0.076	0.251	0.000	29.220	0.731	0.643	18.790	0.346	0.170	0.065
MGp	Leucogranite	PTPM07A_z5-Px23	47.690	0.132	0.328	0.023	30.350	0.722	1.087	18.460	0.392	0.092	0.000
MGp	Leucogranite	PTPM07A_z5-Px24	48.000	0.109	0.379	0.000	30.450	0.766	1.486	18.130	0.365	0.221	0.000
MGp	Leucogranite	PTPM07A_z5-Px25	48.230	0.199	0.381	0.000	29.740	0.804	1.563	18.220	0.450	0.085	0.000
MGp	Leucogranite	PTPM07A_z5-Px26	48.090	0.132	0.383	0.000	29.450	0.669	1.730	18.720	0.464	0.052	0.006
MGp	Leucogranite	PTPM07A_z5-Px27	47.670	0.198	0.281	0.000	30.260	0.758	1.273	18.910	0.346	0.111	0.060
MGp	Leucogranite	PTPM07A_z9-Px29	48.060	0.157	0.262	0.011	30.800	0.683	0.535	18.910	0.484	0.066	0.049
MGp	Leucogranite	PTPM07A_z9-Px30	46.840	0.138	0.363	0.000	33.080	0.806	0.096	17.640	0.552	0.018	0.006
MGp	Leucogranite	PTPM07A_z9-Px31	47.450	0.044	0.355	0.011	32.810	0.767	0.126	17.780	0.481	0.181	0.054
MGp	Leucogranite	PTPM07A_z9-Px32	48.210	0.084	0.260	0.000	30.990	0.708	0.481	19.280	0.399	0.144	0.000
MGp	Leucogranite	PTPM07A_z9-Px33	48.230	0.102	0.217	0.042	31.530	0.675	0.484	18.990	0.593	0.030	0.000
MGp	Leucogranite	PTPM07B_z2-Px01	47.670	0.154	0.245	0.000	31.250	0.663	0.802	18.970	0.350	0.212	0.011
MGp	Leucogranite	PTPM07B_z2-Px02	47.560	0.142	0.195	0.014	30.640	0.718	0.735	19.390	0.460	0.157	0.000
MGp	Leucogranite	PTPM07B_z2-Px03	47.930	0.097	0.226	0.000	30.740	0.710	0.725	19.690	0.555	0.234	0.011
MGp	Leucogranite	PTPM07B_z2-Px04	48.190	0.067	0.191	0.000	30.870	0.702	0.738	19.450	0.486	0.015	0.000
MGp	Leucogranite	PTPM07B_z2-Px05	47.420	0.146	0.255	0.000	30.640	0.764	0.748	18.910	0.445	0.073	0.000
MGp	Leucogranite	PTPM07B_z2-Px06	48.360	0.010	0.289	0.000	30.620	0.839	0.830	19.390	0.497	0.077	0.000
MGp	Leucogranite	PTPM07B_z2-Px07	48.130	0.089	0.257	0.001	30.270	0.731	0.912	19.290	0.494	0.000	0.032
MGp	Leucogranite	PTPM07B_z2-Px08	48.480	0.075	0.204	0.000	31.350	0.748	0.677	19.200	0.452	0.070	0.000

Electron Microprobe Analysis data (Cordierite)

Unit	Lithology	Point	SiO2	Al2O3	FeO	MgO	MnO	ZnO	CaO	K2O	Cr2O3	Na2O	TiO2
LTp	granodiorite	LTB-Cd-32	47.53	33.08	9.3	6.36	1.63	0.0699	0.0396	0.0209	0.0738	0.4591	0
LTp	granodiorite	LTB-Cd-33	47.98	33.36	9.69	6.08	1.71	0	0.008	0.0113	0	0.6285	0.0453
LTp	granodiorite	LTB-Cd-34	47.22	32.66	9.9	5.7	1.8	0.0161	0.0724	0	0	0.623	0
LTp	granodiorite	LTB-Cd-35	47.23	32.86	9.84	5.87	1.73	0.0143	0	0.0123	0.0533	0.5935	0.1358
LTp	granodiorite	LTB-Cd-36	46.95	33.12	10.12	5.43	1.82	0	0.0485	0	0	0.6571	0.0904
LTp	granodiorite	LTB-Cd-37	47.12	33.05	9.98	5.75	1.77	0.068	0.075	0	0.033	0.611	0.1357
LTp	granodiorite	LTB-Cd-38	47.13	32.49	9.88	5.95	1.69	0	0.0055	0	0	0.9839	0.0226
LTp	granodiorite	LTB-Cd-39	47.21	32.63	9.81	5.99	1.64	0.0716	0.021	0	0	1.0698	0
LTp	granodiorite	LTB-Cd-40	46.79	32.37	9.77	6.03	1.56	0	0.0051	0.0417	0	0.9497	0
LTp	granodiorite	LTB-Cd-41	47.04	32.61	9.67	5.98	1.6	0	0.0366	0	0.033	0.8426	0.0906
LTp	granodiorite	LTB-Cd-42	46.8	32.38	9.77	6.18	1.66	0.0859	0.0316	0.0445	0	1.0162	0
LTp	granodiorite	LTB-Cd-43	46.87	32.81	9.74	5.82	1.65	0.0698	0	0.0033	0	0.9424	0.0226
LTp	granodiorite	LTF-Cd-18	47.16	32.84	9.95	5.59	1.76	0	0.0326	0.0147	0.0431	0.7161	0
LTp	granodiorite	LTF-Cd-19	47.16	33.18	9.72	5.77	1.8	0.0483	0.0146	0.0093	0.0481	0.715	0.1355
LTp	granodiorite	LTF-Cd-20	47.66	32.64	9.75	5.75	1.66	0.0716	0.0592	0	0.0406	0.8107	0
LTp	granodiorite	LTF-Cd-21	47.64	32.74	9.7	5.93	1.69	0.0412	0.0346	0.0203	0.0305	0.8508	0
LTp	granodiorite	LTF-Cd-22	47.62	32.93	9.75	5.98	1.58	0.0125	0.0175	0	0	0.7355	0.1133
LTp	granodiorite	LTF-Cd-23	48.01	33.25	9.52	6.17	1.53	0	0.0517	0	0	0.6108	0.1814
LTp	granodiorite	LTF-Cd-24	47.37	33.33	10.44	5.58	1.86	0	0.0301	0.0085	0.0506	0.7159	0
LTp	granodiorite	LTF-Cd-25	47.25	33.21	9.9	5.55	1.82	0	0.0252	0	0	0.7214	0.0679
LTp	granodiorite	LTF-Cd-18	46.55	32.92	9.95	5.59	1.76	0	0.0326	0.0147	0.043	0.7163	0

Electron Microprobe Analysis data (Amphibole)

Unit	Lithology	Point	SIO2	TIO2	AL2O3	CR2O3	FEO	MNO	MGO	CAO	NA2O	K2O	F	Cl
MGp	Leucogranite	Z1 A1	41.82	1.5095	5.49	0.0402	34.85	0.8077	0.3526	9.35	1.76	0.9638	0.4581	0.0461
MGp	Leucogranite	Z1 A2	41.45	1.3853	5.25	0.0252	34.53	0.7482	0.3855	9.25	1.89	0.9303	0.4214	0.0398
MGp	Leucogranite	Z1 A3	41.23	1.4394	5.41	0	34.49	0.8024	0.3677	9.41	1.94	1.0422	0.2735	0.0481
MGp	Leucogranite	Z1 A4	40.87	1.406	5.32	0.0151	34.84	0.7751	0.319	9.25	1.95	0.9628	0.2601	0.0589
MGp	Leucogranite	Z6 A20	40.89	1.597	5.83	0	34.99	0.8219	0.3113	9.35	1.99	1.0669	0.523	0.0509
MGp	Leucogranite	Z6 A21	40.84	1.5962	5.86	0.0505	35.07	0.6969	0.3199	9.4	1.98	1.0539	0.2243	0.047
MGp	Leucogranite	Z6 A22	41.38	1.1441	5.41	0.0303	34.81	0.6038	0.3852	9.33	1.88	0.9741	0.0995	0.0407
MGp	Leucogranite	Z6 A23	41.26	1.477	5.34	0	35.14	0.6814	0.3603	9.2	1.96	0.9026	0.5327	0.0349
MGp	Leucogranite	Z3 A24	40.52	1.213	5.34	0.0254	31.8	0.7301	0.4268	8.97	2.05	0.9515	0.4023	0.0459
MGp	Leucogranite	Z3 A25	40.47	1.2355	5.5	0	31.59	0.5585	0.4562	8.93	1.95	0.9264	0.4019	0.0556
MGp	Leucogranite	Z3 A26	40.38	1.2238	5.55	0	32.06	0.6012	0.4307	8.98	2.17	0.9697	0.737	0.0314
MGp	Leucogranite	Z3 A27	40.61	1.1588	5.14	0	31.75	0.7262	0.4626	8.89	1.94	0.8974	0.4895	0.0421
MGp	Leucogranite	Z3 A28	40.82	1.288	4.93	0.0305	32.08	0.6323	0.3686	8.83	1.85	0.9102	0.2763	0.035
MGp	Leucogranite	Z3 A29	40.15	1.2762	5.18	0.071	32.12	0.7374	0.3861	8.84	2.03	0.8767	0.4511	0.0346
MGp	Leucogranite	Z3 A30	40.17	1.3209	5.2	0.0051	31.88	0.7418	0.4468	8.86	2.1	0.8744	0.3517	0.0363
MGp	Leucogranite	Z3 A31	39.72	1.2125	5.22	0.0457	31.64	0.6911	0.44	8.76	2.03	0.8579	0.1759	0.0363
MGp	Leucogranite	Z3 A32	40.09	1.5916	5.22	0.0305	31.93	0.5935	0.464	8.84	1.9	0.8438	0.1385	0.0327
MGp	Leucogranite	Z7 A33	41.2	1.5929	5.37	0.0712	32.72	0.4999	0.6765	9.29	1.91	0.9758	0.2894	0.0606
MGp	Leucogranite	Z7 A34	40.79	1.4976	5.49	0	32	0.3636	0.7085	9.29	1.93	1.0075	0.3021	0.0292
MGp	Leucogranite	Z7 A35	40.69	1.4394	5.78	0	32.67	0.6325	0.4925	8.76	2.12	0.9315	0.1629	0.0665
MGp	Leucogranite	Z3A A5	40.94	1.5359	5.87	0	34.11	0.6984	0.3892	9.46	1.89	1.0143	0.1621	0.1104
MGp	Leucogranite	Z3A A6	41.26	1.4287	5.51	0	33.84	0.6519	0.3942	9.46	1.96	1.0495	0.1494	0.0309
MGp	Leucogranite	Z3A A7	41.75	1.4822	5.27	0.0507	33.99	0.5972	0.4082	9.26	2.11	0.9443	0.2491	0.0361
MGp	Leucogranite	Z3A A8	41.16	1.73	5.73	0	34.55	0.6514	0.3419	9.48	2.09	1.026	0.137	0.0274
MGp	Leucogranite	Z3A A9	41.29	1.5254	5.41	0	34.25	0.5775	0.5873	9.45	1.92	1.0486	0.1241	0.0428
MGp	Leucogranite	Z3B A10	41.88	1.4099	5.14	0.0707	34.13	0.6055	0.4628	9.58	1.83	0.8717	0.2962	0.0332
MGp	Leucogranite	Z3B A11	42.52	1.3122	4.69	0.0302	34.58	0.6364	0.4386	9.56	1.68	0.8555	0.1868	0.0504
MGp	Leucogranite	Z3B A12	41.83	1.324	5.22	0	34.36	0.6562	0.4568	9.61	1.75	0.9229	0.075	0.0418
MGp	Leucogranite	Z3B A13	42.09	1.5485	4.99	0.005	34.75	0.6598	0.4272	9.47	1.73	0.8548	0.1242	0.0224
MGp	Leucogranite	Z3B A14	42.17	1.1316	5.28	0	34.18	0.4936	0.6737	9.34	2.01	0.921	0.0247	0.0208
MGp	Leucogranite	Z4 A15	41.65	0.4632	5.48	0	34.52	0.5594	0.667	9.66	1.74	0.9057	0.15	0.0307
MGp	Leucogranite	Z4 A16	40.86	1.2711	5.86	0.0404	34.14	0.6254	0.5666	9.6	1.9	1.0432	0.0745	0.0272
MGp	Leucogranite	Z6 A17	40.88	1.1114	5.9	0	33.51	0.5831	0.4157	9.87	1.91	1.0909	0.3487	0.0464
MGp	Leucogranite	Z6 A18	44.58	0.2153	3.56	0.0856	34.85	0.8468	0.465	9.64	1.36	0.5953	0.3611	0.0402
MGp	Leucogranite	Z6 A19	44.05	0.1717	3.26	0.0301	35.54	1.051	0.5494	9.03	1.1854	0.4686	0.5933	0.0412
MGp	Leucogranite	Z6 A20	42.16	1.0677	5.07	0	34	0.6687	0.4429	9.79	1.61	0.8359	0.5708	0.0393
MGp	Leucogranite	Z6 A21	41.69	0.7647	4.81	0.0252	34.2	0.6722	0.4365	9.54	1.68	0.7763	0.0873	0.0614
MGp	Leucogranite	Z6 A22	41.58	1.251	5.26	0.0657	33.79	0.5407	0.3504	9.3	1.81	0.9721	0.2622	0.0447
MGp	Leucogranite	Z6 A23	41.66	1.5922	5.16	0.005	34.74	0.9013	0.3679	9.18	2	0.919	0.1626	0.0451

MGp	Leucogranite	Z6 A24	41.92	1.4506	4.73	0	35.42	0.8231	0.3592	9.07	1.78	0.9117	0	0.0511
MGp	Leucogranite	Z6 A25	41.97	1.2384	4.9	0	34.55	0.754	0.4325	9.31	1.8	0.8944	0	0.032
MGp	Leucogranite	Z6 A26	41.33	1.4432	5.31	0	34.38	0.8437	0.3925	9.18	1.98	0.95	0.2371	0.0409
MGp	Leucogranite	Z1B A1	41.29	1.3265	5.5	0	34.11	0.7236	0.462	9.48	1.81	1.0115	0.3467	0.0233
MGp	Leucogranite	Z1B A2	41.81	1.273	5.17	0.0202	34	0.7043	0.4858	9.5	1.72	0.9121	0.3861	0.0294
MGp	Leucogranite	Z1B A3	41.08	1.541	5.87	0.0607	34.17	0.6843	0.3981	9.38	1.89	1.0148	0	0.0387
MGp	Leucogranite	Z1B A4	41.56	1.4883	5.58	0	33.86	0.6846	0.41	9.47	1.72	0.9469	0.3732	0.0509
MGp	Leucogranite	Z1B A5	41.24	1.5731	5.51	0	34.23	0.5985	0.4422	9.55	1.77	0.9843	0.1242	0.0471
MGp	Leucogranite	Z1B A6	41.06	1.4095	5.28	0.005	35.3	0.7384	0.39	9.28	1.86	0.8977	0.3603	0.0371
MGp	Leucogranite	Z1B A7	41.25	1.5419	5.49	0	34.66	0.7628	0.4269	9.37	2.06	0.9766	0.2872	0.0573
MGp	Leucogranite	Z1B A8	41.37	1.6519	5.55	0.0507	34	0.8493	0.4073	9.38	1.86	1.0025	0.3985	0.064
MGp	Leucogranite	Z1B A9	40.99	1.4349	5.5	0.0051	34.62	0.6541	0.4254	9.37	1.86	0.9848	0.2113	0.0554
MGp	Leucogranite	Z1B A10	42	1.1651	5.05	0.0253	35.11	0.6074	0.5188	9.4	1.9	0.9513	0.2857	0.0445
MGp	Leucogranite	Z1B A11	41.6	1.2851	5.39	0.0354	34.56	0.5026	0.6015	9.45	2	0.9342	0.2493	0.0378
MGp	Leucogranite	Z1B A12	41.01	1.3517	5.65	0.0659	33.72	0.4678	0.557	9.52	2.04	1.0258	0.3845	0.0496
MGp	Leucogranite	Z1B A13	40.87	1.3605	5.87	0.081	34.58	0.5881	0.6305	9.6	1.89	1.0764	0.2129	0.0503
MGp	Leucogranite	Z2B A14	41.41	1.3163	5.7	0.0354	35.12	0.6112	0.6191	9.54	1.92	0.959	0.4484	0.0301
MGp	Leucogranite	Z2B A15	41.63	1.3495	5.62	0.0152	34.83	0.5415	0.6281	9.49	2.09	0.8624	0.3104	0.0483
MGp	Leucogranite	Z2B A16	41.77	1.6394	5.31	0.0607	34.94	0.658	0.4042	9.26	1.96	0.994	0.3606	0.0474
MGp	Leucogranite	Z2B A17	41.75	1.2518	5.36	0	35.19	0.6465	0.4042	9.38	2.02	1.0224	0.1126	0.0356
MGp	Leucogranite	Z2B A18	41.21	1.6219	5.64	0	33.88	0.5499	0.4244	9.4	1.96	1.0312	0.0125	0.0519
MGp	Leucogranite	Z2B A19	41.29	1.3505	5.57	0.0658	34.35	0.6003	0.4365	9.39	2.01	1.0618	0.0125	0.0423
MGp	Leucogranite	Z5 A36	41.58	1.4345	5.61	0	35.27	0.6659	0.3967	9.21	1.88	1.0501	0.2881	0.0417
MGp	Leucogranite	Z5 A37	41.39	1.1996	5.61	0	34.46	0.5262	0.3897	9.46	1.95	1.0618	0.138	0.0561
MGp	Leucogranite	Z5 A38	41.78	1.4264	5.16	0	34.25	0.6237	0.4248	9.41	1.85	0.9797	0.2752	0.0308
MGp	Leucogranite	Z5 A39	41.75	1.2525	5.4	0	34.57	0.7208	0.3378	9.33	1.9	0.9525	0.1628	0.0372
MGp	Leucogranite	Z5 A40	41.59	1.3609	5.47	0.0051	34.35	0.7249	0.3711	9.35	1.97	0.9288	0.3624	0.0625

Electron Microprobe Analysis data (White Mica)

Unit	Lithology	Point	SiO2	TiO2	Al2O3	Cr2O3	FeO	Fe2O3	MnO	MgO	CaO	Na2O	K2O	BaO	F-	Cl-
LTp	granodiorite	LTA_Z8_Wm1	45.74	0.02	33.33	0.00	3.04	0.00	0.00	0.70	0.02	0.62	10.77	0.00	0.10	0.01
LTp	granodiorite	LTA_Z8_Wm2	46.05	0.00	32.37	0.00	3.17	0.00	0.00	0.74	0.01	0.57	10.36	0.00	0.26	0.01
LTp	granodiorite	LTA_Z8_Wm3	46.05	0.00	33.81	0.00	2.56	0.00	0.00	0.55	0.02	0.61	10.47	0.00	0.31	0.00
LTp	granodiorite	LTD - z 7 - WM01	46.16	0.23	34.86	0.00	2.80	0.00	0.00	0.68	0.00	0.65	10.53	0.00	0.57	0.00
LTp	granodiorite	LTD - z 7 - WM02	45.70	0.23	35.13	0.00	2.61	0.37	0.00	0.64	0.00	0.70	10.71	0.00	0.32	0.00
LTp	granodiorite	LTD - z 7 - WM03	46.29	0.37	33.44	0.00	3.16	0.18	0.03	0.96	0.03	0.54	10.10	0.00	0.38	0.01
LTp	granodiorite	LTD - z 7 - WM04	45.92	0.00	34.29	0.00	2.63	0.86	0.04	0.75	0.00	0.51	10.69	0.00	0.20	0.02
LTp	granodiorite	LTD - z 7 - WM05	46.71	0.02	33.90	0.00	3.26	0.04	0.01	0.85	0.01	0.29	10.65	0.00	0.22	0.00
LTp	granodiorite	LTD - z 7 - WM06	45.85	0.05	34.52	0.00	2.65	0.69	0.01	0.73	0.01	0.49	10.84	0.00	0.45	0.01
LTp	granodiorite	LTD - z 7 - WM07	45.80	0.60	34.66	0.00	3.04	0.00	0.00	0.58	0.01	0.60	10.45	0.00	0.55	0.00
LTp	granodiorite	LTD - z 7 - WM08	45.55	0.32	35.20	0.00	2.55	0.59	0.04	0.59	0.00	0.65	10.21	0.00	0.04	0.02
LTp	granodiorite	LTD - z x - WM09	46.15	0.02	34.09	0.00	3.06	0.36	0.02	0.73	0.02	0.33	8.40	0.00	0.22	0.02
LTp	granodiorite	LTD - z x2 - WM10	45.60	0.46	31.88	0.00	2.15	2.42	0.10	1.36	0.00	0.23	10.78	0.00	0.38	0.02
LTp	granodiorite	LTD - z x2 - WM11	45.52	0.14	31.38	0.00	1.14	4.26	0.04	1.71	0.00	0.26	11.07	0.00	0.62	0.00
LTp	granodiorite	LTD - z x2 - WM12	46.73	0.32	33.49	0.00	3.22	0.44	0.02	0.98	0.04	0.31	10.47	0.00	0.46	0.02
LTp	granodiorite	LTD - z x2 - WM13	46.28	0.14	33.97	0.00	2.70	0.90	0.01	0.92	0.00	0.45	10.61	0.00	0.38	0.00
LTp	granodiorite	LTD - z x2 - WM14	46.72	0.39	31.18	0.00	2.58	2.27	0.10	1.59	0.02	0.16	10.96	0.00	0.36	0.02

Electron Microprobe Analysis data (Black Mica)

Unit	Lithology	Point	SiO2	TiO2	Al2O3	Cr2O3	FeO	MnO	MgO	NiO	CaO	Na2O	K2O	BaO	F-	Cl-
LTp	granodiorite	LTA_Z 9_Bt 1	34.13	3.52	17.44	0.00	21.69	0.58	8.08	0.00	0.00	0.18	9.37	0.00	0.52	0.07
LTp	granodiorite	LTA_Z 9_Bt 2	34.23	3.46	17.46	0.00	21.69	0.57	8.16	0.00	0.01	0.18	9.61	0.00	0.30	0.13
LTp	granodiorite	LTA_Z 9_Bt 3	34.90	3.35	16.40	0.00	21.69	0.58	8.08	0.00	0.00	0.20	9.53	0.00	0.54	0.11
LTp	granodiorite	LTA_Z 9_Bt 4	34.82	4.22	16.55	0.00	21.97	0.59	8.10	0.00	0.02	0.13	9.25	0.00	0.49	0.10
LTp	granodiorite	LTA_Z 9_Bt 5	34.02	3.26	17.32	0.00	21.46	0.54	8.13	0.00	0.02	0.22	9.65	0.00	0.27	0.10
LTp	granodiorite	LTA_Z 9_Bt 6	36.24	3.40	16.19	0.00	20.32	0.60	8.60	0.00	0.00	0.23	9.16	0.00	0.57	0.12
LTp	granodiorite	LTA_Z 9_Bt 7	34.44	2.97	16.62	0.00	21.57	0.60	7.90	0.00	0.00	0.28	9.48	0.00	0.32	0.10
LTp	granodiorite	LTA_Z 9_Bt 8	36.19	3.99	16.29	0.00	20.98	0.56	8.39	0.00	0.00	0.16	9.40	0.00	0.41	0.15
LTp	granodiorite	LTA_Z 11_Bt 9	35.89	3.31	15.23	0.00	20.65	0.54	8.95	0.00	0.02	0.21	9.28	0.00	0.61	0.08
LTp	granodiorite	LTA_Z 11_Bt 10	35.85	3.17	15.30	0.00	21.07	0.56	8.95	0.00	0.02	0.29	8.84	0.00	0.95	0.13
LTp	granodiorite	LTB-Bt-50	34.17	3.01	17.15	0.00	22.15	0.48	8.96	0.00	0.10	0.23	8.47	0.00	0.43	0.16
LTp	granodiorite	LTB-Bt-51	35.02	2.77	17.96	0.01	21.51	0.48	8.84	0.00	0.03	0.22	9.20	0.00	0.31	0.17
LTp	granodiorite	LTB-Bt-52	34.17	3.32	17.55	0.00	22.06	0.45	8.19	0.00	0.01	0.28	9.44	0.00	0.74	0.13
LTp	granodiorite	LTB-Bt-53	34.55	3.08	17.52	0.03	21.70	0.51	8.25	0.00	0.02	0.34	9.24	0.00	0.50	0.13
LTp	granodiorite	LTB-Bt-54	34.05	3.45	17.53	0.00	21.96	0.71	8.05	0.00	0.04	0.21	8.94	0.00	0.37	0.10
LTp	granodiorite	LTB-Bt-55	35.59	3.53	16.55	0.00	21.30	0.68	8.56	0.00	0.01	0.28	9.13	0.00	0.88	0.13
LTp	granodiorite	LTB-Bt-56	34.30	3.46	16.89	0.02	22.01	0.60	8.26	0.00	0.04	0.21	9.30	0.00	0.49	0.13
LTp	granodiorite	LTB-Bt-57	34.17	3.50	17.43	0.02	21.79	0.63	7.86	0.00	0.01	0.34	9.56	0.00	0.40	0.25
LTp	granodiorite	Bt-6	34.13	2.89	17.72	0.00	22.27	0.62	7.98	0.00	0.01	0.16	9.30	0.00	0.63	0.14
LTp	granodiorite	Bt-7	35.45	3.88	16.56	0.00	21.13	0.42	8.31	0.00	0.03	0.16	9.37	0.00	0.89	0.17
LTp	granodiorite	Bt-8	35.29	3.91	16.28	0.00	21.03	0.50	8.91	0.00	0.00	0.31	9.43	0.00	0.65	0.15
LTp	granodiorite	LTF-Bt-9	35.51	3.96	16.40	0.00	21.15	0.42	8.44	0.00	0.04	0.24	8.97	0.00	0.48	0.12
LTp	granodiorite	LTF-Bt-10	33.94	3.05	17.59	0.00	21.47	0.52	8.13	0.00	0.00	0.09	9.36	0.00	0.27	0.10
LTp	granodiorite	LTF-Bt-11	34.50	3.05	17.67	0.00	21.26	0.63	8.38	0.00	0.02	0.21	9.18	0.00	0.54	0.13

Electron Microprobe Analysis data (Zircon)

Code	Unit	P (ppm)	Y (ppm)	Hf (ppm)	Zr (ppm)
LTA - z 3 - Zrn23	Los Tilos pluton (LTp)	2045.06	7161.76	12295.71	477129.8
LTA - zona 3 - Zrn 24	Los Tilos pluton (LTp)	490.09	3372.60	10175.76	486087.5
LTA - zona 3 - Zrn 25	Los Tilos pluton (LTp)	3713.93	5931.78	13822.07	475353.1
LTA - zona 4 - Zrn 32	Los Tilos pluton (LTp)	0	0	10854.14	495933.7
LTA - zona 4 - Zrn 33	Los Tilos pluton (LTp)	134.85	2784.38	9063.21	491491.8
LTA - zona 4 - Zrn 34	Los Tilos pluton (LTp)	350.44	1718.19	9122.56	493638.7
LTA - zona 4 - Zrn 35	Los Tilos pluton (LTp)	161.91	355.13	11617.33	493786.8
LTA - zona 4 - Zrn 36	Los Tilos pluton (LTp)	1055.26	4568.72	14330.86	484162.7
LTB - zona 2 - Zrn 79	Los Tilos pluton (LTp)	2715.4	8972.09	12550.1	473798.4
LTB - zona 1 - Zrn 70	Los Tilos pluton (LTp)	1164.39	6045.17	11617.33	482682.1
LTB - zona 1 - Zrn 71	Los Tilos pluton (LTp)	1763.13	2087.5	18401.17	481053.4
LTB - zona 1 - Zrn 72	Los Tilos pluton (LTp)	202.93	2233.96	9379.5	493268.6
LTB - zona 4 - Zrn 80	Los Tilos pluton (LTp)	616.22	3083.61	11617.33	488160.4
LTB - zona 4 - Zrn 81	Los Tilos pluton (LTp)	2335.28	6849.15	14670.05	433525.5
LTD - zona 3 - Zrn 4	Los Tilos pluton (LTp)	1272.16	2640.28	10430.15	490011.2
PTPM07A - zona 2 - Zrn 4	Monte Grande pluton (MGp)	1595.55	14331.41	13737.28	460176.7
PTPM07A - zona 2 - Zrn 5	Monte Grande pluton (MGp)	784.68	8173.62	13398.08	476463.5
PTPM07A - zona 2 - Zrn 6	Monte Grande pluton (MGp)	0	2129.23	10514.95	491936
PTPM07A - zona 2 - Zrn 7	Monte Grande pluton (MGp)	1891.88	15040.1	12634.9	466321.3
PTPM07A - zona 2 - Zrn 8	Monte Grande pluton (MGp)	418.96	1368.57	10684.55	495489.5
PTPM07A - zona 2 - Zrn 9	Monte Grande pluton (MGp)	27.05	914.21	11617.33	488826.7
PTPM07A - zona 2 - Zrn 15	Monte Grande pluton (MGp)	0	507.11	12974.09	488752.7
PTPM07A - zona 7 - Zrn 16	Monte Grande pluton (MGp)	54.116	50.39	8323.77	487420.1
PTPM07A - zona 7 - Zrn 17	Monte Grande pluton (MGp)	243.08	1165.41	9103.91	490381.3
PTPM07A - zona 7 - Zrn 18	Monte Grande pluton (MGp)	0	1774.89	8602.757	498302.7
PTPM07A - zona 8 - Zrn 19	Monte Grande pluton (MGp)	338.66	6764.11	12465.31	472762
PTPM07A - zona 8 - Zrn 20	Monte Grande pluton (MGp)	229.99	1318.96	8856.3	480905.4
PTPM07A - zona 8 - Zrn 21	Monte Grande pluton (MGp)	271.01	1983.56	10599.75	481941.8
PTPM07A - zona 4 - Zrn 22	Monte Grande pluton (MGp)	2258.91	16378.75	9307.42	472613.9
PTPM07A - zona 4 - Zrn 23	Monte Grande pluton (MGp)	746.71	5197.89	12804.5	486087.5
PTPM07B - zona 7 - Zrn 1	Monte Grande pluton (MGp)	0	1077.21	10938.94	493046.5
PTPM07B - zona 7 - Zrn 2	Monte Grande pluton (MGp)	13.52	1025.24	10514.95	491565.8
PTPM07B - zona 4 - Zrn 3	Monte Grande pluton (MGp)	368.33	2813.52	9368.48	493934.8
PTPM07B - zona 5 - Zrn 4	Monte Grande pluton (MGp)	82.046	1178.79	11447.73	493194.5
PTPM07B - zona 9 - Zrn 5	Monte Grande pluton (MGp)	982.81	11024.16	13482.88	478536.4
PTPM07B - zona 9 - Zrn 6	Monte Grande pluton (MGp)	1283.51	12756.53	12719.7	475575.1
PTPM07B - zona 9 - Zrn 7	Monte Grande pluton (MGp)	1517.43	11890.34	13398.08	478018.2
PTPM07B - z 1 - Zrn 08	Monte Grande pluton (MGp)	0	1838.67	10514.95	493194.5

LA-ICP-MS data (Zircon)

PPM	HA-01-01	HA-01-02	HA-01-03	HA-01-04	HA-01-05	HA-01-06	HA-01-07	HA-01-08	HA-01-09	HA-01-10	HA-01-11	HA-01-12	HA-01-13	HA-01-14	HA-01-15	HA-01-16	HA-01-17	HA-01-18	HA-01-19	HA-01-20	HA-01-21	HA-01-22	HA-01-23	HA-01-24	HA-01-25
Li	16.15	1.13	1.22	21.79	5.59	3.24	14.14	15.00	0.51	18.56	18.02	14.47	15.17	6.66	2.99	2.50	1.54	7.95	3.00	0.84	31.19	5.80	13.29	25.26	2.98
P	1988	271	469	1313	1020	287	1371	1052	832	1186	2464	1749	1614	1498	423	429	721	2267	531	413	3620	1330	1091	501	745
Ca	0.00	78.48	22.05	36.77	278.23	0.00	73.85	33.70	12.51	0.00	3910.96	169.26	26.45	2187.77	97.22	0.00	191.56	3.28	0.00	37.33	5778.11	8.55	0.00	0.00	0.00
Ti	3.24	2.67	3.66	4.31	1.20	4.50	1.28	1.91	1.34	2.82	2.92	2.85	1.67	2.08	3.03	5.09	4.86	1.38	2.09	4.04	3.15	1.53	3.96	1.47	2.92
Y	15961	1082	1782	10575	2422	920	8471	6661	4243	7893	3787	16922	15190	1521	1896	1192	2602	16438	3057	2422	5570	7997	15306	4974	5893
Zr	447576	474812	455793	431773	466828	462842	442564	447872	452476	444404	457834	439417	429357	461312	458091	459546	456011	435510	458337	457153	454892	451390	424765	451035	457892
Nb	344.72	3.60	5.42	297.14	11.10	2.96	156.83	139.03	7.68	137.69	63.90	100.57	413.72	8.79	8.71	2.35	12.96	118.60	14.31	5.02	82.17	28.90	506.17	157.96	12.49
La	0.02	0.01	0.03	0.48	0.95	0.02	0.69	1.32	4.75	0.00	16.98	3.52	0.00	13.69	0.21	0.00	6.13	1.36	0.04	0.44	20.46	0.62	1.71	0.11	0.06
Ce	139.06	18.65	33.71	76.77	21.88	17.15	64.58	56.13	33.11	55.73	77.67	94.02	126.85	62.23	28.07	25.75	50.26	90.84	50.43	34.34	106.76	49.87	140.96	34.81	55.44
Pr	0.32	0.06	0.22	0.34	1.00	0.09	0.99	1.61	6.99	0.10	13.25	3.48	0.19	7.06	0.19	0.19	5.12	2.64	0.16	0.52	13.22	1.29	2.58	0.08	0.43
Nd	6.99	1.67	3.91	4.65	4.56	1.67	9.50	13.44	56.38	2.79	79.73	29.13	5.35	40.74	2.70	4.28	37.97	29.54	3.71	7.25	78.96	13.79	24.96	1.07	8.59
Sm	43.46	3.72	9.17	19.32	8.65	3.85	25.64	24.85	65.44	18.34	43.90	58.72	35.40	18.61	7.12	7.95	35.67	71.58	11.88	13.60	41.89	36.21	39.79	6.83	27.57
Eu	0.20	0.35	0.71	0.07	0.19	0.32	0.36	0.33	2.94	0.09	0.57	0.41	0.10	0.55	0.29	0.61	1.55	0.75	0.49	1.27	0.75	0.72	0.48	0.02	0.85
Gd	395.89	29.31	52.15	190.03	58.64	22.56	192.87	159.58	192.24	180.16	112.11	380.05	316.23	42.24	46.41	37.96	107.92	440.52	80.19	75.50	129.05	227.96	213.31	70.60	170.81
Tb	151.51	9.50	16.64	80.72	18.96	7.50	74.58	59.61	53.11	69.13	34.44	146.96	127.84	13.61	16.38	11.32	30.81	160.39	28.28	23.81	43.47	78.13	92.20	32.51	57.83
Dy	1835.34	113.82	193.44	1044.53	248.87	89.64	904.87	722.96	527.41	855.03	401.21	1782.74	1589.49	156.97	197.70	129.56	313.59	1870.25	334.04	268.06	533.80	898.91	1259.89	441.52	664.85
Ho	617.72	42.52	70.51	397.30	94.13	34.05	335.72	260.72	165.72	310.80	144.15	611.06	566.44	58.71	75.02	47.06	103.65	636.23	121.79	96.63	205.45	322.65	501.91	176.39	236.18
Er	2416	184	294	1726	405	149	1376	1056	633	1253	614	2508	2210	251	318	197	402	2456	495	388	933	1280	2196	794	936
Tm	454.41	37.42	58.74	334.48	80.41	31.64	262.01	198.22	113.98	233.98	124.00	487.08	436.85	51.86	63.22	40.15	74.96	472.67	94.07	72.56	197.24	233.92	488.50	161.20	170.89
Yb	3588	341	513	2797	683	295	2150	1611	929	1883	1052	3874	3436	464	549	363	630	3609	770	607	1770	1849	4021	1385	1364
Lu	530.24	58.54	88.96	444.88	115.44	55.68	346.56	248.67	153.22	297.53	172.52	603.55	537.08	83.81	94.73	69.85	108.67	585.27	129.07	107.32	294.51	296.40	672.88	231.30	225.98
Hf	11720	9694	8789	12569	10370	9252	12089	13551	8271	12654	15476	12608	12481	11404	10294	8227	8304	11608	9482	7876	14711	10739	15267	17083	9269
Ta	37.81	1.13	1.52	35.67	2.70	1.13	21.94	22.68	1.15	24.83	15.55	13.28	48.13	2.71	2.55	0.87	1.64	13.79	3.72	1.25	17.56	4.80	44.56	31.42	2.29
Pb	86.19	1.03	2.06	47.21	2.29	1.28	26.86	30.92	3.89	45.38	8.36	44.50	117.56	2.82	2.27	1.57	2.96	44.72	4.75	2.35	15.83	12.22	77.98	20.07	5.60
Th	4177	48	91	1961	105	54	1127	1401	127	1990	374	2084	5303	130	102	82	127	1969	229	109	772	584	3396	953	278
U	3373	82	117	2438	223	100	1597	1397	150	1917	738	2189	3795	218	180	92	141	1934	296	124	1416	686	3537	1448	345

PPM	HA-15-01	HA-15-02	HA-15-03	HA-15-04	HA-15-05	HA-15-06	HA-15-07	HA-15-08	HA-15-09	HA-15-10	HA-15-11	HA-15-12	HA-15-13	HA-15-14	HA-15-15	HA-15-16	HA-15-17	HA-15-18	HA-15-19	HA-15-20
Li	6.87	4.23	4.64	5.04	4.83	1.88	2.94	1.60	1.11	3.08	0.14	6.00	3.54	0.33	4.11	8.20	0.19	1.21	9.83	3.60
P	800	601	1823	679	1275	1561	1622	646	597	1403	1362	731	755	1784	813	1468	2544	659	1068	635
Ca	0.00	0.00	62.98	11.61	75.76	0.00	0.00	47.77	6.53	108.32	46.72	0.00	0.00	0.00	0.03	183.31	0.00	101.24	162.58	57.38
Ti	3.05	5.74	3.64	5.03	3.86	3.95	2.60	5.25	7.29	3.65	3.34	4.38	3.78	2.21	4.07	2.80	3.46	4.16	11.54	4.15
Y	1847	1814	4420	1512	2714	3217	3796	1592	1887	2865	3323	1913	2140	3359	2133	3080	5211	1912	2094	1584
Zr	472168	463075	461785	460649	454824	455533	458131	463311	462591	455976	457247	460721	460067	450065	462161	443159	447415	461465	462072	462637
Nb	4.19	4.16	12.79	3.42	6.27	8.95	10.52	3.60	3.04	7.82	9.67	4.40	1.89	7.88	5.67	7.40	15.68	4.55	5.09	3.44
La	0.01	0.02	0.05	0.00	0.01	0.02	0.01	0.09	0.00	0.50	0.01	0.01	0.00	0.00	0.04	0.18	0.05	0.16	0.17	0.02
Ce	13.46	19.75	23.01	17.50	21.81	19.83	26.39	16.36	19.08	26.85	20.41	15.22	13.18	11.20	18.22	10.65	31.94	23.95	13.49	15.23
Pr	0.06	0.05	0.09	0.04	0.06	0.04	0.06	0.10	0.08	0.30	0.06	0.07	0.21	0.04	0.05	0.09	0.17	0.10	0.09	0.05
Nd	0.61	1.26	1.56	1.13	1.65	1.10	2.01	1.42	1.49	2.74	1.38	1.25	4.28	0.85	1.23	1.96	2.54	1.56	0.86	1.16
Sm	3.52	3.75	7.73	3.34	5.72	5.47	8.15	3.81	5.39	6.91	5.56	3.55	9.00	5.54	4.02	5.17	9.75	3.46	3.68	3.69
Eu	0.72	1.06	1.38	0.81	1.15	0.99	1.50	1.11	1.96	1.24	1.04	0.89	2.32	0.80	0.93	1.00	1.62	0.99	0.70	1.04
Gd	26.11	28.15	69.95	25.99	46.77	48.36	68.21	25.31	36.75	53.11	46.32	30.08	51.18	50.93	32.52	41.20	81.80	30.86	31.18	26.16
Tb	11.41	10.94	29.26	9.96	18.86	20.89	28.01	10.12	13.41	20.42	20.04	12.09	17.95	22.29	13.18	18.41	35.79	12.41	12.94	10.26
Dy	156.42	148.65	397.26	132.75	249.23	286.39	356.88	136.66	170.21	264.99	281.98	165.65	210.54	302.12	182.14	258.38	473.57	163.70	178.70	135.39
Ho	64.94	64.01	161.33	54.16	98.75	117.25	140.97	56.59	68.52	105.25	121.38	69.29	79.73	123.12	76.17	110.96	189.73	68.04	74.93	56.43
Er	314.56	308.06	743.95	255.05	446.33	536.86	626.02	267.85	309.35	476.11	572.63	323.54	349.91	568.66	356.24	531.16	870.48	315.88	357.34	267.36
Tm	69.01	68.08	157.78	54.50	93.32	114.29	129.57	58.08	66.86	100.73	125.12	70.28	73.01	122.06	77.72	117.84	186.27	69.08	80.38	59.37
Yb	671	658	1475	519	863	1071	1188	563	633	943	1176	672	679	1147	741	1117	1738	661	771	576
Lu	134.81	133.62	283.45	103.90	167.62	204.70	225.24	112.99	126.75	180.71	227.68	131.04	129.56	215.66	142.67	217.19	323.67	130.77	149.06	112.77
Hf	11620	9594	12722	10739	11679	11963	12321	9889	9635	11733	12061	10820	9552	13657	11016	11719	12258	10546	11931	10335
Ta	1.55	1.34	4.16	1.34	2.38	3.27	3.64	1.16	0.99	2.93	2.98	1.48	0.70	3.13	1.92	2.64	5.37	1.62	2.04	1.20
Pb	2.86	3.10	12.58	5.30	11.50	9.70	21.34	3.35	3.98	11.96	6.42	3.53	3.42	9.21	3.49	3.39	16.36	3.90	3.87	2.55
Th	138.99	152.54	616.56	225.35	573.47	469.86	970.42	163.60	193.42	585.10	310.05	167.39	162.31	427.94	173.75	142.12	711.79	184.96	185.36	119.93
U	348.38	265.72	1214.50	326.67	841.33	886.69	1351.40	277.23	258.61	876.14	675.95	349.00	241.90	1091.51	366.57	510.03	1480.62	331.70	503.82	237.20

Zircon U-Pb LA-IC-MS data (corrected ratios)

	207Pb/ 206Pb	207Pb/ 206Pb	207Pb/ 235U	207Pb/ 235U	206Pb/ 238U	206Pb/ 238U	208Pb/ 232Th	208Pb/ 232Th	238U/ 232Th	
	Age (Ma)	1sigma (Ma)	Age (Ma)	1sigma (Ma)	Age (Ma)	1sigma (Ma)	Age (Ma)	1sigma (Ma)		Conc.
LTp										
HA15-01	287	78	238	7	232	3	218	5	1	97%
HA15-02	191	87	212	7	214	2	217	6	1	98%
HA15-03	206	42	220	4	221	2	215	4	1	99%
HA15-04	209	78	237	7	240	3	252	6	1	98%
HA15-05	195	56	230	5	233	2	213	4	1	98%
HA15-06	232	62	240	5	241	2	217	4	1	99%
HA15-07	220	43	236	4	237	2	234	3	1	99%
HA15-08	346	86	235	7	224	2	219	5	1	95%
HA15-09	272	92	220	7	215	2	212	5	1	97%
HA15-10	217	86	231	5	232	2	209	4	1	99%
HA15-11	211	59	219	5	219	2	210	5	1	99%
HA15-12	265	76	224	7	220	3	213	6	1	98%
HA15-13	213	115	217	9	218	3	214	6	1	99%
HA15-14	167	42	228	4	234	2	220	4	1	97%
HA15-15	220	98	215	8	215	2	197	6	1	99%
HA15-16	211	63	214	5	214	2	234	7	1	99%
HA15-17	243	46	237	4	237	2	234	4	1	99%
HA15-18	220	77	220	6	218	2	215	5	1	99%
HA15-19	254	63	224	6	219	2	213	5	1	97%
HA15-20	146	83	222	7	229	2	222	6	1	97%

	207Pb/ 206Pb	207Pb/ 206Pb	207Pb/ 235U	207Pb/ 235U	206Pb/ 238U	206Pb/ 238U	208Pb/ 232Th	208Pb/ 232Th	238U/ 232Th	
	Age (Ma)	1sigma (Ma)	Age (Ma)	1sigma (Ma)	Age (Ma)	1sigma (Ma)	Age (Ma)	1sigma (Ma)		Conc.
MGp										
HA-01-01	256	31	229	3	227	1	239	3	1	98%
HA-01-02	367	156	225	13	219	3	237	9	1	97%
HA-01-03	309	123	226	10	221	3	230	6	1	97%
HA-01-04	239	32	237	3	236	1	249	3	1	99%
HA-01-05	394	130	229	12	214	3	230	10	1	93%
HA-01-06	376	125	240	11	232	3	247	9	1	96%
HA-01-07	332	36	242	4	232	1	242	3	1	95%
HA-01-08	206	39	224	3	225	1	230	3	1	99%
HA-01-09	1567	73	387	11	222	3	315	6	1	45%
HA-01-10	306	39	237	4	230	1	232	3	1	96%
HA-01-11	656	50	279	6	236	2	252	5	1	83%
HA-01-12	272	35	240	3	236	1	235	3	1	98%
HA-01-13	256	30	237	3	235	1	230	3	1	99%
HA-01-14	300	80	230	7	223	2	233	5	1	97%
HA-01-15	146	94	227	8	235	3	237	6	1	96%
HA-01-16	309	133	220	12	213	3	210	7	1	96%
HA-01-17	354	189	225	15	214	3	220	11	1	95%
HA-01-18	217	32	229	3	229	1	231	3	1	99%
HA-01-19	87	-116	204	6	215	2	214	4	1	94%
HA-01-20	117	126	200	10	209	3	224	6	1	95%
HA-01-21	198	53	227	4	229	1	242	4	1	99%
HA-01-22	333	52	225	4	220	1	215	3	1	97%
HA-01-23	256	31	232	3	229	1	235	3	1	98%
HA-01-24	150	39	219	3	224	1	219	3	1	97%
HA-01-25	217	70	209	5	209	2	211	3	1	99%

G. The petrogenesis of selected cordierite granites in South America (published in JSAES)

Journal of South American Earth Sciences 92 (2019) 417–434

Contents lists available at ScienceDirect

Journal of South American Earth Sciences

journal homepage: www.elsevier.com/locate/jsames

Cordierite-bearing granitic rocks in South America: Contrasting sources and conditions of formation

V.P. Ferreira[a,*], A.N. Sial[a], A.J. Toselli[b], J.R. de Toselli[b], P.G. Molina[c], M.A. Parada[c], J.J. Celino[d], J. Saavedra[e]

[a] NEG-LABISE, Departamento de Geologia, UFPE, Recife, PE, 50740-550, Brazil
[b] INSUGEO, Universidad de Tucuman, Tucuman, 4000, Argentina
[c] Departamento de Geología, Centro de Excelencia en Geotermia de los Andes, Universidad de Chile, Santiago, Chile
[d] Departamento de Geologia e Geofísica Aplicada, Instituto de Geociências, UFBA, Salvador, BA, 40170-290, Brazil
[e] Instituto de Agrobiología y Recursos Naturales CSIC, 37071, Salamanca, Spain

ARTICLE INFO

Keywords:
Cordierite granites
Peraluminous granites
Mineral chemistry
Granite petrogenesis

ABSTRACT

Mineralogy, geochemistry and isotopic data for Ediacaran, Ordovician to Devonian, and Upper Triassic cordierite-bearing granitoids respectively from Brazil, Argentina and Chile are discussed here. Syn-collisional Lower to Middle Ordovician, and post-collisional Upper Devonian garnet-free granitoids from Argentina intruded greenschist-to amphibolite-facies metasedimentary rocks. Garnet-bearing and garnet-free monzogranites of the Nanuque Suite, Brazil, intruded high-grade gneisses and migmatites, and in the High Andes Belt, the Los Tilos garnet-free granite was emplaced into an early Permian batholith during an extensional event. Mineralogical, geochemical and isotopic characteristics of the granites from Argentina and Brazil, such as presence of peritectic and (±) restictic cordierite, low-magnetic susceptibility (MS) values ($0.03–0.2 \times 10^{-3}$ SI), negative εNd (−7.3 to −5.0) and high δ^{18}Ozircon values (> 9‰), suggest a major aluminous metasedimentary source. Data for the Chilean pluton (small volume, associated with coeval metaluminous granites, low δ^{18}Ozircon values (6.6–7.4‰), slightly negative εNd (−4), and high MS values ($1.4–2.5 \times 10^{-3}$ SI) are compatible with a less-evolved source, possibly a metaluminous granitic rock. P-T magma crystallization conditions of the cordierite-bearing granites from Argentina are 2–4 kbar and 630–720 °C; and 3.6–4.0 kbar and at 670 − 700 °C for their cordierite. The Nanuque magma formed P > 6 kbar; T = 750–800 °C, and magma emplaced at ~3 kbar. Their cordierite formed at P = 5.0–5.2 kbar and T = 720 − 740 °C. P-T conditions of the Los Tilos magma emplacement are P ~ 3 kbar and T ~670 °C. Cordierite-paramorph β-quartz nodules in this pluton, surrounded by leucocratic rims, have been formed by biotite dehydration reactions. This study confirms that cordierite in granites can be produced from different source rocks by a number of processes, at different P-T conditions.

1. Introduction

The formation of peraluminous magmas produced by partial melting of continental crust rocks (e.g. Miller, 1985; White and Chappell, 1977; Wickham, 1987) can occur at relatively low temperatures either by (a) supply of water from dehydration reactions (e.g., Gardien et al., 1995) or (b) volatile influx at the source region (e.g., Ebadi and Johannes, 1991; Weinberg & Hasalová, 2015). Higher temperatures are required to generate crustal granites at dry conditions (Johannes and Holtz, 1996). These high temperatures can be achieved by radiogenic heating in a thickened crust (Bea, 2012), mechanical heating in shear zones (e.g., Nabelek et al., 2010), increased mantle heat flow in back arc settings (Currie and Hyndman, 2006), or a combination of them (Clark et al., 2011).

The formation of large volumes of peraluminous melts is controlled mainly by the P-T-X_{H2O} anatexis conditions (e.g. Clemens and Wall, 1981; Holtz and Johannes, 1991), whereas the P-X_{H2O} conditions (Patiño Douce, 1999) and source-rock composition play a major control on the resulting peraluminosity of primary magmas (e.g. Barbarin, 1996; Villaseca et al., 1998). The resulting mineralogical accessory assemblages found in peraluminous granitoids consist mainly of muscovite, garnet, tourmaline and lesser biotite (Clarke, 1995). Biotite-rich peraluminous tonalites, granodiorites and monzogranites contain cordierite, garnet, and in lesser amount, aluminum silicates (Barbarin, 1996, 1999; Villaseca et al., 1998). Moreover, a high abundance of primary muscovite or cordierite is commonly found in suites of peraluminous granitoids characterized by an alumina index > 1 (Barbarin, 1999).

* Corresponding author.
E-mail addresses: valderez@ufpe.br (V.P. Ferreira), sial@ufpe.br (A.N. Sial), ajtoselli@yahoo.com.ar (A.J. Toselli), juanitarossi@gmail.com (J.R. de Toselli), pamolina@ing.uchile.cl (P.G. Molina), maparada@cec.uchile.cl (M.A. Parada), joil@ufba.br (J.J. Celino), julio.saavedra@irnasa.csic.es (J. Saavedra).

https://doi.org/10.1016/j.jsames.2019.03.022
Received 24 November 2018; Received in revised form 20 March 2019; Accepted 20 March 2019
Available online 01 April 2019
0895-9811/

Cordierite is a low-pressure mineral that appears above the solidus of peraluminous felsic granites, in low P and high T terrains that have suffered extensive partial melting (Barbero and Villaseca, 1992). Experimentally-determined phase relationships of an S-type ignimbrite indicate that in reduced felsic and iron-rich (FeO_{total} > 1.5 wt %) magmas and at P > 4–5 kbar, cordierite crystallizes at near-solidus conditions, while near-liquidus cordierite occurs at or below 2 kbar (Clemens and Birch, 2012; Scaillet et al., 2016). Magmatic cordierite could be formed in cooling or ascending magmas, as peritectic or cotectic phases (Clarke, 1995). Peritectic cordierite, ascribed to melt-producing reactions, is formed in response to rising temperature (typically found within leucosomes of migmatites), the most common being the reaction aluminum silicate + biotite + quartz → liquid + K-feldspar + cordierite. Furthermore, experimental studies developed by Patiño Douce (1999) indicate that cordierite can be formed in magmas derived from partial melting of amphibolite, suggesting that presence of cordierite is not always indicative of melts derived from interaction of basaltic magmas with metapelites, as previously suggested by White and Chappell (1977).

In summary, considering the multiple possible origins of cordierite in peraluminous granites, unravelling the context of its formation is subject to inference of source materials or emplacement depth (and transport) conditions. As a consequence, several authors have dealt with the mineralogical composition of cordierite (e.g., Pereira a& Bea, 1994; Schreyer, 1965; Villaseca et al., 2008) to discriminate between a metamorphic, near solidus, or high-temperature magmatic origin. Thus, the comparison of contrasting cordierite-bearing granitoids, formed in distinct geodynamic settings, is of particular interest to better conceptualize diverse deep-crustal/shallow magmatic or metamorphic processes, crust fertility and the associated thermal structure.

The main scope of this study is to compare cordierite-bearing granitoids of selected plutons of different ages and tectonic settings from the Paleozoic Pampean Ranges, Argentina, Neoproterozoic Nanuque Suite, eastern Brazil, and Upper Triassic Frontal Range belt, north-central Chile.

2. Analytical methods

Unless a reference is specified, new major and trace-element chemical analyses were performed by XRF in a Rigaku RIX 3000 unit, at the NEG-LABISE, Department of Geology, Federal University of Pernambuco, Brazil, by standard procedures of comparing sample X-rays intensity with those of certified standard samples (calibration curves method), using fused disks in which dried lithium tetraborate/sample powder = 5. Precision is better than 1%. Zircon grains were separated by conventional procedures using heavy liquids and magnetic separator after concentration by panning. Zircon concentrates were further purified using HF, as described by Valley et al. (1995). Quartz grains were hand-picked under a binocular microscope. Oxygen isotope ratios of quartz and zircon grains was determined after O2 extraction of mineral concentrates in a CO2 laser-based high vacuum extraction line, using bromine pentafluoride as reagent, following the procedures described in Valley et al. (1995). The isotopic ratios were determined in a Thermo-finningan Delta V Advantage mass spectrometer at the NEG-LABISE. Results are expressed in the ‰ VSMOW notation. CO_2 generated from Borborema Skarn Calcite (BSC), calibrated against international standards, was used as the reference gas; reproducibility of the measurements was better than ± 0.1‰. The values determined for the standard NBS-20 in a separate run against BSC yielded δ^{13}CVPDB = −1.05‰, and δ^{18}OV-PDB = −4.22‰. These results are in close agreement with the values reported by the US National Bureau of Standards (−1.06‰ and −4.14‰, respectively). Sr and Nd isotopic composition data were determined at the Institute of Geosciences, University of São Paulo, according to the methology described by Sato et al. (1995). Non-magnetic zircon grains were analyzed for U–Pb and Hf isotopic by MAICP-MS at the Institute of Geosciences, University of Brasília, Brazil. Details on the methodology are described in Matteini et al. (2010). Quantitative electron microprobe analyses of major and trace elements of samples from Chile and Argentina were conducted using a JEOL JXA-8230 electronic microprobe at the Laboratorio de Microscopía Electrónica y Análisis por Rayos X, Universidad Nacional de Cordoba, Argentina. Spot analyses were performed using a 15 kV accelerating voltage, a 10 nA current, and a 10 μm diameter beam. Reference standard materials were measured before each session for peak overlap, background and offline corrections. Different crystals were used to perform the different analyses of biotite and cordierite, respectively: TAP (F, Na, Mg, Al) and (Na, Mg, Al, Si); PETJ (K, Cl, Ca) and (K, Cl, Ca); LIF (Ti) and LIFH (Cr, Mn, Fe, Zn) for both phases; and PETH (Si) in biotite. Results were corrected for instrumental beam-matrix effects and instrumental drift by the phi-rho-Z method (CITZAF; Armstrong, 1995) Total magnetic susceptibility (MS) was measured using a field portable MS meter digital kappameter KT-5; measurements are reported in SI units. Representative whole rock and mineral chemical analyses and isotopic data are listed in Tables 1 through 7 of the Supplementary Material.

3. Geological setting and petrography

Major petrographic, geochemical and isotopic features of studied granites are summarized in Table 1.

3.1. Cordierite-bearing granitoids of the central belt, NW Argentina

Paleozoic magmatism in the Sierras Pampeanas of northwestern Argentina is marked by four magmatic pulses: a) Pampean magmatism, 515–535 Ma; (b) Famatinian magmatism, 463–484 Ma; (c) Achalian magmatism, 366–393 Ma and (d) Early Gondwana magmatism, 322–357 Ma (Dahlquist et al., 2018, and references therein). Cambrian–Ordovician granitoids of the Sierras Pampeanas of northwestern Argentina were generated during the Famatinian orogenic cycle, and most of them are related to the main subduction phase of this cycle (Grosse et al., 2009). These granitoids are distributed along two subparallel NNW-SSE trending belts, including a calc-alkaline I-type granitic belt and a peraluminous S-type granitic belt (Toselli et al., 2002). The Sierra de Velasco, Mazan and Capillitas batholiths are part of this peraluminous belt and will be focused in this paper (Fig. 1).

The Capillitas batholith was emplaced into low-grade metamorphic rocks of the Central Batholith Zone (Fig. 1) and is characterized by high abundance of microcline megacrysts and micas. They exhibit two granitic facies, a porphyritic to equigranular cordierite-bearing monzogranite mafic facies that shows high abundance of biotite and muscovite, and a usually equigranular cordierite-free felsic facies, with low abundance of two micas. The mafic two-mica porphyritic cordierite-bearing monzogranites constitute the largest outcrops of the batholith. Cordierite in these rocks occurs as anhedral corroded grains, surrounded by micaceous material. (Rossi et al., 2002).

A U–Pb zircon age of 470 ± 3 Ma (Rapela et al., 1999) was determined for the Capillitas granite.

The Mazan batholith exibits several lithological types that show distinct grain sizes and accessory minerals (Toselli et al., 2014). Two granite facies are recognized: deformed, coarse-grained, equigranular to porphyritic rocks and (b) more differentiated, coarse-grained to pegmatitic granites, with remarkable mineralogical banding, lacking deformation and alteration. Large blocks of cordierite-bearing granites are hosted within this granite. A SHRIMP U–Pb zircon age of 484 ± 3 Ma (Pankhurst et al., 2000) was determined for the Mazan granite. A TIMS U–Pb zircon age of 492 ± 11 Ma was measured in the current study.

The Ordovician–Devonian Sierra de Velasco batholith is mainly composed of metaluminous to peraluminous, weakly to strongly-foliated granites intruded by Carboniferous post-tectonic undeformed granites. The older granitoids are strongly peraluminous, porphyritic two mica-garnet- sillimanite- and kyanite-bearing metamonzogranites, with subordinate strongly peraluminous porphyritic biotite-cordierite

Table 1
Major geological, chemical and isotopic features of the studied cordierite granites.

	Argentina	Brazil	Chile
Rock type	monzogranites, ± granodiorite and tonalite	monzogranite	granite
Host rocks	low-grade metasedimentary rocks (1) Señor de la Peña = granitoids (2,3)	pyroxene granulite, garnet-bearing paragneisses and migmatites (8, 9)	Hbl-Bi tonalite/granodiorite; two-mica granite (12)
Tectonic setting	subduction related, syn-to late tectonic (4)	syn-collisional (11)	extensional (post-collisional) (13)
Age	Capillitas = 470 ± 3 Ma (5) Mazan = 484 ± 3 Ma (6); 492 ± 11 (16)	573 ± 5 Ma (10)	227- 204 Ma (13,15)
Diagnostic minerals	anhedral corroded ± pinnitized cordierite, muscovite, ± andalusite, ± sillimanite, ± monazite. Cm-scale garnet-bearing enclaves	pinnitized cordierite: euhedral, in nodules, fine-grained anhedral, small euhedral included in K-feldspar megacryst, intergrowth with garnet. Garnet, monazite, hercynite, ± sillimanite (11)	pinnitized cordierite in nodules surrounded by leucocratic rims: subhedral, poikilitic, interstitial (12). Bipyramidal quartz, ± monazite, ± xenotime.
A/CNK	1.1–1.7	1.5–2.3	0.96–1.3
magnetic susceptibility (x 10^{-3}SI)	Capillitas, Mazan = 0.1–0.7; Señor de la Peña = 2.5–7.3 (16)	0.03–0.15 (16)	1.3–2.7 (16)
($^{87}Sr/^{86}Sr$)i (back calculated)	Mazan = 0.71249; Señor de la Peña = 0.71229; Capillitas = 0.7146; Velasco = 0.7109 (7)		0.7145 (14)
εNd(t)	Mazan = −8.6; Señor de la Peña = 7.6 (16)	Nanuque = 6.6; Lajedão = −7.3 (11)	−4.0 (14)
tDM	Mazan = 1.83 Ga; Señor de la Peña = 1.68 Ga (16)	Nanuque = 1.83 GA; Lajedão = 1.79 Ga (11)	
$\delta^{18}O$ (zircon) ‰VSMOW	Capillitas = +7.8; Velasco = +9.5 (16)	Nanuque = +10.92 to +11.82 (16)	+6.1 to +7.4 (16)

1 = Rossi et al. (2002); 2 = Rossi de Toselli et al., 1985; 3 = Toselli et al. (1991); 4 = Grosse et al. (2009); 5 = Rapela et al. (1999); 6 = Pankhurst et al. (2000); 7 = Toselli et al. (2002); 8 = Celino et al. (2000); 9 = Celino and Conceição, 1993; 10 = Silva et al. (2002); 11 = Celino, 1999; 12 = Parada (1988); 13 = Hervé et al. (2014); 14 = Parada et al. (2007); 15 = Coloma et al. (2017); 16 = this work.

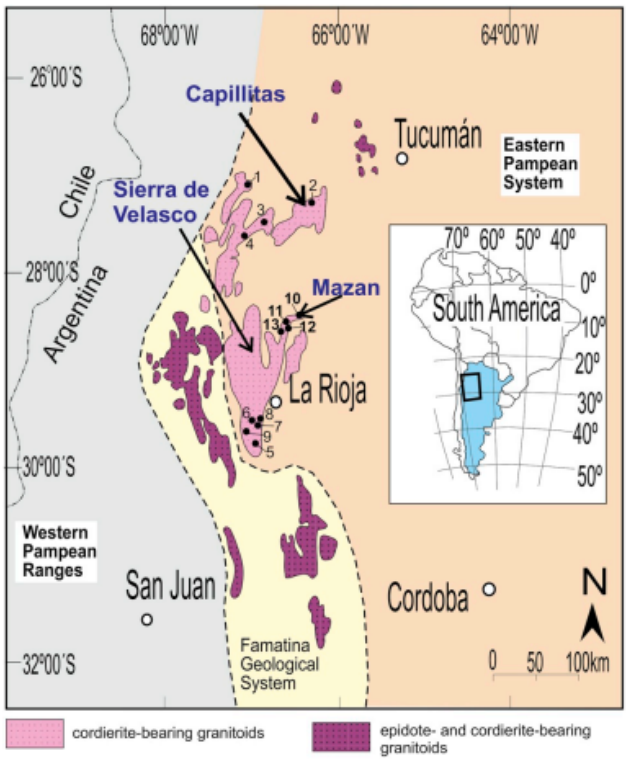

Fig. 1. Sketch of the geological map of northwestern Argentina showing the major cordierite-bearing and magmatic epidote-bearing granitoids in the Pampean Ranges (modified from Rossi et al., 2002). Numbers indicate location of the sample analyzed by EPMA.

metamonzogranites and moderately peraluminous coarse-to medium-grained biotite metagranodiorites and metatonalites (Grosse et al., 2009, and references therein). Among the Ordovician–Devonian granitoids are the Señor de la Peña and the Velasco plutons, described in this study.

The Velasco pluton of the Sierra de Velasco batholith consists of a granular monzogranite that contains abundant cordierite (up to 10%; Fig. 2a); a U–Pb monazite age of 465 ± 12 Ma was determined in this pluton by De los Hoyos et al. (2011), and a U–Pb zircon age of 481 ± 3 Ma by Pankhurst et al. (2000).

The Señor de la Peña cordierite-bearing granite is a late-tectonic Devonian pluton, intruded into Ordovician granitoids. The rocks have perthitic microcline megacrysts and are characterized by pinnitized cordierite, as well as sillimanite and andalusite. Tonalitic enclaves are common. In contrast to altered corderite from host rock, fresh cordierite with magnetite inclusions is found at the contact between enclaves and the host granite. A TIMS U–Pb zircon age of 376 ± 8 Ma was determined for this pluton (Toselli et al., 2003b).

3.2. Cordierite-bearing granites of the Araçuaí Belt, eastern Brasil

The studied granitoids occur in the Araçuaí Belt, eastern Brazil, next to the border of the São Francisco Craton, hosted in the Archean/Paleoproterozoic Caraíba-Paramirim Complex, Mesoproterozoic Paraíba do Sul Complex and Neoproterozoic Macaúbas Group (Fig. 3). There are three major granitic suites in the eastern Araçuaí Belt: strongly peraluminous Nanuque Suite (cordierite-bearing granites), peraluminous São Paulinho Suite (two-mica monzogranite, quartz monzonite), and metaluminous to weakly peraluminous Itagimirim Suite (magmatic epidote-bearing monzogranites and granodiorites). The Nanuque Suite in the southernmost portion of the state of Bahia and north of the state of Minas Gerais is the only one among these granitoids that contains cordierite (Fig. 2; Celino et al., 2000). A common feature of the granites of this suite is local interfingering between granitoids and garnet-spinel granulites that suggests in-situ partial melting at high pressure.

The Nanuque Suite encompasses the Nanuque, Lajedão, Serra dos Aimorés and Cajuita plutons and includes coarse-to very coarse-grained two-mica or muscovite-bearing porphyritic monzogranites. The Nanuque pluton consists of weakly foliated garnet- and cordierite-bearing monzogranites in which cordierite shows two textural types: (a) euhedral crystals usually up to 2.5 cm long, associated with biotite, garnet and cm-sized nodules and (b) fine-grained anhedral crystals; both types pinnitized. The former type is interpreted as magmatic, while the latter, is interpreted as restitic crystals (Celino and Conceição, 1993). An important feature of these granites is the presence of both microgranular mafic magmatic and metamorphic enclaves. The magmatic enclaves are non-foliated diorite to quartz-diorite that while the metamorphic ones are surmicaceous enclaves with cordierite and garnet aggregates (Celino and Conceição, 1993).

The Lajedão pluton exhibits texture and mineralogical composition similar to those of the Nanuque pluton except for its fine-grained

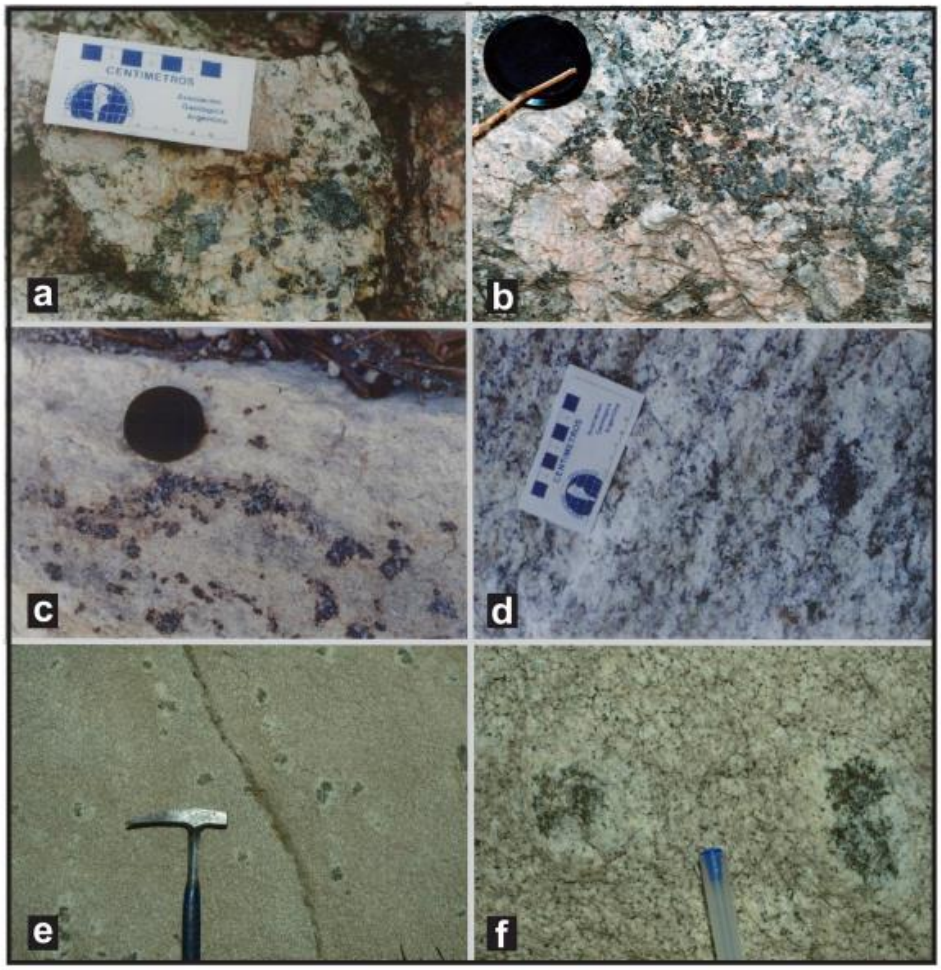

Fig. 2. (a) Cordierite in the Velasco pluton, Sierra de Velasco, near Aimogasta, Argentina. (b) Well-developed cordierite crystals in the Señor de la Peña pluton, replaced by pinnite. (c) Garnet, plagioclase, quartz in a cordierite nodule in monzogranite of the Nanuque suite, Brazil. Magnification is about 10x. (d) Aggregate of cordierite and garnet in monzogranite of the Nanuque suite, Brazil. (e) Fine-grained granite with cordierite nodules in Los Tilos pluton, Elqui Valley, Chile. (f) Altered subhedral cordierite and β quartz nodules with notorious quartz-feldspar leucocratic rims of the Los Tilos pluton, Chile.

texture, and presence of small lamellae of muscovite associated with biotite. These granitoids are cut by cordierite-bearing aplitic dikes that, according to Celino (1999), are cogenetic with the host granite, and represent a more evolved facies.

The Serra dos Aimorés pluton exhibits structures that vary from foliated fabrics in its central portion to cataclastic margins, Compared to the Nanuque pluton, this pluton shows larger amounts of muscovite (1%) and smaller of cordierite (1%). Garnet crystals form clots of up to 3 cm long.

The NE-SW elongated Cajuita pluton is composed of porphyritic granitoids In which cordierite occurs as (a) 3–4 cm long euhedral crystals, which are sometimes pinnitized, (b) small euhedral crystals included in K feldspar megacrysts or in intergrown with garnet, or (c) small irregular relict crystals included in plagioclase and biotite. (Celino and Conceição, 1993).

A Sm–Nd isochron (whole rock, feldspar-garnet, monazite and heavy mineral concentrate) yielded an age of 761 ± 67 Ma for the Nanuque Suite (Celino, 1999). Silva et al. (2002) determined a SHRIMP U–Pb zircon age of 573 ± 5 Ma for the Nanuque pluton, interpreted as crystallization age.

3.3. Cordierite-bearing granites of the High Andes, central Chile

In the High Andes of Central Chile, Upper Triassic cordierite-bearing leucogranites of the Los Tilos pluton form part of a Late Triassic peraluminous and metaluminous suite together with a singular ferrohedenbergite-bearing peralkaline A-type granite (Monte Grande pluton), and minor cumulate-gabbro stocks (Fig. 4). All together these plutons form part of the subsolvus-hypersolvus suite as defined by Parada (1988), which in part belongs to the Permian–Triassic Ingaguás Superunit (Mpodozis and Kay, 1992). These magmas were emplaced coevally with a mafic dike swarm at shallow levels, into a partially exhumed Carboniferous–Early Permian basement (Hervé et al., 2014 and references therein). The plutons formed during an attenuation in subduction (Coloma et al., 2017; del Rey et al., 2016; González et al., 2017) between upper Paleozoic and Middle Jurassic arc magmatism, when extensional conditions prevailed (Mpodozis and Kay, 1992; Parada, 1988; Parada et al., 1991).

Parada et al. (1991) inferred a crustal extension of up to 30% to roughly accommodate the volume of both, the Upper Triassic plutons and mafic dike swarm.

Lu–Hf and O isotopic values of zircon from granitic plutons indicate an evolution from crustally derived-magmas during the Late Paleozoic magmatic arc phase to more mantle-like compositions during the Late Permian–Triassic, when extensional conditions prevailed after an episode of exhumation (Hervé et al., 2014). The influence of crustal components in the Los Tilos pluton have been locally recognized (Hervé et al., 2014). The Los Tilos pluton as defined by Parada (1988) shows intrusive contacts without significant interaction with the host rocks, which are Upper Paleozoic metaluminous granitoids and two-mica peraluminous leucogranodiorites (Parada et al., 1981). The presence of cordierite-bearing nodules is the most outstanding feature of this pluton (Fig. 2e and f). They consist of rounded 2–5 cm aggregates of quartz, cordierite and plagioclase, surrounded

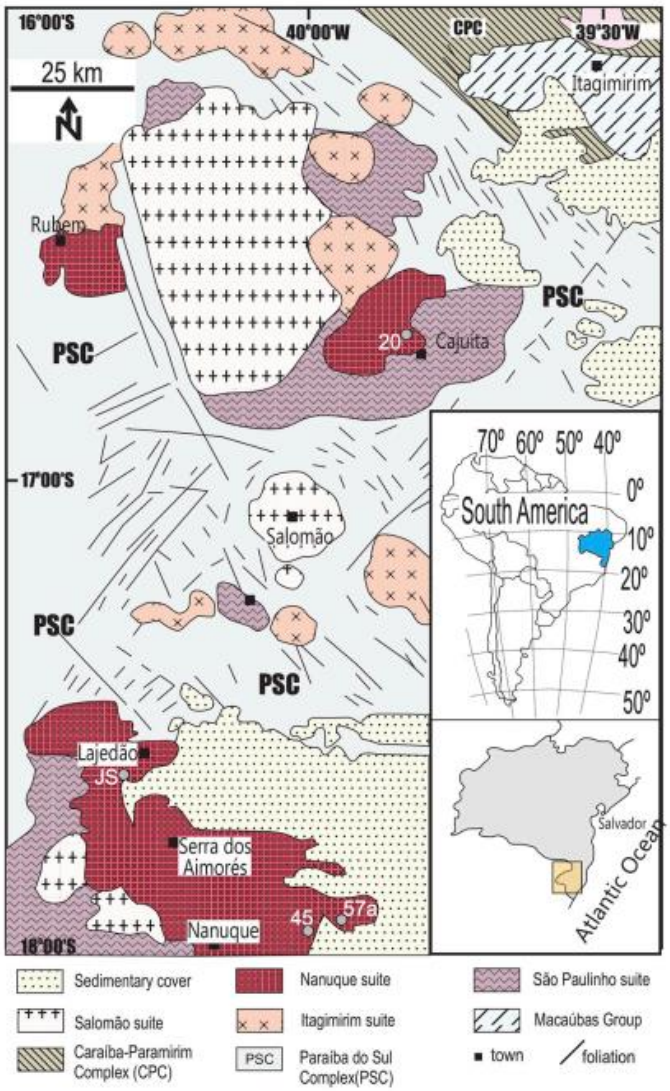

Fig. 3. Simplified geological map of the southern Araçuaí Belt, eastern Brazil, showing the studied granitic suite (modified from Celino, 1999). Numbers indicate location of the sample analyzed by EPMA.

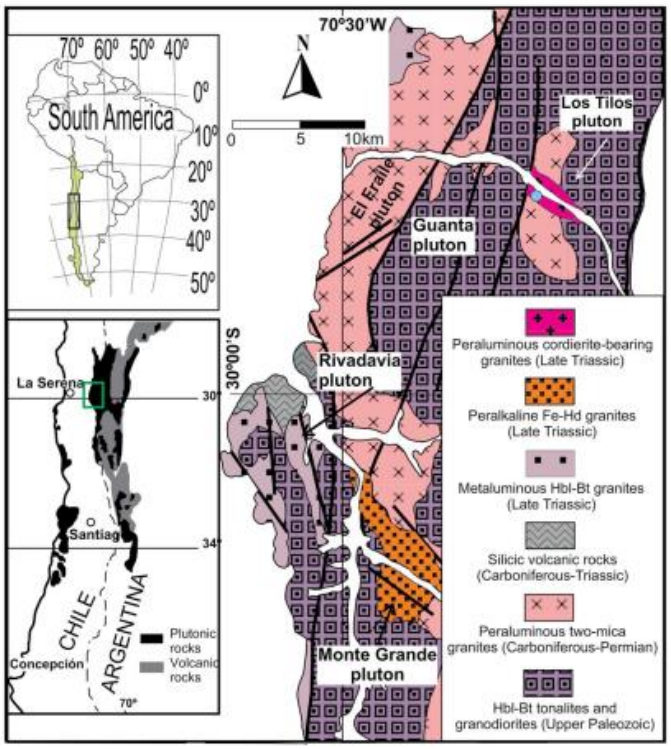

Fig. 4. Simplified geological map of the High Andes batholith, central Chile, showing the Los Tilos cordierite-bearing granite (modified from Parada, 1988). Location of the sample analyzed by EPMA is indicated by a filled blue circle. (For interpretation of the references to colour in this figure legend, the reader is referred to the Web version of this article.)

by thin leucocratic rims. Quartz may occur as large subhedral grains, commonly with hexagonal-bipyramidal habit. Cordierite grains contain small euhedral bipyramidal β-quartz paramorphs and plagioclase inclusions, suggesting magmatic conditions. Presence of partially resorbed β quartz grains suggests they were pushed away outside their stability field during fast emplacement, and this is consistent with previous works advocating to shallow, near eutectic, rapidly cooling emplacement conditions. For instance, Parada (1988) describes granophyric textures (low pressure, high undercooling) in other plutons (Paiguano and Rivadavia plutons) of the same Upper Triassic hypersolvus-subsolvus suite. Small and scarce andalusite-bearing inclusions are locally observed.

A wide range of U–Pb zircon ages distributed from *ca.* 227 to 204 Ma for the Los Tilos cordierite-bearing leucogranitoids have been determined in former studies by SHRIMP and LA-ICP-MS (Hervé et al., 2014; Coloma et al., 2017). Hervé et al. (2014) also reported seemingly inherited zircon cores and variable width overgrowth textures in cathodoluminescence images. These ages are roughly analogous to the K–Ar ages of the Upper Triassic–Lower Jurassic Tranquilla-Millahue intrusive bimodal (leucogranites and mafic dikes) complex, located far to the west (*ca.* 150 km) in the Coastal Range (Gana, 1991). The analyzed Los Tilos zircon grains have Th/U ~ 0.5 consistent with a magmatic origin, according to the Hoskin and Schaltegger (2003) criteria.

4. Geochemical characteristics

In silica versus oxides diagrams, the Capillitas, Mazán, Señor de la Peña, Velasco plutons present a negative correlation between CaO, total Fe_2O_3, MgO and TiO_2 and silica (Fig. 5a, b, c, d), which ranges from 64.5 to 77.1%. The granites have (Fe_2O_3 + MgO + TiO_2) > 3 (Fig. 5e), with exception of the felsic facies of the Capillitas granite that have values < 3. The rocks are calc-alkalic, peraluminous, and have A/CNK (molar Al_2O_3/(CaO + Na_2O + K_2O) values between 1.1 and 1.7 (Fig. 5f), and present La/Yb ratios mostly < 25 (Fig. 5g). Together with the presence of cordierite, andalusite and sillimanite, these features suggest that the studied plutons crystallized from melts derived from garnet-free source.

The plutons of the Nanuque Suite, Brazil, are calc-alkalic and silica ranges from 66.0 to 75.2%, the cordierite garnet bearing-granites (Nanuque and Lajedão) showing higher values than the cordierite granites (Serra dos Aimorés and Cajuíta plutons). The garnet-cordierite-bearing granitoids have (Fe_2O_3 + MgO + TiO_2) > 4 (Fig. 5e); in the cordierite-bearing leucogranites this value can be as low as 2. The cordierite-bearing granites present more variable and higher A/CNK values (~1.5–2.3) and have positive correlation with whole-rock silica contents than cordierite garnet bearing granites, which show these values around 1.5, and no apparent no correlation with silica contents (Fig. 5f). The majority of these granitoids has La/Yb values > 25 up to 950 (Fig. 5g), which together with steep upper crust-normalized REE patterns (Fig. 6) suggest a deep garnet-bearing crustal-source.

In the Los Tilos pluton from Chile SiO_2 ranges from 68.4 to 77.67%, and A/CNK values from 0.96 to 1.3, indicating peraluminous to weakly metaluminous character (Fig. 5f). In Harker's diagrams, CaO, total Fe_2O_3, MgO and TiO_2 show negative correlation with increasing silica (Fig. 5a, b, c, e). The values of (Fe_2O_3 + MgO + TiO_2) < 3 are the lowest among the studied cordierite-bearing granitoids (Fig. 5e). La/Yb ratios are generally below 25 (Fig. 5g) in a pattern that suggests a

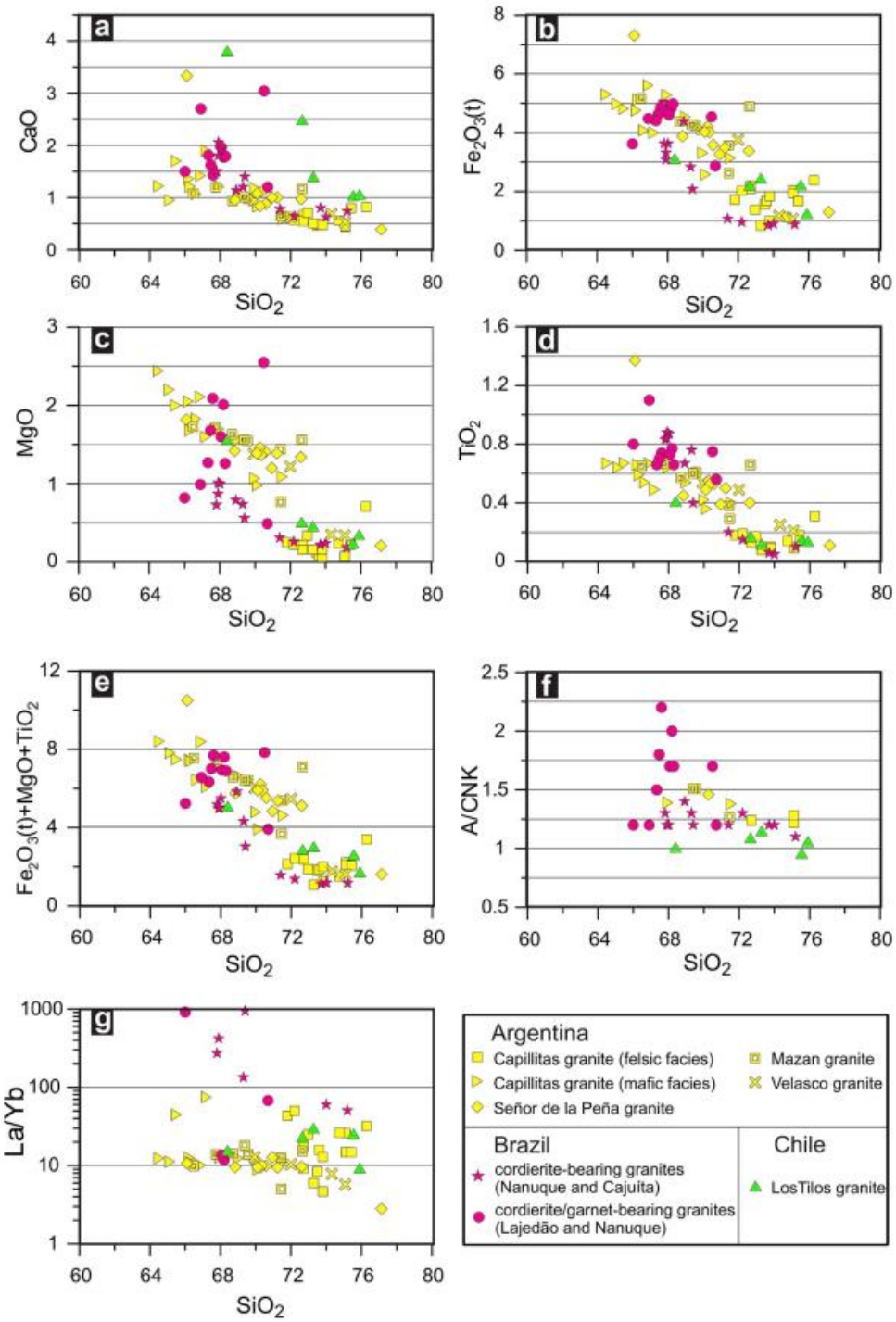

Fig. 5. Binary plots for cordierite-bearing granitoids from Argentina, Brazil and Chile.

garnet-free source. This, together with presence of andalusite and muscovite, suggests shallow depth (< 14 km) of magma crystallization. Similar shallow-pressure conditions are suggested by flat bulk upper crust-normalized REE patterns, values around 1 or lower (Fig. 6).

5. Mineral chemistry

5.1. Cordierite composition

The analyzed cordierite grains from the studied Argentinian and Chilean plutons are mostly magnesian (Fe/(Fe + Mg) < 0.5), and Al varies from 4.0 to 4.10 a.p.f.u. The Brazilian cordierite, on the other hand, is ferroan Fe/(Fe + Mg) > 0.5, and presents higher Al a.p.u.f. values (4.22–4.33).

The values of Fe/(Fe + Mg) of cordierite from the Los Tilos granite (0.48–0.50) and Brazilian plutons (0.50–0.57) are ascribed as typical of cordierite formed from peraluminous magma according to the Schreyer (1965) criteria (Fig. 7a). Cordierite composition of all granites from Argentina shows larger variation, from 0.36 to 0.52 (average 0.40 ± 0.05), in a compositional range that could be ascribed either to metamorphic or igneous origin according to the criteria of Schreyer (1965). This dubious character of the cordierite from Argentina is also observed in other discriminating diagrams such as (Na_2O + K_2O + CaO) versus MnO (Fig. 7b) and (K + Na) plotted against Mg/(Mg + Fe + Mn) (Fig. 7c). The analyzed cordierite grains from Brazil and Chile, on the other hand, plot in the field of typical magmatic cordierite. In these diagrams the compositions of these cordierites plot together with the

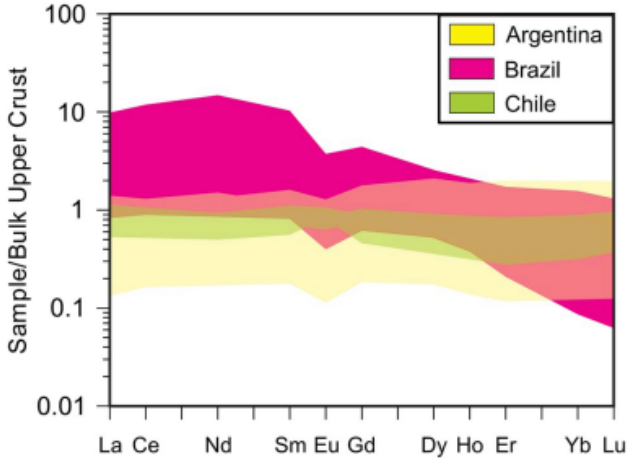

Fig. 6. Rare earth element compositional fields for cordierite-bearing granitoids from Argentina, Brazil and Chile. Bulk upper crust normalization values are from Taylor and McLennan (1985).

compositions of magmatic cordierite as described in Canada (Erdmann et al., 2004), Spain (Villaseca and Barbero, 1994; Pereira and Bea, 1994), Argentina (Alasino et al., 2010) and France (Barbey et al., 1999).

5.2. Biotite composition

Biotites shows mean Fe/(Fe + Mg) ratios of 0.60 ± 0.04, 0.55 ± 0.09, and 0.59 ± 0.02 (1σ), for the granites from Argentina, Brazil, and Chile, respectively. F is present in all biotite grains from Argentina (0.43–0.99%) and Chile (0.27–0.61%), and in most analyzed grains from Brazil (1.72–1.97%).

Ti a.p.f.u. of biotite from the Brazilian granites are higher (average 0.48 ± 0.12) than those from Argentina (average 0.37 ± 0.08) and Chile (average 0.36 ± 0.04). On the other hand, the average Al^{IV} (2.41 ± 0.12) for the biotite from the Brazilian granites are lower than in the other plutons (2.68 ± 0.01 and 2.58 ± 0.13, respectively in Argentina and Chile). Ti in biotite is believed to be dependent on the temperature of crystallization, while Al^{IV} is higher in biotite formed at lower temperature of crystallization to balance for the substitution of Al^{IV} for Mg^{2+} and Fe^{2+} (Albuquerque, 1973). So, the higher Ti and lower Al^{IV} in the Brazilian biotite suggest its crystallization at higher temperature than biotite from the Argentinian and Chilean plutons.

6. Magmatic series

The use of chemistry of biotite to discriminate magmatic series has been proposed by Nachit et al. (1985) and Abdel-Rahman (1994), who also proposed discriminating between alkalic, calc-alkalic and peraluminous granite suites and associated tectonic setting based on MgO, Al_2O_3, and FeO compositions. Using these diagrams, biotite composition of granites from Chile plots in the field of biotite from subduction-related calc-alkalic granites straddling the field of peraluminous granites, while those from Argentina plot in the field of biotite crystallized from peraluminous granites, which includes syn-collisional S-type granites (Fig. 8). One biotite analysis from Señor de la Peña granite plots in the field of calc-alkalic granites. Biotite from Brazilian granites show no clear classification in the diagram of Fig. 8a,c; however, in the FeO versus MgO diagram of Fig. 8b, compositions define a negative correlation within the field of biotite from peraluminous granites straddling the field of biotite from calc-alkalic granites.

Trends of peraluminosity of the cordierite-bearing granites in this study are illustrated in the A versus B diagram (Fig. 9) that shows the fields of different peraluminosity of peraluminous granites, as depicted by Villaseca et al. (1998). The studied samples form different trends in this diagram. Samples of granites from Argentina plot either within the highly peraluminous (h-P) granites (cordierite-bearing facies of the Capillitas granite, Mazan and Señor de la Peña granites), or form a near-vertical trend, within the field of felsic peraluminous (f-P) granites (felsic facies of the Capillitas granites, Velasco and some samples of the cordierite-bearing facies of the Capillitas and Señor de la Peña granites). The compositional gap between the two trends suggests independent differentiation trends. In fact, the two facies of the Capillitas granite were interpreted as originated from different sources (Rossi et al., 2002). Samples from the Argentinian granites that plot in the field of f-P granites, which correspond to the traditionally termed anatectic granites (Villaseca et al., 1998), could represent primary anatectic granites, a lower partial melt fraction or highly-fractionated magmas of the h-P granites. Samples that plot in the h-P granite field, which corresponds to the typical S-type trend according to Villaseca et al. (1998), could have resulted from partial melting of metapelitic protoliths, for which the compositional path of the resultant series plots inside the hP field (although some of h-P types do not necessarily involve melting of a pelitic protolith; Villaseca et al., 1998).

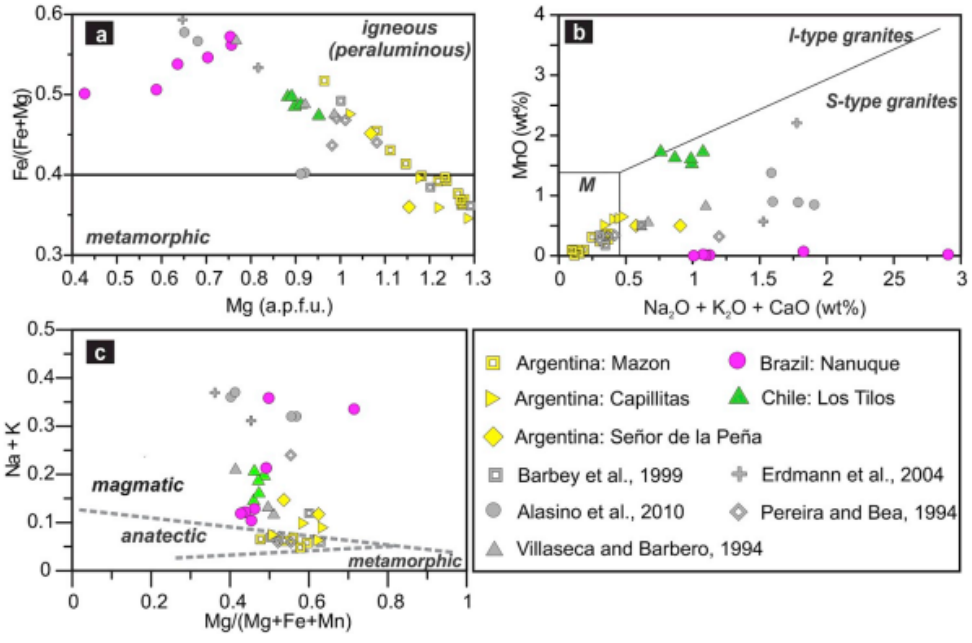

Fig. 7. Compositions of cordierite from Argentina, Brazil and Chile represented in: (a) Mg versus Fe/(Fe + Mg) plot to discriminat metamorphic from igneous cordierites (Schreyer, 1965); (b) (Na_2O + K_2O + CaO) versus MnO diagram to discriminat metamorphic, I– and S-types granite cordierites (Villaseca et al., 2008); and (c) Mg/(Mg + Fe + Mn) versus (Na + K) diagram to discriminat cordierite from various origins (Pereira and Bea, 1994).

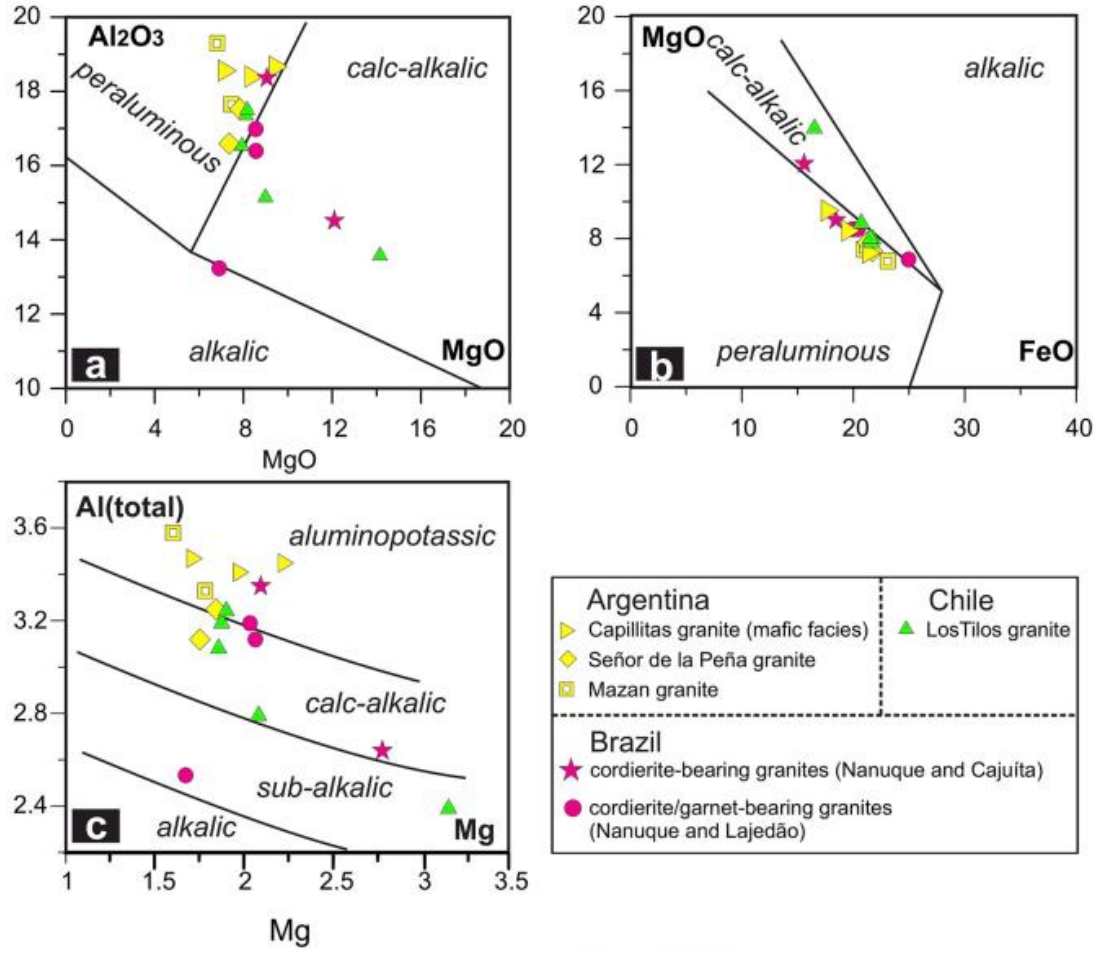

Fig. 8. Compositions of biotite of cordierite-bearing granites from Argentina, Brazil (Celino et al., 2000), and Chile (average of 10 analyses; data from Parada, 1988) represented in the Abdel-Rahman (1994) (a, b) and Nachit et al. (1985) (c) diagrams for discriminating biotite from granites of different magma series.

Samples of garnet cordierite-bearing granites from the Brazilian Nanuque Suite form distinct trends. Most samples from the garnet cordierite bearing granites plot in the field of h-P granites. Some samples from the cordierite-bearing granites, together with two samples of the garnet cordierite-bearing granites form a negative trend in the field of moderately peraluminous (m-P) granites towards the field of f-P granites, i.e. there is increase of peraluminosity towards the more differentiated samples. A third trend is formed by cordierite-bearing granite samples which define a near vertical trend in the f-P field. Samples from the Los Tilos granite samples plot both in the field of m-P and low peraluminous (l-P) granitoids forming a negative trend that straddles the I/S line. This does not support derivation from an aluminum-rich crustal source.

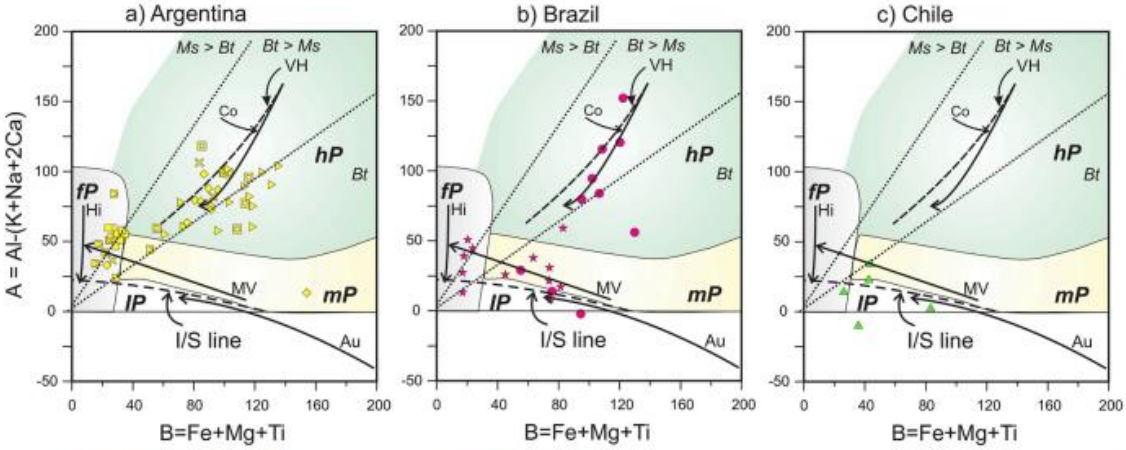

Fig. 9. A–B diagram of Debon and Le Fort (1983) later modified by Villaseca et al. (1998) with compositions of the studied granites (symbols as in Fig. 5). Fields of peraluminous granite series hP (highly peraluminous), mP (moderately peraluminous), lP (low peraluminous) and fP (highly felsic peraluminous), differentiation trends from peraluminous suites (Co = Cooma granite Lachlan foldbelt, Australia; Ly = Layos granite, MV = Mora Venta granite NM = Las Navas del Marques, Central Spain Hercinian belt; Hi = Himalayan leucogranites), and the I-type and S-type granites boundary line compiled by Villaseca et al. (1998). PJ and VH are melting trajectories of different pelitic protoliths, after Patiño Douce and Johnston (1991), and Vielzeuf and Holloway (1988), respectively.

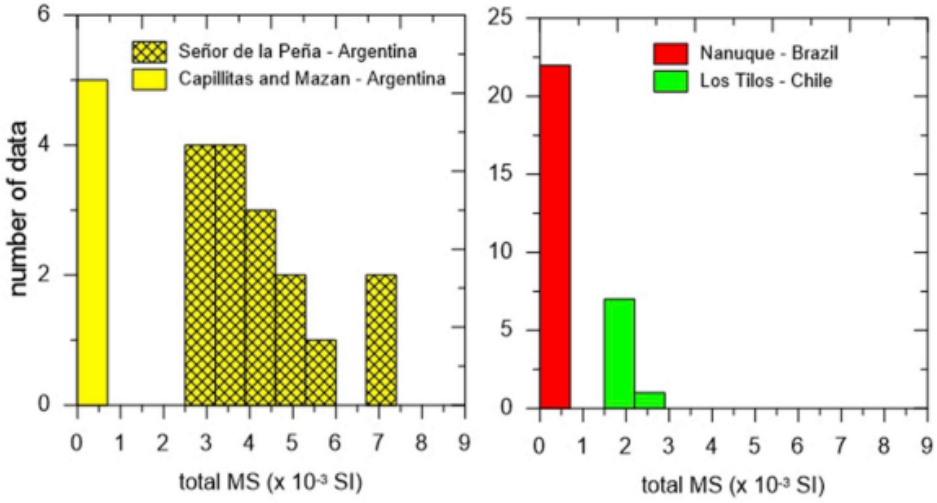

Fig. 10. Histogram of magnetic susceptibility values of cordierite-bearing granites from Argentina, Brazil and Chile.

7. Magnetic susceptibility

Magnetic susceptibility (MS) for the studied granites are represented in Fig. 10. The MS values of Argentinian plutons range from *ca.* 0.1 to 0.7×10^{-3} SI in the Capillitas and Mazan plutons and are higher and more variable ranging for the Señor de La Peña pluton, from 2.5 to 7.3×10^{-3} SI. The MS values for the Nanuque Suite are the lowest among all the studied plutons, varying from 0.03 to 0.15×10^{-3} SI. The MS values of the Los Tilos pluton of Chile are high, ranging from 1.3 to 2.7×10^{-3} SI.

Values of MS lower than 3×10^{-3} SI for the Capillitas, Mazan and Nanuque plutons are in the range for the ilmenite-series granites of Ishihara (1977) and suggest oxygen fugacity between the QFM and NNO buffers of S-type granites (Chappel and White's classification, 1974), as pointed out by Takahashi et al. (1980). Data for the Los Tilos pluton plot near the lower limit between ilmenite and magnetite-series granitoids. The high MS values for Señor de la Peña granite are not well understood and are, perhaps, due to the presence of magnetite inclusions in fresh cordierite that is present in large amounts throughout the pluton.

8. Sr, Nd, Hf and O-isotopes

Values of εHf(zircon) for the Señor de la Peña granite are negative (−4.6 to −8.8), as well as whole rock $\varepsilon Nd_{(0.37Ga)}$ value (−7.8) (Table 7 of the supplementary material). Back-calculated initial $^{87}Sr/^{86}Sr$ ratios determined in this study for the Señor de La Peña and Mazan granites are high, 0.71229 and 0.71249, respectively, similarly to the initial $^{87}Sr/^{86}Sr$ ratios for the Capillitas (0.7146) and Velasco (0.7109) granites as reported by Toselli et al. (2002). A Nd model age of 1.68 Ga for the Señor de la Peña granite was determined in this study, and of 1.83 Ga for the Mazan granite; these ages are in the range (1.8–1.6 Ga) reported by Toselli et al. (2002) for other cordierite-bearing granites in the region. Hf model ages for the Señor de la Peña granite vary from 1.4 to 1.9 Ga in the range (~1.6–1.8 Ma) of those determined in the Proterozoic–Lower Paleozoic basement of the Sierras Pampeanas (Grosse et al., 2009, and references therein). These Nd, Sr and Hf isotope values are compatible with crustal source for these granites. Considering the Nd and Sr isotopes for the Ordovician granites from the region, potential crustal protoliths that outcrop in the Sierras Pampeanas with appropriate Nd isotope values are the Sierra de Velasco low-grade metasedimentary rocks, which have εNd between −8.2 and −9.4 (Grosse et al., 2009 and references therein).

The Nanuque Suite shows negative $\varepsilon Nd_{(0.57\,Ga)}$ from −6.6 to −7.3 and Nd model ages from 1.83 to 1.79 Ga. (Celino et al., 2000). These values are in the range for regional Neoproterozoic paragneisses of the Paraiba do Sul Complex, reported by Celino et al. (2000) which, perhaps, served as source for the granitic magmas.

The cordierite-bearing Los Tilos granite shows high initial $^{87}Sr/^{86}Sr$ ratio of 0.7145, and εNd value of −4.0 (Parada et al., 2007), suggesting crustal source. On the other hand, Mpodozis and Kay (1992) indicate that the Upper Triassic metaluminous granites (e.g. Monte Grande), coeval with Los Tilos pluton, show relatively lower $^{87}Sr/^{86}Sr$ ratios (0.7050–0.7065), suggesting more mafic sources.

Value of $\delta^{18}O$ (zircon) from the Capillitas granite is lower (7.8‰) than those for the Velasco zircon (9.5‰). Values of $\delta^{18}O$ (quartz) are > 10‰ in the Velasco, and > 13‰ in the Mazan and Señor de la Peña plutons (Fig. 11). These oxygen-isotope data imply high $\delta^{18}O$ whole-rock values for the magmas, suggesting that they were derived from high $\delta^{18}O$ crustal protoliths. Values of $\delta^{18}O$ (zircon) for the Nanuque Suite are the highest among the zircon grains analyzed in this study (10.9–11.8‰) implying on $\delta^{18}O$ > 13‰ for the host magma. The $\delta^{18}O$ magmatic whole-rock values > 10‰ for the cordierite-bearing granites from Argentina and Brazil are compatible with magma derivation from melting of high $\delta^{18}O$ metasedimentary rocks, as proposed for S-type cordierite-bearing granitoids in the Lachlan Foldbelt, Australia (O'Neil et al., 1977). The $\delta^{18}O$ values for zircon grains from the Los Tilos granite are the lowest among the studied ones (6.1–7.4‰), suggesting a less differentiated crustal protolith in comparison to protoliths for the Argentinian and Brazilian cordierite-bearing granitic magmas. This behavior implies magmatic whole-rock $\delta^{18}O$ values < 10‰, within the range of I-type granitoids in the Lachlan Foldbelt.

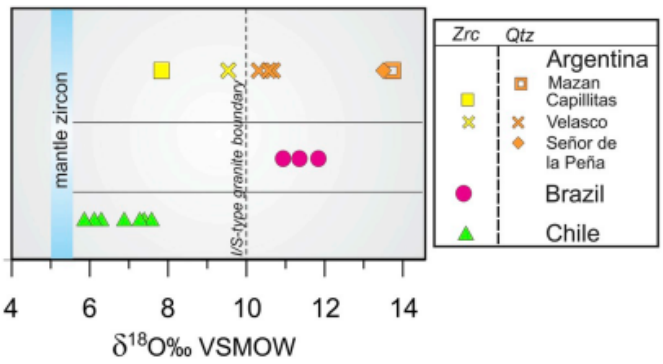

Fig. 11. Oxygen isotope values of zircon and quartz from cordierite-bearing granites from Argentina, Brazil and Chile. Zrn = zircon; Qtz = quartz. Mantle zircon $\delta^{18}O$ values after Valley et al. (2005).

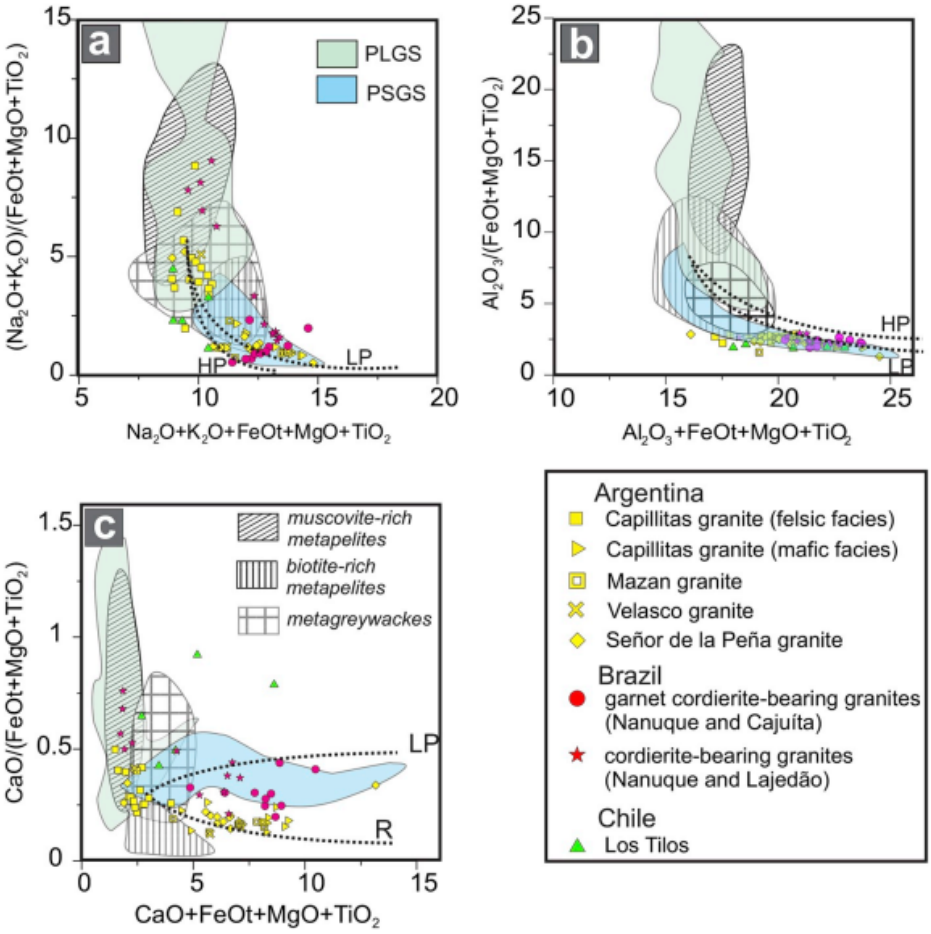

Fig. 12. Compositions of the studied cordierite-bearing granites compared to compositions of peraluminous leucogranites (PLGS), peraluminous S-type granites (PSGS), and melts produced by experimental dehydration-melting of metasedimentary rocks. The thick solid lines are reaction curves that model the melt compositions that would be produced by hybridization of high-Al olivine tholeiite with metapelite at low (LP) and high (HP) pressure (compositional fields and solid lines from Patiño Douce, 1999).

9. Discussion

9.1. Source rocks

Major-element compositions of experimentally-derived melts from several sources can be used to infer source rocks (Patiño Douce, 1999). The studied granites form distinct trends in diagrams of Patiño Douce (1999) in which major element compositions of crustal melts produced from metapelites and metagreywackes are shown (Fig. 12). These diagrams also show the compositional fields of peraluminous leucogranites (PLGS) and peraluminous S-type granites (PSGS). The cordierite-bearing granites from Brazil and the felsic facies of the Capillitas granite have compositions that are mostly similar to those formed by melting of a muscovite-rich metapelite protolith (Fig. 12 a,c). In contrast, the garnet cordierite-bearing granites from Brazil together with most samples from the Señor de la Peña, Mazan, and the mafic facies of the Capillitas granite from Argentina, as well as two samples of the Los Tilos granite, fall outside the fields for crustal melts of Fig. 12. These Argentinian and Brazilian granites, which present low alkalies and alumina compared with ferromagnesian components, plot in the field of PSGS (Fig. 12 a,b), and are not pure melts according to Patiño Douce (1999). In fact, the samples from Argentina form a linear trend in Fig. 12c along the trend that results from melt-restite mixing in a pelitic system with no addition of basaltic components. The Brazilian granites, on the other hand, plot in the region of Fig. 12 between low (≤5 kbar) and high (12–15 kba) pressure curves, which model the compositions that would be produced by reaction between a crustal melt end member with a basaltic melt. Therefore, they do not represent pure crustal magmas, instead, they crystallized from hybrid magmas.

Most analyzed samples from the Los Tilos granite do not show a regular pattern in Fig. 12. They seem to plot in the compositional field of metagraywacke melts. Two samples have higher CaO/(MgO + FeO + TiO_2) than any of the compositions (PLGS, PSGS, melts) shown in the diagram (Fig. 12c) and may reflect plagioclase or amphibole in the source rock. As a whole this unclear behavior may be indicating a mixed source for the Los Tilos granite.

The chemical compositions of the studied granites form distinct clusters in the molar K_2O/Na_2O versus ASI (molecular Al/(Ca-1.67P + Na + K), and molar CaO/(MgO + FeO_{total}) versus molar K_2O/Na_2O diagrams (Fig. 13). These diagrams show the compositional fields of partial melts obtained in experimental studies of dehydration melting of various bulk compositions, as compiled by Altherr and Siebel (2002). Results are unlike those shown by experiments of Patiño Douce (1999). The composition of the granites from Argentina are analogous to those obtained by melting of metapelites, whereas those from the Brazilian suite plot in the field of metagryawacke melts; in contrast, those from Chile plot in the field of metabasalts. These findings are in agreement with a crustal origin for the Argentinian and Brazilian cordierite-bearing granites, and probably with a secondary mantle-derived component for the Chilean Los Tilos granite.

9.2. P-T magma generation and crystallization

Thermobarometric estimates for the crystallization conditions of the Capillitas and Mazan plutons indicate pressure between 2 and 4 kbar and temperature in the 630–720 °C interval, based on the upper limit of the biotite dehydration melting field of mafic pelites, in H_2O-undersaturated conditions (Toselli et al., 2002, 2003a; Rossi et al., 2002). Evidence for rather low pressure of crystalization is further given by the REE patterns, which are flat, around the upper crustal REE contents (Fig. 6) and similar to patterns of many strongly peraluminous granites. This is consistent with magma crystallization under relatively shallow

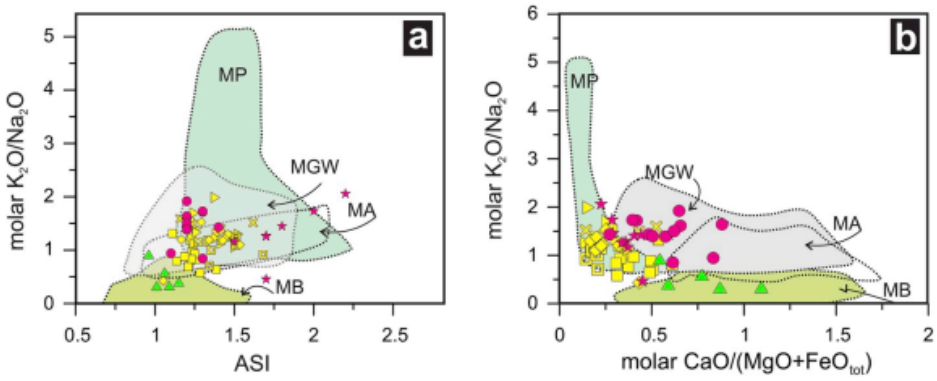

Fig. 13. Chemical compositions of cordierite-bearing granites from Argentina, Brazil and Chile represented in ASI (molecular Al/(Ca-1.67P + Na + K) versus molar K_2O/Na_2O and molar CaO/(MgO + FeOtotal) versus molar K_2O/Na_2O diagrams.Outlined fields denote compositions of partial melts obtained in experimental studies by dehydration melting of various bulk compositions, as compiled by Altherr and Siebel (2002). MB = metabasalts; MA = metaandesites; MGW = metagreywackes; MP = metapelites. Symbols as in Fig. 11.

crustal P-T conditions (e.g. Rossi et al., 2002; Villaseca et al., 2008). In fact, high abundance of biotite, cordierite and andalusite, and absence of garnet in migmatitic enclaves in the Argentinian plutons suggest shallow melting with little upward migration. Melting of biotite-rich metapelitic sources require an extra heat source (e.g. basalt underplating, post-thickening radiogenic heating; e.g. Patiño Douce, 1999; Bea, 2012). There is no geological record of mafic magma responsible for heat transfer into the crust to promote partial melting in the Pampean Ranges, under these P-T conditions. Hence anatexis could have resulted from radiogenic heat stored during crustal deformation and thickening by K, Rb, Th and U, a mechanism proposed by England and Thompson (1984) and discussed by Rossi et al. (2002).

Metamorphic garnet-bearing enclaves in granites of the Nanuque Suite suggest that partial fusion took place deep in the crust, at 750–800 °C and P > 6 kbar, with magma emplacement at a depth around 3 kbar (Celino, 1999). Fe–Mg exchange between garnet and cordierite from the Brazilian granitoids indicates that this mineral pair reached equilibrium conditions at pressure between 3.7 and 4.5 kbar and temperature ~700 °C (Celino, 1999). These P-T conditions are compatible with those estimated for regional basement rocks (P = 4–5 kbar; T ~750 °C; Celino and Botelho, 2001; in Celino, 1999). The assemblage biotite + cordierite + hercynite suggests their formation under oxygen fugacity close to the NNO buffer, low-alumina activity, and pressures < 5 kbar, as indicated by experiments on water-saturated peraluminous granitic systems of Puziewicz and Johannes (1988). At lower oxygen fugacities (~QFM), hercynite is replaced by almandine (Hsu, 1968). In fluid-absent conditions, melting temperature from ~750 to 850 °C can produce up to 40% volume of peraluminous granitic liquid (Gardien et al., 1995). In experiments using natural pelites, however, higher melting temperatures (850–875 °C) are required (Vielzeuf and Holloway, 1988). The presence of only minor modal biotite and muscovite (whose crystallization is favoured by high-water activity; e.g. Zen, 1988) suggests that these granitic magmas are not derived from water-rich pelitic source. Therefore, it would require an extra heat source, probably provided by hot mafic-magma input to trigger melt. The presence of microgranular mafic enclaves suggests participation of mantle-derived magma, although mafic intrusions are absent in the region (Celino, 1999). These mafic enclaves are perhaps relicts of the mafic magmatic underplating or injection into the continental crust that provided heat enough to lead to the Nanuque magma formation.

Emplacement conditions of the Los Tilos pluton of < 3 kbar and ~670 °C were indirectly estimated from the crystallization P-T conditions of celadonite-rich muscovite, feldspar, biotite and Fe–Ti oxides (Parada, 1988). Oxidation conditions between QFM and HM buffers are inferred for Los Tilos, from the biotite stability with magnetite and K-feldspar (Wones, 1989). Figs. 12 and 13 suggest that metabasalts have been probably source rocks for Los Tilos magmas, whose differentiation, hybridization and crystallization gave rise to a peraluminous S-type granite (Los Tilos pluton). This granite-type in comparison with the peraluminous leucogranites (considered as 'pure anatectic melts') represents hybrid magmas possibly formed by interaction of crustal and mantle-derived magmas (Patiño Douce, 1999). The input of mantle-derived mafic magmas could provide heat source to partially melt the crust in a thinned lithosphere context, as suggested by Parada (1988). . Anatexis due to an increased crustal temperature in a thinned lithosphere, provided by subcontinental mafic magma input, has been recognized elsewhere in the Coastal Range of Chile (Vásquez et al., 2011).

9.3. P-T conditions of cordierite formation

The P-T cordierite forming conditions of the plutonic units from Brazil and Argentina were determined by calculating isochemical P-T projections, using Perple_X software (Connolly, 2005; version 6.8.3). The thermodynamic simulations considered the K_2O–FeO–MgO–Al_2O_3–SiO_2–H_2O–Na_2O (KFMASHN) system, using the thermodynamic data set of Holland and Powell (1998). Different solution models (from the hp02ver.dat file) were used for each phase as follows: Bio(HP) for biotite, Gt (HP) for garnet, Chl (HP) for chlorite, melt (HP) for Na–Mg–Al–⊕ Si–K–Ca–Fe hydrous silicate melt, Mica(M) for mica, Sp(HP) for spinel, St (HP) for staurolite, hCrd for cordierite, Opx (HP) for orthopyroxene, and feldspar for ternary feldspar. Pressure and temperature intervals of 1–15 kbar and 550-850 °C were considered, respectively. Representative whole rock compositions of each studied pluton (these are detailed in the Supplementary Material) were considered in modeling. Based on EPMA results and whole-rock compositions, conditions of coexistence of cordierite and biotite (paragenetic association found in all studied granites with exception of the Chilean Los Tilos pluton) were obtained from intersections of molar Fe/(Fe + Mg) in cordierite and MgO (wt %) in biotite compositional isopleths. Also, the reported paragenetic associations observed in each pluton (summarized in the Supplementary Material) were compared with those obtained by modeling, and were cross-checked as a match-requisite to validate the cordierite P-T forming conditions.

Magmatic cordierite formation is restricted to pressures below ca. 5.5 kbar (considering the minimum water content of H_2O-saturated magmas in the haplogranite system; Johannes and Holtz, 1996). The mentioned compositional isopleths for the studied rocks can be used as a fairly good geothermometer (see Appendix 1). As a broad estimate, the projected biotite and cordierite EPMA compositional data result in the following forming conditions (Fig. 14) for the Argentinian and Brazilian cordierites, respectively: (a) Conditions for the Capillitas (mafic facies), Señor de la Peña, Velasco and Mazan rocks of 3.6–4.0 kbar and 670 −700 °C interval, corresponding to a ca. 37 °C/km geothermal gradient; (b) Conditions for the Lajedão, Cajuita and Nanuque units of 5.0–5.2 kbar and 720 −740 °C interval corresponding to a ca. 50 °C/km geothermal gradient.

Calculated-zircon saturation temperatures (Tzr) for the Argentinian granites (using the equation of Gervasoni et al., 2016) lie within a range (~600–720 °C; inset in Fig. 14) analogous to that for cordierite formation temperature (670–700 °C), justifying the observed inclusions of zircon in cordierite (Rossi et al., 2002), and implying early magma saturation in zircon. However, these Tzr are low for granite liquidus, and as this thermometer is calibrated for T > 800 °C, uncertainties are

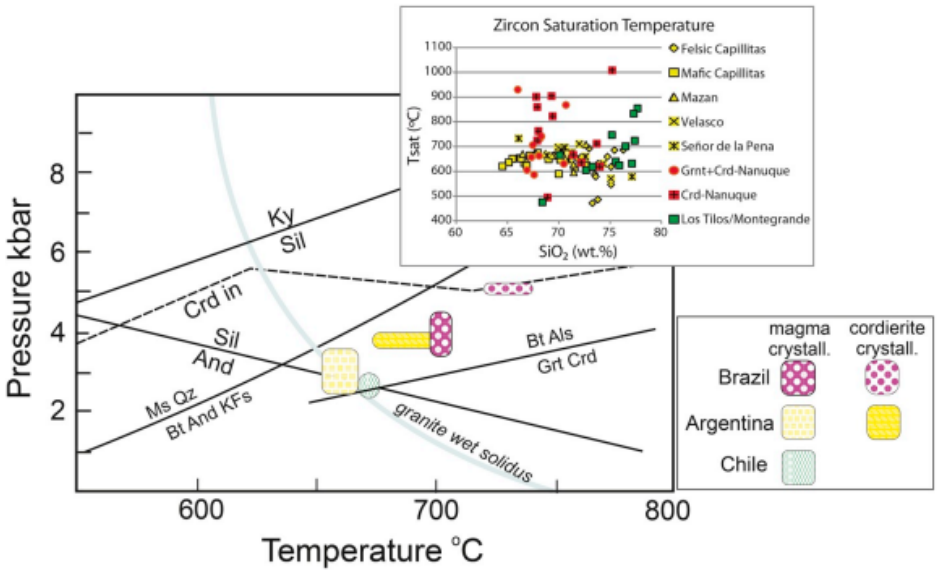

Fig. 14. P–T forming conditions of the Argentina and Brazil cordierite-bearing granites. Average water-saturated solidus (Johannes and Holtz, 1996) is shown in gray band, obtained from the modeled isochemical pseudosections (see text for explanation). Inset show zircon saturation temperatures calculated for each granite sample (equation after Gervasoni et al., 2016).

at least 50 °C (Gervasoni et al., 2016). Hence, Tzr are probably higher but either certainly do not represent near-liquidus magma temperatures, or it implies a Zr-poor source rock. The felsic facies of the Capillitas pluton shows anomalously-low Zr (ppm) content (reflected in subsolidus zircon saturation temperatures). This could be interpreted as zirconium depletion by fractional crystallization of Zr-bearing phases at some point of the magmatic evolution (Evans and Hanson, 1993; Bea et al., 2006). The T conditions of cordierite formation of the Argentinian plutons (670 – 700 °C) are roughly analogous to those of the magmatic crystallization temperature (630–720 °C, see above), but pressures are relatively higher (3.6–4.0 kbar) than those for magmatic P (around 2–4 kbar), and this would indicate that cordierite is not a near solidus phase. Mica-rich metapelite is likely the source rock for the magmas (Figs. 12 and 13), and melting could have been a consequence of water release by biotite-dehydration reactions and consequent peritectic formation of cordierite. This, together with the low Tzr, would explain metamorphic origin (restite) of some cordierites, but also cordierite formed by peritectic reactions (Fig. 7a and b). Peritectic cordierite is also suggested by the whole rock and cordierite chemistries. The sum of FeO, MgO and TiO_2 oxides in granitic magmas usually does not exceed 3% due to their limited solubility in these melts (Patiño Douce, 1999), thus cordierite crystallized from highly-fractionated felsic magmas or pegmatites has high X_{Fe} (Fe/(Fe + Mg)), as well as high Na, Mn, Li and Be contents (e.g. Gordillo et al., 1985; Villaseca and Barbero, 1994). The studied granites from Argentina exibit high and variable FeO + MgO + TiO_2 (from 1.0 to 9.8%), and their cordierite crystals have low X_{Fe} (0.4–0.5). This could be interpreted as they formed early in the melt and represent peritectic assemblages. Therefore, cordierite aggregates (Fig. 2a and b) from cordierite-bearing granites of the Capillitas, Señor de la Peña and Mazan plutons could be interpreted either as restites or peritectic products formed early during magmatic evolution, entrained and not separated from the melt throughout its formation and emplacement. This is in consonance with the P-T conditions of cordierite formation estimated here.

Cordierite of the Nanuque Suite was formed at higher pressures (5.0–5.2 kbar) and temperatures (720–740 °C) than those from Argentina. Calculated Tzr values for the garnet + cordierite-bearing granites of the Nanuque Suite are the highest among the studied plutons. These Tzr are minimum temperature estimates for melting conditions (*ca.* 700 °C) that could have reached over 900 °C (inset in Fig. 14). The studied cordierites have high X_{Fe} (> 0.5), and together with the high whole-rock contents of FeO, MgO and TiO_2 (> 6%) suggest that cordierite magmatic crystallization was not in equilibrium, rather it was partially fractionated/resorbed at some point of its evolution (Celino, 1999). These observations are consistent with a residual cordierite and/or peritectic entrainment of it, while still reacting with the melt (e.g. Harley et al., 2002).

The magma generation of the Chilean Los Tilos pluton has occurred at moderate temperature and pressures below 3 kbar (depth of emplacement) as suggested by β-quartz paramorph inclusions in cordierite, with magma emplacement in an already exhumed basement (Parada, 1988; Hervé et al., 2014). The calculated Tzr for the Los Tilos pluton (from 600 to 800 °C) is in good agreement with the estimated crystallization temperatures (~670 °C) calculated by Parada (1988). This provides a maximum magma temperature (Miller et al., 2003) to preserve the inherited zircon cores (Hervé et al., 2014; and Supplementary data) and inclusions of β-quartz paramorphs found in nodules in this pluton. Preserved crystals of β quartz might imply an exceptional fast emplacement and cooling. Cordierite from Los Tilos pluton presents high Fe (X_{Fe} ~ 0.5), and shows higher MnO contents (> 1.5 wt%) than cordierite from the Argentinian and Brazilian granites. The observed cordierite-quartz nodules that are surrounded by leucocratic rims are interpreted as late-stage quenching of aggregates that were assembled by heterogeneous nucleation around pre-existing β-quartz crystals (e.g., Oberc-Dziedzic et al., 2015); they could have been formed by biotite dehydration reactions in the presence of melt during emplacement of the magma (e.g. Barbey et al., 1999), transported and re-equilibrated up to a shallow level of emplacement (Parada, 1988).

Peraluminous granitic rocks are produced by: (a) partial melting of peraluminous metasedimentary rocks; (b) differentiation of metaluminous magma whatever its origin, with or without assimilation, or (c) late-stage metasomatic loss of alkali through vapor phase transport (Zen, 1988). Mineralogical, geochemical and isotopic characteristics of the studied cordierite-bearing granites from Argentina and Brazil, such as the presence of cordierite with chemistry compatible with peritectic origin (restitic and magmatic cordierite are also present), low magnetic susceptibility values, negative εNd and high $\delta^{18}O$ (zircon) values, suggest a crustal aluminous metasedimentary source. Contrastingly, data for the Los Tilos pluton (rather small volume, association with metaluminous granites, low $\delta^{18}O$ zircon values, slightly negative εNd and higher magnetic susceptibility approaching that of the lower limit of magnetite-granite series) are compatible with a more primitive source that could be either melting of a metaluminous granitic rock or crystal fractionation of metaluminous granitic melt.

Altogether, the data indicate that formation of cordierite in the studied plutons is related to aluminous metasedimentary source rocks, but also to partial melting of metaluminous granites or crystal fractionation of a metaluminous granitic melt. The studied cordierites are

either formed from peritectic reactions, are magmatic or restites, formed under variable oxygen fugacity conditions. Besides, granitic magmas formed in different tectonic settings.

10. Conclusions

Our data indicate that the studied cordierite-bearing granitoids from Brazil, Argentina and Chile formed from distinct source rocks at different P–T conditions that are reflected in their mineralogy, geochemistry and isotopic features. The felsic facies of the Capillitas granite seems to represent pure crustal melts, probably an aluminous metasedimentary source, while the mafic facies, together with Mazan and Señor de la Peña granites may represent a hybrid source from reaction between a crustal and basaltic melts. The examined data for the Los Tilos pluton is dubious but compatible with a less evolved source, possibly melting of a metaluminous granitic rock, or crystal fractionation of a metaluminous melt. Subduction-related granites from Chile and Argentina formed cordierite at relatively shallow conditions, whereas cordierite from post-collisional peraluminous granites of the Nanuque Suite of Brazil formed deeper in the crust, closer to their source. The formation of cordierite in Argentina and Brazil granites is related either to peritectic reactions or cordierite represents restite, while cordierite from Chile is peritectic. This study confirms that cordierite in granites can be produced by a number of processes from different source rocks, at distinct P-T conditions of formation.

Acknowledgements

Part of this study was made possible thanks to two grants from the VITAE Foundation to ANS and VPF, and CNPq-PROSUL (grant 490408/2008-7) to VPF. PGM thanks the CONICYT doctoral grant 21150905. This is the NEG-LABISE contribution N. 280. We thanks to Michael Roden and an anonymous reviewer for their very constructive reviews that significantly improved the manuscript.

Appendix A. Supplementary data

Supplementary data to this article can be found online at https://doi.org/10.1016/j.jsames.2019.03.022.

Appendix 1. Cordierite forming conditions for the Brazilian and Argentinian cordierite-bearing rocks

Figs. 1–7 (below). Left: Representative isochemical P-T KFMASHN compositional system pseudosections for each studied pluton. Abbreviations for each phase (as pure endmembers and solid solutions) are: Crd (cordierite), Fsp (K-Feldspar), Mica (white mica), Bio (biotite), sill (sillimanite/fibrolite), q (quartz), Plg (plagioclase), Melt (Na– Al–Si–K–Ca hydrous silicate melt), Opx (orthopyroxene), Gt (garnet), H2O (water). Right: Compositional isopleths of molar Fe/(Fe + Mg) in cordierite and MgO (wt.%) in biotite. Metamorphic conditions are estimated intersecting compositional isopleths that match the observed EMPA data presented here.

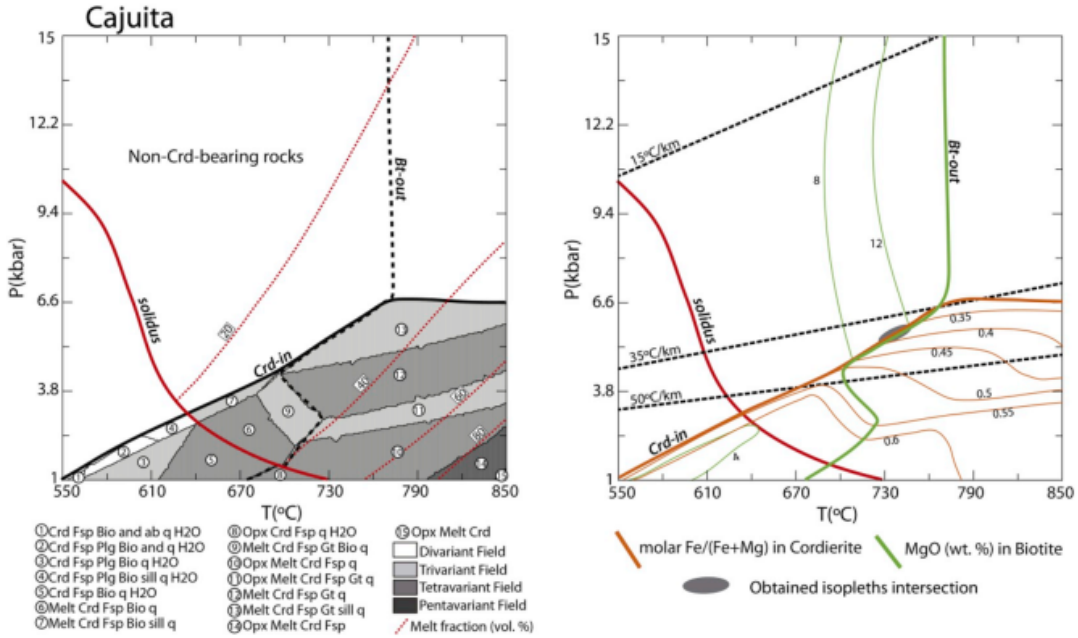

Fig. 1.

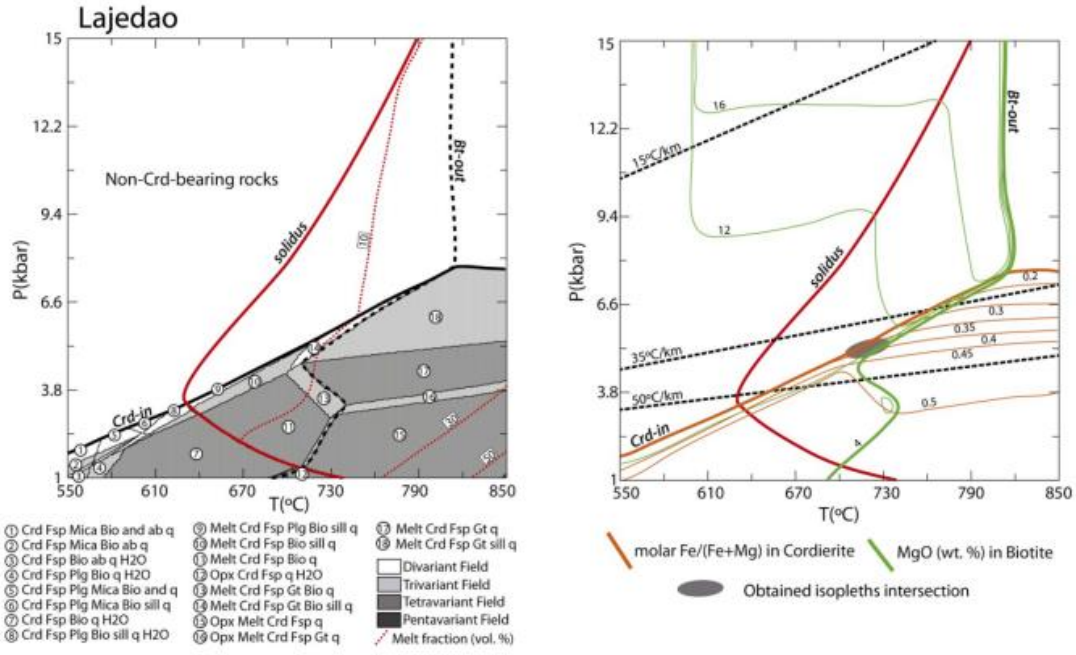
Lajedao
Non-Crd-bearing rocks
solidus
Bt-out
Crd-in
P(kbar)
T(°C)
15
12.2
9.4
6.6
3.8
1
550
610
670
730
790
850
① Crd Fsp Mica Bio and ab q
② Crd Fsp Mica Bio ab q
③ Crd Fsp Bio ab q H2O
④ Crd Fsp Plg Bio q H2O
⑤ Crd Fsp Plg Mica Bio and q
⑥ Crd Fsp Plg Mica Bio sill q
⑦ Crd Fsp Bio q H2O
⑧ Crd Fsp Plg Bio sill q H2O
⑨ Melt Crd Fsp Plg Bio sill q
⑩ Melt Crd Fsp Bio sill q
⑪ Melt Crd Fsp Bio q
⑫ Opx Crd Fsp q H2O
⑬ Melt Crd Fsp Gt Bio q
⑭ Melt Crd Fsp Gt Bio sill q
⑮ Opx Melt Crd Fsp q
⑯ Opx Melt Crd Fsp Gt q
⑰ Melt Crd Fsp Gt q
⑱ Melt Crd Fsp Gt sill q
Divariant Field
Trivariant Field
Tetravariant Field
Pentavariant Field
Melt fraction (vol. %)
16
12
15°C/km
35°C/km
50°C/km
0.2
0.3
0.35
0.4
0.45
0.5
molar Fe/(Fe+Mg) in Cordierite
MgO (wt. %) in Biotite
Obtained isopleths intersection

Fig. 2.

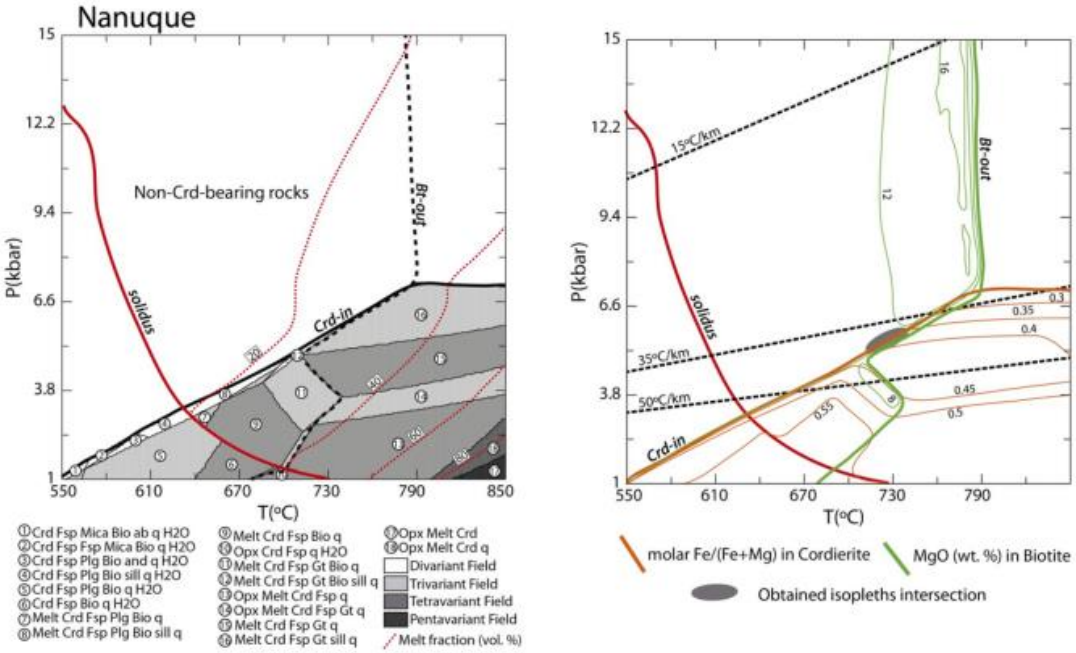
Nanuque
Non-Crd-bearing rocks
solidus
Bt-out
Crd-in
P(kbar)
T(°C)
15
12.2
9.4
6.6
3.8
1
550
610
670
730
790
850
①Crd Fsp Mica Bio ab q H2O
②Crd Fsp Fsp Mica Bio q H2O
③Crd Fsp Plg Bio and q H2O
④Crd Fsp Plg Bio sill q H2O
⑤Crd Fsp Plg Bio q H2O
⑥Crd Fsp Bio q H2O
⑦Melt Crd Fsp Plg Bio q
⑧Melt Crd Fsp Plg Bio sill q
⑨Melt Crd Fsp Bio q
⑩Opx Crd Fsp q H2O
⑪Melt Crd Fsp Gt Bio q
⑫Melt Crd Fsp Gt Bio sill q
⑬Opx Melt Crd Fsp q
⑭Opx Melt Crd Fsp Gt q
⑮Melt Crd Fsp Gt q
⑯Melt Crd Fsp Gt sill q
⑰Opx Melt Crd
⑱Opx Melt Crd q
Divariant Field
Trivariant Field
Tetravariant Field
Pentavariant Field
Melt fraction (vol. %)
16
12
15°C/km
35°C/km
50°C/km
0.3
0.35
0.4
0.45
0.5
0.55
molar Fe/(Fe+Mg) in Cordierite
MgO (wt. %) in Biotite
Obtained isopleths intersection

Fig. 3.

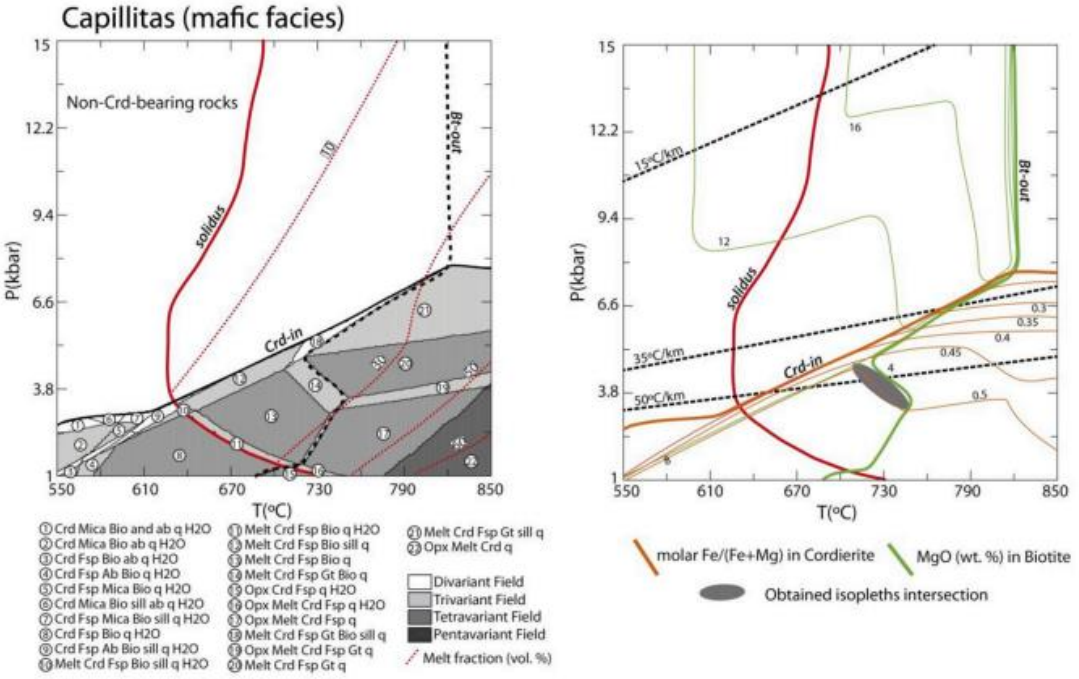
Capillitas (mafic facies)
Non-Crd-bearing rocks
solidus
Crd-in
Bt-out
P(kbar)
T(°C)
15
12.2
9.4
6.6
3.8
1
550
610
670
730
790
850
① Crd Mica Bio and ab q H2O
② Crd Mica Bio ab q H2O
③ Crd Fsp Bio ab q H2O
④ Crd Fsp Ab Bio q H2O
⑤ Crd Fsp Mica Bio q H2O
⑥ Crd Mica Bio sill ab q H2O
⑦ Crd Fsp Mica Bio sill q H2O
⑧ Crd Fsp Bio q H2O
⑨ Crd Fsp Ab Bio sill q H2O
⑩ Melt Crd Fsp Bio sill q H2O
⑪ Melt Crd Fsp Bio q H2O
⑫ Melt Crd Fsp Bio sill q
⑬ Melt Crd Fsp Bio q
⑭ Melt Crd Fsp Gt Bio q
⑮ Opx Crd Fsp q H2O
⑯ Opx Melt Crd Fsp q H2O
⑰ Opx Melt Crd Fsp q
⑱ Melt Crd Fsp Gt Bio sill q
⑲ Opx Melt Crd Fsp Gt q
⑳ Melt Crd Fsp Gt q
㉑ Melt Crd Fsp Gt sill q
㉒ Opx Melt Crd q
Divariant Field
Trivariant Field
Tetravariant Field
Pentavariant Field
Melt fraction (vol. %)
15°C/km
35°C/km
50°C/km
molar Fe/(Fe+Mg) in Cordierite
MgO (wt. %) in Biotite
Obtained isopleths intersection

Fig. 4.

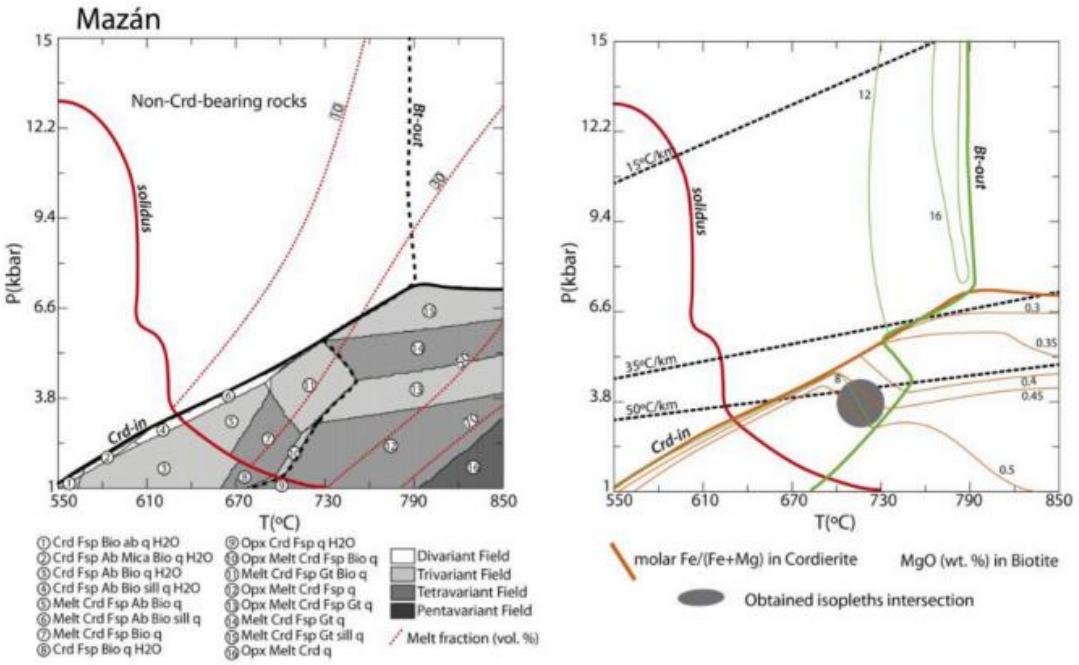
Mazán
Non-Crd-bearing rocks
solidus
Crd-in
Bt-out
P(kbar)
T(°C)
15
12.2
9.4
6.6
3.8
1
550
610
670
730
790
850
① Crd Fsp Bio ab q H2O
② Crd Fsp Ab Mica Bio q H2O
③ Crd Fsp Ab Bio q H2O
④ Crd Fsp Ab Bio sill q H2O
⑤ Melt Crd Fsp Ab Bio q
⑥ Melt Crd Fsp Ab Bio sill q
⑦ Melt Crd Fsp Bio q
⑧ Crd Fsp Bio q H2O
⑨ Opx Crd Fsp q H2O
⑩ Opx Melt Crd Fsp Bio q
⑪ Melt Crd Fsp Gt Bio q
⑫ Opx Melt Crd Fsp q
⑬ Opx Melt Crd Fsp Gt q
⑭ Melt Crd Fsp Gt q
⑮ Melt Crd Fsp Gt sill q
⑯ Opx Melt Crd q
Divariant Field
Trivariant Field
Tetravariant Field
Pentavariant Field
Melt fraction (vol. %)
15°C/km
35°C/km
50°C/km
molar Fe/(Fe+Mg) in Cordierite
MgO (wt. %) in Biotite
Obtained isopleths intersection

Fig. 5.

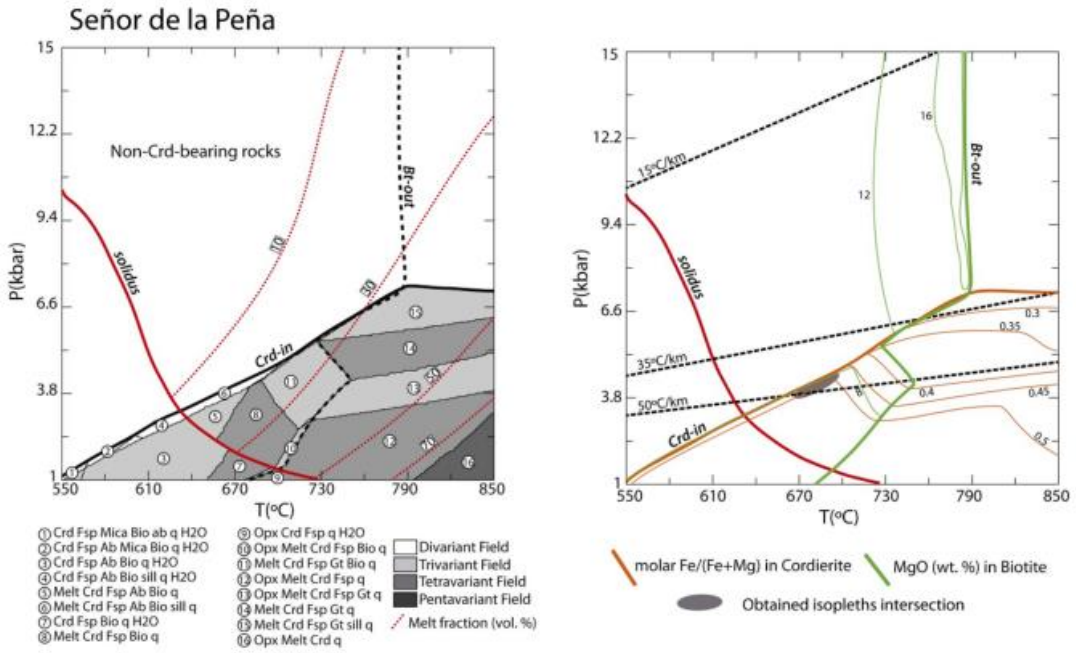
Señor de la Peña
Non-Crd-bearing rocks
solidus
Crd-in
Bt-out
P(kbar)
T(°C)
15
12.2
9.4
6.6
3.8
1
550
610
670
730
790
850
10
30
50
70
①Crd Fsp Mica Bio ab q H2O
②Crd Fsp Ab Mica Bio q H2O
③Crd Fsp Ab Bio q H2O
④Crd Fsp Ab Bio sill q H2O
⑤Melt Crd Fsp Ab Bio q
⑥Melt Crd Fsp Ab Bio sill q
⑦Crd Fsp Bio q H2O
⑧Melt Crd Fsp Bio q
⑨Opx Crd Fsp q H2O
⑩Opx Melt Crd Fsp Bio q
⑪Melt Crd Fsp Gt Bio q
⑫Opx Melt Crd Fsp q
⑬Opx Melt Crd Fsp Gt q
⑭Melt Crd Fsp Gt q
⑮Melt Crd Fsp Gt sill q
⑯Opx Melt Crd q
Divariant Field
Trivariant Field
Tetravariant Field
Pentavariant Field
Melt fraction (vol. %)
15°C/km
35°C/km
50°C/km
16
12
0.3
0.35
0.4
0.45
0.5
0.55
molar Fe/(Fe+Mg) in Cordierite
MgO (wt. %) in Biotite
Obtained isopleths intersection

Fig. 6.

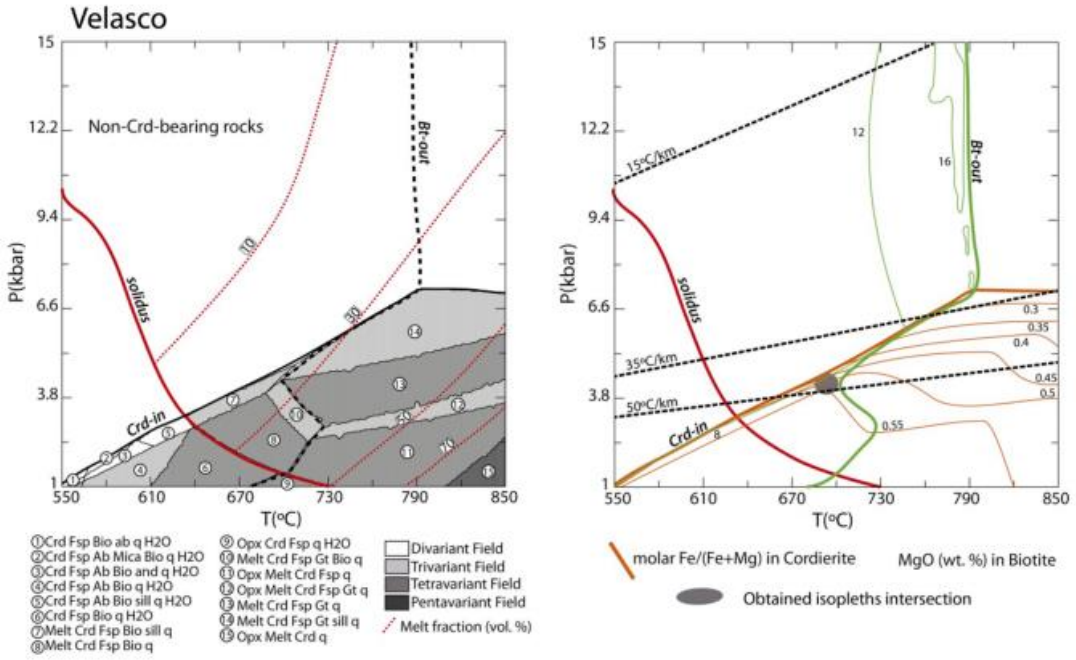
Velasco
Non-Crd-bearing rocks
solidus
Crd-in
Bt-out
P(kbar)
T(°C)
15
12.2
9.4
6.6
3.8
1
550
610
670
730
790
850
10
30
50
70
①Crd Fsp Bio ab q H2O
②Crd Fsp Ab Mica Bio q H2O
③Crd Fsp Ab Bio and q H2O
④Crd Fsp Ab Bio q H2O
⑤Crd Fsp Ab Bio sill q H2O
⑥Crd Fsp Bio q H2O
⑦Melt Crd Fsp Bio sill q
⑧Melt Crd Fsp Bio q
⑨Opx Crd Fsp q H2O
⑩Melt Crd Fsp Gt Bio q
⑪Opx Melt Crd Fsp q
⑫Opx Melt Crd Fsp Gt q
⑬Melt Crd Fsp Gt q
⑭Melt Crd Fsp Gt sill q
⑮Opx Melt Crd q
Divariant Field
Trivariant Field
Tetravariant Field
Pentavariant Field
Melt fraction (vol. %)
15°C/km
35°C/km
50°C/km
16
12
0.3
0.35
0.4
0.45
0.5
0.55
molar Fe/(Fe+Mg) in Cordierite
MgO (wt. %) in Biotite
Obtained isopleths intersection

Fig. 7.

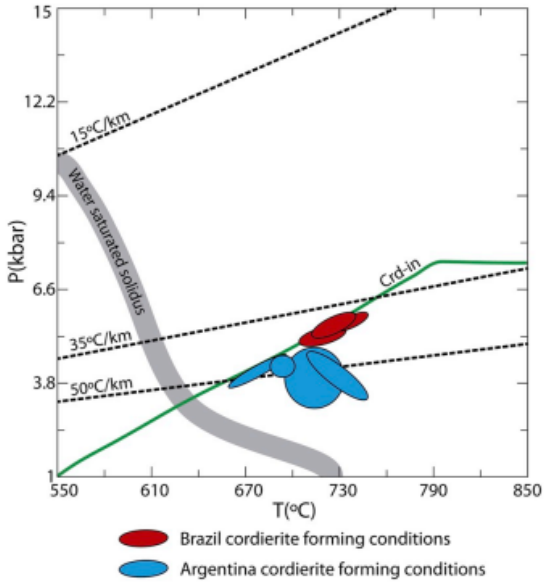

Fig. 8. Synthesis of the Argentina and Brazil cordierite forming conditions. Average water saturated solidus (minimum melt) in gray band, obtained from the modeled isochemical pseudosections.

References

Abdel-Rahman, A.F.M., 1994. Nature of biotites from alkaline, calc-alkaline, and peraluminous magmas. J. Petrol. 35, 525–541.

Alasino, P.H., Dahlquist, J.A., Galindo, Casquet, C., Saavedra, J., 2010. Andalusite and Na- and Li-rich cordierite in the La Costa pluton, Sierras Pampeanas, Argentina: textural and chemical evidence for a magmatic origin. Int. Res.. J. Earth Sci. 99, 1051–1065.

Albuquerque, C.A.R., 1973. Geochemistry of biotites from granitic rocks, Northern Portugal. Geochem. Cosmochim. Acta 317 1779-1302.

Altherr, R., Siebel, W., 2002. I-type plutonism in a continental back-arc setting: Miocene granitoids and monzonites from the central Aegean Sea, Greece. Contrib. Mineral. Petrol. 143, 397–415.

Armstrong, J.T., 1995. CITZAF: a package of correction programs for the quantitative electron microbeam X-ray analysis of thick polished materials, thin films, and particles. Microbeam Anal. 4, 177–200.

Barbarin, B., 1996. Genesis of two main types of peraluminous granitoids. Geology 24, 295–298.

Barbarin, B., 1999. A review of the relationships between granitoid types, their origins and their geodynamic environments. Lithos 46, 605–626.

Barbero, L., Villaseca, C., 1992. The Layos granite, Hercynian complex of Toledo (Spain): an example of parautochthonous restite-rich granite in a granulitic area. Trans. R. Soc. Edinb. Earth Sci. 83, 127–138.

Barbey, P., Marignac, C., Montel, J.M., Macaudiere, J., Gasquet, D., Jabbori, J., 1999. Cordierite growth texture and the conditions of genesis and emplacement of crustal granitic magmas: the Velay granite complex (Massif Central, France). J. Petrol. 40, 1425–1441.

Bea, F., Montero, P.G., Gonzalez-Lodeiro, F., Talavera, C., Molina, J.F., Scarrow, J.H., Whitehouse, M.J., Zinger, T., 2006. Zircon thermometry and U–Pb ion-microprobe dating of the gabbros and associated migmatites of the Variscan Toledo Anatectic Complex, Central Iberia. J. Geol. Soc. 163 (2006), 847–855.

Bea, F., 2012. The sources of energy for crustal melting and the geochemistry of heat-producing elements. Lithos 153, 278–291.

Celino, J.J., 1999. Variação Composicional em Suites de Granitóides Neoproterozóicos e sua implicação na evolução do orógeno Araçuaí (Brasil) – oeste Congolês (África). Tese de doutorado. Universidade de Brasília, Brasília 266pp.

Celino, J.J., Conceição, H., 1993. Reconhecimento Geológico dos Granitóides da Faixa de Dobramentos Araçuaí no extremo sul da Bahia e Nordeste de Minas Gerais. In: Anais do II Simpósio do Craton de São Francisco, pp. 252–255.

Celino, J., Botelho, N.F., 2001. Petrologia e Mineraloquímica dos Granitóides Peraluminosos com Cordierita no Extremo Sul da Bahia. Cadernos de Geociências 6, 99–132.

Celino, J.J., Botelho, N.F., Pimentel, M.M., 2000. Genesis of neoproterozoic granitoid magmatism in the eastern Araçuaí fold belt, eastern Brazil: field, geochemical and Sr-Nd isotopic evidente. Rev. Bras. Geociencias 30, 135–139.

Clark, C., Fitzsimons, I.C.W., Healy, D., Harley, S.M., 2011. How does the continental crust get really hot? Elements 7, 235–240.

Clarke, D.B., 1995. Cordierite in felsic igneous rocks: a synthesis. Mineral. Mag. 59, 311–325.

Clemens, J.D., Birch, W.D., 2012. Assembly of a zoned volcanic magma chamber from multiple magma batches: the Cerberean Cauldron, Marysville Igneous Complex, Australia. Lithos 155, 272–288.

Clemens, J.D., Wall, V.J., 1981. Origin and crystallization of some peraluminous (S-type) granitic magmas. Can. Mineral. 19, 111–131.

Coloma, F., Valin, X., Oliveros, V., Vásquez, P., Creixell, C., Salazar, E., Ducea, N., 2017. Andean Geology Geochemistry of Permian to Triassic igneous rocks from northern Chile (28°-30°15'S): implications on the dynamics of the proto-Andean margin. Andean Geol. 44, 147–178. https://doi.org/10.5027/andgeoV44n2-a03.

Connolly, J., 2005. Computation of phase equilibria by linear programming: a tool for geodynamic modeling and its application to subduction zone decarbonation. Earth Planet. Sci. Lett. 236, 524–541.

Currie, C.A., Hyndman, R.D., 2006. The thermal structure of subduction zone back arcs. J. Geophys. Res. 111, 1–22.

Dahlquist, J.A., Alasino, P.H., Basei, M.A.S., Cámera, M.M.M., Grande, M.M., Campos Neto, M.da C., 2018. Petrological, geochemical, isotopic, and geochronological constraints for the Late Devonian–Early Carboniferous magmatism in SW Gondwana (27–32°LS): an example of geodynamic switching. Int. J. Earth Sci. 107, 2575–2603.

De los Hoyos, C.R., Willner, A.P., Larrovere, M.A., Rossi, J.N., Toselli, A.J., Basei, M.A.S., 2011. Tectonothermal evolution and exhumation history of the Paleozoic proto-Andean Gondwana margin crust: the Famatinian belt in NW Argentina. Gondwana Res. 20, 309–324.

Debon, F., Le Fort, P., 1983. A chemical-mineralogical classification of common plutonic rocks and associations. Transactions of the Royal Society of Edinburgh Earth 73, 135–149.

del Rey, A., Deckart, K., Arriagada, C., Martinez, F., 2016. Resolving the paradigm of the late Paleozoic?Triassic Chilean magmatism: isotopic approach. Gondwana Res. 37, 172–181. https://doi.org/10.1016/j.gr.2016.06.008.

Ebadi, A., Johannes, W., 1991. Beginning of melting and composition of first melts I the system Qz-Ab-Or-H_2O-CO_2. Contrib. Mineral. Petrol. 106, 286–295.

England, P., Thompson, A.B., 1984. Pressure-temperature time path of regional metamorphism Part I: heat transfer during the evolution of regions of thickened continental crust. J. Petrol. 25, 894–928.

Erdmann, S., Clarke, D.B., MacDonald, A., 2004. Origin of chemically zoned and unzoned cordierites from the South Mountain and Musquodoboit Batholiths, Nova Scotia. Trans. R. Soc. Edinb. Earth Sci. 95, 99–110.

Evans, O.C., Hanson, G.N., 1993. Accessory-mineral fractionation of rare-earth element (REE) abundances in granitoid rocks. Chem. Geol. 110, 69–93.

Gana, P., 1991. Magmatismo bimodal del Triásico Superior-Jurásico Inferior, en la Cordillera de la Costa, provincias de Elqui y Limarí, Chile. Rev. Geol. Chile 18, 55–67.

Gardien, V., Thompson, A.B., Grujic, D., Ulmer, P., 1995. Experimental melting of biotite + plagioclase + quartz + muscovite assemblages and implications of crustal melting. J. Geophys. Res. 100 (B8), 581–591.

Gervasoni, F., Klemme, S., Rocha-Júnior, E.R.V., Berndt, J., 2016. Zircon saturation in silicate melts: a new and improved model for aluminous and alkaline melts. Contrib. Mineral. Petrol. 171, 21.

González, J., Oliveros, V., Creixell, C., Velásquez, R., Vásquez, P., Lucassen, F., 2017. The Triassic magmatism and its relation with the Pre-Andean tectonic evolution: geochemical and petrographic constrains from the High Andes of north central Chile (29°30′ – 30°S). J. South Am. Earth Sci. 87, 95–112.

Gordillo, C.E., Schreyer, W., Werding, G., Abraham, K., 1985. Lithium in NaBe-cordierites from El Peñón, Sierra de Córdoba, Argentina. Contrib. Mineral. Petrol. 90, 93–101.

Grosse, P., Sollner, F., Baez, M.A., Toselli, A.J., Rossi, J.N., De La Rosa, J.D., 2009. Lower Carboniferous post-orogenic granites in central-eastern Sierra de Velasco, Sierras

Pampeanas, Argentina: U– Pb monazite geochronology, geochemistry and Sr–Nd isotopes. Int. J. Earth Sci. 98, 1001–1025.
Harley, S.L., Thompson, P., Hensen, B.J., Buick, I.S., 2002. Cordierite as a sensor of fluid compositions in high-grade metamorphism and crustal anatexis. J. Metamorph. Geol. 20, 71–86.
Hervé, F., Fanning, C.M., Calderón, M., Mpodozis, C., 2014. Early Permian to late Triassic batholiths of the Chilean Frontal Cordillera (28°–31°S): SHRIMP U–Pb zircon ages and Lu–Hf and O isotope systematics. Lithos 184−187, 436–446.
Holland, T., Powell, R., 1998. An internally consistent thermodynamic data set for phases of petrological interest. J. Metamorph. Geol. 16, 309–343.
Holtz, F., Johannes, W., 1991. Genesis of peraluminous granites I. Experimental investigation of melt compositions at 3 and 5 kbar and various H_2O activities. J. Petrol. 32, 935–958.
Hoskin, P.W.O., Schaltegger, U., 2003. The composition of zircon and igneous and metamorphic petrogenesis. In: In: Hanchar, J.M., Hoskin, P.W.O. (Eds.), Zircon. Mineralogical Society of America, Reviews in Mineralogy and Geochemistry, vol. 53. pp. 27–62.
Hsu, L.C., 1968. Selected phase relationships in the system Al-Mn-Fe-Si-O-H: a model for Garnet Equilibria. J. Petrol. 9, 40–83.
Ishihara, S., 1977. The magnetite-series and ilmenite-series granitic rocks. Min. Geol. 27, 293–305.
Johannes, W., Holtz, F., 1996. Petrogenesis and experimental petrology of granitic rocks. In: In: Wyllie, P.J., El Goresy, A., Engelhardt, W. von, Hahn, T. (Eds.), Minerals and Rocks, vol. 22 Springer-Verlag, Berlin (335 pp.).
Matteini, M., Dantas, E.L., Pimentel, M.M., Buhn, B., 2010. Combined U-Pb and Lu-Hf isotope analyses by laser ablation MC-ICP-MS: methodology and applications. Anais of the Brazilian Academy of Sciences 82, 479–491.
Miller, C.F., 1985. Are strongly peraluminous magmas derived from pelitic sedimentary sources? J. Geol. 93, 673–689.
Miller, C.F., McDowell, S.M., Mapes, R.W., 2003. Hot and Cold Granites? Implications of Zircon Saturation Temperatures and Preservation of Inheritance.
Mpodozis, C., Kay, S.M., 1992. Late Paleozoic to Triassic evolution of the Gondwana margin: evidence from Chilean Frontal Cordilleran batholiths (28°S to 31°S). Geol. Soc. Am. Bull. 104, 999–1014.
Nabelek, P.I., Whittington, A.G., Hofmeister, A.M., 2010. Strain heating as a mechanism for partial melting and ultrahigh temperature metamorphism in convergent orogens: implications of temperature-dependent thermal diffusivity and rheology. J. Geophys. Res. Solid Earth 115, 1–17.
Nachit, H., Razafimahefa, N., Stussi, J.M., Carron, J., 1985. Composition chimique des biotites et typologie magmatique des granitoides. Comptes Rendus de l'Académie des Sciences Paris 301, 813–817.
Oberc-Dziedzic, T., Kryza, R., Pin, C., 2015. Last stage of Variscan granitoid magmatism in the Strzelin Massif (SW Poland): petrology and age of the biotite-muscovite granites. Geol. Q. 59, 718–737.
O´Neil, J., Shaw, S.E., Flood, R.H., 1977. Oxygen and hydrogen isotope compositions as indicators of granite genesis in the new England batholith, Australia. Contrib. Mineral. Petrol. 62, 313–328.
Pankhurst, R.J., Rapela, C.W., Fanning, C.M., 2000. Age and origin of coeval TTG, I- and S-type granites in the Famatinian belt of NW Argentina. Trans. R. Soc. Edinb. Earth Sci. 91, 151–168.
Parada, M.A., 1988. Pre-Andean peraluminous and metaluminous leucogranitoid suites in the High Andes of Central Chile. J. South Am. Earth Sci. 4, 211–221.
Parada, M.A., Munizaga, F., Kawashita, K., 1981. Edades Rb-Sr roca total del batolito compuesto de los ríos Elqui–Limarí a la latitud 30°S. Rev. Geol. Chile 13–14, 87–93.
Parada, M.A., Levi, B., Nyström, J.O., 1991. Geochemistry of the Triassic to Jurassic plutonism of Central Chile (30° - 33°S): petrogenetic implications and a tectonic discussion. In: In: Harmon, R.S., Rapela, C.W. (Eds.), Andean Magmatism and its Tectonic Setting. Geological Society of America Special Paper, vol. 265. pp. 99–112.
Parada, M.A., López-Escobar, L., Fuentes, F., Morata, D., Calderón, M., Aguirre, L., Feraud, F., Spinoza, F., Moreno, H., Figueroa, O., Muñoz Bravo, J., Troncoso Vasquez, R., Stern, C.R., 2007. Andean magmatism. In: Gibson, W., Moreno, T. (Eds.), The Geology of Chile. The Geological Society of London (115–146 pp.).
Patiño Douce, A.E., 1999. What do experiments tell us about the relative contributions of crust and mantle to the origin of granitic magmas? In: In: Castro, A., Fernández, C., Vigneresse, J.L. (Eds.), Understanding Granites: Integrating New and Classical Techniques, vol. 168. Geological Society, London, pp. 55–75 Special Publication.
Patiño Douce, A.E., Johnston, A.D., 1991. Phase equilibria and melt productivity in the pelitic system: implications for the origin of peraluminous granitoids and aluminous granulites. Contrib. Mineral. Petrol. 107, 202–218.
Pereira, M.D., Bea, F., 1994. Cordierite-producing reactions in the Pefia Negra Complex, Avila batholith, Central Spain: the key role of cordierite in low-pressure anatexis. Can. Mineral. 32, 763–780.
Puziewicz, J., Johannes, W., 1988. Phase equilibria and compositions of Fe-Mg-Al inerals and melts in water-saturated peraluminous granitic systems. Contrib. Mineral. Petrol. 11, 156–168.
Rapela, C.W., Pankhurst, R.J., Dahlquist, J., Fanning, C.M., 1999. U–Pb SHRIMP ages of Famatinian Granites: new constraints on the timing, origin and tectonic setting of I- and S-type magmas in an ensialic arc. In: Carlos Paz, Actas II South American Symposium on Isotope Geology, pp. 264–267.
Rossi, J.N., Toselli, A.J., Saavedra, J., Sial, A.N., Pellitero, E., Ferreira, V.P., 2002. Common crustal source for contrasting peraluminous facies in the early Paleozoic Capillitas batholith, NW Argentina. Gondwana Res. 5, 325–337.
Sato, K., Tassinari, C.C.G., Kawashita, K., Petronillo, L.A., 1995. O método geocronológico Sm-Nd no IGc-USP e suas aplicações. Anais of the Brazilian Academy of Sciences 3, 313–336.
Scaillet, B., Holtz, F., Pichavant, M., 2016. Experimental constraints on the formation of silicic magmas. Elements 12, 109–114.
Schreyer, W., 1965. Synthetische und natürliche Cordierite II: die chemischen Zusammensetzungen natürlicher Cordierite und ihre Abhängigkeit von den PTX-Bedigungen bei der Gesteinbildung. Neues Jahrbuch für Mineralogie 10, 35–79.
Silva, L.C. da, Armstrong, R., Noce, C.M., Carneiro, M.S., Pimentel, M., Soares, A.C.P., Leite, C.A., Vieira, V.S., Silva, M.A. da, Castro Paes, V.J. de, Cardoso Filho, J.M., 2002. Reavaliação da evolução geológica em terrenos pré-cambrianos brasileiros com base em novos dados U-Pb SHRIMP, parte II: orógeno Araçuaí, cinturão mineiro e cráton São Francisco meridional. Rev. Bras. Geociencias 32, 513–528.
Takahashi, M., Aramaki, S., Ishihara, S., 1980. Magnetite series ilmenite-series vs. I-type S-type granitoids. Mining Geology Special Issue 8, 13–28.
Taylor, R.S., McLennan, S., 1985. The Continental Crust: its Composition and Evolution. Blackwell, Oxford 312 pp.
Toselli, G., Saavedra, J., Córdoba, G., Medina, M., 1991. Petrología y geoquímica de los granitos de la zona Carrizal-Mazán, La Rioja-Catamarca. Asociación Geológica Argentina Revista 56, 36–50.
Toselli, A.J., Sial, A.N., Rossi, J.N., 2002. Ordovician magmatism of the Sierras Pampeanas, Sistema de Famatina and Cordillera Oriental, NW Argentina. INSUGEO, Série Correlación Geologica 16, 313–326.
Toselli, A.J., Sial, A., Parada, M.A., Saavedra, J., Ferreira, V., Rossi, J., Celino, J., 2003a. Cordierite-bearing granitoids from contrasting terranes of Brazil, Argentina and Chile: a comparative study. In: V Hutton Symposium, the Origin of Granites and Related Rocks. Abstract with Program, pp. 154.
Toselli, A.J., Basei, M.A., Rossi de Toselli, J.N., Dudas, R., 2003b. Análisis geoquímico-geocronológico de rocas granulíticas y calcosilicáticas de las Sierras Pampeanas Noroccidentales. Rev. Asoc. Geol. Argent. 58, 629–642.
Toselli, A.J., Rossi, J.N., Basei, M.A., 2014. Geología e interpretación petrológica de los granitos y pegmatitas de la Sierra de Mazán, La Rioja, Argentina. *INSUGEO*. Ser. Correlación Geol. 30, 35–73.
Valley, J.W., Kitchen, N.E., Kohn, M.J., Niendorf, C.R., Spicuzza, M.J., 1995. UWG-2, a garnet standard for oxygen isotope ratio: strategies for high precision and accuracy with laser heating. Geochem. Cosmochim. Acta 59, 5223–5231.
Valley, J.W., Lackey, J.S., Cavosie, A.J., Clechenko, C.C., Spicuzza, M.J., Basei, M.A.S., Bindeman, I.N., Ferreira, V.P., Sial, A.N., King, E.M., Peck, W.H., Sinha, A.K., Wei, C.S., 2005. 4.4 billion years of crustal maturation: oxygen isotope ratios of magmatic zircon. Contrib. Mineral. Petrol. 150, 561–580.
Vásquez, P., Glodny, J., Franz, G., Frei, D., Romer, R.L., 2011. Early Mesozoic plutonism of the Cordillera de la Costa (34°–37°S), Chile: constraints on the Onset of the Andean Orogeny. J. Geol. 119, 159–184. https://doi.org/10.1086/658296.
Vielzeuf, D., Holloway, J.R., 1988. Experimental determination of the fluid-absent melting relations in the pelitic system. Consequences for crustal differentiation. Contrib. Mineral. Petrol. 98, 257–276.
Villaseca, C., Barbero, L., 1994. Chemical variability of Al-Ti-Fe-Mg minerals in peraluminous granitoid rocks from central Spain. Eur. J. Mineral. 6, 691–710.
Villaseca, C., Barbero, L., Herreros, V., 1998. A reexamination of the typology of peraluminous granite types in intracontinental orogenic belts. Trans. R. Soc. Edinb. Earth Sci. 89, 113–119.
Villaseca, C., Pérez-Soba, C., Merino, E., Orejana, D., López-García, J.A., Billstrom, K., 2008. Contrasting crystal sources for peraluminous granites of the segmented Montes de Toledo batholith (iberian Variscan belt). J. Geosci. 53, 263–280.
Weinberg, R.F., Hasalová, P., 2015. Water-fluxed melting of the continental crust: A review. Lithos 212–215, 158–188.
White, A.J.R., Chappell, B.W., 1977. Ultrametamorphism and granitoid genesis. Tectonophysics 43, 7–22.
Wickham, S.M., 1987. The segregation and emplacement of granitic magmas. J. Geol. Soc. Lond. 144, 281–297.
Wones, D.R., 1989. Significance of the assemblage titanite + magnetite + quartz in granitic rocks. Am. Mineral. 74, 744–749.
Zen, E-an, 1988. Phase relations of peraluminous granitic rocks and their petrogenetic implications. Ann. Rev. Earth Planet. Sci. Lett. 16, 21–51.